JAXA Research and Development Report

In-orbit Control Experiment on ETS-VIII Spacecraft

ETS-VIII In-orbit Attitude Control Experiment Team

September 2012

Japan Aerospace Exploration Agency

ETS-VIII In-orbit Attitude Control Experiment Team:

Takashi Ohtani*, Yoshiro Hamada*, Takashi Kida[†], Tomoyuki Nagashio[†1], Isao Yamaguchi[*2], Tokio Kasai*, Takahiro Igawa*, Shinji Mitani*, Kei Sunagawa[‡3], Masafumi Ikeda[‡4]

   *: Aerospace Research and Development Directorate (ARD),
     Japan Aerospace Exploration Agency (JAXA)
   †: University of Electro-Communicatios
   ‡: Space Applications Mission Directorate, JAXA

Corresponding Author:

   Y. Hamada (hamada.yoshiro@jaxa.jp)

Lead Authors:

   Section 1. T. Kida
   Section 2. Y. Hamada
   Section 3. Y. Hamada
   Section 4. T. Nagashio
   Section 5. T. Nagashio
   Section 6. T. Ohtani
   Section 7. Y. Hamada
   Section 8. T. Nagashio
   Section 9. Y. Hamada

---

[1] Present affiliation: Osaka Prefecture University
[2] Present affiliation: National Defense Academy of Japan
[3] Present affiliation: Information Gathering Satellite Systems Development Group, JAXA
[4] Present affiliation: Human Resources Department, JAXA

Contents

In-orbit Control Experiment on ETS-VIII Spacecraft

ETS-VIII In-orbit Attitude Control Experiment Team[*],[**]

*: Japan Aerospace Exploration Agency (JAXA)

**: University of Electro-Communicatios

Abstract: This paper describes an in-orbit attitude control experiment carried out on ETS (Engineering Test Satellite)-VIII in June 2009 and March 2010. This experiment aims to develop a technical basis for the attitude control of a class of future large flexible spacecraft. Four novel robust control laws were developed and tested through the experiment; DVDFB (Direct Velocity and Displacement FeedBack) control law, DDFB (Dynamic Displacement FeedBack) control law, μ-synthesis based control law, and linearly interpolated gain scheduling law. Experimental results of each control law are presented to show its high control performance compared with a conventional control law.

1 Introduction

This report describes the results of the project on in-orbit advanced robust attitude control experiment using Engineering Test Satellite VIII (ETS-VIII) carried out by Japan Aerospace Exploration Agency (JAXA) during 2009 and 2010. It gives a full detail of the spacecraft system configuration, modeling, robust control laws, pre-launch evaluation, in-orbit experiment and post-flight evaluation results.

In the recent space program, there is a trend that spacecraft is equipped with large flexible solar paddles and antenna reflectors. Controlling such flexible spacecraft with high accuracy requires control of structural vibrations as well as attitude. The critical issue of vibration control is the spillover phenomenon caused by coupling between the control system and higher frequency vibration modes [1]. In face of this, many control laws have been studied up to now. Their common research objective is to guarantee robust stability against the higher vibration modes and modal parameter uncertainties based on the advanced control theories. On the other hand, industry engineers still continue to devote their efforts to designing classical controllers even for flexible spacecraft in spite of their apparent limitation. This fact implies that there is a certain gap between practitioners and researchers.

In view of this, some in-orbit robust control experiments have been performed and reported [2, 3]. Their final goal is to demonstrate the ability of advanced robust control laws in the same environment as the classical control technology and to certify the role of the theoretical achievement in space program.

With the same goal, an in-orbit attitude control experiment using Engineering Test Satellite VI (ETS-VI) was carried out by National Space Development Agency (NASDA) and National Aerospace Laboratory (NAL) in 1994 [4, 5]. In the project, several types of a class of single input single output (SISO) H_∞ dynamic output feedback controllers were designed and their effectiveness has been confirmed. Although the experiment was successful, some research issues have remained. One of them is the design of multi input multi output (MIMO) controllers for linear parameter varying (LPV) spacecraft systems.

Based on the experience, we have planned and carried out another robust control in-orbit experiment on ETS-VIII from 2009 to 2010. ETS-VIII was launched into Geo-synchronous orbit by JAXA in 2006 using H-IIA launch vehicle which is the largest spacecraft that Japan has developed to date. Since the spacecraft has two large deployable reflectors and two solar paddles that rotate around the pitch axis, the dynamics has coupling between three axes, and the system parameters drastically change according to the paddle rotation. Therefore the control problem is to design robust controllers for MIMO LPV flexible spacecraft.

For the problem, we have prepared three classes of controllers after trade-off study. They are μ-synthesis based controller, robust gain scheduling controller and robust symmetric output feedback controller [6, 7, 8]. The μ-synthesis based on the structured singular value gives the linear time invariant controller which ensures the robust stability for all paddle angles [6]. For the gain scheduled controller, we have

proposed the linearly interpolated gain scheduling according to the paddle rotation angle [7]. The final symmetric output feedback controller has a salient robust stability under the input output collocation condition [8]. Besides robust stability, every controller is designed so as to satisfy excellent control performances on disturbance rejection and step command response by taking into account of the implementation constraints such as the actuator torque maximum level, the onboard computer memory capacity and computation ability.

After the pre-launch evaluation using the full software simulator of Attitude and Orbit Control Subsystem (AOCS) and the Static Closed-Loop Test (SCLT), the control algorithm has been installed into the onboard computer. Then the in-orbit experiment has been carried out during two weeks, in Summer 2009 and Winter 2010. The telemetry data has been successfully obtained and analyzed.

This report is organized as follows. The ETS-VIII spacecraft system configuration concerned with in-orbit experiment is outlined in Section 2. Section 3 describes spacecraft dynamical equation used in control law design. The baseline PD control law is described in Section 4, followed by the algorithms of proposed robust control laws in Section 5, 6 and 7. The in-orbit experiment results of these control laws are shown and compared with each other in Section 8. Section 9 concludes the overall results and discusses our scope.

2   Spacecraft System Configuration and In-orbit Control Experiment

2.1   ETS-VIII Spacecraft

The large flexible spacecraft ETS-VIII was launched in 2006 by Japan's H-IIA launch vehicle No. 11. ETS-VIII was developed primarily to establish and validate the world's largest geostationary satellite bus technology aimed at mainly at handling the increasing demand for digital communications from mobile devices. This spacecraft, with a gross weight of around three tonnes and a diameter of 40 meters, has two large deployable antenna reflectors (LDRs) and two solar array paddles which are deployed in the pitch
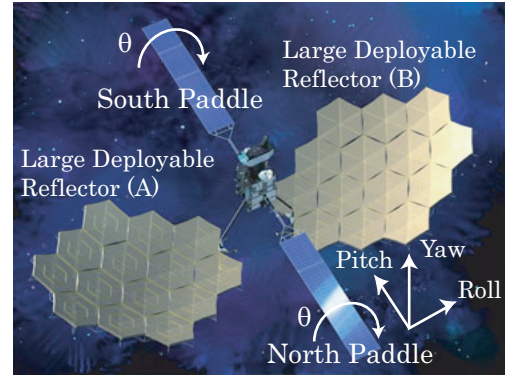

Figure 1: ETS-VIII and its rigid body coordinate system.
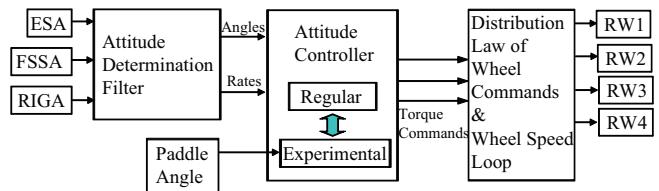
Figure 2: ETS-VIII attitude control system.

direction and rotate 360 degrees each day so that each wing constantly faces the sun (Fig. 1).

2.2   Attitude Control System

The attitude control system used in the experiment is shown in Fig. 2.

Sensors   The spacecraft's attitude is monitored by an earth sensor assembly (ESA), a fine sun sensor (FSS) and an rate integrating gyro assembly (RIGA). Attitude angles and rates for each axis are estimated from the sensor outputs by an attitude determination filter.

Controllers   The spacecraft is equipped with an experimental controller in addition to a regular (bus) controller. Control outputs are torque commands for the roll, pitch and yaw axes. The experimental controller can utilize not only attitude angle and rate information but also paddle rotation angle. For safety, the spacecraft's attitude is continuously monitored by a fault detection and isolation system, which in the event of an emergency automatically discontinues the experiment and switches control to a safety control mode.

The following control laws can be installed in the experimental controller:

- PD+LPF (Low Pass Filter) control law

- DVDFB (Direct Velocity and Displacement Feed-Back) control law

- DDFB (Dynamic Displacement FeedBack) control law

- μ-synthesis based control law

- Linearly interpolated gain scheduling control law

The PD+LPF control law is described in Section 4, which is almost the same as the bus control law and serves as a baseline. Both DVDFB and DDFB control laws take advantage of symmetric structure of the spacecraft in order to guarantee robust stability against the paddle rotation. They also utilize the paddle rotation angle for improving tracking performance by feedforward control laws. Their full details are given together in Section 5. Although the μ-synthesis based control law is rather conservative, it is an authentic robust control law and easily designed by commonly used controller design procedure. This is precisely expressed in Section 6. Finally, the linearly interpolated gain scheduling control law, which is depicted in Section 7, changes feedback gains linearly on the paddle rotation angle in order to guarantee robust stability against the paddle rotation.

Actuators Four reaction wheels (RWs) with a 0.04 Nm maximum torque are installed in a skewed arrangement. Torque commands from the control law are converted into wheel commands by a distribution law. A wheel speed loop is also provided to control the reaction wheels according to the wheel commands.

In addition to the reaction wheels, the spacecraft has also eight attitude control thrusters and four station-keeping thrusters. In the control experiment, these are used not for attitude control system but as a disturbance generator.

2.3   Overview of the Experiment

The in-orbit experiment was conducted in two periods, during June 2009 and March 2010. The five

control laws described in Section 4-7 were tested and the following responses were obtained for each control law. These results are summarized in Appendix E.

- Step command response
  Since the main mission of ETS-VIII is an in-orbit experiment on direct communication with handheld terminals, highly accurate attitude control is required. In this experiment, the accuracy of attitude control was validated by analysing responses to ± 0.05 deg step commands (Fig. 3).

- Impulse disturbance response
  Station-keeping maneuvers required for ETS-VIII to maintain its orbit cause torque disturbances to the attitude control system. The spacecraft is required to maintain its attitude error against these torque disturbances to within 0.05 deg. To validate disturbance attenuation performance, this experiment simulated the east-west station-keeping maneuver by firing the station-keeping thrusters.

- Rectangular disturbance response
  This experiment aimed to validate disturbance attenuation performance for each axis individually by applying a rectangular torque input of 0.04 Nm for 30 seconds around axis using the reaction wheels.

- Large disturbance response
  This aimed to determine how the control system reacts to large disturbances with smaller torque control inputs. The attitude control thrusters applied disturbance torques of 35.5, 65.5, 20.4 Nm of 62.5 msec duration around the roll, pitch, yaw axes individually.

- Random disturbance response (A)
  This was carried out primarily to obtain in-orbit data for system identification. The reaction wheels were driven by m-sequences with a 0.5 Hz oscillation band and a maximum amplitude of 0.04 Nm. The disturbance was created for 1800 seconds simultaneously in each axis.

- Random disturbance response (B)
 The reaction wheels were driven by m-sequences
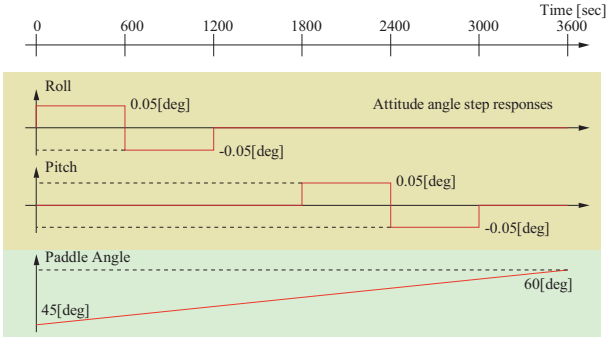
Figure 3: Step commands.
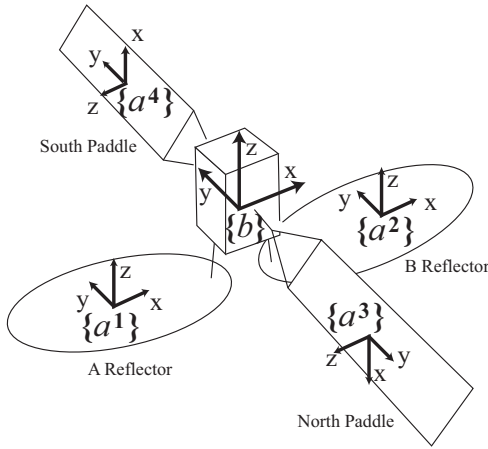
Figure 4: Coordinate systems of the rigid body ($\{b\}$) and each appendage ($\{a^i\}$).

with a 0.5 Hz oscillation band and a maximum amplitude of 0.04 Nm. Unlike disturbance response (A), the disturbance was created individually in each axis.

3 Spacecraft Model

3.1 Mathematical Model of the Spacecraft

This section illustrates the mathematical model of ETS-VIII spacecraft. This is described as a rigid body with four flexible appendages labeled as

$i = 1$: large deployable reflector A (LDR-A)
$i = 2$: large deployable reflector B (LDR-B)
$i = 3$: north solar paddle
$i = 4$: south solar paddle

The coordinate systems of the rigid body and each appendage are shown in Fig. 4. The following parameters are defined:

m_b : mass of the rigid body
m_{ai} : mass of the i-th appendage
J_b : moment of inertia tensor of the rigid body
J_{ai} : moment of inertia tensor of the i-th appendage
r_b : position vector of the center of mass of the rigid body
r_{ai} : position vector of the center of mass of the i-th appendage
R_{ai} : interface point of the i-th appendage
C_i : DCM (Direction Cosine Matrix) of the i-th appendage coordinate system from the rigid body coordinate system
d_{ai}^0 : coupling matrix between the i-th appendage and the linear motion.
d_{ai}^1 : coupling matrix between the i-th appendage and the rotation.

The paddle rotation angle is denoted by $\delta \in \boldsymbol{R}$ and defined as $\delta := 0$ when each solar cell faces the $-x_b$ direction. Then the DCMs are described as the following matrix functions of δ:

$$
\begin{aligned}
C_1 &= C_2 = \begin{bmatrix} 1 & 0 & 0 \\ 0 & 1 & 0 \\ 0 & 0 & 1 \end{bmatrix} \\
C_3(\delta) &= \begin{bmatrix} -\sin\delta & 0 & -\cos\delta \\ 0 & -1 & 0 \\ -\cos\delta & 0 & \sin\delta \end{bmatrix} \\
C_4(\delta) &= \begin{bmatrix} \sin\delta & 0 & \cos\delta \\ 0 & 1 & 0 \\ -\cos\delta & 0 & \sin\delta \end{bmatrix}
\end{aligned} \tag{1}
$$

The paddle rotation speed is assumed sufficiently slow (4.17×10^{-3} deg/sec ($= 360$ deg/day)) to allow the following relatively simple formulations for the rigid-body equations of motion and flexible component vibration [9]:

$$
M\ddot{r} + \Upsilon^T\ddot{\theta} + \sum_{i=1}^{4}\Gamma_i\ddot{\eta}_i = f \tag{2}
$$

$$
\Upsilon\ddot{r} + J\ddot{\theta} + \sum_{i=1}^{4}P_i\ddot{\eta}_i = t \tag{3}
$$

$$
\Gamma_i^T\ddot{r} + P_i^T\ddot{\theta} + \ddot{\eta}_i + 2Z_i\Omega_i\dot{\eta}_i + \Omega_i^2\eta_i = 0 \tag{4}
$$
$$
(\text{for } i = 1, \dots, 4),
$$

where $r = [r_x,\ r_y,\ r_z]^T$ is the position vector of the center of mass of the whole system, $\theta = [\theta_{roll}, \theta_{pitch}, \theta_{yaw}]$ is the attitude angle vector, $\eta_i \in \boldsymbol{R}^{n_i}$ is the modal coordinate of the i-th appendage. Thirty vibration modes are identified for all appendages by finite element analysis ($n_1 = n_2 = 8$, $n_3 = n_4 =$

7). $Z_i = \text{diag}[\zeta_{ai,1}, \ldots, \zeta_{ai,n_i}] \in \mathbf{R}^{n_i \times n_i}$ and $\Omega_i = \text{diag}[\omega_{ai,1}, \ldots, \omega_{ai,n_i}] \in \mathbf{R}^{n_i \times n_i}$ are damping ratio and modal frequency matrix corresponding to η_i respectively, $f \in \mathbf{R}^3$ is the force input and $t \in \mathbf{R}^3$ is the torque input. M, J, Υ, Γ_i and P_i are defined as:

$$
\begin{aligned}
M &:= m_b + \sum_{i=1}^{4} m_{ai} \\
J &:= J_b - m_b \tilde{r}_b \tilde{r}_b + \sum_{i=1}^{4} C_i^T J_{ai} C_i - \sum_{i=1}^{4} m_{ai} \tilde{r}_{ai} \tilde{r}_{ai} \\
\Upsilon &:= m_b \tilde{r}_b + \sum_{i=1}^{4} m_{ai} \tilde{r}_{ai} \\
\Gamma_i &:= C_i^T d_{ai}^0 \\
P_i &:= \tilde{R}_{ai} C_i^T d_{ai}^0 + C_i^T d_{ai}^1,
\end{aligned}
$$

where $\tilde{r}_*$ is a skew-symmetric matrix of r_*.

3.2 Spacecraft Model for Attitude Controller Design

Some versions of the spacecraft model were obtained during the development phase. Basically the PSR model, which was constructed for PSR (Pre-Shipment Review), was used in controller design. The PSR model parameters vary according to the model version:

PSR-BOL This model is based on the assumption that the spacecraft is in BOL (Beginning Of Life) phase. This is used for both controller design and simulation.

PSR-EOL This model is derived assuming that the spacecraft is in EOL (End Of Life) phase. This is used for simulation in order to assure that designed controllers are robust against fuel consumption.

PSR-ID This is based on the results of preliminary identification experiments carried out during the in-orbit checkout phase, where modal parameters of flexible appendages were identified. This is used for simulation.

The parameter values defined in Section 3.1 are described for each version in Appendix A.

Since the experiment deals with only attitude control, the force input f is rather small during the experiment and the effect of linear motion on vibration can also be ignored. Linear motions are therefore omitted from the spacecraft dynamics and following hybrid equations are used in controller design:

$$
J(\delta)\ddot{\theta} + \sum_{i=1}^{4} P_i(\delta)\ddot{\eta}_i = t \tag{5}
$$

$$
P_i^T(\delta)\ddot{\theta} + \ddot{\eta}_i + \Lambda_i \dot{\eta}_i + \Omega_i^2 \eta_i = 0 \tag{6}
$$

$$
(\text{for } i = 1, \ldots, 4),
$$

where $\Lambda_i = 2Z_i \Omega_i$. Matrices J and P_i are now replaced by $J(\delta)$ and $P_i(\delta)$ in order to clarify δ-dependence of these terms. The torque input t includes the three-axis torque control input generated by reaction wheels and disturbance input.

For the measurement outputs, estimates of the attitude angles and their rates are available from attitude determination logic based on the ESA, FSSA and RIGA sensors:

$$
y = \left[\begin{array}{c} y_1 \\ y_2 \end{array}\right] = \left[\begin{array}{c} \theta \\ \dot{\theta} \end{array}\right] \tag{7}
$$

The dependency of the spacecraft model on paddle rotation angle δ is also evaluated by singular value plots of the open-loop plant from the control torque input t to the attitude angles y_1 for paddle angles of $\delta = 0, 45$ and 90 deg (Fig. 5). It can be seen that there is variation of the mode frequencies and that many vibration modes exist in the lower frequency range.

Equations (5), (6) and (7) are compactly described in the following "constrained mode model" [10] of the spacecraft with attached components:

$$
M(\delta)\ddot{q} + D\dot{q} + Kq = Lu + Lw, \tag{8}
$$

$$
y = \left[\begin{array}{c} y_1 \\ y_2 \end{array}\right] = \left[\begin{array}{cc} L^T & 0 \\ 0 & L^T \end{array}\right] \left[\begin{array}{c} q \\ \dot{q} \end{array}\right],
$$

where

$$
\begin{aligned}
M(\delta) &= \left[\begin{array}{c|cccc} J(\delta) & P_1(\delta) & P_2(\delta) & P_3(\delta) & P_4(\delta) \\ \hline P_1^T(\delta) & I_{n_1} & 0 & 0 & 0 \\ P_2^T(\delta) & 0 & I_{n_2} & 0 & 0 \\ P_3^T(\delta) & 0 & 0 & I_{n_3} & 0 \\ P_4^T(\delta) & 0 & 0 & 0 & I_{n_4} \end{array}\right], \\
&= \left[\begin{array}{cc} J(\delta) & P(\delta) \\ P^T(\delta) & I_{\Sigma_i n_i} \end{array}\right]
\end{aligned}
$$
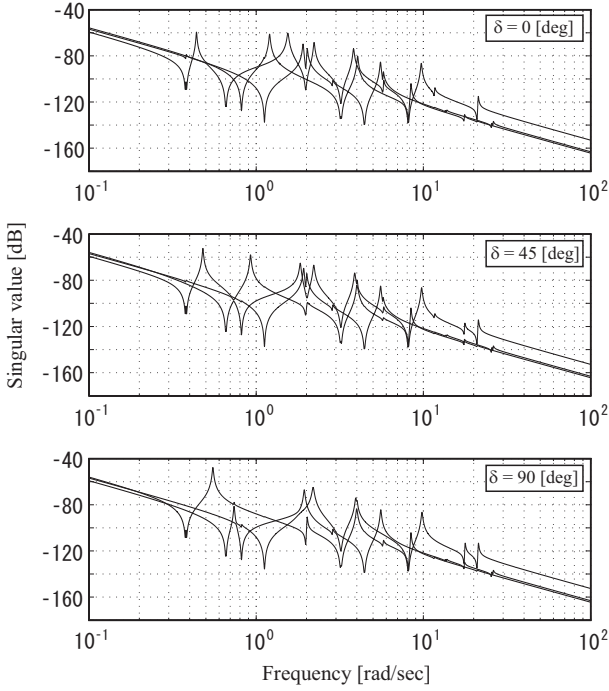
Figure 5: Singular value plots of the spacecraft model (PSR-BOL) for $\delta = 0$ (top), 45 (middle) and 90 (bottom).

$$D = \begin{bmatrix} 0_{3\times3} & & & & \mathbf{0} \\ & \Lambda_1 & & & \\ & & \Lambda_2 & & \\ \mathbf{0} & & & \Lambda_3 & \\ & & & & \Lambda_4 \end{bmatrix}$$

$$= \begin{bmatrix} 0_{3\times3} & 0_{3\times\Sigma_i n_i} \\ 0_{\Sigma_i n_i \times 3} & \Lambda \end{bmatrix},$$

$$K = \begin{bmatrix} 0_{3\times3} & & & & \mathbf{0} \\ & \Omega_1^2 & & & \\ & & \Omega_2^2 & & \\ \mathbf{0} & & & \Omega_3^2 & \\ & & & & \Omega_4^2 \end{bmatrix}$$

$$= \begin{bmatrix} 0_{3\times3} & 0_{3\times\Sigma_i n_i} \\ 0_{\Sigma_i n_i \times 3} & \Omega^2 \end{bmatrix},$$

$$L = \begin{bmatrix} I_3 \\ 0_{\Sigma_j n_j \times 3} \end{bmatrix},$$

$$q = \begin{bmatrix} \theta^T & \eta_1{}^T & \eta_2{}^T & \eta_3{}^T & \eta_4{}^T \end{bmatrix}^T \in \boldsymbol{R}^{(3+\Sigma_j n_j)\times1}.$$

Here $u \in \boldsymbol{R}^3$ and $w \in \boldsymbol{R}^3$ are the three-axis torque control input and disturbance input $(t = u + w)$. The output equations $y_1 = L^T q$ and $y_2 = L^T \dot{q}$ hold since sensors and actuators are co-located on the rigid spacecraft body.

This constrained mode model is used for control law design in the following sections; DVDFB and DDFB control laws are designed using the model directly, μ-synthesis based design is achieved by describing the model as a descriptor form, and the gain scheduling control law is designed using the "unconstrained mode model" that is derived from (8).

4   Baseline PD Control Law

In this section, we describe a design scheme for a baseline PD control law which is used in the in-orbit experiment for comparison with our proposed control laws. This control law is designed by applying standard design scheme of flexible spacecraft's linear time invariant (LTI) SISO model. The following requirements must be satisfied in the experiment.

1. The torque control input does not oscillate the vibration modes of the flexible appendages.

2. The torque control input does not saturate at the all response cases except the large disturbance response case caused by the attitude thruster firing.

Additionally, it is desirable that the control law keeps same control performance irrespective of the paddle angle. In order to satisfy these requirements, we design the control law by using the following procedure[5].

First, a frequency shaping filter is designed for cutting off the control input on the high frequency range. For the purpose, four types of filters, which are a first order lead-lag, a second order lead-lag, a first order low-pass and a second order low-pass, are evaluated. Fig. 6 shows bode diagrams of these filters. The cut off frequencies of the filters have been decided to be lower than the all vibration mode frequencies of ETS-VIII. The performance is estimated by the frequency property of the open-loop system which consists of the filter, a suitable PD gain and the spacecraft dynamics model (4) - (6) of each attitude axis. The extracted bode diagrams of the open-loop systems are shown in Figs. 7 - 9. In view of the facts that the phase margin is sufficient and that there does not exist the direct feedthrough term, we

---

[5]It is known that a control law using MDM / MDP technique is effective for LPV systems[11]. However, we design a simple standard PD control law in order to estimate control performances of general case.
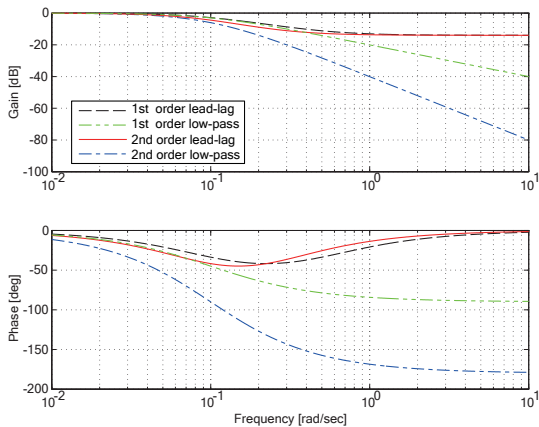
Figure 6: Bode diagram of each filter.

have decided to use the first order low-pass filter so as to have

$$F_i(s) = \frac{\omega}{s + \omega}, \ \omega = 0.1, \ i = \text{roll, pitch, yaw} \quad (9)$$

as its diagonal elements.

Next, the gain values of PD control law are decided through trial and error. By applying several sets of P and D gain values with the above low-pass filter to the plant, we have calculated the step responses. The extracted results are shown in Figs. 10, 11. From each performance of the settling time, the maximum amplitude and the torque control input level in the results, the gain value matrices have been decided as

$$\begin{aligned} K_p &= \text{diag}[\ 20\ 20\ 20\ ] \\ K_d &= \text{diag}[\ 1100\ 1100\ 1100\ ]. \end{aligned} \quad (10)$$

The block diagram of the closed-loop system is shown in Fig. 12. The open-loop bode diagrams using the control gain values with the low-pass filter are shown in Figs. 13 - 15. From these figures, it is apparent that the phase margin is secure at each paddle angle.
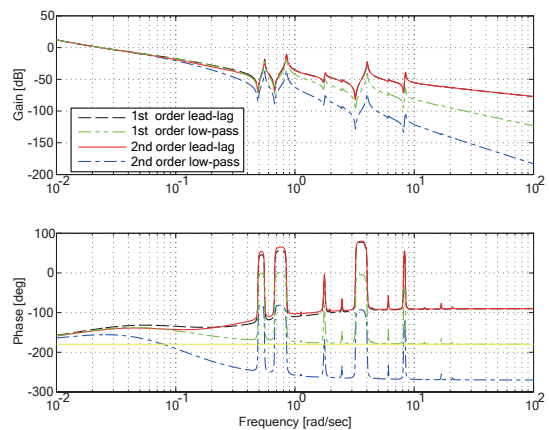
Figure 7: Bode diagram of open-loop system with paddle angle 45 deg : roll axis.
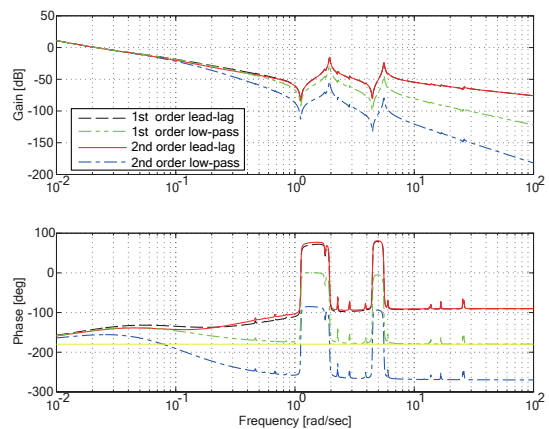

Figure 8: Bode diagram of open-loop system with paddle angle 45 deg : pitch axis.
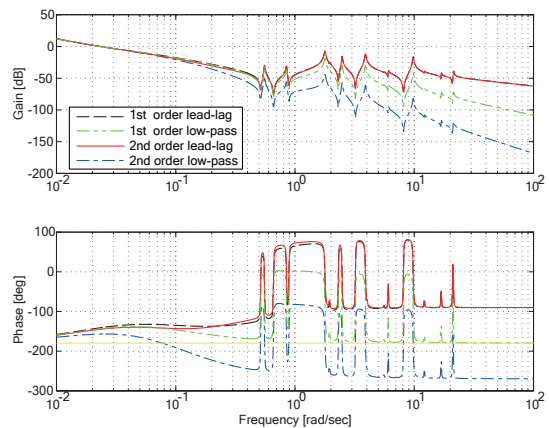
Figure 9: Bode diagram of open-loop system with paddle angle 45 deg : yaw axis.
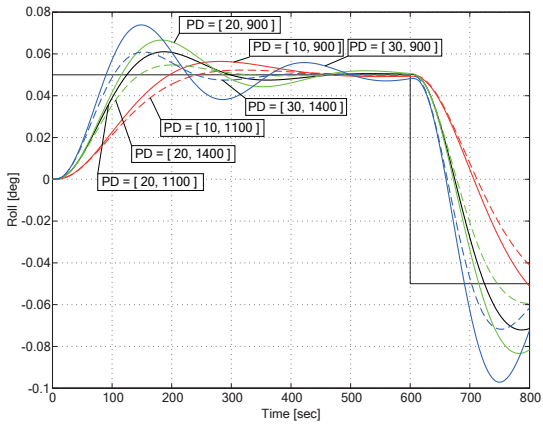
Figure 10: Time history of attitude angle on step response : Initial paddle angle 0 deg.
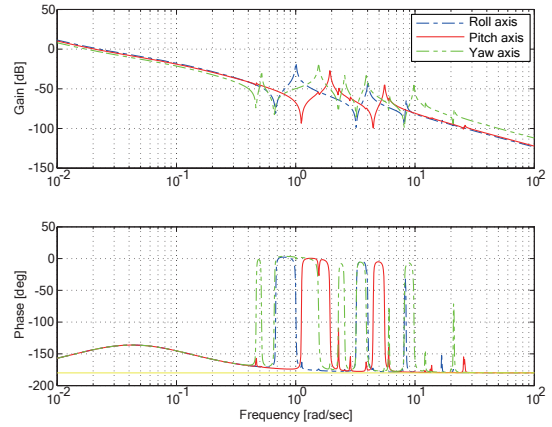

Figure 13: Bode diagram of open-loop system with paddle angle 0 deg.
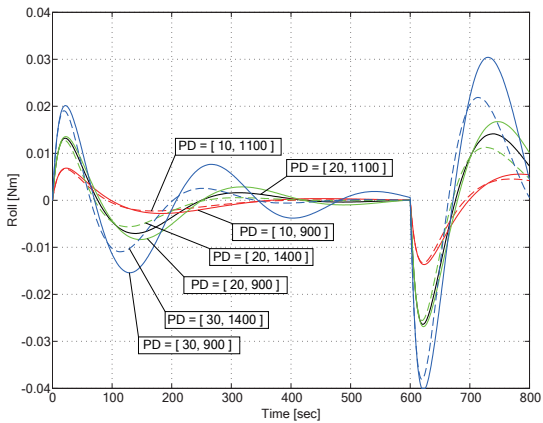
Figure 11: Time history of control input on step response : Initial paddle angle 0 deg.
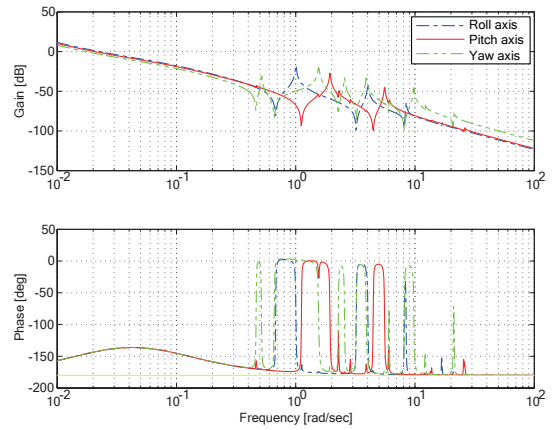
Figure 14: Bode diagram of open-loop system with paddle angle 45 deg.
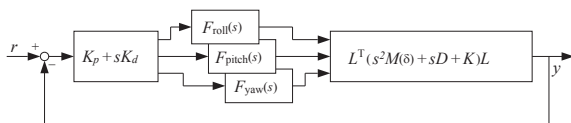
Figure 12: Block diagram of the closed-loop system using the baseline PD control law.
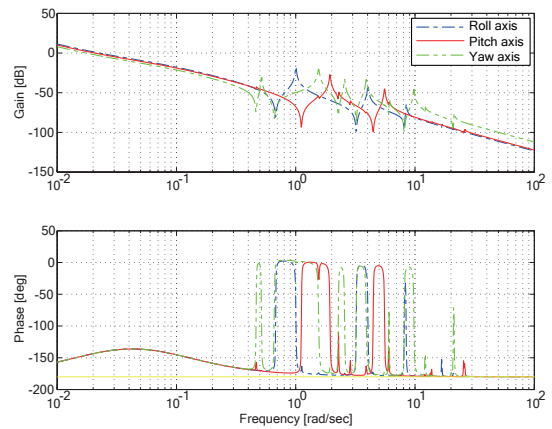
Figure 15: Bode diagram of open-loop system with paddle angle 90 deg.

5 Two Degrees-of-freedom Control Based on Symmetric Feedback Control Law

Our design objective here is to obtain a reduced order control law that robustly stabilizes the LPV MIMO spacecraft against the unstructured uncertainties of higher vibration modes and the structured uncertainties caused by the inaccuracy of modal identification before launch. Additionally, it must satisfy the trade-off control specifications of the disturbance attenuation and attitude tracking capabilities. In order to satisfy these requirements, we apply a two degrees-of-freedom control system which consists of a feedback control part for the stabilization and a feedforward control part for the reference tracking. A block diagram of proposed control system is shown in Fig. 16. This consists of a feedback control part C_{fb} and a feedforward part comprising stable transfer functions $K_1(\delta, s)$ and $K_2(\delta, s)$ [6]. The input-output relation from attitude reference signal r and disturbance w to measurement output is:

$$y_p = G_{yr}(\delta, s)r + G_{yw}(\delta, s)w,$$

where

$$G_{yw}(\delta, s) = (I + P(\delta, s)C_{fb})^{-1}P(\delta, s),$$
$$G_{yr}(\delta, s) = G_{yw}(\delta, s)(K_2(\delta, s) + C_{fb}K_1(\delta, s))$$

and $P(\delta, s)$ is the plant transfer function. Then, we have proposed two optimal design methods for the feedback control law which preserves symmetric properties [8, 12]. Each symmetric control law guarantees the internal stability of the closed-loop system and the robustness against the model errors based only on the non-parametric structure condition [13, 14, 15]. By using the design methods, two types of symmetric control laws can be obtained; one is the static output feedback C_{st} using the measured outputs y_1 and y_2, the other is the dynamic output feedback $C_{dy}(s)$ using the measured outputs y_1. In addition, the combination of two feedforward control laws $K_1(\delta, s)$ and $K_2(\delta, s)$ is designed as a gain scheduling control law [16] by applying a model matching method to the LPV system [8]. It is noted that the closed-loop system is composed of the plant,

---

[6]In this section, the symbols $P(\delta, s)$, $K_x(\delta, s)$ and $G_x(\delta, s)$ denote parameter dependent transfer functions.
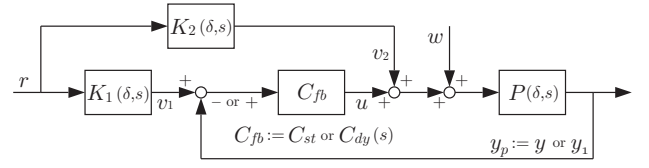

Figure 16: Block diagram of two degrees-of-freedom control system.

the feedforward control laws and either of the feedback control laws.

5.1 Description of the Spacecraft Model

It is noted that (8) has two features: firstly

$$M(\delta) > 0,\ D \geq 0,\ K \geq 0,\ \forall \delta \in \boldsymbol{R} \qquad (11)$$

holds from the modal identity [17] and secondly, the system (8) is stabilizable and detectable since the rank conditions

$$\mathrm{rank}[K, L] = \mathrm{rank}[D, L] = n$$

are satisfied for all δ [18].

In order to optimize each control law for all δ, we utilize the fact that $M(\delta)$ is bounded for all δ and gives its convex decomposition as [16]

$$M(\delta) = \sum_{i=1}^{\sigma} a_i M_i,\ M_i > 0,\ a_i \geq 0,\ \sum_{i=1}^{\sigma} a_i = 1,$$

where σ denotes the number of the convex hull vertex point which is given through parametrization to the elements of $M(\delta)$. By applying the decomposition, $M(\delta)$ can be described by the constant matrices M_i and the varying coefficients a_i depends on δ.

5.2 Static Output Feedback Control law

First, let us consider a static output feedback control law

$$u = -C_{st}y = -C_d y_1 - C_v y_2 \qquad (12)$$

where

$$C_d = C_d^T > 0,\ \ C_v = C_v^T > 0. \qquad (13)$$

By applying the control law to the plant (8), the closed-loop system can be described as

$$M(\delta)\ddot{p} + D^*\dot{p} + K^*p = Lw \qquad (14)$$

where

$$K^* = K + LC_dL^T > 0, \quad D^* = D + LC_vL^T > 0. \quad (15)$$

In order to examine the stability of (14), the following lemma is used.

Lemma 1 [18] The coefficient matrices of (14) satisfy

$$D^* > 0, \quad K^* > 0,$$

if the system (8) is stabilizable and detectable.

Then, the following stability condition can be stated.

Theorem 1 System (14) is asymptotically stable for all $\delta \in \mathbf{R}$ if $M(\delta) > 0$ and $K^*, D^* > 0$ when disturbance input $w = 0$.

Proof See Appendix B.

Note that stability is ensured only by the qualitative properties of sign definiteness (11) and (13) and is independent of the parameters and dimensions of the plant and controller. In this sense, the closed-loop system is robustly stable. This is called direct displacement and velocity feedback (DVDFB) control. For the design, we consider to optimize the disturbance attenuation capabilities for the controlled output $z_{dv} = y_1 = L^Tp$ in the framework of H_∞ control law synthesis as follows.

$$\begin{aligned}
&||G_{yw}(\delta, s)||_\infty \\
&= ||L^T(s^2M(\delta) + sD^* + K^*)L||_\infty < \gamma_{dv}, \quad \forall \delta
\end{aligned} \qquad (16)$$

where $\gamma_{dv} > 0$ is the H_∞ norm [7] of the closed-loop system. To this end, let us rewrite (14) in the state space,

$$\begin{aligned}
\dot{x}_{dv} &= A_{dv}(\delta)x_{dv} + B_{dv}(\delta)w, \\
z_{dv} &= C_{dv}x_{dv}
\end{aligned} \qquad (17)$$

_____
[7]In the strict sense of definition, it should be stated that the system has L_2 gain less than $\gamma_{dv} > 0$, $\forall \delta \in \mathbf{R}$. However, for brevity the term H_∞ norm is used throughout this section.

where $x_{dv} = [\, p^T \ \dot{p}^T \,]^T$,

$$\begin{aligned}
A_{dv}(\delta) &= \begin{bmatrix} 0 & I \\ -M^{-1}(\delta)K^* & -M^{-1}(\delta)D^* \end{bmatrix}, \\
B_{dv}(\delta) &= \begin{bmatrix} 0 \\ M^{-1}(\delta)L \end{bmatrix}, \quad C_{dv} = \begin{bmatrix} L^T & 0 \end{bmatrix}
\end{aligned} \qquad (18)$$

Then from the bounded real lemma (BRL), the condition (16) is satisfied if and only if there exists a symmetric matrix $X_{dv} = X_{dv}^T > 0$ such that

$$\begin{bmatrix} S_{dv}(\delta) + S_{dv}(\delta)^T & \text{sym} & \text{sym} \\ B_{dv}(\delta)^T X_{dv} & -\gamma_{dv}I & \text{sym} \\ C_{dv} & 0 & -\gamma_{dv}I \end{bmatrix} < 0 \qquad (19)$$

where $S_{dv}(\delta) = X_{dv}A_{dv}(\delta)$, " sym " denotes the symmetric element in the matrix. It is known that standard H_∞ control law design problem is feasible if the system is stabilizable and detectable [19]. However, since this problem imposes the positive definiteness constraints (13) upon (19), it must be examined whether such a controller can exist. Then, the following theorem can be derived.

Theorem 2 There always exists a controller (12) such that the closed-loop system (17) has an H_∞ norm less than $\gamma > 0$ for all δ.

Proof See Appendix C.

The design condition (19) for the static output feedback H_∞ control law is given by a bilinear matrix inequality, that is not efficiently solved. To cope with this difficulty, we have proposed the design method by giving the following structure to the solution of the BRL:

$$X_{dv} = \begin{bmatrix} K^* & \alpha M(\delta) \\ \alpha M(\delta) & M(\delta) \end{bmatrix} > 0$$

where α is the design parameter with sufficiently small. Then, the design condition becomes simultaneous linear matrix inequalities (LMIs)

$$\begin{aligned}
&-Q_{dvi} + \frac{1}{\gamma_{dv}}N_{dv}N_{dv}^T < 0, \quad i = 1, \cdots, \sigma \\
&C_d > 0, \quad C_v > 0, \quad \gamma_{dv} > 0
\end{aligned}$$

where

$$\begin{aligned}
Q_{dvi} &= \begin{bmatrix} 2\alpha K^* & \alpha D^* \\ \alpha D^* & 2D^* - 2\alpha M_i \end{bmatrix}, \\
N_{dv} &= \begin{bmatrix} \alpha L & L \\ L & 0 \end{bmatrix}.
\end{aligned}$$

5.3 Dynamic Output Feedback Control law

Next, consider a dynamic output feedback control law

$$
C_{dy}(s) := \begin{cases} \dot{x}_c &=& A_c x_c + B_c y_1 \\ u &=& C_c x_c + D_c y_1 \end{cases}
$$

where

$$
\begin{bmatrix} A_c & B_c \\ C_c & D_c \end{bmatrix} = H = H^T < 0. \tag{20}
$$

Then, it is also known that the closed-loop system

$$
\begin{aligned}
M(\delta)\ddot{p} + D\dot{p} + (K - LD_cL^T)p - LC_cx_c &= Lw \\
\dot{x}_c - A_cx_c - B_cL^Tp &= 0
\end{aligned} \tag{21}
$$

is always internally stable irrespective of the control law dimensions when the disturbance $w = 0$. This is called dynamic displacement feedback (DDFB) control. The stability is guaranteed based only on the non-parametric structure conditions (11) and (20). Therefore, this control law is also effective for our purpose. In the experiment, the control law is designed as $x_c \in \mathbf{R}^3$. For the control law, we have proposed a design method to optimize the disturbance attenuation capability for the controlled output $z_{dd} = y_1 = L^T p$ of the LPV system by extending general framework of H$_\infty$ control law synthesis. Then, the control performance is optimized by minimizing the H$_\infty$ norm γ_{dd} based on similar condition to (16). It consists of two steps of the H$_\infty$ norm minimization and the control law calculation as follows.

Step 1: The solutions $P_{dd} = P_{dd}^T > 0$, $Q_{dd} = Q_{dd}^T > 0$ and γ_{dd} are obtained by solving the convex optimization problem of γ_{dd} under the simultaneous LMI conditions

$$
N_{ddR}^\perp \begin{bmatrix} S_{ddpi} + S_{ddpi}^T & \text{sym} & \text{sym} \\ B_{dd1}^T E_{ddi}^{-1} P_{dd} & -\gamma_{dd}I & \text{sym} \\ C_{dd1} & 0 & -\gamma_{dd}I \end{bmatrix} N_{ddR}^{\perp T} < 0
$$

$$
N_{ddL}^\perp \begin{bmatrix} S_{ddqi} + S_{ddqi}^T & \text{sym} & \text{sym} \\ C_{dd1}Q_{dd}E_{ddi} & -\gamma_{dd}I & \text{sym} \\ B_{dd1}^T & 0 & -\gamma_{dd}I \end{bmatrix} N_{ddL}^{\perp T} < 0 \tag{22}
$$

$$
\begin{bmatrix} P_{dd} & I \\ I & Q_{dd} \end{bmatrix} > 0, \quad i = 1, \cdots, \sigma
$$

where $S_{dvpi} = P_{dd}E_{ddi}^{-1}A_{dd}$, $S_{ddqi} = A_{dd}Q_{dd}E_{ddi}$, the matrices $N_{ddR}^\perp$ and $N_{ddL}^\perp$ are the bases of the null spaces of $N_{ddR} = [\; C_{dd2} \; 0 \; 0\;]^T$ and $N_{ddL} = [\; B_{dd2}^T \; 0 \; 0\;]^T$, and

$$
E_{ddi} = \begin{bmatrix} I & 0 \\ 0 & M_i \end{bmatrix}, \quad A_{dd} = \begin{bmatrix} 0 & I \\ -K & -D \end{bmatrix}
$$

$$
B_{dd1} = B_{dd2} = \begin{bmatrix} 0 \\ L \end{bmatrix}, \quad C_{dd1} = C_{dd2} = \begin{bmatrix} L^T & 0 \end{bmatrix}.
$$

Note that the solutions P_{dd} and Q_{dd} always guarantee the existence of control law satisfying (20) based on the collocated controlled output condition $z_{dd} = y_1 = L^T p$ to the disturbance [18], although A_c, B_c, C_c and D_c do not appear in (22).

Step 2: The controller A_c, B_c, C_c, D_c is obtained by solving the convex feasibility problem under the simultaneous LMI conditions

$$
\begin{bmatrix} S_{ddcli} + S_{ddcli}^T & \text{sym} & \text{sym} \\ C_{ddcl}X_{dd}E_{ddcli} & -\gamma_{dd}I & \text{sym} \\ B_{ddcl}^T & 0 & -\gamma_{dd}I \end{bmatrix} < 0,
$$

$$
\begin{bmatrix} A_c & B_c \\ C_c & D_c \end{bmatrix} < 0, \quad \gamma_{dd} > 0, \quad i = 1, \cdots, \sigma
$$

where $S_{ddcli} = A_{ddcl}X_{dd}E_{ddcli}$ and

$$
X_{dd} = \begin{bmatrix} Q_{dd} & W_{dd} \\ W_{dd}^T & T_{dd} \end{bmatrix} \begin{bmatrix} P_{dd} & V_{dd} \\ V_{dd}^T & U_{dd} \end{bmatrix}^{-1},
$$

$$
E_{ddcli} = \begin{bmatrix} E_{ddi} & 0 \\ 0 & I \end{bmatrix},
$$

$$
A_{ddcl} = \begin{bmatrix} A_{dd} + B_{dd2}D_cC_{dd2} & B_{dd2}C_c \\ B_cC_{dd2} & A_c \end{bmatrix},
$$

$$
B_{ddcl} = \begin{bmatrix} B_{dd1} \\ 0 \end{bmatrix}, \quad C_{ddcl} = \begin{bmatrix} C_{dd1} & 0 \end{bmatrix}.
$$

Note that matrices T_{dd} and U_{dd} are derived from the singular value decomposition of $I - P_{dd}Q_{dd}$.
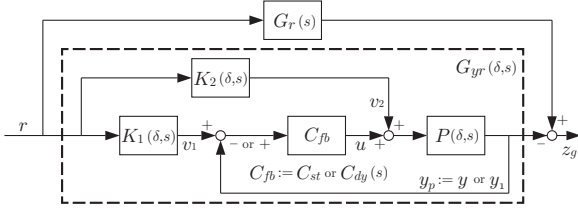
Figure 17: Block diagram of two degrees-of-freedom control system for feedforward control law synthesis.

5.4 Feedforward Control Law

Finally, In order to improve attitude maneuver performance to the reference signal $r \in \mathbf{R}^3$, feedforward control laws $K_1(\delta, s)$ and $K_2(\delta, s)$ are designed by the model matching method. It is given by minimizing $\gamma_g > 0$ such that

$$||G_r(s) - G_{yr}(\delta, s)||_\infty < \gamma_g, \ \forall \delta$$

where $z_r = G_r(s)r$ denotes a given LTI transfer function matrix of the reference model, $z_g = G_{yr}(\delta, s)r$ is the closed-loop system which consists of the plant, the feedforward control laws and one of the above feedback control laws, and $z_g = y_1$ (Fig. 17). When the plant is LTI, it is a standard H$_\infty$ model matching problem to obtain $v = [\ v_1^T\ v_2^T\ ]^T = [\ K_1(s)^T\ K_2(s)^T\ ]^T r$ for the generalized plant

$$z_g = G_r(s)r - G_{yw}(s)[\ C_{fb}\ I\ ]v$$
$$y_g = r \tag{23}$$

However, in the LPV problem, feedforward control laws $K_1(\delta, s)$ and $K_2(\delta, s)$ must be scheduled according to the change of δ. To this end, we consider the gain scheduling H$_\infty$ model matching problem.

Let the state equation of the feedforward control law be expressed as

$$\dot{x}_k = A_k(\delta)x_k + B_k(\delta)r$$
$$v = C_k(\delta)x_k + D_k(\delta)r \tag{24}$$

and that of the reference model as

$$\dot{x}_r = A_r x_r + B_r r$$
$$z_r = C_r x_r$$

where A_r is a constant stable matrix. The closed-loop system (8) or (21) driven by feedforward control

inputs v_1, v_2 when $w = 0$ is written in the following descriptor form:

$$E_p(\delta)\dot{x}_p = A_p x_p + B_p v$$
$$y = C_p x_p$$

where

$$x_p = [\ p^T\ \dot{p}^T\ ]^T$$
$$E_p(\delta) = \begin{bmatrix} I & 0 \\ 0 & M(\delta) \end{bmatrix}, \quad A_p = \begin{bmatrix} 0 & I \\ -K^* & -D^* \end{bmatrix}$$
$$B_p = \begin{bmatrix} 0 & 0 \\ LC_{st} & L \end{bmatrix}, \quad C_p = \begin{bmatrix} L^T & 0 \\ 0 & L^T \end{bmatrix}$$

as the static output feedback control case, on the other hand,

$$x_p = [\ p^T\ \dot{p}^T\ x_c^T\ ]^T,$$
$$E_p(\delta) = \begin{bmatrix} I & 0 & 0 \\ 0 & M(\delta) & 0 \\ 0 & 0 & I \end{bmatrix},$$
$$A_p = \begin{bmatrix} 0 & I & 0 \\ -K + LD_cL^T & -D & LC_c \\ B_cL^T & 0 & A_c \end{bmatrix},$$
$$B_p = \begin{bmatrix} 0 & 0 \\ LD_c & L \\ 0 & 0 \end{bmatrix}, \quad C_p = \begin{bmatrix} L^T & 0 & 0 \\ 0 & L^T & 0 \end{bmatrix}$$

as the dynamic output feedback control case. Then, the LPV counterpart of the generalized plant used for scheduled control law design that corresponds to the LTI generalized plant (23) is

$$E_g(\delta)\dot{x} = A_g x_g + B_{g1}r + B_{g2}v$$
$$z_g = C_{g1}x_g \tag{25}$$
$$y_g = r$$

where $x_g = [\ x_r^T\ x_p^T\ ]^T$ and

$$E_g(\delta) = \begin{bmatrix} I & 0 \\ 0 & E_p(\delta) \end{bmatrix}, \quad A_g = \begin{bmatrix} A_r & 0 \\ 0 & A_p \end{bmatrix}$$
$$B_{g1} = \begin{bmatrix} B_r \\ 0 \end{bmatrix}, \quad B_{g2} = \begin{bmatrix} 0 \\ B_p \end{bmatrix}$$
$$C_{g1} = \begin{bmatrix} C_r & -C_p \end{bmatrix} \ .$$

There are two reasons for using descriptor equations instead of state equations: one is to localize the parameter varying elements only to the mass matrix, and the other is to avoid constraints encountered in

solving LMIs where the matrix B_{g2} is independent of the parameter δ. It is noted here that this generalized plant is not required to be stabilizable and detectable because the feedforward control law is designed for the already stabilized closed-loop system.

The closed-loop system of the generalized plant (25) with the control law (24) is given as

$$E_{c\ell}(\delta)\dot{x}_{c\ell} = A_{c\ell}(\delta)x_{c\ell} + B_{c\ell}(\delta)r$$
$$z_g = C_{c\ell}x_{c\ell}$$

where $x_{c\ell} = [\, x_g^T \ x_k^T \,]^T$ and

$$E_{c\ell}(\delta) = \begin{bmatrix} E_g(\delta) & 0 \\ 0 & I \end{bmatrix},$$
$$A_{c\ell}(\delta) = \begin{bmatrix} A_g & B_{g2}C_k(\delta) \\ 0 & A_k(\delta) \end{bmatrix},$$
$$B_{c\ell}(\delta) = \begin{bmatrix} B_{g1} + B_{g2}D_k(\delta) \\ B_k(\delta) \end{bmatrix}, \ \ C_{c\ell} = \begin{bmatrix} C_{g1} & 0 \end{bmatrix}$$

From the BRL, the optimal model matching control law (24) is designed by minimizing $\gamma_g > 0$ for all δ under the condition

$$\begin{bmatrix} S_g + S_g^T & \text{sym} & \text{sym} \\ C_{c\ell}X_g E_{c\ell}(\delta)^T & -\gamma_g I & \text{sym} \\ B_{c\ell}(\delta)^T & 0 & -\gamma_g I \end{bmatrix} < 0 \qquad (26)$$

where $X_g = X_g^T > 0$ and $S_g = A_{c\ell}(\delta)X_g E_{c\ell}(\delta)^T$. The gain scheduling control law is derived by slightly extending the standard algorithm for state equation [16]. First, let the following parameter-dependent matrices be convex combinations of constant matrices

$$E_{c\ell}(\delta) = \sum_{i=1}^{\sigma} a_i E_{c\ell i}, \quad A_{c\ell}(\delta) = \sum_{i=1}^{\sigma} a_i A_{c\ell i},$$
$$B_{c\ell}(\delta) = \sum_{i=1}^{\sigma} a_i B_{c\ell i}. \qquad (27)$$

Substituting (27) into (26) yields

$$\sum_{i=1}^{\sigma} a_i^2 \Phi_i + \sum_{i=1}^{\sigma} a_i a_j (\Psi_{ij} + \Psi_{ji}) < 0$$

where $j = i+1, \cdots, \sigma$,

$$\Phi_i = \begin{bmatrix} Y_i + Y_i^T & E_{c\ell i}X_g C_{c\ell}^T & B_{c\ell i} \\ C_{c\ell}X_g E_{c\ell i}^T & -\gamma_g I & 0 \\ B_{c\ell i}^T & 0 & -\gamma_g I \end{bmatrix}$$
$$\Psi_{ij} = \begin{bmatrix} Z_{ij} + Z_{ji}^T & E_{c\ell j}X_g C_{c\ell}^T & B_{c\ell i} \\ C_{c\ell}X_g E_{c\ell j}^T & -\gamma_g I & 0 \\ B_{c\ell i}^T & 0 & -\gamma_g I \end{bmatrix}$$

and $Y_i = A_{c\ell i}X_g E_{c\ell i}^T$, $Z_{ij} = A_{c\ell i}X_g E_{c\ell j}$. Therefore, if the following inequalities can be solved simultaneously at each vertex of convex decomposition

$$\Phi_i < 0, \ \Psi_{ij} + \Psi_{ji} < 0, \ \ \begin{array}{l} i = 1, \cdots, \sigma \\ j = i+1, \cdots, \sigma \end{array} \qquad (28)$$

for vertex control laws $A_{ki}, B_{ki}, C_{ki}, D_{ki}$ and $X_g > 0$ so as to minimize $\gamma_g > 0$, then the gain scheduled feedforward control law is constructed as

$$A_k(\delta) = \sum_{i=1}^{\sigma} a_i A_{ki}, \ \ B_k(\delta) = \sum_{i=1}^{\sigma} a_i B_{ki}$$
$$C_k(\delta) = \sum_{i=1}^{\sigma} a_i C_{ki}, \ \ D_k(\delta) = \sum_{i=1}^{\sigma} a_i D_{ki}$$

Since inequalities (28) are reduced to LMIs by eliminating matrix variables using Parrot and Finsler's lemma [19], the problem is again solved using convex optimization tools.

5.5   Simulation Results

In order to verify the capability of the proposed control laws, we performed numerical simulations which applied the discrete control system with a sampling period of 62.5 msec to a continuous full-order ETS-VIII model. In the simulations, white noise of standard deviation 1.11×10^{-4} deg/sec was used as an angular velocity observation noise [8]. Further, the paddles rotated around the pitch axis at a rate of 360/24 deg/hour, and the initial paddle angle was varied from 0 deg to 360 deg in 1 deg increments. This paper shows typical simulation results at initial angles of 0, 45 and 90 deg.

First, the feedback control laws are designed so that the closed-loop system has a high disturbance suppression ability, using the model with three rigid modes and two elastic modes ($n = 5$) for four vertexes ($\sigma = 4$). In the convex optimization for the

---

[8]In order to attenuate this noise, 1st-order low-pass filter is added to the angular velocity measurement y_2 for only the static output feedback control case.
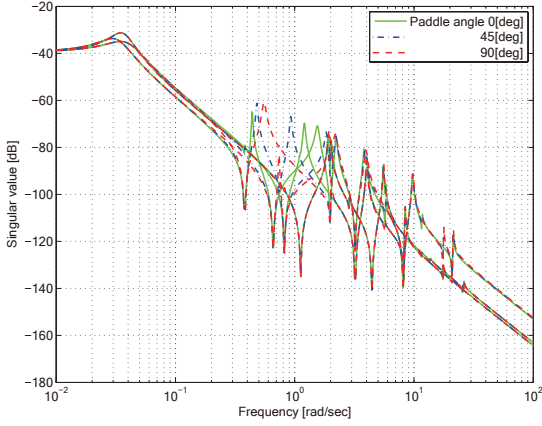
Figure 18: Singular values of feedback closed-loop systems using static output feedback control law.
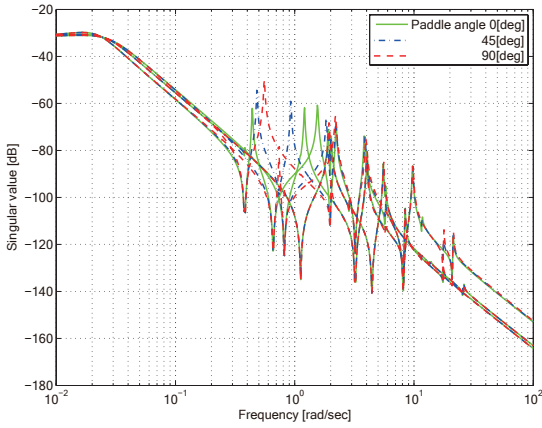

Figure 19: Singular values of feedback closed-loop systems using dynamic output feedback control law.

control law design, we used the MATLAB "mincx" command which utilizes the projective method for the interior point polynomial [20, 21, 22].

At the design phase of the static output feedback case, the achieved minimal value was $\gamma_{dv} = 6.79$ which is the disturbance attenuation ratio. However, a value of $\gamma = 0.024$ was calculated from (19) substituted with the obtained control law for $\delta = 45$ deg. The difference arises due to the conservativeness brought in solving LMIs. On the other hand, values of γ_{dd} in the static and dynamic output feedback case were 0.004 and 0.032 respectively. Figs. 18 and 19 show the singular values in each case.

The responses to impulse disturbance caused by the east-west station-keeping thruster firing are shown in Figs. 20 - 25. In these figures, dashed-and-dotted lines denote the results of the static output feedback

control, broken lines are the dynamic output feedback control, and solid lines are the baseline PD control. The spacecraft attitudes are observed to stay between $+0.002$ deg and -0.002 deg, which is sufficiently smaller than the specification, and the required control inputs are smaller than the maximum output of the reaction wheel. Moreover, it is apparent that the proposed feedback control laws are effective in reducing the influence of disturbances compared with the PD control, as well as they are robustly stable against the paddle rotation. The maximum attitude angle amplitude using the static type has been smaller than the dynamic type. This is because the optimization of control performance using the LMI has functioned more effectively in the static type, and the static type has wide frequency range.

Next, in order to obtain feedforward control laws $K_1(\delta, s)$ and $K_2(\delta, s)$, we sets the reference transfer function matrix $G_r(s)$ so as to have

$$\frac{\omega_r^2}{s^2 + 2\zeta_r\omega_r s + \omega_r^2} \qquad (29)$$

as its diagonal elements, where $\omega_r^2 = 5.0 \times 10^{-4}$, $\zeta_r = 0.7$. The responses of this reference model (29) to step command is shown in Fig. 26.

By solving LMIs (28), the gain scheduling model matching control laws are obtained for $n = 5$ and $\sigma = 4$. In the design, $\gamma_g = 0.45$ with the static output feedback control law and $\gamma_g = 0.63$ with the dynamic output feedback control law have been achieved. Figs. 27 and 28 show the singular values of the reference model and the two degrees-of-freedom control system. From these figures, it is confirmed that the singular values are almost the same in the lower frequency ranges.

Simulation results of attitude maneuvering using the two degrees-of-freedom control system are shown in Figs. 29 - 34. Each response is seen to follow the reference model well for all paddle angles, and the required control inputs are smaller than the reaction wheel output limitation.

The proposed control laws have achieved shorter settling time than the PD control law, and both static and dynamic feedback control laws achieve the similar good performance. These facts show that the model-matching design method in the two-degrees-of freedom control system works well. Since the results
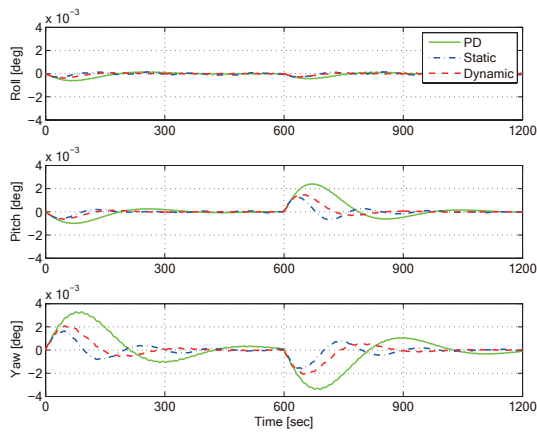
Figure 20: Time history of roll, pitch, yaw attitude angles in response to east-west station-keeping thruster firing for initial paddle angles $\delta = 0$ deg.
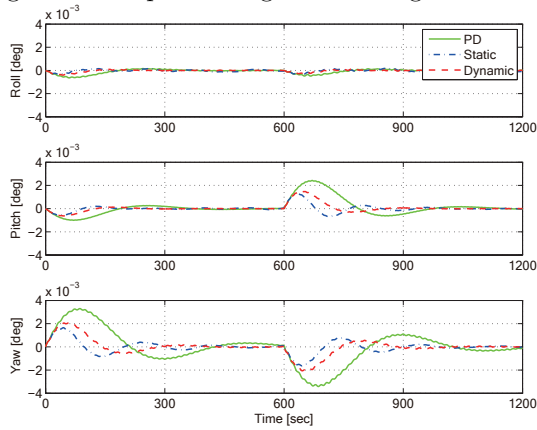

Figure 21: Time history of roll, pitch, yaw attitude angles in response to east-west station-keeping thruster firing for initial paddle angles $\delta = 45$ deg.
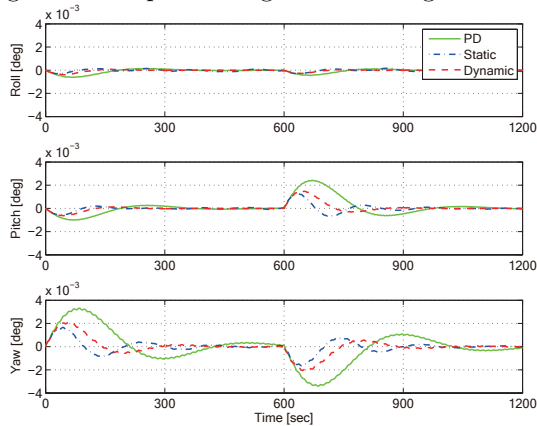

Figure 22: Time history of roll, pitch, yaw attitude angles in response to east-west station-keeping thruster firing for initial paddle angles $\delta = 90$ deg.
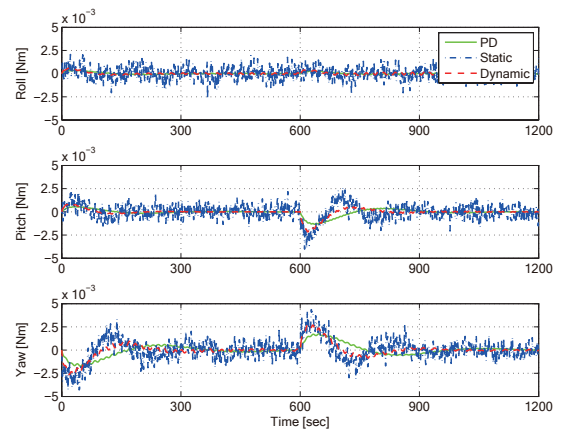
Figure 23: Time history of roll, pitch, yaw control inputs in response to east-west station-keeping thruster firing for initial paddle angles $\delta = 0$ deg.
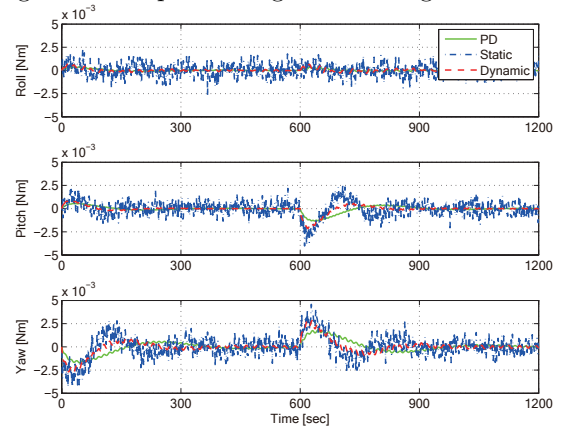
Figure 24: Time history of roll, pitch, yaw control inputs in response to east-west station-keeping thruster firing for initial paddle angles $\delta = 45$ deg.
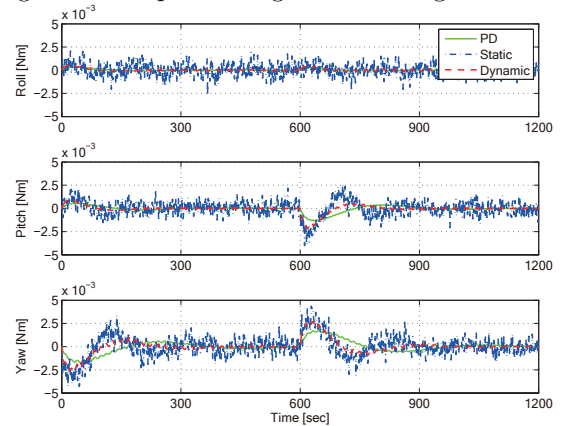
Figure 25: Time history of roll, pitch, yaw control inputs in response to east-west station-keeping thruster firing for initial paddle angles $\delta = 90$ deg.
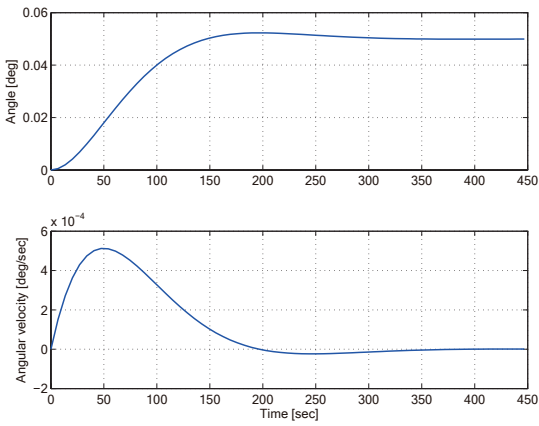
Figure 26: Singular values of feedback closed-loop systems using dynamic output feedback control law.
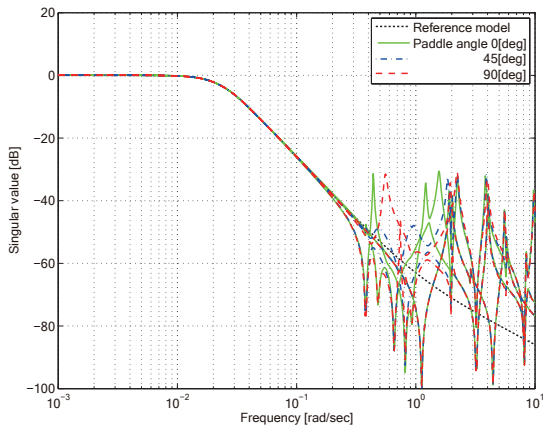
Figure 27: Singular values of two degrees-of-freedom control system with static output feedback control law and reference model.
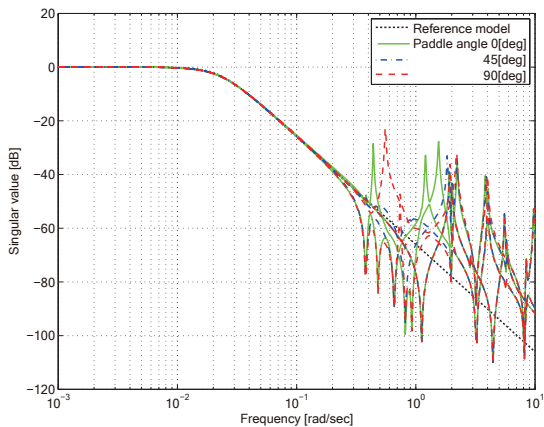

Figure 28: Singular values of two degrees-of-freedom control system with dynamic output feedback control law and reference model.
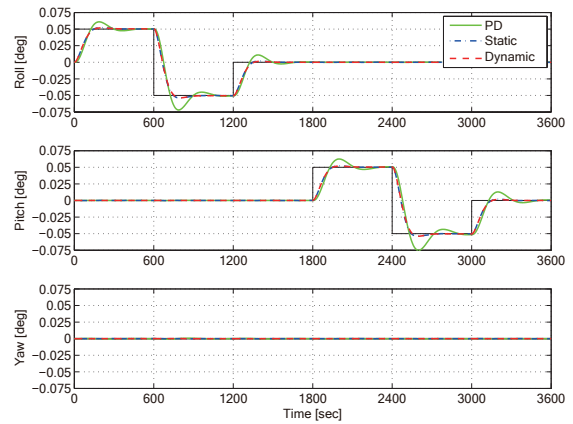

Figure 29: Time history of roll, pitch, yaw attitude angle responses to step command for initial paddle angles $\delta = 0$ deg.
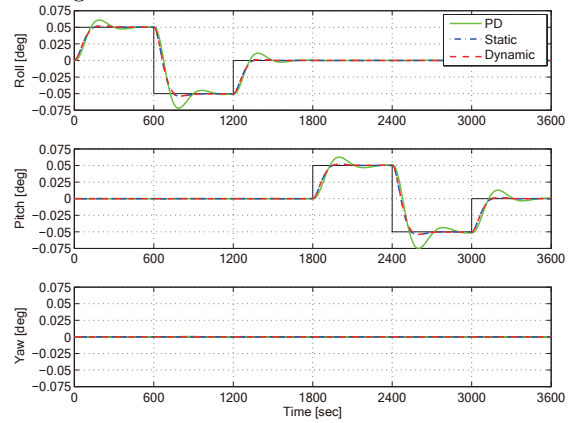
Figure 30: Time history of roll, pitch, yaw attitude angle responses to step command for initial paddle angles $\delta = 45$ deg.
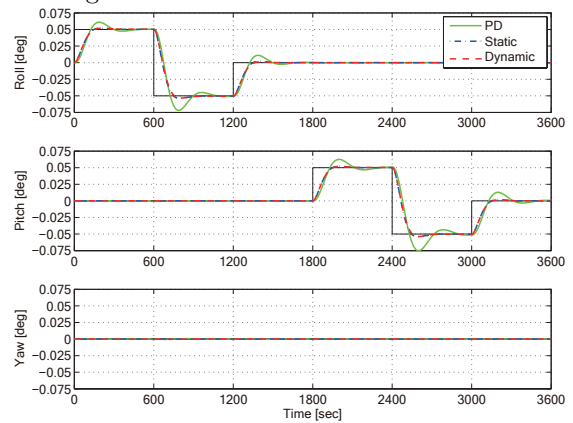
Figure 31: Time history of roll, pitch, yaw attitude angle responses to step command for initial paddle angles $\delta = 90$ deg.

of different initial paddle angle using the proposed control system are also the same, it is confirmed that the gain scheduling function of the feedforward control law is effective to the LPV system caused by the paddle rotation.
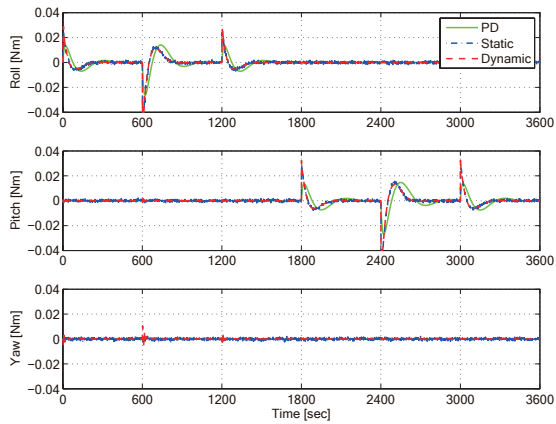

Figure 32: Time history of roll, pitch, yaw control inputs in response to step command for initial paddle angles $\delta = 0$ deg.
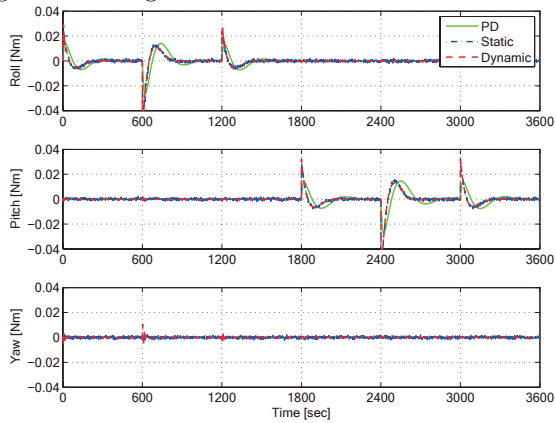

Figure 33: Time history of roll, pitch, yaw control inputs in response to step command for initial paddle angles $\delta = 45$ deg.
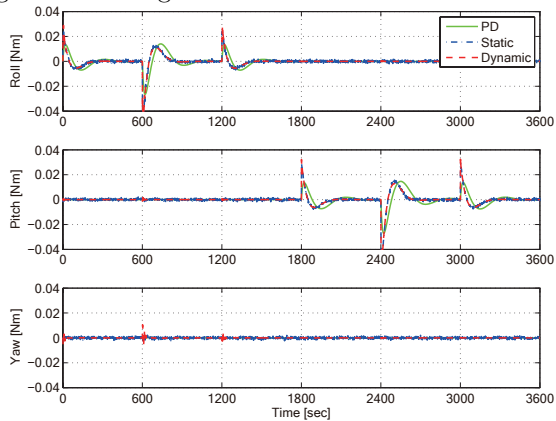

Figure 34: Time history of roll, pitch, yaw control inputs in response to step command for initial paddle angles $\delta = 90$ deg.

6 μ-synthesis Based Control Law

In this section, an LTI μ-synthesis based control law is presented; it is designed parametrically by decomposing the spacecraft model into control modes and residual modes. In the μ-synthesis, the varying parameters are treated as structured uncertainty that is stabilized robustly along with unstructured uncertainty by setting the μ-value to less than one. The final LTI control law is designed through D-K iteration.

6.1   Model and Perturbation

To begin with, we present the spacecraft model and description of the handling of the perturbation, which is an important point in our study of μ-synthesis application. In the constrained mode model of (8), the coefficient matrix that varies depending on the paddle angle is only $M(\delta)$; its influence is localized. Then, in order to take advantage of this feature in robust control system design, we use the descriptor form in μ-synthesis.

Reduced order model   First, we reduce the order of the model (8) in order to design the reduced-order controller that guarantees robust stability against higher vibration mode that is represented as unstructured uncertainty. We change the order of the elements in $\eta \in \boldsymbol{R}^{\Sigma_j n_j}$ and divide the flexible vibration mode as $\eta = [\eta_c^T \ \eta_r^T]^T$ $(\eta_c \in \boldsymbol{R}^g)$. Then coefficient matrices in (8) are also divided into corresponding submatrices:

$$
\begin{aligned}
P(\delta) &= \begin{bmatrix} P_c(\delta) & P_r(\delta) \end{bmatrix} \\
\Lambda &= \mathrm{diag}[\Lambda_c, \ \Lambda_r] \\
\Omega^2 &= \mathrm{diag}[\Omega_c^2, \ \Omega_r^2]
\end{aligned}
$$

We express $q_c = [\theta^T \ \eta_c^T]^T$ as the control mode and $q_r = \eta_r$ as the residual mode. Then (5) and (6) can be described in the frequency domain as:

$$
\hat{y}(s) = G(s)\hat{u}(s) = (G_c(s) + G_r(s))^{-1}\hat{u}(s) \quad (30)
$$

The transfer function $G(s)$ can be rewritten using $G_c^{-1}(s)$ and an additive perturbation:

$$
G(s) = G_c^{-1}(s) + G_\Delta(s)
$$

Here, we design the weighting function $W(s)$ that is stable and proper for the additive model error margin

$G_\Delta(s)$ as follows.

$$
G_\Delta(s) = \Delta_w(s)W(s), \quad \|\Delta_w\|_\infty < 1
$$

Furthermore, we describe the influence of unstructured uncertainty $\Delta_w(s)$ as

$$
w_w = \Delta_w(s)z_w, \quad w_w, z_w \in \boldsymbol{R}^6
$$

where w_s and z_w are fictitious disturbance input and controlled output of the plant. Consequently, we can treat the influence of the residual mode in the high frequency domain as a virtual disturbance.

Here, for making the generalized plant, we describe the state space realization of this weight function $W(s)$ as

$$
\begin{aligned}
\dot{x}_w &= A_w x_w + B_w u, \\
z_w &= C_w x_w + D_w u.
\end{aligned}
$$

Descriptor form   Next, to treat the parameter change of the control mode as structured uncertainty, we describe $G_c^{-1}(s)$ using the descriptor form as

$$
\begin{aligned}
E_c(\delta)\dot{x} &= (E_c + E_\Delta(\delta))\dot{x} \\
&= A_c x + B_c u, \quad (31) \\
y &= C_c x.
\end{aligned}
$$

In those equations, $x = [q_c^T \ \dot{q}_c^T]^T \in \boldsymbol{R}^{2n}$ are descriptor variables, where $n = 3 + g$. The matrix $E_c(\delta)$ is divided into the nominal model E_c and the additive model error margin $E_\Delta(\delta)$ in the specific angle. They are given as

$$
\begin{aligned}
E_c &= \mathrm{diag}[I_n, \ M_c], \\
E_\Delta(\delta) &= \mathrm{diag}[0_{n\times n}, \ M_\Delta(\delta)],
\end{aligned}
$$

where

$$
M_c = \begin{bmatrix} J & P_c \\ P_c^T & I_g \end{bmatrix}, \ M_\Delta(\delta) = \begin{bmatrix} J_\Delta(\delta) & P_{c\Delta}(\delta) \\ P_{c\Delta}^T(\delta) & 0_{g\times g} \end{bmatrix}
$$

The matrices A_c, B_c and C_c are given as:

$$
A_c = \begin{bmatrix} 0_{n\times n} & I_n \\ -K_c & -D_c \end{bmatrix}, \ B_c = \begin{bmatrix} 0_{n\times 3} \\ L_c \end{bmatrix},
$$

$$
C_c = \begin{bmatrix} L_c^T & 0_{3\times n} \\ 0_{3\times n} & L_c^T \end{bmatrix},
$$

where

$$
\begin{aligned}
D_c &= \mathrm{diag}[0_{3\times 3}, \ \Lambda_c], \\
K_c &= \mathrm{diag}[0_{3\times 3}, \ \Omega_c^2], \\
L_c^T &= [I_3 \ \ 0_{3\times g}].
\end{aligned}
$$

Then, we describe $E_\Delta(\delta)$ using the following equation with scalar parameter α_i depending on δ

$$E_\Delta(\delta) = \sum_{i=1}^{k} \alpha_i(\delta) E_i,$$

where $|\alpha_i(\delta)| < 1$ for all δ. Noting that E_c is a nonsingular matrix, the following equation is obtained using full rank decomposition:

$$\begin{aligned} E_c^{-1} E_\Delta &= \text{diag}[0,\ M_c^{-1} M_\Delta(\delta)] \\ &= F_L \Delta_E F_R, \quad \|\Delta_E\| < 1, \end{aligned}$$

where

$$\begin{aligned} \Delta_E &= \text{diag}[\alpha_1 I_{h_1},\ \ldots,\ \alpha_k I_{h_k}] \\ F_L &= [F_{L_1} \ldots F_{L_k}], \quad F_{L_i} \in \mathbf{R}^{2n \times h_i} \\ F_R &= [F_{R_1}^T \ldots F_{R_k}^T]^T, \quad F_{R_i} \in \mathbf{R}^{h_i \times 2n}. \end{aligned}$$

Matrices F_L and F_R are used for defining the structured uncertainty Δ_E. Note that (31) is equivalent to

$$\dot{x} = E_c^{-1} A_c x + E_c^{-1} B_c u - E_c^{-1} E_\Delta(\delta)\dot{x}.$$

Then, by describing the input and output of structured uncertainty Δ_E as

$$w_E = \Delta_E z_E = -\Delta_E F_R \dot{x},$$

we can express the extended system incorporating the influence of parameter variation as follows.

$$\begin{aligned} \dot{x} &= E_c^{-1} A_c x + E_c^{-1} B_c u + F_L w_E, \\ y &= C_c x \\ z_E &= -F_R E_c^{-1} A_c x - F_R E_c^{-1} B_c u - F_R F_L w_E. \end{aligned}$$

Generalized plant Then, to reduce sensitivity and achieve robust performance, we define controlled output $z_\lambda \in \mathbf{R}^6$ as

$$\begin{aligned} z_\lambda &= \begin{bmatrix} \lambda(s) & 0 \\ 0 & \lambda_D \end{bmatrix} e, \\ w_\lambda &= \Delta_\lambda z_\lambda,\ w_\lambda \in \mathbf{R}^6,\ \|\Delta_\lambda\|_\infty < 1 \end{aligned}$$

where e is defined as

$$\begin{aligned} e &= \begin{bmatrix} e_d \\ e_v \end{bmatrix} \\ &= \begin{bmatrix} d_d \\ 0 \end{bmatrix} - \begin{bmatrix} y_1 \\ y_2 \end{bmatrix} \\ &= d - y \end{aligned}$$
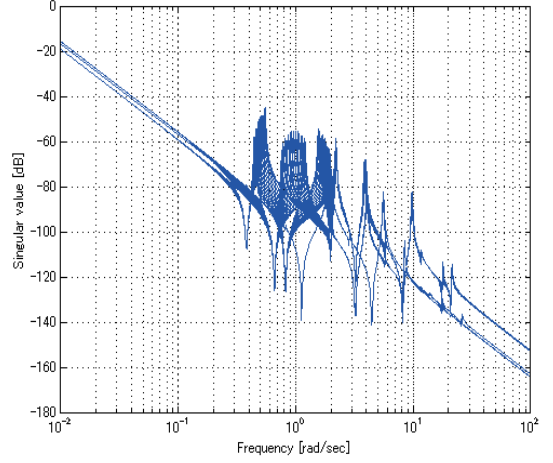

Figure 35: Singular value plot of full order plant.
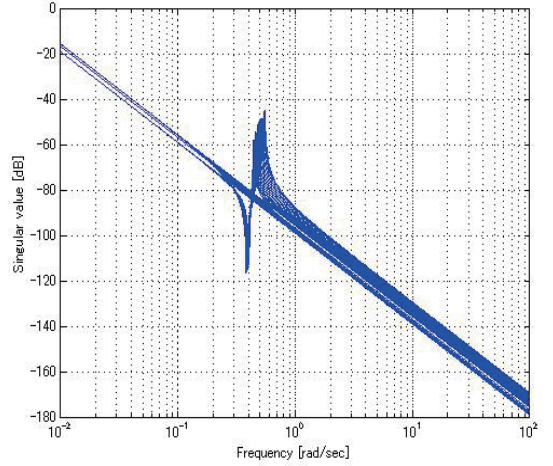
Figure 36: Singular value plot of control mode.

and $\lambda(s)$ is a design parameter for the trade-off between the control and the robust performances. Here d_d acts as target value for the attitude angle.

We express these perturbations described separately above as follows

$$\Delta = \text{diag}\,[\Delta_E,\ \Delta_w(s),\ \Delta_\lambda].$$

It should be noted that Δ is the structured uncertainty composed of unstructured uncertainty $\Delta_w(s)$ and structured uncertainties Δ_E and Δ_λ.

Singular value plots of ETS-VIII spacecraft model are shown below; full order plant in Fig. 35, control mode in Fig. 36, and residual mode with weighting functions in Figs. 37 and 38 every 5 deg from $\delta = 0$ to 90 deg. The number of control modes is
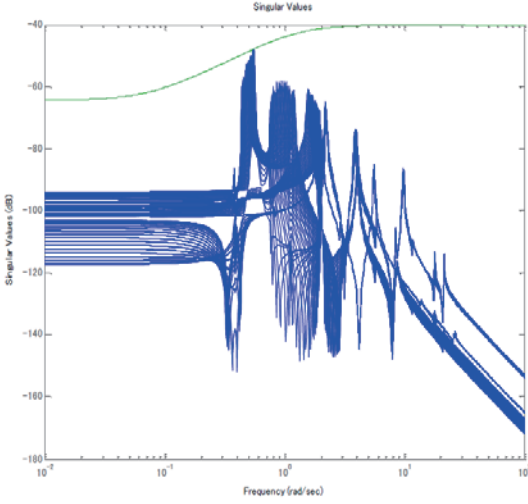
Figure 37: Singular value plot of residual mode and the weighting function for attitude angle.
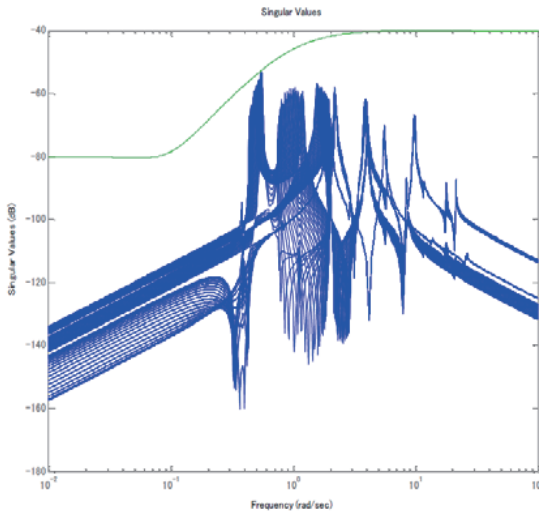

Figure 38: Singular value plot of residual mode and the weighting function for attitude rate.

four (three rigid modes and one elastic mode); that is, $n = 4$. The weighting functions are selected to satisfy robust stability for all δ.

6.2   Control System Design

During the control system design process, the spacecraft model at $\delta = 45$ acts as a nominal model, and we treat only $\delta \in [0, 90]$ as a range of the paddle rotation angle in consideration of symmetry of spacecraft structure. There are symmetric vibration modes in the body frame that are uncontrollable by attitude control systems, because these vibration modes affect only transitional motion of spacecraft [17]. In order to exclude these uncontrollable modes, we take twice of the coupling matrix $P_c(\delta)$ and describe the central rigid-body rotation equation and the vibration equation of flexible components using the south paddle coordinate system, as shown below in (32). We perform coordinate transformation using the DCM $C_4(\delta)$, which expresses the relationship between the central rigid-body frame and the south paddle frame (see (1) in Section 3.1):

$$\bar{\theta} = C_4(\delta)\theta = \begin{bmatrix} \sin\delta & 0 & \cos\delta \\ 0 & 1 & 0 \\ -\cos\delta & 0 & \sin\delta \end{bmatrix}\theta,$$

where $\bar{\theta}$ is the estimated attitude angle. Then the equation of the control mode can be described as follows:

$$C_4(\delta)J(\delta)C_4^T(\delta)\ddot{\bar{\theta}} + 2C_4(\delta)P_c(\delta)\ddot{\eta}_c^s = C_4(\delta)u$$
$$P_c^T(\delta)C_4^T(\delta)\ddot{\bar{\theta}} + \ddot{\eta}_c^s + \Lambda_c\dot{\eta}_c^s + \Omega_c^2\eta_c^s = 0,$$
$$\tag{32}$$

$$y = \bar{y} = \begin{bmatrix} C_4^T(\delta)\bar{\theta} \\ C_4^T(\delta)\dot{\bar{\theta}} \end{bmatrix} = \begin{bmatrix} \theta \\ \dot{\theta} \end{bmatrix}. \tag{33}$$

The generalized plant discussed in Section 6.1 is described with (32) and (33), and then μ-synthesis is performed by D-K iteration. The state space expression of the generalized plant G is given as (34) and (35), where

$$A_c = \begin{bmatrix} 0_{4\times4} & I_4 \\ -M_c^{-1}K_c & -M_c^{-1}D_c \end{bmatrix}, B_c = \begin{bmatrix} 0_{4\times3} \\ M_c^{-1}H_c \end{bmatrix},$$

$$C_{c1} = \begin{bmatrix} H_c^T & 0_{3\times4} \end{bmatrix}, C_{c2} = \begin{bmatrix} 0_{3\times4} & H_c^T \end{bmatrix},$$

$$M_c = \begin{bmatrix} C_4(\delta)J(\delta)C_4^T(\delta) & 2C_4(\delta)P_c(\delta) \\ P_c^T(\delta)C_4^T(\delta) & I_1 \end{bmatrix},$$

$$H_c^T = \begin{bmatrix} C_4^T(\delta) & 0_{3\times1} \end{bmatrix}.$$
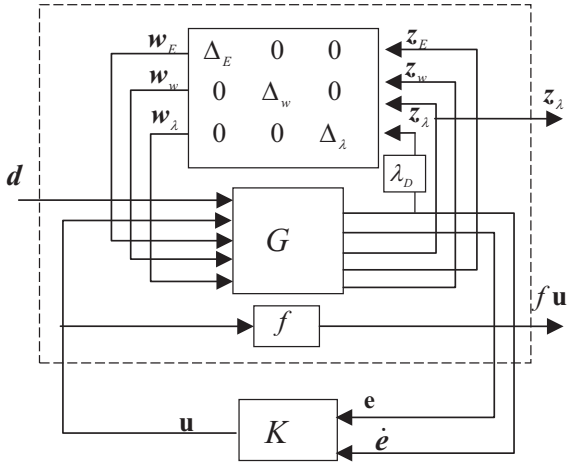
Figure 39: μ-synthesis.
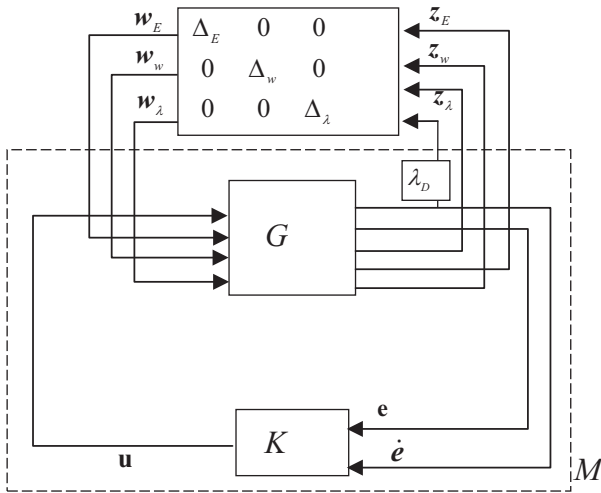
Figure 40: μ-analysis.
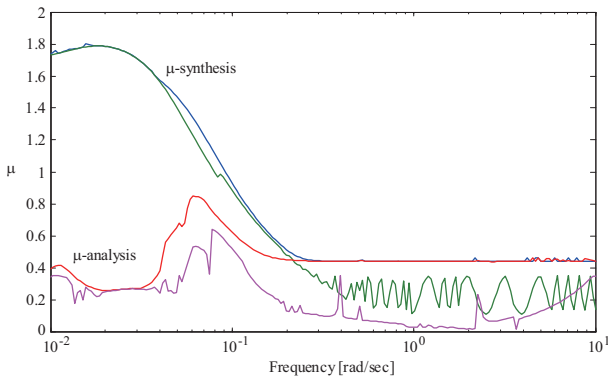
Figure 41: μ upper and lower bounds.

If the control algorithm $\hat{u} = K(s)\hat{y}$ is derived that satisfies the following inequality of structured singular value μ,

$$\sup_{\omega} \mu_{\Delta}(F_l(G(j\omega), K(j\omega))) < 1,$$

then the algorithm guarantees robust stability for all perturbations. However, it is known that in general the μ-synthesis designs a control law with conservative control performance. Therefore, we also apply the μ-analysis after the μ-synthesis as shown in Figs. 39 and 40. Here, λ_D is the weighting function to reduce sensitivity for the error margin of attitude rates, and f is the weighting function for control inputs.

In this scheme, the weighting functions λ_D and f are modified according to the result of μ-analysis. The designed final control law in this study is selected so as to achieve the best control performance among the control laws whose μ-values obtained by μ-analysis are less than one. The obtained structured singular value is depicted in Fig. 41.

6.3 Robust Stability on All Mission Life

In general, the model parameters of spacecraft representing mass properties vary according to the decrease of fuel used for orbit control. In this study, our control law is designed using the PSR-BOL model. Moreover, we obtain the PSR-EOL model simultaneously, so we verified the varying width of PSR-EOL and PSR-BOL model (Fig. 42). Parameters' width change of each model is calculated from the nominal values at 45 deg model.

It is revealed that the difference between PSR-BOL and PSR-EOL models is small, but the varying width of PSR-EOL model is not fully included in that of PSR-BOL. For this reason, we redesigned the control law adding a 3% error margin to the varying width of the PSR-BOL model to include the error margin of the PSR-EOL model into that of PSR-BOL model. Consequently, we can guarantee robust stability for the spacecraft's entire mission life.

6.4 Simulation Results

We now apply the designed LTI μ-synthesis based control law to the attitude control problem of ETS-VIII. For this study, we use two simulation cases that

$$\left[\begin{array}{c} \dot{x} \\ \dot{x}_w \end{array} \right] = \left[\begin{array}{cc} A_c & 0_{8\times 6} \\ 0_{6\times 8} & A_w \end{array} \right] \left[\begin{array}{c} x \\ x_w \end{array} \right] + \left[\begin{array}{ccccc} 0_{8\times 3} & B_c & F_L & 0_{8\times 6} & B_c \\ 0_{6\times 3} & B_w & 0_{6\times 4} & 0_{6\times 6} & B_w \end{array} \right] \left[\begin{array}{c} d \\ u \\ w_E \\ w_w \\ w_\lambda \end{array} \right], \tag{34}$$

$$\left[\begin{array}{c} \dot{e} \\ e \\ z_\lambda \\ z_E \\ z_w \end{array} \right] = \left[\begin{array}{cc} -C_{c2} & 0_{3\times 6} \\ -C_{c1} & 0_{3\times 6} \\ -\lambda C_{c1} & 0_{3\times 6} \\ -F_R A_c & 0_{4\times 6} \\ 0_{6\times 8} & C_w \end{array} \right] \left[\begin{array}{c} x \\ x_w \end{array} \right]$$

$$+ \left[\begin{array}{ccccc} 0_{3\times 3} & 0_{3\times 3} & 0_{3\times 4} & [0_{3\times 3} \; -I_3] & 0_{3\times 3} \\ I_3 & 0_{3\times 3} & 0_{3\times 4} & [-I_3 \; 0_{3\times 3}] & 0_{3\times 3} \\ \lambda I_3 & 0_{3\times 3} & 0_{3\times 4} & \lambda[-I_3 \; 0_{3\times 3}] & 0_{3\times 3} \\ 0_{4\times 3} & -F_R B_c & -F_R F_L & 0_{4\times 6} & -F_R B_c \\ 0_{6\times 3} & D_w & 0_{6\times 4} & 0_{6\times 6} & D_w \end{array} \right] \left[\begin{array}{c} d \\ u \\ w_E \\ w_w \\ w_\lambda \end{array} \right]. \tag{35}$$
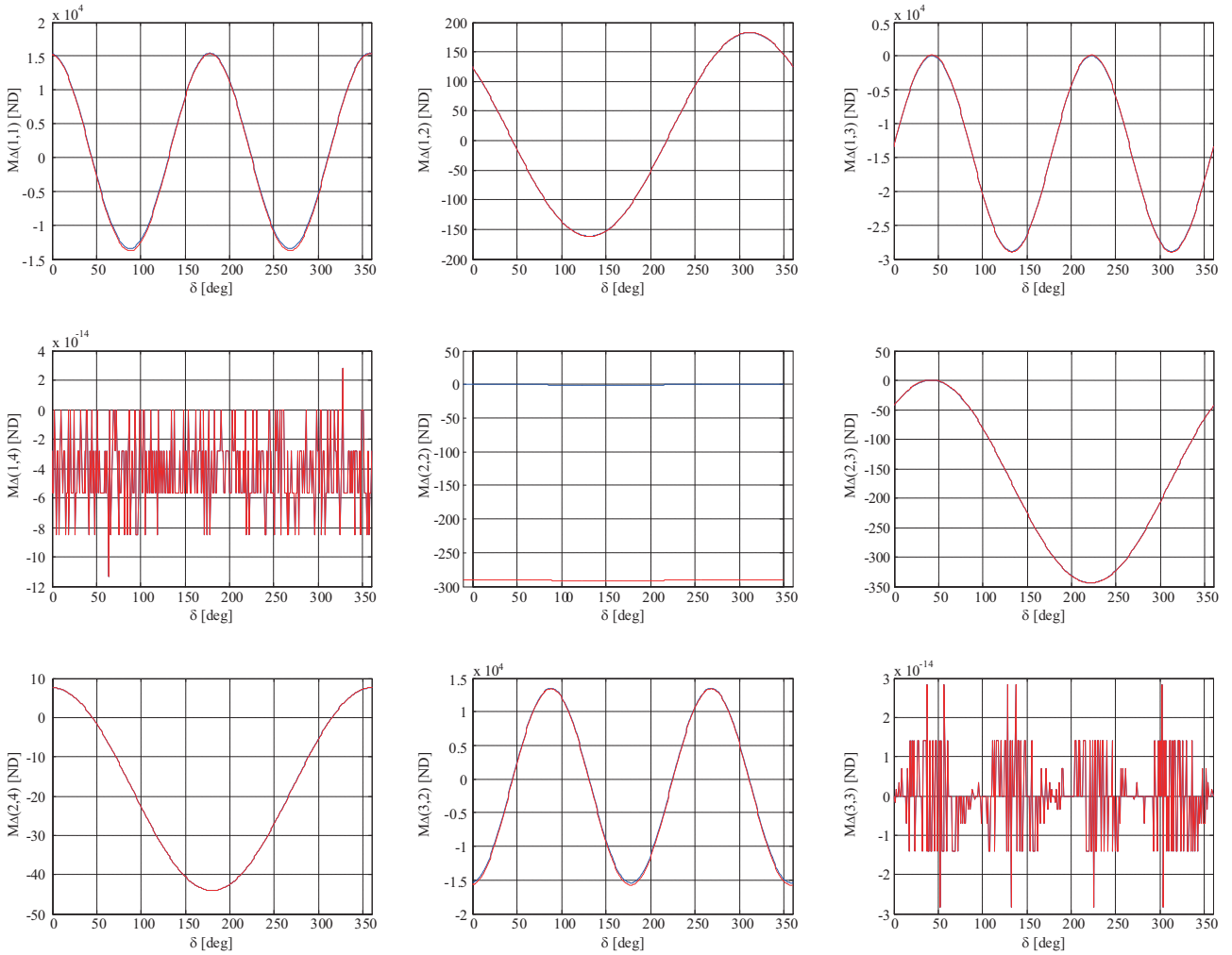

Figure 42: Varying width $M_\Delta(\delta)$ from nominal M_c of $M_c(\delta)$ (Blue: PSR-BOL, Red: PSR-EOL).
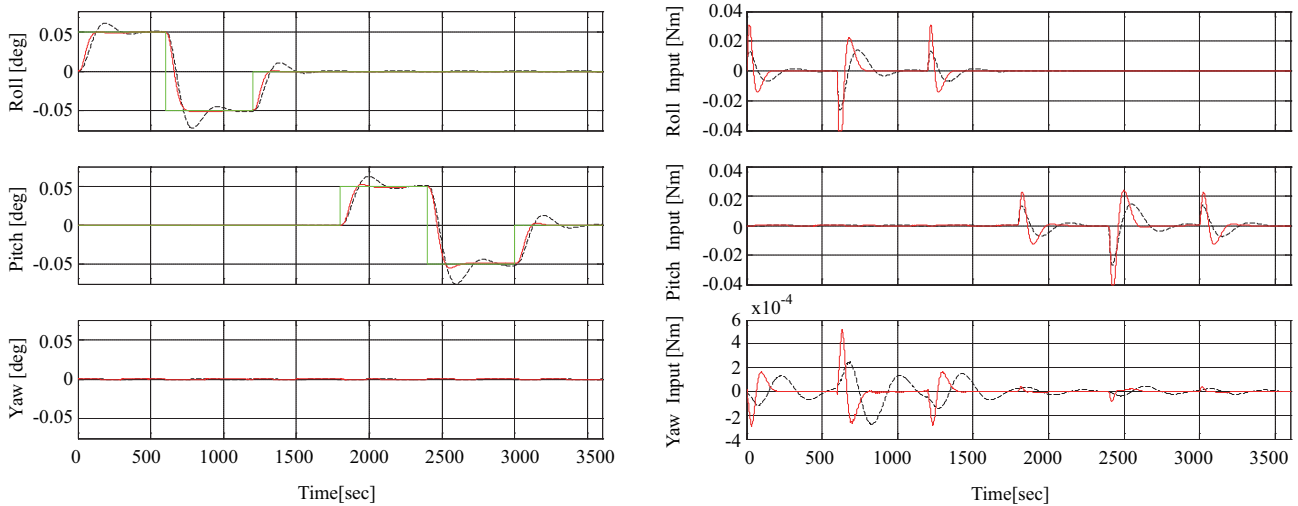
Figure 43: Step responses and corresponding input signals. Solid lines: μ-synthesis based control law. Broken lines: PD control law.
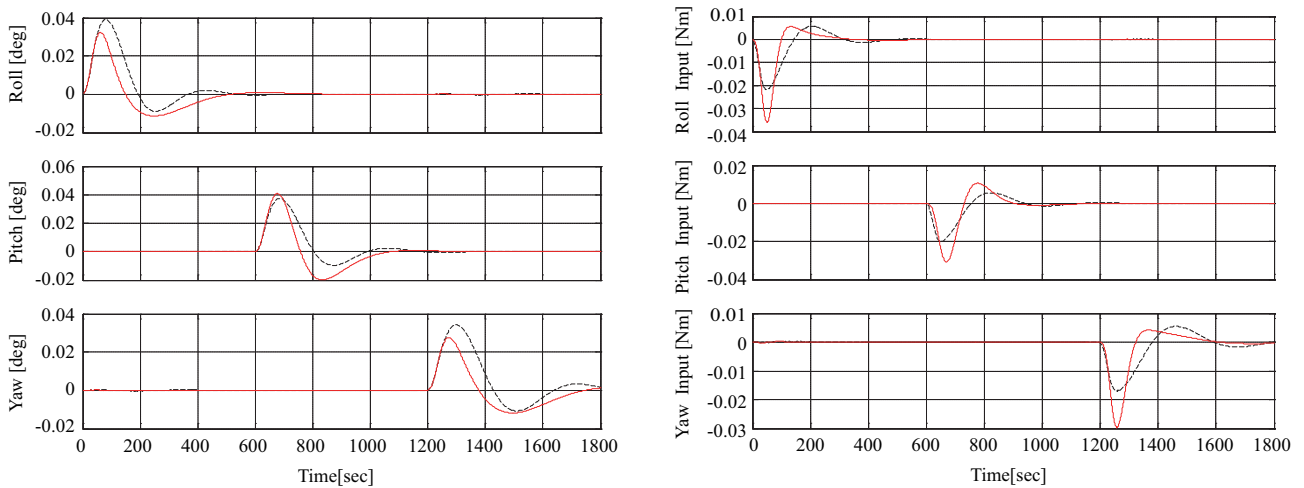

Figure 44: Impulse responses to disturbance input and corresponding input signals. Solid lines: μ-synthesis based control law. Broken lines: PD control law.

are set according to actual in-orbit experiment sequences. The first case is the bias response by the step reference attitude angle added to each axis for 600 sec, and the second case is the impulse disturbance response by reaction wheels. The disturbance causes 0.04 Nm torque during 30 sec added to each axis for 600 sec. The initial paddle angle is set to 45 deg; a conventional PD control law is also used in each case for comparison. These simulation results are presented in Figs. 43 and 44.

Results show that the closed-loop systems are stable and that our proposed LTI control law using μ-synthesis achieved better control performance than the conventional PD control law. The control input

signals remain within the limitation ($|u| \leq 0.04$ Nm) in each case.

7 Linearly Interpolated Gain Scheduling Control Law

This section presents the design procedure of the gain scheduling control law used in the experiment. The control law is scheduled in accordance with solar paddle rotation angle, which provides good control performance at all paddle angles. Since the scheduling law has only two grid points and is calculated simply by linear interpolation, it has low memory requirements and short processing time, which are desirable characteristics from the standpoint of implementability.

7.1 LPV Description of the Spacecraft Model

In the control law design, the so-called "unconstrained mode model" is employed in order to derive the reduced order model, by which high order control laws can be avoided. The model is then approximated using piecewise-linear functions of the parameter δ so as to apply the proposed synthesis condition.

Unconstrained mode model To start with, the constrained mode model (8) is modified in the following form:

$$M(\delta)\ddot{q} + Kq = Lu + Lw. \qquad (36)$$

Since the damping term $D\dot{q}$ is relatively small, it is ignored here. This makes the corresponding eigenvalue problem feasible, which shall be mentioned below. The damping term is to be added again after coordinate transformation.

Define a new modal coordinate $\mu \in \boldsymbol{R}^{(3+\Sigma_j n_j)\times 1}$ as

$$q := \boldsymbol{\phi}(\delta)\mu, \quad \boldsymbol{\phi}(\delta) := \left[\phi_1(\delta), \phi_2(\delta), \dots, \phi_{3+\Sigma_j n_j}(\delta)\right].$$

$\boldsymbol{\phi}(\delta)$ is a transformation matrix obtained by solving generalized eigenvalue problems related to the constraint modal equations (8):

$$K\phi_i(\delta) = \sigma_i^2(\delta)M(\delta)\phi_i(\delta), \ (i = 1, ..., 3 + \Sigma_j n_j),$$
$$(37)$$
$$(\sigma_1^2(0) \le \sigma_2^2(0) \le \cdots \le \sigma_{3+\Sigma_j n_j}^2(0)).$$

Since K and $M(\delta)$ are symmetric and $M(\delta)$ is positive-definite, the eigenvalues here are all non-negative
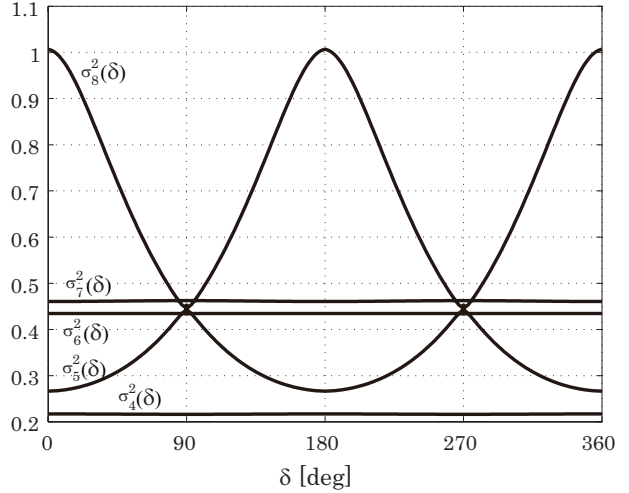
Figure 45: Paddle angle dependence of $\Sigma^2(\delta)$.

$(\sigma_i^2 \ge 0)$ and the eigenvectors satisfy

$$\begin{aligned}
\boldsymbol{\phi}^T(\delta)M(\delta)\boldsymbol{\phi}(\delta) &= I_{3+\Sigma_j n_j}, \\
\boldsymbol{\phi}^T(\delta)K\boldsymbol{\phi}(\delta) &= \mathrm{diag}\{\sigma_i^2(\delta)\} := \Sigma^2(\delta).
\end{aligned}$$

$\sigma_i(\delta)$ is called the i-th modal frequency. Note that $\sigma_1(\delta) = \sigma_2(\delta) = \sigma_3(\delta) = 0$ since these correspond to three rigid modes of the spacecraft. Fig. 45 shows paddle angle dependence of $\sigma_i^2(\delta)$ $(i = 4, 5, 6, 7, 8)$. Among these elements, σ_5^2 and σ_8^2 affect rotational dynamics of the spacecraft, whereas σ_4^2, σ_6^2 and σ_7^2 affect almost only translational dynamics.

Since δ is slowly varying, an "unconstrained" modal equation is yielded by transforming q to μ and adding the modal damping term $\Delta(\delta)\dot{\mu}$ as follows:

$$\Pi(\delta) : \begin{cases} \ddot{\mu} + \Delta(\delta)\dot{\mu} + \Sigma^2(\delta)\mu = \Phi(\delta)u, \\ y = \begin{bmatrix} \Phi^T(\delta) & 0 \\ 0 & \Phi^T(\delta) \end{bmatrix} \begin{bmatrix} \mu \\ \dot{\mu} \end{bmatrix}, \end{cases} \quad (38)$$

$$\begin{aligned} \text{where} \quad \Phi(\delta) &:= \boldsymbol{\phi}^T(\delta)L, \\ \Delta(\delta) &:= \mathrm{diag}\{2\zeta_i\sigma_i(\delta)\}. \end{aligned}$$

The disturbance input w is omitted here for simplicity. Each element of the modal damping matrix $\Delta(\delta)$ is supposed to be proportional to the modal frequency $\sigma_i(\delta)$ with constant of proportionality $2\zeta_i$. Note that eigenvalue problems (37) should be solved at each parameter value δ. As a result, parameter dependencies of matrices $\Delta(\delta)$, $\Sigma(\delta)$ and $\Phi(\delta)$ cannot be defined by mathematical expressions of δ.

Reduced order model Fig. 45 shows that $\Sigma^2(\delta)$ has reflectional symmetry in $\delta = 0$ and 180. In addi-

tion, each element $\sigma_i(\delta)$ which affects the rotational dynamics has a partner element $\sigma_j(\delta)$ that satisfies

$$\sigma_i(\delta) = \sigma_j(180 - \delta), \quad \text{for } \delta \in [0, 90].$$

Fig. 45 shows the case of $(i, j) = (5, 8)$. At the same time, the following holds for the pair (i, j):

$$\Phi_{(i,k)}(\delta) = \begin{cases} -\Phi_{(j,k)}(180 - \delta), & \text{for } i, j \geq 4, \ k = 1, \\ \Phi_{(j,k)}(180 - \delta), & \text{otherwise} \end{cases}$$

Consequently, the singular values of $\Pi(\delta)$ have reflectional symmetry in $\delta = 90$, that is,

$$|\Pi(\delta)| = |\Pi(180 - \delta)|, \quad \text{for } \delta \in [0, 90].$$

The transfer functions of $\Pi(\delta)$ and $\Pi(180 - \delta)$ are almost the same, except for the signs of the elements from roll to yaw and from yaw to roll. Moreover, especially in the case of ETS-VIII, the gains of those elements are relatively small and so negligible. Consequently, noting that μ_i and μ_j do not affect each other in (38) and are therefore interchangeable, the spacecraft model can be regarded almost symmetric in $\delta = 90$ and the range of the paddle rotation angle can be restricted to $\delta \in [0, 90] =: \Theta_{\text{val}}$ in the subsequent discussion. Although the nominal paddle rotation speed $\dot{\delta}$ is 4.17×10^{-3} deg/sec (= 360 deg/day), its range is set to $\dot{\delta} \in [-4.17 \times 10^{-3}, 4.17 \times 10^{-3}] =: \Omega_{\text{val}}$ in consideration of reflectional symmetry.

Since the matrices $\Sigma(\delta)$ and $\Delta(\delta)$ are diagonal, by changing the order of the elements in μ it is easy to divide the full order model (38) into a reduced order model, which is composed of low frequency modes, and residual modes, which are composed of higher frequency modes (see Fig. 46 (left)). The total number of vibration modes of ETS-VIII in equation (38) is 30 (i.e. $\sum_j n_v(j) = 30$). In this research the reduced order model comprises the three rigid modes, $\mu_1, \mu_2,$ and $\mu_3,$ and the lowest frequency mode among the vibration modes that affect rotational dynamics, μ_5 (recall that μ_4 affects only translational dynamics). This vibration mode is chosen because its frequency is lower than 0.1 Hz and it may affect attitude control system.

$$\begin{bmatrix} \ddot{\mu}_{rom} \\ \ddot{\mu}_{res} \end{bmatrix} + \begin{bmatrix} \Delta_{rom}(\delta) & 0 \\ 0 & \Delta_{res}(\delta) \end{bmatrix} \begin{bmatrix} \dot{\mu}_{rom} \\ \dot{\mu}_{res} \end{bmatrix}$$

$$+ \begin{bmatrix} \Sigma_{rom}^2(\delta) & 0 \\ 0 & \Sigma_{res}^2(\delta) \end{bmatrix} \begin{bmatrix} \mu_{rom} \\ \mu_{res} \end{bmatrix} = \begin{bmatrix} \Phi_{rom}(\delta) \\ \Phi_{res}(\delta) \end{bmatrix} u,$$
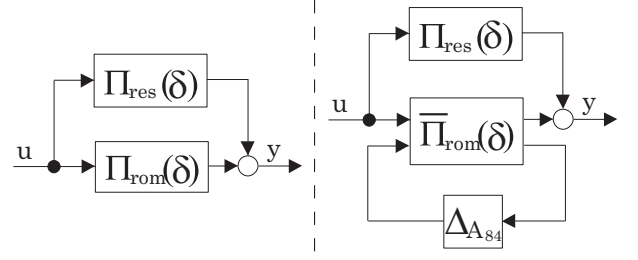

Figure 46: Left: The spacecraft model is divided into a reduced order model Π_{rom} and residual modes Π_{res}. Right: The reduced order model is described using the approximate system $\bar{\Pi}_{rom}$ and the norm-bounded perturbation $\Delta_{A_{84}}$.

where $(*)_{rom}$ denotes the reduced order model and $(*)_{res}$ denotes the residual modes ($\mu_{rom} = [\mu_1, \mu_2, \mu_3, \mu_5]^T$). Then the residual modes are clearly stable since they are second order systems with $\Delta_{res}(\delta) > 0$ and $\Sigma_{res}^2(\delta) > 0$. The followings are the state-space representations of the reduced order model and the residual modes:

$$\Pi_{rom}(\delta) : \begin{cases} \dot{x}_{rom} = A_{rom}(\delta)x_{rom} + B_{rom}(\delta)u, \\ y_{rom} = C_{rom}(\delta)x_{rom}, \end{cases}$$

$$\Pi_{res}(\delta) : \begin{cases} \dot{x}_{res} = A_{res}(\delta)x_{res} + B_{res}(\delta)u, \\ y_{res} = C_{res}(\delta)x_{res}, \end{cases} \tag{39}$$

$$y = y_{rom} + y_{res},$$

where

$$x_{rom} = [\mu_{rom}^T, \dot{\mu}_{rom}^T]^T \in \mathbf{R}^{8 \times 1},$$

$$x_{res} = [\mu_{res}^T, \dot{\mu}_{res}^T]^T \in \mathbf{R}^{62 \times 1},$$

$$A_*(\delta) = \begin{bmatrix} 0 & I \\ -\Sigma_*^2(\delta) & -\Delta_*(\delta) \end{bmatrix}, \ B_* = [0, \Phi_*(\delta)^T]^T,$$

$$C_* = \begin{bmatrix} \Phi_*^T(\delta) & 0 \\ 0 & \Phi_*^T(\delta) \end{bmatrix}, \ * = \{rom, res\}.$$

A low order control law can be obtained using only the reduced order model. However, if the higher order model composed of residual modes is ignored, spillover may occur and the system might become unstable. Therefore the residual modes should be taken into account in the controller design as an additive perturbation to the control system so that the closed-loop system possesses robust stability against residual modes. The residual modes, together with the approximation error described in the following section, are dealt with as uncertain blocks.

Piecewise-linear approximation The reduced order model (39) is an LPV system with paddle rotation angle δ as its parameter. Since eigenvalue problems (37) should be solved for each δ in order to obtain the unconstrained mode model (38), parameter-dependent matrices in (39) cannot be described using mathematical expressions of δ. In order to design a gain scheduling control law in conventional ways, parameter dependence of the LPV system should be reformulated in a polytopic [16] or linear fractional transformation (LFT) representation [23]. Here, so as to apply the synthesis condition described in Section 7.2, this system is approximated using piecewise-linear functions of δ, where corresponding approximation errors are modeled as a norm-bounded perturbation. It is apparent that a larger number of grid points leads to smaller approximation errors and consequently to less conservative results.

Here the nine grid points for the interval $\delta \in \Theta_{\text{val}}$ are set as

$$
\begin{aligned}
D^\Pi &:= \{0, 11.25, 22.5, 33.75, 45, 56.25, 67.5, 78.75, 90\} \\
&= \{\delta_0^\Pi, \delta_1^\Pi, \delta_2^\Pi, \delta_3^\Pi, \delta_4^\Pi, \delta_5^\Pi, \delta_6^\Pi, \delta_7^\Pi, \delta_8^\Pi\}. \quad (40)
\end{aligned}
$$

Then the three matrices in (39) are approximated using piecewise-linear functions with D^Π. For example, the approximate matrix of $A_{rom}(\delta)$ is as follows:

$$
\begin{aligned}
\bar{A}_{rom}(\delta) &= A_{rom(i)} \\
&\quad + \frac{\delta - \delta_i^\Pi}{\delta_{i+1}^\Pi - \delta_i^\Pi}(A_{rom(i+1)} - A_{rom(i)}), \\
\delta &\in [\delta_i^\Pi, \delta_{i+1}^\Pi], i = 0, 1, \ldots, 7. \quad (41)
\end{aligned}
$$

As for ETS-VIII model, the approximation error of only $\{A_{rom}(\delta)\}_{(8,4)}$ is taken into account. This is because $\{A_{rom}(\delta)\}_{(8,4)}$ corresponds to σ_5, the lowest modal frequency, and accordingly its error greatly affects the vibration dynamics of the reduced order model, while errors of other matrix elements have little effect on the vibration dynamics. Let

$$
e_{(8,4)\,\max} = \max_{\delta \in \Theta_{\text{val}}} \left| \{A_{rom}(\delta)\}_{(8,4)} - \{\bar{A}_{rom}(\delta)\}_{(8,4)} \right|.
$$

Then, $A_{rom}(\delta)$ is included in a certain set defined by a norm-bounded perturbation $\Delta_{A_{84}}$:

$$
A_{rom}(\delta) \in \bar{A}_{rom}(\delta) + E_a \Delta_{A_{84}} F_a, \quad |\Delta_{A_{84}}| \le 1, \tag{42}
$$

$$
E_a := [\mathbf{0}_{1\times7}, e_{(8,4)\,\max}]^T, \quad F_a := [\mathbf{0}_{1\times3}, 1, \mathbf{0}_{1\times4}].
$$
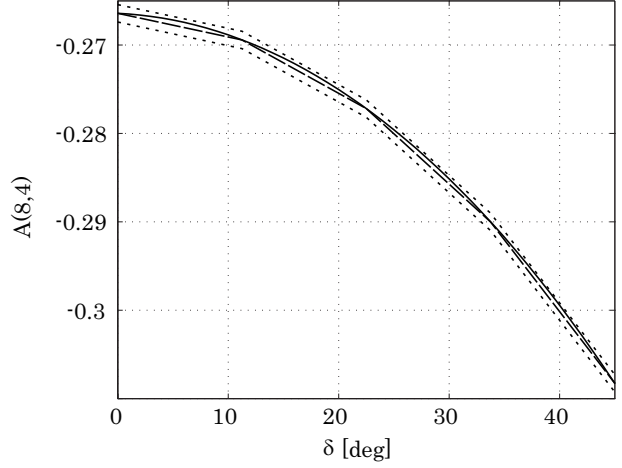
Figure 47: The (8,4)'th element of $A_{rom}(\delta)$ (solid line) and its approximate matrix $\bar{A}_{rom}(\delta)$ (broken line). The solid line lies between two dotted lines which represent the (8,4)'th element of the right side of (42) at $\Delta_{A_{84}} = \pm 1$.

This means that the use of the piecewise-linear model with (42) can be justified by standard robust control methods against norm-bounded perturbations. Fig. 47 shows $\{A_{rom}(\delta)\}_{(8,4)}$ (solid line) and $\{\bar{A}_{rom}(\delta)\}_{(8,4)}$ (broken line) of $\delta \in [0, 45]$. The dotted lines represent the (8,4)'th element of the right side of (42) at $\Delta_{A_{84}} = \pm 1$. Obviously $\{A_{rom}(\delta)\}_{(8,4)}$ is within the region bounded by the two dotted lines.

Using these matrices, the approximate reduced order model is described by

$$
\bar{\Pi}_{rom}(\delta) \begin{cases} \dot{\bar{x}}_{rom} &= \bar{A}_{rom}(\delta)\bar{x}_{rom} + \bar{B}_{rom}(\delta)u + E_a w_1 \\ y &= \bar{C}_{rom}(\delta)\bar{x}_{rom} \\ z_1 &= F_a \bar{x}_{rom} \end{cases}
$$

(43)

where $\bar{B}_{rom}(\delta)$ and $\bar{C}_{rom}(\delta)$ are piecewise-linear approximate matrices of $B_{rom}(\delta)$ and $C_{rom}(\delta)$. As is shown in Fig. 46 (right), the reduced order model is described by $\bar{\Pi}_{rom}(\delta)$ with

$$
w_1 = \Delta_{A_{84}} z_1, \quad |\Delta_{A_{84}}| \le 1. \tag{44}
$$

Since (42) holds, the stability and performance of the reduced order system $\Pi_{rom}(\delta)$ are guaranteed by a control law which guarantees the robust stability and performance of the system $\bar{\Pi}_{rom}(\delta)$ against the perturbation $\Delta_{A_{84}}$. Such a control law is designed in the following section.

7.2   Control Law Design

This section describes the proposed design method for a linearly interpolated gain scheduling control law. The following control law $\Gamma(\delta)$ is to be designed:

$$\Gamma(\delta) : \begin{cases} \dot{x}_c = A_c(\delta)x_c + B_c y, \\ u = C_c(\delta)x_c, \end{cases} \quad (45)$$

where $A_c(\delta)$ and $C_c(\delta)$ are piecewise-linear matrix functions of δ:

$$\begin{aligned} A_c(\delta) &= A_{c1} \cdot \tfrac{\delta}{90} + A_{c0} \cdot (1 - \tfrac{\delta}{90}), \\ C_c(\delta) &= C_{c1} \cdot \tfrac{\delta}{90} + C_{c0} \cdot (1 - \tfrac{\delta}{90}) \end{aligned} \quad (46)$$

for $\delta \in [0, 90](= \Theta_{\mathrm{val}})$. The scheduling law (46) has only two grid points and therefore consists of only two pairs of matrices (A_{c0}, C_{c0}) and (A_{c1}, C_{c1}). This structure is chosen to minimize the onboard memory requirement. Moreover, these matrices are piecewise-linear on the parameter δ and are easily scheduled, which is also desirable for spacecraft control systems.

It should be noted that the control law (45) is restricted to strictly proper and that B_c is assumed to be given *a priori* and to be independent of δ. This comes from the limitation of the synthesis condition mentioned below. In spite of the limitation, however, the control law gives better performance than the baseline PD control law regardless of the paddle rotation, as shown in Section 7.3.

The control requirements here are as follows:

- Robustness against the residual modes,

- Robustness against the perturbation $\delta_{A_{84}}$ (approximation error),

- Control input limitation ($|u| \leq 0.04$ Nm), and

- Attitude tracking following a step command to an accuracy of ± 0.05 deg with a settling time of 300 sec.

The control law is designed so as to satisfy these requirements for all paddle angles by the following procedure.

Generalized plant   A generalized plant $M(\delta)$ corresponding to the control requirements is defined using the LPV system $\bar{\Pi}_{rom}(\delta)$ as shown in Fig. 48, where $\bar{\Pi}_{rom}(\delta)$ is the approximate system of the reduced order model, $\Gamma(\delta)$ is a control law to be designed and W is a weighting function corresponding
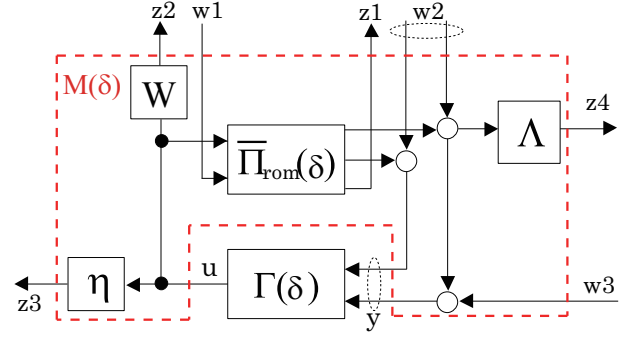
Figure 48: Generalized plant $M(\delta)$ (within the broken lines).

to the residual modes.   The other blocks, Λ and η, are constant and diagonal matrices used as design parameters. Roughly speaking, $T_{z_1 w_1}$, the transfer function from w_1 to z_1, and $T_{z_2 w_2}$ are related to robustness against approximation error and the residual modes respectively, $T_{z_3 w_3}$ and η are concerned with the magnitudes of the torque inputs, and $T_{z_4 w_3}$ and Λ are concerned with angle command tracking performance. Fig. 49 shows the gain of the weighting function and singular values of the residual modes at all $\delta \in \Theta_{\mathrm{val}}$. The weighting function $W(s)$ is selected so that its gain is always larger than the singular values of the residual modes. Here $W(s)$ is a sixth order system: a second order system for each axis. Consequently the generalized plant $M(\delta)$ has 14 states and is represented by the following form:

$$M(\delta) : \begin{cases} \dot{x} = A(\delta)x + B_1(\delta)w + B_2(\delta)u, \\ z = C_1(\delta)x + D_{11}(\delta)w + D_{12}(\delta)u, \\ y = C_2(\delta)x + D_{21}(\delta)w. \end{cases} \quad (47)$$

These state-space matrices have piecewise-linear parameter dependency with D^Π of (40) since these are defined using $\bar{A}_{rom}(\delta)$, $\bar{B}_{rom}(\delta)$ and $\bar{C}_{rom}(\delta)$. From the main loop theorem [24], the control requirements are satisfied if

$$||T_{\boldsymbol{zw}}||_{L2} < 1, \quad \text{for all } \delta \in \Theta_{\mathrm{val}}, \quad (48)$$

where $\boldsymbol{w} = [w_1, w_2, w_3]$, $\boldsymbol{z} = [z_1, z_2, z_3, z_4]$ and $T_{\boldsymbol{zw}}$ is the transfer function from $\boldsymbol{w}$ to $\boldsymbol{z}$.   As is mentioned above, only some parts of the transfer function $T_{\boldsymbol{zw}}$ should be considered (that is, $T_{z_1 w_1}, T_{z_2 w_2}, T_{z_3 w_3}$ and $T_{z_4 w_3}$). Thus scaling matrices with an adequate structure are used in the control law design.
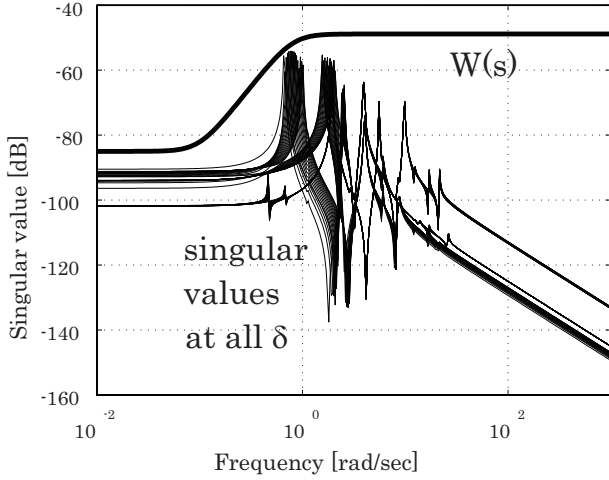
Figure 49: Weighting function and singular values of the residual modes.

Synthesis condition Assuming that the controller matrix B_c is given beforehand, the next theorem gives a sufficient condition for a gain scheduling control law $\Gamma(\delta)$ of (45) that satisfies the control requirements. The order of the designed control law is the same as that of the generalized plant $M(\delta)$, that is, 14. Some of the matrix variables in the theorem are labelled with a superscript Γ (G^Γ for example) to indicate that those matrices are used to derive the control law $\Gamma(\delta)$ in (45).

Theorem 3 [9] *There exist matrices $A_c(\delta)$ and $C_c(\delta)$ of (45) which satisfy (48) for any $(\delta, \dot\delta) \in (\Theta_{val} \times \Omega_{val})$, if there exist a positive constant ϵ, a positive constant $\gamma < 1$, symmetric matrices $Y_k, S_k (k = \{0, 1, \ldots, 8\})$, matrices $G^\Gamma, V_0^\Gamma, V_1^\Gamma, W_0^\Gamma$ and W_1^Γ which satisfy (49)–(52) for $\omega = \pm 4.17 \times 10^{-3}$ (recall that $\Omega_{val} := [-4.17 \times 10^{-3}, 4.17 \times 10^{-3}]$), where*

$$
\begin{aligned}
V_k &:= (1 - \frac{\delta_k^\Pi}{90})V_0^\Gamma + \frac{\delta_k^\Pi}{90}V_1^\Gamma \\
W_k &:= (1 - \frac{\delta_k^\Pi}{90})W_0^\Gamma + \frac{\delta_k^\Pi}{90}W_1^\Gamma \\
Q_{cl(k)}^{11} &:= A_k Y_k + Y_k A_k^T + B_{2(k)} W_k + W_k^T B_{2(k)}^T \\
&\quad - \frac{\omega}{\Delta \delta_k^\Pi} \Delta Y_k, \\
Q_{cl(k)}^{11(-)} &:= A_k Y_k + Y_k A_k^T + B_{2(k)} W_k + W_k^T B_{2(k)}^T \\
&\quad - \frac{\omega}{\Delta \delta_{k-1}^\Pi} \Delta Y_{k-1}, \\
Q_{cl(k)}^{12} &:= A_k S_k + Y_k C_{2(k)}^T B_c^T + B_{2(k)} W_k + V_k^T \\
&\quad - \frac{\omega}{\Delta \delta_k^\Pi} \Delta S_k, \\
Q_{cl(k)}^{12(-)} &:= A_k S_k + Y_k C_{2(k)}^T B_c^T + B_{2(k)} W_k + V_k^T \\
&\quad - \frac{\omega}{\Delta \delta_{k-1}^\Pi} \Delta S_{k-1}, \\
Q_{cl(k)}^{22} &:= B_c C_{2(k)} S_k + S_k C_{2(k)}^T B_c^T + V_k + V_k^T \\
&\quad - \frac{\omega}{\Delta \delta_k^\Pi} \Delta S_k, \\
Q_{cl(k)}^{22(-)} &:= B_c C_{2(k)} S_k + S_k C_{2(k)}^T B_c^T + V_k + V_k^T \\
&\quad - \frac{\omega}{\Delta \delta_{k-1}^\Pi} \Delta S_{k-1}, \\
R_k^1 &:= G^{\Gamma T} - S_k - \epsilon B_{2(k)} W_k, \\
R_k^2 &:= G^{\Gamma T} - S_k - \epsilon V_k, \\
U_k^1 &:= C_{1(k)} Y_k + D_{12(k)} W_k, \\
U_k^2 &:= C_{1(k)} S_k + D_{12(k)} W_k, \\
L_{cl(k)}^{11} &:= (\Delta A_k Y_k + A_k \Delta Y_k) \\
&\quad + (\Delta B_{2(k)} W_k + B_{2(k)} \Delta W_k), \\
L_{cl(k)}^{12} &:= (\Delta A_k S_k + A_k \Delta S_k) \\
&\quad + (\Delta B_{2(k)} W_k + B_{2(k)} \Delta W_k), \\
L_{cl(k)}^{21} &:= B_c(\Delta C_{2(k)} Y_k + C_{2(k)} \Delta Y_k) + \Delta V_k, \\
L_{cl(k)}^{22} &:= B_c(\Delta C_{2(k)} S_k + C_{2(k)} \Delta S_k) + \Delta V_k, \\
L_{cl(k)}^{15} &:= -\Delta S_k - \epsilon(\Delta B_{2(k)} W_k + B_{2(k)} \Delta W_k), \\
L_{cl(k)}^{16} &:= -\epsilon(\Delta B_{2(k)} W_k + B_{2(k)} \Delta W_k), \\
L_{cl(k)}^{26} &:= -\Delta S_k - \epsilon \Delta V_k, \\
L_{cl(k)}^{31} &:= (\Delta C_{1(k)} Y_k + C_{1(k)} \Delta Y_k) \\
&\quad + (\Delta D_{12(k)} W_k + D_{12(k)} \Delta W_k), \\
L_{cl(k)}^{32} &:= (\Delta C_{1(k)} S_k + C_{1(k)} \Delta S_k) \\
&\quad + (\Delta D_{12(k)} W_k + D_{12(k)} \Delta W_k), \\
L_{cl(k)}^{35} &= L_{cl(k)}^{36} := -\epsilon(\Delta D_{12(k)} W_k + D_{12(k)} \Delta W_k), \\
\Delta\{*\} &:= \{*\}_{k+1} - \{*\}_k, \\
&\quad (\Delta Y_k := Y_{k+1} - Y_k, \text{ for example})
\end{aligned}
$$

---

[9] This is a special case of Theorem 1 in [25]. See the reference for details of the generalized theorem.

$$\begin{bmatrix} Y_k & S_k \\ S_k & S_k \end{bmatrix} > 0, \quad k = 0, 1, \ldots, 8, \tag{49}$$

$$\begin{bmatrix} Q_{cl(k)}^{11} & Q_{cl(k)}^{12} & U_k^{1T} & B_{1(k)} & R_k^1 & -\epsilon B_{2(k)}W_k \\ Q_{cl(k)}^{12\,T} & Q_{cl(k)}^{22} & U_k^{2T} & B_c D_{21(k)} & -\epsilon V_k & R_k^2 \\ U_k^1 & U_k^2 & -\gamma I & D_{11(k)} & -\epsilon D_{12(k)}W_k & -\epsilon D_{12(k)}W_k \\ B_{1(k)}^T & D_{21(k)}^T B_c^T & D_{11(k)}^T & -\gamma I & 0 & 0 \\ R_k^{1\,T} & -\epsilon V_k^T & -\epsilon W_k^T D_{12(k)}^T & 0 & -\epsilon(G^\Gamma + G^{\Gamma\,T}) & 0 \\ -\epsilon W_k^T B_{2(k)}^T & R_k^{2\,T} & -\epsilon W_k^T D_{12(k)}^T & 0 & 0 & -\epsilon(G^\Gamma + G^{\Gamma\,T}) \end{bmatrix}$$

$$=: J_{cl(k)} < 0, \quad k = 0, 1, \ldots, 7, \tag{50}$$

$$\begin{bmatrix} Q_{cl(k)}^{11(-)} & Q_{cl(k)}^{12(-)} & U_k^{1T} & B_{1(k)} & R_k^1 & -\epsilon B_{2(k)}W_k \\ Q_{cl(k)}^{12(-)\,T} & Q_{cl(k)}^{22(-)} & U_k^{2T} & B_c D_{21(k)} & -\epsilon V_k & R_k^2 \\ U_k^1 & U_k^2 & -\gamma I & D_{11(k)} & -\epsilon D_{12(k)}W_k & -\epsilon D_{12(k)}W_k \\ B_{1(k)}^T & D_{21(k)}^T B_c^T & D_{11(k)}^T & -\gamma I & 0 & 0 \\ R_k^{1\,T} & -\epsilon V_k^T & -\epsilon W_k^T D_{12(k)}^T & 0 & -\epsilon(G^\Gamma + G^{\Gamma\,T}) & 0 \\ -\epsilon W_k^T B_{2(k)}^T & R_k^{2\,T} & -\epsilon W_k^T D_{12(k)}^T & 0 & 0 & -\epsilon(G^\Gamma + G^{\Gamma\,T}) \end{bmatrix} < 0,$$

$$k = 1, 2, \ldots, 8, \tag{51}$$

$$J_{cl(k)} + \frac{1}{2}(L_{cl(k)} + L_{cl(k)}^T) < 0, \quad k = 0, 1, \ldots, 7, \tag{52}$$

$$L_{cl(k)} := \begin{bmatrix} L_{cl(k)}^{11} & L_{cl(k)}^{12} & 0 & \Delta B_{1(k)} & L_{cl(k)}^{15} & L_{cl(k)}^{16} \\ L_{cl(k)}^{21} & L_{cl(k)}^{22} & 0 & B_c \Delta D_{21(k)} & -\epsilon \Delta V_k & L_{cl(k)}^{26} \\ L_{cl(k)}^{31} & L_{cl(k)}^{32} & 0 & \Delta D_{11(k)} & L_{cl(k)}^{35} & L_{cl(k)}^{36} \\ 0 & 0 & 0 & 0 & 0 & 0 \\ 0 & 0 & 0 & 0 & 0 & 0 \\ 0 & 0 & 0 & 0 & 0 & 0 \end{bmatrix}$$

---

and $A_k := A(\delta_k^\Pi)$. *Other system matrices, such as* $B_{1(k)}$ *and* $B_{2(k)}$, *are defined in the same way.*

One of the solutions $A_c(\delta)$ *and* $C_c(\delta)$ *is given as:*

$$A_c(\delta) = V_S^\Gamma(\delta)G^{\Gamma-1},$$
$$C_c(\delta) = W_S^\Gamma(\delta)G^{\Gamma-1},$$

where

$$V_S^\Gamma(\delta) = V_1^\Gamma \cdot \frac{\delta}{90} + V_0^\Gamma \cdot (1 - \frac{\delta}{90}),$$
$$W_S^\Gamma(\delta) = W_1^\Gamma \cdot \frac{\delta}{90} + W_0^\Gamma \cdot (1 - \frac{\delta}{90}).$$

The corresponding Lyapunov function is $x^T Y_{cl}(\delta)x$, *where*

$$Y_{cl}(\delta) = \begin{bmatrix} Y(\delta) & S(\delta) \\ S(\delta) & S(\delta) \end{bmatrix},$$
$$Y(\delta) = \frac{1}{l} \int_{\delta - \frac{l}{2}}^{\delta + \frac{l}{2}} Y_S(h)dh,$$
$$S(\delta) = \frac{1}{l} \int_{\delta - \frac{l}{2}}^{\delta + \frac{l}{2}} S_S(h)dh,$$

and l *is some small positive constant such that the interval* $[\delta_k^\Pi - \frac{l}{2}, \delta_k^\Pi + \frac{l}{2}]$ *contains at most one grid point,*

$$Y_S(\delta) = Y_k + \frac{\delta - \delta_k^\Pi}{\delta_{k+1}^\Pi - \delta_k^\Pi}(Y_{k+1} - Y_k),$$
$$S_S(\delta) = S_k + \frac{\delta - \delta_k^\Pi}{\delta_{k+1}^\Pi - \delta_k^\Pi}(S_{k+1} - S_k),$$

for $\delta \in [\delta_k^\Pi, \delta_{k+1}^\Pi]$.

Proof *See Appendix D.*

In the synthesis condition, ω corresponds to $\dot{\delta}$, the time derivative of δ. The condition is derived by letting ω be a parameter which is independent of δ but which lies within the region of Ω_{val} as shown in [26] and [27].

Although inequalities (49)–(52) may appear rather complicated compared to synthesis conditions in other

papers [28, 23, 27, 29, 30], they can be solved using standard LMI solvers by letting ϵ be a line-search parameter [31, 32]. The important point of the theorem is that the derived control law guarantees stability and performance for *all* parameter values despite the fact that the control law itself has only two grid points, which are the boundary points of the parameter range. In addition, the Lyapunov function has more grid points than the control law since $Y_{cl}(\delta)$ has nine grid points of D^Π. This implies that even though the derived control law has a simple structure, the class of Lyapunov functions can be wider, and this is another reason why the proposed method is less conservative than existing methods. These features make this method totally different from other gridding methods such as [27]. How the stability and performance are guaranteed is shown through the proof in Appendix D.

Synthesis result A gain scheduling control law was designed for the PSR-BOL model of ETS-VIII using the generalized plant (47) and the proposed synthesis condition. Firstly, a standard H_∞ control problem of (48) at $\delta = 0$ was solved, and B_c of the derived H_∞ control law was chosen for the given matrix in (49)–(52)[10]. Then the matrix inequalities (49)–(52) were feasible and the matrices $G^\Gamma, V_0^\Gamma, V_1^\Gamma, W_0^\Gamma$ and W_1^Γ were obtained. The matrices in the scheduling laws (46) were given as

$$A_{c0} = V_0^\Gamma G^{\Gamma-1}, \qquad A_{c1} = V_1^\Gamma G^{\Gamma-1},$$
$$C_{c0} = W_0^\Gamma G^{\Gamma-1}, \qquad C_{c1} = W_1^\Gamma G^{\Gamma-1}.$$

The controller matrices $A_{c0}, A_{c1}, B_c, C_{c0}$ and C_{c1} are shown in Appendix C. Singular values of the derived control law are shown in Fig. 50. It can be seen that singular values around the frequency corresponding to the lowest vibration mode vary with paddle angle δ.

Although the derived control law (45) is defined for $\delta \in [0, 90] = \Theta_{\mathrm{val}}$, it is used for $\delta \in [0, 360]$ in practice. Because of the symmetry of the spacecraft model, as is shown in Fig. 45, $\Pi(180) = \Pi(0)$ and $\Pi(270) = \Pi(90)$ hold, and so this piecewise-linear scheduling law can be applied to $\delta \in [0, 360]$ by letting $\Gamma(180) = \Gamma(0)$ and $\Gamma(270) = \Gamma(90)$ and linearly

---
[10]This B_c was selected from three B_c matrices that were obtained at $\delta = 0, 45$ and 90 as the one that gave the best performance.
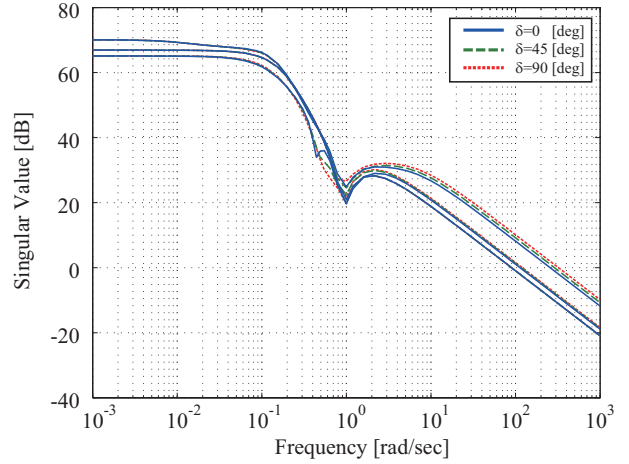
Figure 50: Singular values of the derived control law $\Gamma(\delta)$.
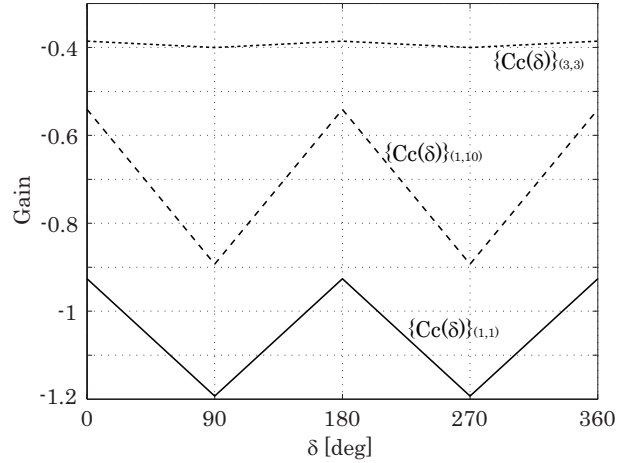
Figure 51: Some elements of the extended controller matrix $C_c(\delta)$.

interpolating them. As is mentioned in Section 7.1, the symmetry of the model in $\delta = 90$ is given by an approximation. The condition (48) was therefore checked with the extended scheduling law for the interval $\delta \in [90, 180]$ and, as a result, the use of the extended law was justified. This extended law is used in the following simulations. Some elements of the extended controller matrix $C_c(\delta)$ are shown in Fig. 51.

Computational burden The designed gain scheduling control law is compared from the viewpoint of computational burden with three other proposed control laws. Table 1 shows the controller order, the processing time of one control cycle and the mem-

Table 1: Processing time and memory requirement of each control law.

	order	processing time [msec]	required memory [byte]
Gain scheduling	14	1.40	4 140
μ-synthesis	36	2.28	7 948
DDFB	22	4.26	14 220
DVDFB	22	4.77	14 780
PD	3	0.22	668

ory required by each control law. These were estimated using an ETS-VIII SCLT facility. Because of its higher order structure, the μ-synthesis-based control law's processing time is about 1.6 times longer than that of the gain scheduling control law. Although the DVDFB law itself has a simple structure, its processing time is about 3.4 times longer due to the complexity of its added feedforward structure. Regarding memory size, the gain scheduling law requires less memory than three other control laws. Consequently, the computational burden of the gain scheduling law is the least among these experimental control laws.

7.3   Simulation Results

To evaluate the proposed synthesis and the designed control law, simulations were conducted using the control law (45) and the continuous full order ETS-VIII PSR-ID model. In these simulations, the full order ETS-VIII model is time-varying since the paddles rotate at a rate of 360 deg/day. The results are compared with those obtained using a baseline PD control law. White noises of standard deviation 1.11×10^{-4} are introduced as angular velocity observation noises. The noise characteristics were estimated from orbital flight data obtained during several years of the spacecraft's in-orbit operation.

Step response   Fig. 52 shows responses to ± 0.05 deg step commands injected into the roll and pitch axes for 600 seconds with initial paddle angle $\delta_0 = 0$. Corresponding input signals are also shown in the figure. Figs. 53 and 54 show the responses and input signals for $\delta_0 = 45$ and $\delta_0 = 90$ respectively. The attitude angles follow the step command signals well
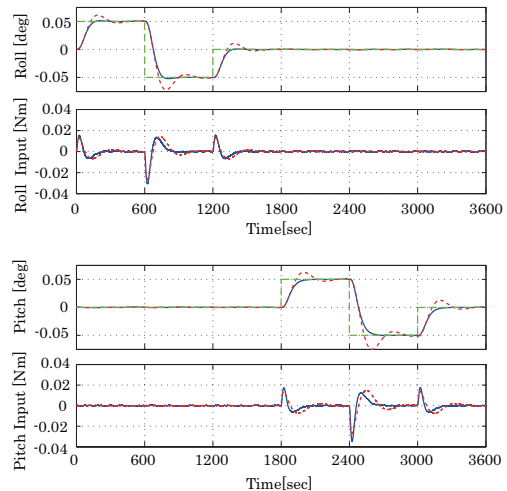
Figure 52: Step responses of $\delta_0=0$ and corresponding input signals. Solid lines: gain scheduling control law. Broken lines: baseline PD control law.
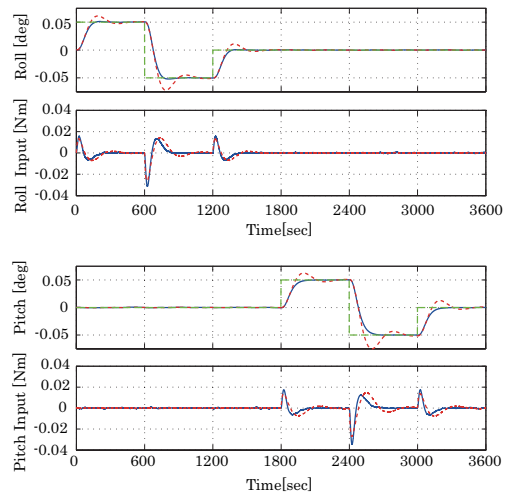
Figure 53: Step responses of $\delta_0=45$ and corresponding input signals.
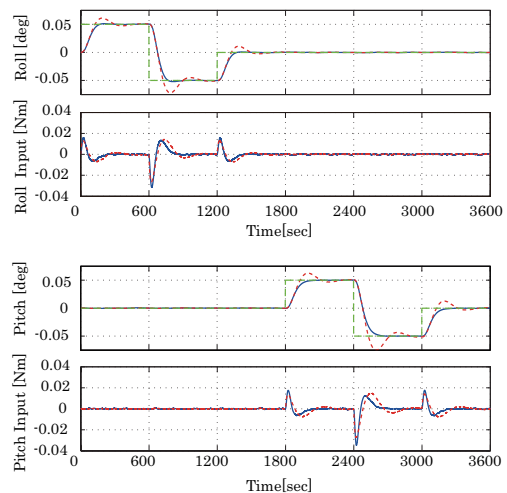
Figure 54: Step responses of $\delta_0=90$ and corresponding input signals.
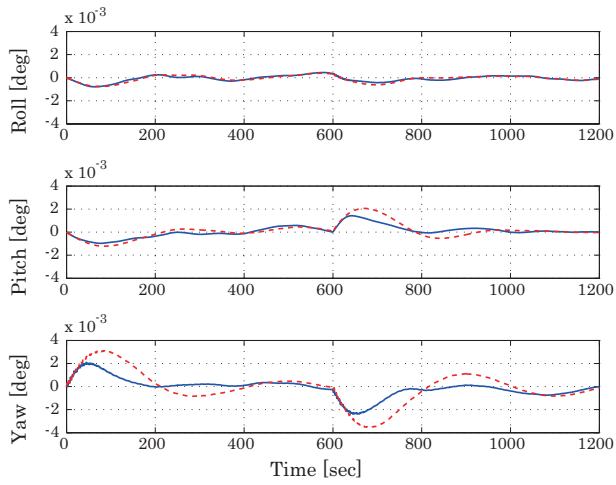
Figure 55: Impulse responses of δ_0=0. Solid lines: gain scheduling control law. Broken lines: baseline PD control law.
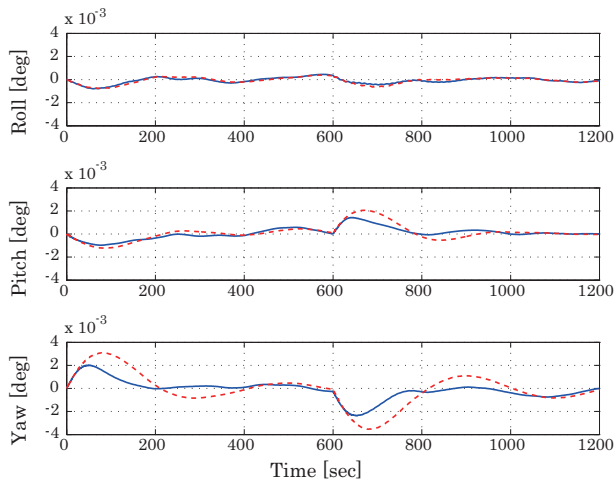
Figure 56: Impulse responses of δ_0=45.
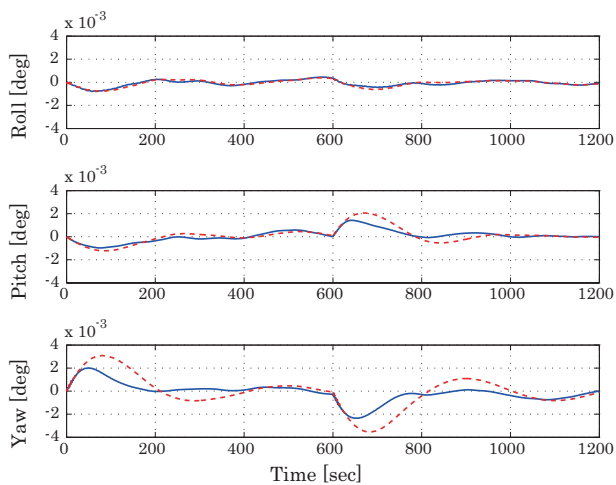
Figure 57: Impulse responses of δ_0=90.

and the input signals are always within the limitations ($|u| \leq 0.04$) in each case. Compared to the baseline PD control law (broken lines), the derived control law (solid lines) achieves about a 40% faster settling time in each case.

Impulse response The east-west station-keeping maneuver is also simulated by adding impulsive torque disturbances to the control system. Figs. 55–57 show attitude angles for each initial paddle angle $\delta_0 = 0, 45$, and 90. Solid lines show simulation results using the designed gain scheduling control law and broken lines show results using a baseline PD control law. In each case, attitude angle variation remains within ± 0.003 deg for each axis and satisfy the requirement in spite of the rotation of the solar paddles. Furthermore, the derived control law suppresses attitude angle change better than the baseline control law.

8 In-orbit Experiment Results

The in-orbit experiment has been carried out during two periods: June 21-29 in 2009, and February 28 - March 7 in 2010. The data of each response explained in Section 2.3 have been obtained twice so that the paddle angles have different initial values to verify the control performance as the LPV system. The extracted experiment results are shown in Figs. 58 - 65. All experiment results are summarized in Appendix E.

Fig. 58 shows the attitude angles of the first step response, Fig. 59 is the enlargement of the pitch axis result in this case. Additionally, Fig. 60 is the results of the second step response, and Fig. 61 is the enlargement of the roll axis. On the other hand, Figs. 62 and 64 show the results of the first and second rectangular disturbance responses caused by the RW respectively. Figs. 63 and 65 are the enlargements of the roll and the pitch axes respectively. The features of the experiment results are summarized below.

Step response In this response case, the reference attitude angle commands are given as ± 0.05 deg for the roll and pitch axes individually. The proposed control laws have achieved shorter settling time than the PD control law. Since the results of first and
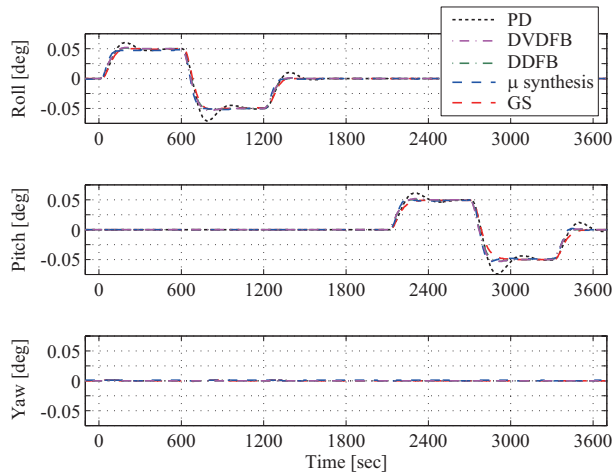
Figure 58: Time history of roll, pitch, yaw attitude angle responses to the first step command.
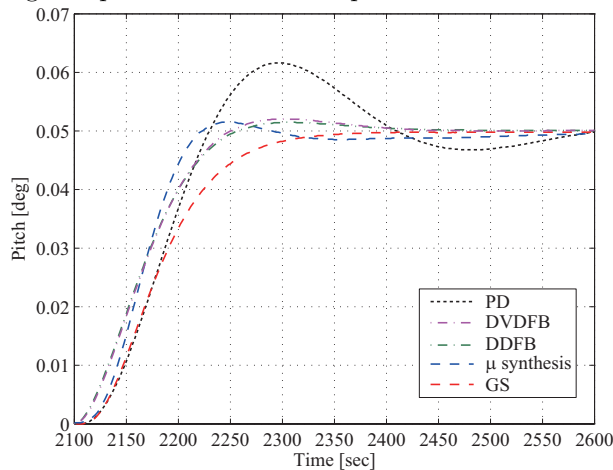
Figure 59: Time history of pitch attitude angle responses to the first step command.


Figure 60: Time history of roll, pitch, yaw attitude angle responses to the second step command.
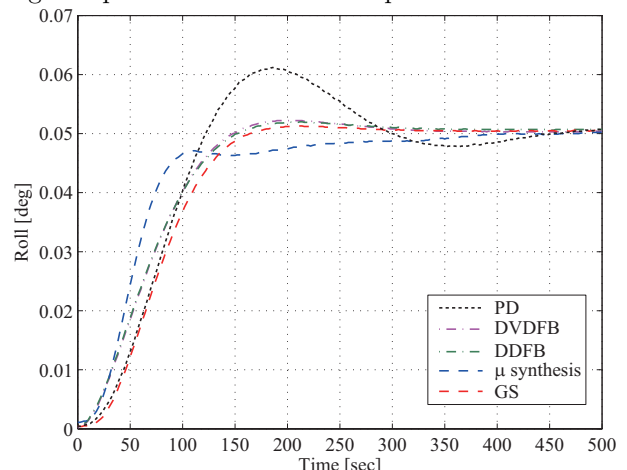
Figure 61: Time history of roll angle responses to the second step command.

second responses are also the same, it is confirmed that the proposed control laws are effective to the LPV system caused by the paddle rotation. Both of the DVDFB and DDFB control laws have achieved same results on all axes in the first and second responses. This is because the model-matching design method works well. The gain scheduling control law has achieved the same performance to the parameter change by the paddle rotation, while the results of rise time, settling time and overshoot are different in each axis. It depends on the modal vibration direction which is included in the reduced order plant for the controller design. In almost all response cases, μ-synthesis has achieved shortest rise time in the proposed control laws although the settling time is the longest. The reason is supposed to be that the order of the control law is higher than others.

Rectangular disturbance response In this response case, the disturbances caused by the RW are added as the rectangular torque 0.04 Nm for 30 sec to each axis individually. From the results, it is apparent that the proposed control laws are effective in reducing the influence of disturbances compared with the PD control law, as well as they are robustly stable against the paddle rotation. The performances of the maximum amplitude and the settling time using each control law are shown to have the same tendency as those shown in the step response case.

Finally, the average of the settling time of step responses and the maximum amplitude ratio of all disturbance responses is shown in Table 2. The DVDFB control law has achieved the best performance in both capabilities. This is because the optimization
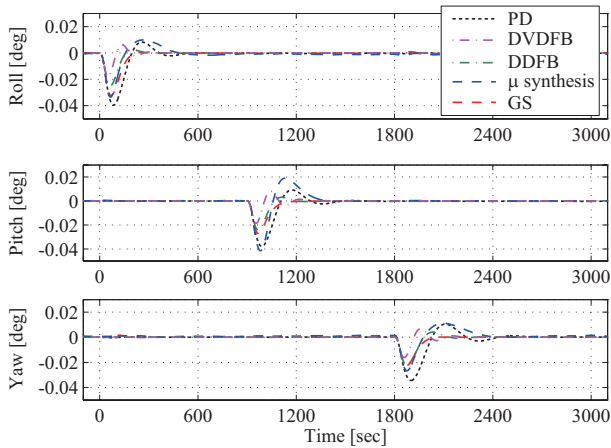
Figure 62: Time history of roll, pitch, yaw angles in response to the first rectangular disturbance.
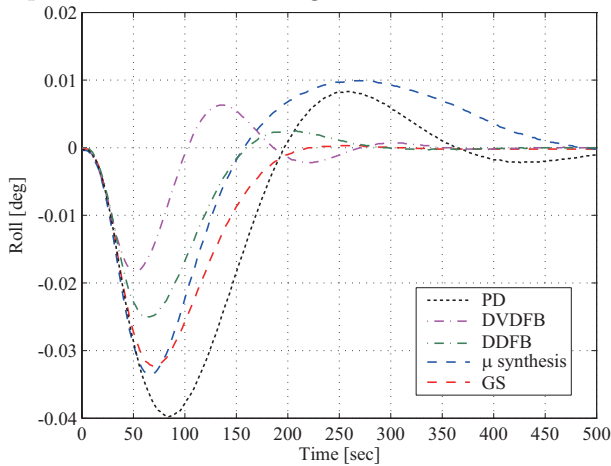
Figure 63: Time history of roll angles in response to the first rectangular disturbance.


Figure 64: Time history of roll, pitch, yaw attitude angles in response to the second rectangular disturbance.
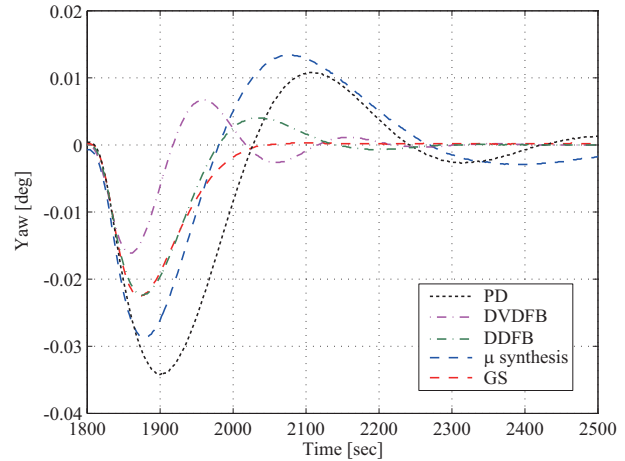
Figure 65: Time history of yaw angles in response to the second rectangular disturbance.

of control performance using the LMI has functioned more effectively compared with the other control law optimization, and the DVDFB has the wide bandwidth. On the other hand, the gain scheduling control law has also achieved good performances under the lowest required memory size and the shortest processing time among the proposed control laws as in Table 1. The μ-synthesis based control law works sufficiently well as an LTI controller for LPV MIMO system.

9 Conclusion

This report gave an overview of the in-orbit robust control experiment using ETS-VIII and described full results of the experiment obtained by four novel robust control laws along with the conventional PD control law. Since each proposed control law does

not impose heavy computational burden, it can be applied even to the current spacecraft onboard computers with little memory capacity and low computational power. The proposed control laws showed the ability to control MIMO LPV flexible spacecraft well. It was also shown that all proposed control laws can achieve better performance than PD control law that is generally used as a bus controller for many Japanese spacecrafts. The results demonstrated some characteristics of each control law: DVDFB and DDFB control laws achieve the shortest settling time with non-parametric robust stability, the μ-synthesis based control law can be designed by well known and commonly used controller design procedure, the gain scheduling law gives moderate performance despite of its simple structure.

It should be noted that this is the world's first in-orbit experiment in that an LPV flexible space-

Table 2: Average data of performance

	Settling time [sec]	Maximum amplitude [%]
PD	250	100.0
DVDFB	126	51.4
DDFB	130	67.5
μ-synthesis	153	85.0
Gain scheduling	144	82.5

craft is controlled by MIMO control laws. The obtained results will provide a basis for controller design methodologies for large flexible spacecrafts. It is expected that robust control laws, including proposed control laws in this report, become general algorithms as not experimental but bus control system for future spacecrafts.

Acknowledgement

We would like to acknowledge two supervisors of the experiment, Dr. Hideto Suzuki and Dr. Takanori Iwata. We also wish to thank the engineers of Mitsubishi Electric's Kamakura Works, Mitsubishi Space Software Co., Ltd. and Space Engineering Development Co., Ltd. for their sincere support.

References

[1] M. J. Balas. Active control of flexible systems. *Journal of Optimization Theory and Applications*, 25(3):415–436, 1978.

[2] S. Grocott, D. Miller J. How, D. MacMartin, and K. Liu. Robust control design and implementation on the middeck active control experiment. *Journal of Guidance, Control and Dynamics*, 17(6):1163–1170, 1994.

[3] A. Bukley. Hubble space telescope pointing control system design improvement study results. *Journal of Guidance, Control and Dynamics*, 18(2):194–199, 1995.

[4] T. Kida and I. Yamaguchi. On-orbit robust control experiment of flexible spacecraft ETS-VI. *Journal of Guidance, Control and Dynamics*, 20(5):865–872, 1997.

[5] Y. Chida, H. Soga, Y. Yamaguchi, T. Kida, I. Yamaguchi, and T. Sekiguchi. On-orbit attitude control experiments using ETS-VI by H_∞ control and two-degree-of freedom control. *Control Engineering Practice*, 6(9):1109–1116, 1998.

[6] T. Ohtani, Y. Hamada, T. Nagashio, T. Kida, S. Mitani, I. Yamaguchi, T. Kasai, and H. Igawa. Robust attitude control using mu-synthesis for the large flexible satellite ETS-VIII. *Journal of Space Technology and Science*, 25(1):27–40, 2009.

[7] Y. Hamada, T. Ohtani, T. Kida, and T. Nagashio. Synthesis of a linearly interpolated gain scheduling controller for large flexible spacecraft ETS-VIII. *Control Engineering Practice*, 19(6):611–625, 2011.

[8] T. Nagashio, T. Kida, T. Ohtani, and Y. Hamada. Design and implementation of robust symmetric attitude controller for ETS-VIII spacecraft. *Control Engineering Practice*, 18(12):1440–1451, 2010.

[9] M.J. Sidi. *Spacecraft Dynamics & Control*. Cambridge University Press, Cambridge, 1997.

[10] H.B. Hablani. Constrained and unconstrained modes: Some modeling aspects of flexible spacecraft. *Journal of Guidance*, 5:164–173, 1982.

[11] Y. Miyazawa. Design with multiple-delay-model and multiple-design-point approach. *Journal of Guidance, Control and Dynamics*, 18(3):508–515, 1995.

[12] T. Nagashio and T. Kida. Robust control of flexible mechanical systems by utilizing symmetry and its application to large space structures. *IEEE Transactions on Control Systems Technology*, 17(3):671–680, 2009.

[13] M. J. Balas. Direct velocity feedback control of large space structures. *Journal of Guidance, Control, and Dynamics*, 2(3):252–253, 1979.

[14] S. M. Joshi. Robust properties of collocated controllers for flexible spacecraft. *Journal of Guidance, Control, and Dynamics*, 9(1):85–91, 1986.

[15] A. Arbel and N. K. Gupta. Robust colocated control for large flexible space structures. *Journal of Guidance, Control, and Dynamics*, 4(5):480–486, 1981.

[16] P. Apkarian, P. Gahinet, and G. Becker. Self-scheduled H_∞ control of linear parameter-varying systems: A design example. *Automatica*, 31(9):1251–1261, 1995.

[17] P. W. Likins. *Dynamics and Control of Flexible Space Vehicle*. Technical Report 32-1329, Revision 1, Jet Propulsion Laboratory, NASA, 1970.

[18] M. Ikeda, M. Koujitani, and T. Kida. Optimality of direct velocity and displacement feedback for large space structures with collocated sensors and actuators. In *Proceedings of the 12th IFAC World Congress*, pages 91–94, 1993.

[19] P. Gahinet and P. Apkarian. A linear matrix inequality approach to H_∞ control. *International Journal of Robust and Nonlinear Control*, 4(4):421–448, 1994.

[20] P. Gahinet, A. Nemirovski, A. J. Laub, and M. Chilali. *LMI Control Toolbox*. The MathWorks, Inc., Massachusetts, USA, 1996.

[21] Y. Nesterov and A. Nemirovski. *Interior Point Polynominal Method in Convex Programming: Theory and Applications*. Society for Industrial and Applied Mathematics, Philadelphia, USA, 1994.

[22] A. Nemirovski and P. Gahinet. The projective method for solving linear matrix inequalities. In *Proceedings of the American Control Conference*, pages 840–844, 1994.

[23] P. Apkarian and P. Gahinet. A convex characterization of gain-scheduled H_∞ controllers. *IEEE Transactions on Automatic Control*, 40(7):853–864, 1995.

[24] A. Packard and J. Doyle. The complex structured singular value. *Automatica*, 29(1):71–109, 1993.

[25] Y. Hamada, T. Ohtani, T. Kida, and T. Nagashio. A new gain scheduling controller synthesis and its application to attitude control systems of a large flexible satellite. In *Proceedings of the 2006 IEEE International Conference on Control Applications*, pages 2914–2920, 2006.

[26] R. Watanabe, K. Uchida, M. Fujita, and E. Shimemura. L^2 gain and H^∞ control of linear systems with scheduling parameter. In *Proceedings of the 33rd IEEE Conference on Decision and Control*, pages 1412–1414, 1994.

[27] F. Wu, X. H. Yang, A. Packard, and G. Becker. Induced l_2-norm control for lpv systems with bounded parameter-variation rates. *International Journal of Robust and Nonlinear Control*, 6(9):983–998, 1996.

[28] G. Becker and A. Packard. Gain-scheduled state-feedback with quadratic stability for uncertain systems. In *Proceedings of the American Control Conference*, pages 2702–2703, 1991.

[29] F. Wu and S. Kim. Lpv controller interpolation for improved gain-scheduling control performance. In *Proceedings of the AIAA Guidance, Navigation and Control Conference*, 2002.

[30] D. J. Stilwell and W. J. Rugh. Stability preserving interpolation methods for the synthesis of gain scheduled controllers. *Automatica*, 36(5):665–671, 2000.

[31] T. Shimomura, M. Takahashi, and T. Fujii. Extended-space control design with parameter-dependent lyapunov functions. In *Proceedings of the 40th IEEE Conference on Decision and Control*, pages 2157–2162, 2001.

[32] U. Shaked. Improved lmi representations for the analysis and the design of continuous-time systems with polytopic type uncertainty. *IEEE Transactions on Automatic Control*, 46:652–656, 2001.

[33] P. Apkarian and R. J. Adams. Advanced gain-scheduling techniques for uncertain systems. *IEEE Transactions on Control Systems Technology*, 6(1):21–32, 1998.

[34] S. Lim. *Analysis and Control of Linear Parameter-Varying Systems.* Ph.D. dissertation, Stanford University, 1999.

[35] M. C. de Oliveira, J. C. Geromel, and J. Bernussou. Extended H_2 and H_∞ norm characterizations and controller parameterizations for discrete-time systems. *International Journal of Control*, 75(9):666–679, 2002.

[36] Y. Ebihara and T. Hagiwara. New dilated lmi characterizations for continuous-time control design and robust multiobjective control. In *Proceedings of the American Control Conference*, pages 47–52, 2002.

[37] I. Masubuchi, A. Kume, and E. Shimemura. Spline-type solution to parameter dependent lmis. In *Proceedings of the 37th IEEE Conference on Decision and Control*, pages 1753–1758, 1998.

[38] I. Masubuchi. On numerical solution to parameter-dependent convex differential inequalities. In *Proceedings of the 38th IEEE Conference on Decision and Control*, pages 305–309, 1999.

A Quantitive Details of Model Parameters

This section presents parameter values for PSR-BOL, PSR-EOL and PSR-ID model described in Section 3.2. As for the inertia of each component, J_b (rigid body), J_{a1} (LDR-A) and J_{a2} (LDR-B) could not be parameterized individually in this study. However, we have parameterized $J_{ab} := J_b + J_{a1} + J_{a2}$ instead. Then, since $C_1 = C_2 = I_3$, J is redefined as:

$$J := J_{ab} - m_b \tilde{r}_b \tilde{r}_b + \sum_{i=3}^{4} C_i^T J_{ai} C_i - \sum_{i=1}^{4} m_{ai} \tilde{r}_{ai} \tilde{r}_{ai}$$

(recall Section 3.1).

A.1 PSR-BOL

Mass and inertia

m_b	2911.1		
m_{a1}	259.48		
m_{a2}	259.47		
m_{a3}	122.70		
m_{a4}	122.70		
J_{ab}	25959	−128.85	−975.68
	−128.85	69334	114.21
	−975.68	114.21	54802
J_{a3}	3337.4	0.30000	−0.050000
	0.30000	52.600	2.6422
	−0.050000	2.6422	3400.0
J_{a4}	3568.1	4.5600	−0.050000
	4.5600	52.600	37.300
	−0.050000	37.300	3400.5

Position vector

r_b	$[0.050718 \quad -0.0047709 \quad 1.3838]^T$
r_{a1}	$[-7.2649 \quad -14.300 \quad -2.7020]^T$
r_{a2}	$[7.6531 \quad -13.400 \quad -2.6810]^T$
r_{a3}	$[-0.00064313 \quad -10.670 \quad 1.5087]^T$
r_{a4}	$[-0.00064313 \quad 10.670 \quad 1.5087]^T$
R_{a1}	$[-0.84000 \quad 0.0 \quad 0.25000]^T$
R_{a2}	$[0.84000 \quad 0.0 \quad 0.25000]^T$
R_{a3}	$[0.0 \quad -1.2000 \quad 1.5000]^T$
R_{a4}	$[0.0 \quad 1.2000 \quad 1.5000]^T$

Modal parameter: LDR-A

$$d_{a1}^0 = \begin{bmatrix} 0.20121 & -10.101 & -0.68559 \\ 0.38043 & -0.68517 & 10.683 \\ -0.23620 & 6.1884 & 0.32110 \\ -13.646 & -0.48521 & 4.4258 \\ 0.15832 & -9.3110 & -0.41159 \\ 4.8917 & 0.065401 & 1.7667 \\ 0.042880 & -2.8251 & -0.093706 \\ -0.11945 & -0.22451 & 3.8676 \end{bmatrix}^T$$

$$d_{a1}^1 = \begin{bmatrix} -6.6112 & -9.9476 & 144.72 \\ -3.2422 & 143.10 & 9.5742 \\ 71.741 & 2.5921 & -23.630 \\ -1.6547 & 58.849 & 2.7306 \\ -26.501 & -1.2207 & 20.020 \\ 0.32223 & -7.1875 & -0.28798 \\ -4.4653 & -0.25159 & 5.3411 \\ -0.18186 & 4.3574 & 0.20221 \end{bmatrix}^T$$

j	$\omega_{a1,j}$ [unit: Hz]	$\zeta_{a1,j}$
1	0.10450	0.005
2	0.17820	0.005
3	0.51510	0.005
4	0.70880	0.005
5	1.2980	0.005
6	2.1414	0.005
7	3.3301	0.005
8	4.1516	0.005

Modal parameter: LDR-B

$$d_{a2}^0 = \begin{bmatrix} 0.16286 & 10.007 & 0.69381 \\ -0.82700 & -0.68721 & 10.643 \\ 0.22674 & 6.2748 & 0.34809 \\ 13.107 & -0.49215 & 5.3197 \\ -0.12437 & -9.2367 & -0.42749 \\ 4.7880 & -0.081699 & -1.0556 \\ 0.033440 & 2.7394 & 0.098686 \\ 0.83810 & 0.25767 & -4.6301 \end{bmatrix}^T$$

$$d_{a2}^1 = \begin{bmatrix} -1.4203 & -10.117 & 146.53 \\ -2.6859 & -145.63 & -9.9278 \\ 69.930 & -2.7402 & 29.691 \\ -1.5271 & -58.469 & -2.8910 \\ -24.438 & 1.2927 & -23.748 \\ -0.29826 & -7.1043 & -0.33810 \\ 3.9039 & -0.26735 & 6.1092 \\ 0.18720 & 4.7794 & 0.27080 \end{bmatrix}^T$$

j	$\omega_{a2,j}$ [unit: Hz]	$\zeta_{a2,j}$
1	0.10530	0.005
2	0.17850	0.005
3	0.50710	0.005
4	0.70490	0.005
5	1.2892	0.005
6	2.1931	0.005
7	3.3380	0.005
8	4.0706	0.005

Modal parameter: North paddle

$$d_{a3}^0 \quad \begin{bmatrix} 0.0 & 0.0 & 8.6000 \\ 9.3000 & 0.0 & 0.0 \\ 0.0 & 0.0 & 4.9000 \\ 0.0 & 0.0 & 0.0 \\ 0.0 & 0.0 & -2.3000 \\ 0.0 & 0.10000 & -1.5000 \\ 4.6000 & 0.0 & 0.0 \end{bmatrix}^T$$

$$d_{a3}^1 \quad \begin{bmatrix} 116.30 & 0.0 & 0.0 \\ 0.0 & 0.10000 & -118.30 \\ 19.400 & 0.0 & 0.0 \\ 0.0 & 7.4000 & 0.10000 \\ -4.5000 & 0.0 & 0.0 \\ -1.7000 & 0.0 & 0.0 \\ 0.0 & 0.0 & -1.8000 \end{bmatrix}^T$$

j	$\omega_{a3,j}$ [unit: Hz]	$\zeta_{a3,j}$
1	0.060000	0.005
2	0.13000	0.005
3	0.31500	0.005
4	0.45500	0.005
5	0.90900	0.005
6	1.8470	0.005
7	2.7890	0.005

Modal parameter: South paddle

$$d_{a4}^0 \quad \begin{bmatrix} 0.0 & 0.0 & -8.6000 \\ -9.3000 & 0.0 & 0.0 \\ 0.0 & 0.0 & -4.9000 \\ 0.0 & 0.0 & 0.0 \\ 0.0 & 0.0 & 2.3000 \\ 0.0 & 0.10000 & -1.5000 \\ 4.6000 & 0.0 & 0.0 \end{bmatrix}^T$$

$$d_{a4}^1 \quad \begin{bmatrix} -116.30 & 0.0 & 0.0 \\ 0.0 & -0.10000 & 118.30 \\ -19.400 & 0.0 & 0.0 \\ 0.0 & -7.4000 & -0.10000 \\ 4.4000 & 0.0 & 0.0 \\ -1.8000 & 0.0 & 0.0 \\ 0.0 & 0.0 & -1.8000 \end{bmatrix}^T$$

j	$\omega_{a4,j}$ [unit: Hz]	$\zeta_{a4,j}$
1	.061000	0.005
2	0.13000	0.005
3	0.31500	0.005
4	0.45500	0.005
5	0.91500	0.005
6	1.8540	0.005
7	2.7910	0.005

A.2 PSR-EOL

The major difference between PSR-BOL and PSR-EOL is the amount of remaining fuel. Thus some parameters concerning mass and inertia differ from those of PSR-BOL, whereas other modal parameters are the same.

Mass and inertia

m_b	2673.2
m_{a1}	259.48
m_{a2}	259.47
m_{a3}	122.70
m_{a4}	122.70

$$J_{ab} \quad \begin{bmatrix} 25619 & -129.05 & -976.35 \\ -129.05 & 69043 & 114.60 \\ -976.35 & 114.60 & 54702 \end{bmatrix}$$

$$J_{a3} \quad \begin{bmatrix} 3337.4 & 0.30000 & -0.050000 \\ 0.30000 & 52.600 & 2.6422 \\ -0.050000 & 2.6422 & 3400.0 \end{bmatrix}$$

$$J_{a4} \quad \begin{bmatrix} 3568.1 & 4.5600 & -0.050000 \\ 4.5600 & 52.600 & 37.300 \\ -0.050000 & 37.300 & 3400.5 \end{bmatrix}$$

Position vector

r_b	$[0.055218 \quad -0.0051315 \quad 1.3775]^T$
r_{a1}	$[-7.2649 \quad -14.300 \quad -2.7020]^T$
r_{a2}	$[7.6531 \quad -13.400 \quad -2.6810]^T$
r_{a3}	$[-0.00011893 \quad -10.670 \quad 1.5089]^T$
r_{a4}	$[-0.00011893 \quad 10.670 \quad 1.5089]^T$
R_{a1}	$[-0.84000 \quad 0.0 \quad 0.25000]^T$
R_{a2}	$[0.84000 \quad 0.0 \quad 0.25000]^T$
R_{a3}	$[0.0 \quad -1.2000 \quad 1.5000]^T$
R_{a4}	$[0.0 \quad 1.2000 \quad 1.5000]^T$

Modal parameter All modal parameters of the flexible components are the same as in Appendix A.1.

A.3 PSR-ID

Since PSR-ID model is based on the spacecraft data in the checkout phase, the mass and inertia parameters are the same as those of PSR-BOL. Some modal parameters are different from PSR-BOL.

Mass and inertia All parameters are the same as in Appendix A.1.

Position vector All parameters are the same as in Appendix A.1.

Modal parameter: LDR-A d_{a1}^0 and d_{a1}^1 are the same as in Appendix A.1.

j	$\omega_{a1,j}$ [unit: Hz]	$\zeta_{a1,j}$
1	0.10200	0.0059
2	0.18100	0.0233
3	0.50700	0.0085
4	0.70880	0.005
5	1.2980	0.005
6	2.1414	0.005
7	3.3301	0.005
8	4.1516	0.005

Modal parameter: LDR-B d_{a2}^0 and d_{a2}^1 are the same as in Appendix A.1.

j	$\omega_{a2,j}$ [unit: Hz]	$\zeta_{a2,j}$
1	0.10200	0.0059
2	0.18100	0.0233
3	0.50700	0.0085
4	0.70490	0.005
5	1.2892	0.005
6	2.1931	0.005
7	3.3380	0.005
8	4.0706	0.005

Modal parameter: North paddle d_{a3}^0 and d_{a3}^1 are the same as in Appendix A.1.

j	$\omega_{a3,j}$ [unit: Hz]	$\zeta_{a3,j}$
1	0.064000	0.0072
2	0.16700	0.0179
3	0.35300	0.0056
4	0.46400	0.005
5	0.90900	0.005
6	1.8470	0.005
7	2.7890	0.005

Modal parameter: South paddle d_{a4}^0 and d_{a4}^1 are the same as in Appendix A.1.

j	$\omega_{a4,j}$ [unit: Hz]	$\zeta_{a4,j}$
1	0.064000	0.0072
2	0.16700	0.0179
3	0.35300	0.0056
4	0.46400	0.005
5	0.91500	0.005
6	1.8540	0.005
7	2.7910	0.005

B Proof of Theorem 1

The asymptotic stability of (14) is equivalent to

$$A(\delta) = \begin{bmatrix} 0 & I \\ -M^{-1}(\delta)K^* & -M^{-1}(\delta)D^* \end{bmatrix}$$

being stable. Matrix $A(\delta)$ is stable if and only if there exists a matrix $X > 0$ such that

$$XA(\delta) + A(\delta)^T X < 0 \qquad (53)$$

The Lyapunov inequality obviously has a solution

$$X_e(\delta) = \begin{bmatrix} K^* & \alpha M(\delta) \\ \alpha M(\delta) & M(\delta) \end{bmatrix} > 0 \qquad (54)$$

because

$$X_e(\delta)A(\delta) + A(\delta)^T X_e(\delta) = -Q(\delta) \qquad (55)$$

where

$$Q(\delta) = \begin{bmatrix} 2\alpha K^* & \alpha D^* \\ \alpha D^* & 2D^* - 2\alpha M(\delta) \end{bmatrix} > 0$$

form Lemma 1 and the Schur complement.

C Proof of Theorem 2

From the Schur complement, (19) is equivalent to (53) and

$$XA(\delta) + A(\delta)^T X + \frac{1}{\gamma}\begin{bmatrix} XB(\delta) & C^T \end{bmatrix}\begin{bmatrix} B(\delta)^T X \\ C \end{bmatrix} < 0 \qquad (56)$$

As stated in Theorem 1, $X_e(\delta) > 0$ given in (54) is a solution of (53). And from (55), (56) is

$$\frac{1}{\gamma}NN^T - Q(\delta) < 0 \qquad (57)$$

where $Q(\delta) > 0$ and from (54), (18)

$$N = \begin{bmatrix} \alpha L & L \\ L & 0 \end{bmatrix}.$$

Inequality (57) holds for sufficiently large $\gamma > \gamma_{min}$ for all δ. Indeed, the lower bound of γ can be obtained as

$$\gamma_{min} = \max_{\delta \in \boldsymbol{R}} \lambda_{max}\left(Q(\delta)^{-1/2}NN^T Q(\delta)^{-1/2}\right)$$

by eigenvalue analysis of (57).

D Proof of Theorem 3

D.1 Basic concept

Gain scheduling control laws for LPV systems have been parameterized with parameter-dependent Lyapunov functions in some references [33, 34]. However, these parameterizations include time derivatives ($\dot{\delta}$), matrix multiplications of system matrices

and parameter-dependent LMI solutions, and matrix inversions of parameter-dependent solutions, which render the controller matrices too complex for implementation in resource-limited onboard computers.

The following are used to avoid these issues and to derive a synthesis condition for piecewise-linear scheduling laws:

- Restriction of the class of parameter-dependent solutions: this eliminates time derivative parameters from the controller matrices.

- Assumptions about the controller input matrix B_c: the synthesis condition is reduced to parameter-dependent LMIs without introducing matrix products of system matrices and parameter-dependent solutions.

- Extension (or dilation) of LMI [35, 36]: parameter-dependent solutions in controller matrices are replaced by another matrix variable.

- Spline-type solutions to parameter-dependent LMIs [37]: the condition is reduced to finite number of LMIs by restricting B_c to be a parameter-independent matrix.

These are shown in the following two Lemmas.

D.2 L_2 gain performance

The lemma below gives a sufficient condition for the L_2 gain performance of a closed loop system. In this lemma, parameter-dependent matrices are expressed by calligraphic characters and the argument (δ) is omitted for simplicity (for example, $\mathcal{A}$ represents $A(\delta)$).

Lemma 2 *Consider the following LPV plant*

$$
\begin{aligned}
\dot{x} &= \mathcal{A}x + \mathcal{B}_1 w + \mathcal{B}_2 u \\
z &= \mathcal{C}_1 x + \mathcal{D}_{11} w + \mathcal{D}_{12} u \\
y &= \mathcal{C}_2 x + \mathcal{D}_{21} w,
\end{aligned}
$$

and the gain scheduling control law

$$
\begin{aligned}
\dot{x}_c &= \mathcal{A}_c x_c + \mathcal{B}_c y \\
u &= \mathcal{C}_c x_c,
\end{aligned}
$$

with $\delta(t) \in \Theta_{val} := [\underline{\delta}, \overline{\delta}]$ and $\dot{\delta}(t) \in \Omega_{val} := [\underline{\omega}, \overline{\omega}]$. Then, the L_2 gain of the above closed loop system is

less than γ if there exist symmetric matrices $\mathcal{Y}$ and $\mathcal{S}$, a square matrix G, and a positive constant ϵ that satisfy the parameter-dependent differential matrix inequalities (58)[11] and (59) for any $(\delta, \omega) \in (\Theta_{val} \times \Omega_{val})$, where $(\textbf{*})^T$ is a transpose of the precedent term.

Proof *By multiplying*

$$
\begin{bmatrix}
\mathcal{B}_2 \mathcal{C}_c G & \mathcal{B}_2 \mathcal{C}_c G \\
\mathcal{A}_c G & \mathcal{A}_c G \\
\mathcal{D}_{12} \mathcal{C}_c G & \mathcal{D}_{12} \mathcal{C}_c G \\
0 & 0 \\
G & 0 \\
0 & G
\end{bmatrix}^{\perp}
$$

$$
= \begin{bmatrix}
I & 0 & 0 & 0 & -\mathcal{B}_2 \mathcal{C}_c & -\mathcal{B}_2 \mathcal{C}_c \\
0 & I & 0 & 0 & -\mathcal{A}_c & -\mathcal{A}_c \\
0 & 0 & I & 0 & -\mathcal{D}_{12} \mathcal{C}_c & -\mathcal{D}_{12} \mathcal{C}_c \\
0 & 0 & 0 & I & 0 & 0
\end{bmatrix}
$$

and its transpose from the left and right sides respectively, the inequality (59) leads to:

$$
\begin{bmatrix}
\mathcal{A}_{cl} \mathcal{Y}_{cl} + \mathcal{Y}_{cl} \mathcal{A}_{cl}^T - \omega \frac{\partial \mathcal{Y}_{cl}}{\partial \delta} & \mathcal{Y}_{cl} \mathcal{C}_{cl}^T & \mathcal{B}_{cl} \\
\mathcal{C}_{cl} \mathcal{Y}_{cl} & -\gamma I & \mathcal{D}_{cl} \\
\mathcal{B}_{cl}^T & \mathcal{D}_{cl}^T & -\gamma I
\end{bmatrix} \ll 0,
\tag{60}
$$

where

$$
\mathcal{A}_{cl} = \begin{bmatrix} \mathcal{A} & \mathcal{B}_2 \mathcal{C}_c \\ \mathcal{B}_c \mathcal{C}_2 & \mathcal{A}_c \end{bmatrix}, \mathcal{B}_{cl} = \begin{bmatrix} \mathcal{B}_1 \\ \mathcal{B}_c \mathcal{D}_{21} \end{bmatrix},
$$

$$
\mathcal{C}_{cl} = \begin{bmatrix} \mathcal{C}_1 & \mathcal{D}_{12} \mathcal{C}_c \end{bmatrix}, \mathcal{D}_{cl} = \mathcal{D}_{11}.
$$

Since (60) holds for any $(\delta, \omega) \in (\Theta_{val} \times \Omega_{val})$, this is a sufficient condition for the stability and L_2 gain performance of the LPV system [26, 27]. It is concluded that the L_2 gain of the closed loop system is less than γ.

The condition (59) is simpler than other existing conditions in the sense that it does not include any matrix products of a solution and its time derivative, such as $\mathcal{Y}\dot{\mathcal{Y}}$. This is because the solution of the L_2 gain condition (60) is restricted to the form in (58).

Although the controller matrices are all assumed to be given in Lemma 1, readers may notice that the lemma can be reduced to parameter-dependent LMIs (with a line search parameter ϵ) and used for synthesis by letting $\mathcal{A}_c G = \mathcal{V}$ and $\mathcal{C}_c G = \mathcal{W}$ and assuming that $\mathcal{B}_c$ is given. Then, controller matrices

---

[11]Inequality $\mathcal{Y}_{cl} \gg 0$ ($\mathcal{Y}_{cl} \ll 0$) means that $\mathcal{Y}_{cl} \geq \alpha I$ ($\mathcal{Y}_{cl} \leq -\alpha I$) holds for some positive number α and any $\delta \in \Theta_{\text{val}}$.

$$\mathcal{Y}_{cl} := \begin{bmatrix} \mathcal{Y} & \mathcal{S} \\ \mathcal{S} & \mathcal{S} \end{bmatrix} \gg 0, \tag{58}$$

$$\begin{bmatrix} \mathcal{A}\mathcal{Y} + \mathcal{Y}A^T - \omega\frac{\partial \mathcal{Y}}{\partial \delta} & \mathcal{A}\mathcal{S} + \mathcal{Y}\mathcal{C}_2^T\mathcal{B}_c^T - \omega\frac{\partial \mathcal{S}}{\partial \delta} & \mathcal{Y}\mathcal{C}_1^T & \mathcal{B}_1 & -\mathcal{S} & 0 \\ \mathcal{S}\mathcal{A}^T + \mathcal{B}_c\mathcal{C}_2\mathcal{Y} - \omega\frac{\partial \mathcal{S}}{\partial \delta} & \mathcal{B}_c\mathcal{C}_2\mathcal{S} + \mathcal{S}\mathcal{C}_2^T\mathcal{B}_c^T - \omega\frac{\partial \mathcal{S}}{\partial \delta} & \mathcal{S}\mathcal{C}_1^T & \mathcal{B}_c\mathcal{D}_{21} & 0 & -\mathcal{S} \\ \mathcal{C}_1\mathcal{Y} & \mathcal{C}_1\mathcal{S} & -\gamma I & \mathcal{D}_{11} & 0 & 0 \\ \mathcal{B}_1^T & \mathcal{D}_{21}^T\mathcal{B}_c^T & \mathcal{D}_{11}^T & -\gamma I & 0 & 0 \\ -\mathcal{S} & 0 & 0 & 0 & 0 & 0 \\ 0 & -\mathcal{S} & 0 & 0 & 0 & 0 \end{bmatrix}$$

$$+ \begin{bmatrix} \mathcal{B}_2\mathcal{C}_cG & \mathcal{B}_2\mathcal{C}_cG \\ \mathcal{A}_cG & \mathcal{A}_cG \\ \mathcal{D}_{12}\mathcal{C}_cG & \mathcal{D}_{12}\mathcal{C}_cG \\ 0 & 0 \\ G & 0 \\ 0 & G \end{bmatrix} \begin{bmatrix} I & 0 & 0 & 0 & -\epsilon I & 0 \\ 0 & I & 0 & 0 & 0 & -\epsilon I \end{bmatrix} + \Big(\ast\Big)^T \ll 0, \tag{59}$$

$\mathcal{A}_c$ and $\mathcal{C}_c$ are obtained using solutions of parameter-dependent LMIs $\mathcal{V}, \mathcal{W}$ and G. Since solutions $\mathcal{Y}$ and $\mathcal{S}$, which are related to the Lyapunov function, are not involved in deriving these controller matrices, it is possible to obtain piecewise-linear matrices $\mathcal{A}_c$ and $\mathcal{C}_c$ with fewer grid points even if the Lyapunov function has more grid points. This is due to the extension of LMIs from (60) to (59), and makes the proposed method different from that in [34].

D.3   Derivation of finite number of LMIs

The next lemma was proved in [37], which gives finite number of LMIs equivalent to a class of parameter-dependent differential inequalities.

Lemma 3 *Suppose the matrix $A(\delta)$ is a piecewise linear function of δ with grid points $D^\Pi = \{\delta_0^\Pi, \delta_1^\Pi, \ldots, \delta_{N_\Pi+1}^\Pi\}$.*

$$A(\delta) = A_i + \frac{\delta - \delta_i^\Pi}{\delta_{i+1}^\Pi - \delta_i^\Pi}(A_{i+1} - A_i),$$

$$\delta \in [\delta_i^\Pi, \delta_{i+1}^\Pi], i = 0, 1, \ldots, N_\Pi.$$

The following statements (I) and (II) are equivalent:
(I) There exists a continuously differentiable symmetric parameter-dependent matrix $P(\delta)$ that satisfies the following inequalities:

$$P(\delta) \gg 0, \quad \omega\frac{\partial P(\delta)}{\partial \delta} + A^T(\delta)P(\delta) + P(\delta)A(\delta) \ll 0 \tag{61}$$

for any $(\delta, \omega) \in (\Theta_{val} \times \Omega_{val})$.
(II) There exist a subdivision D of D^Π ($D = \{\delta_0, \delta_1, \ldots, \delta_N\}$) and symmetric matrices $P_0, P_1, \ldots, P_{N+1}$ that

satisfy the following LMIs for $\omega = \underline{\omega}, \overline{\omega}$:

$$P_k > 0, \quad k = 0, 1, \ldots, N+1, \tag{62}$$

$$\frac{\omega}{\Delta\delta_k}\Delta P_k + A_k^T P_k + P_k A_k < 0, \quad k = 0, 1, \ldots, N, \tag{63}$$

$$\frac{\omega}{\Delta\delta_{k-1}}\Delta P_k + A_k^T P_k + P_k A_k < 0, \quad k = 1, 2, \ldots, N+1, \tag{64}$$

$$\frac{\omega}{\Delta\delta_k}\Delta P_k + A_k^T P_k + P_k A_k + \frac{1}{2}(\hat{L}_k + \hat{L}_k^T) < 0,$$
$$k = 0, 1, \ldots, N, \tag{65}$$

where $A_k = A(\delta_k), \Delta A_k = A_{k+1} - A_k, \Delta\delta_k = \delta_{k+1} - \delta_k, \Delta P_k = P_{k+1} - P_k$, and $\hat{L}_k := A_k^T \Delta P_k + \Delta A_k^T P_k$. If (II) holds, one of the solutions $P(\delta)$ is given as:

$$P(\delta) = \frac{1}{l} \int_{\delta - \frac{l}{2}}^{\delta + \frac{l}{2}} P_S(h)dh, \tag{66}$$

$$P_S(\delta) = P_k + \frac{\delta - \delta_k}{\delta_{k+1} - \delta_k}(P_{k+1} - P_k),$$
$$\delta \in [\delta_k, \delta_{k+1}], k = 0, 1, \ldots, N,$$

with some positive constant l small enough.

Proof *See the references: [37] and [38].*

  The major difference between other gridding methods and this lemma is that, if there exist a subdivision D and matrices $P_i (i = 0, \ldots, N+1)$ that satisfy the LMIs in the statement (II), the parameter-dependent inequalities in (I) automatically hold not only at $\delta \in D^\Pi$ but also for *all parameter values* of $\delta \in \Theta_{\text{val}}$. A similar idea can be seen in [34], which differs from the lemma in how to deal with time-derivatives of Lyapunov functions. The lemma uses smoothed functions in the form of (66) for solutions $P(\delta)$ in order to make them differentiable.

$$\left[\begin{array}{cc} Y(\delta) & S(\delta) \\ S(\delta) & S(\delta) \end{array}\right] \gg 0,$$

$$\left[\begin{array}{cccccc} Q_{11}(\delta) & Q_{12}(\delta) & Y(\delta)C_1^T(\delta) & B_1(\delta) & -S(\delta) & 0 \\ Q_{12}^T(\delta) & Q_{22}(\delta) & S(\delta)C_1^T(\delta) & B_cD_{21}(\delta) & 0 & -S(\delta) \\ C_1(\delta)Y(\delta) & C_1(\delta)S(\delta) & -\gamma I & D_{11}(\delta) & 0 & 0 \\ B_1^T(\delta) & D_{21}^T(\delta)B_c^T & D_{11}^T(\delta) & -\gamma I & 0 & 0 \\ -S(\delta) & 0 & 0 & 0 & 0 & 0 \\ 0 & -S(\delta) & 0 & 0 & 0 & 0 \end{array}\right]$$

$$+ \left[\begin{array}{cc} B_2(\delta)W_S^\Gamma(\delta) & B_2(\delta)W_S^\Gamma(\delta) \\ V_S^\Gamma(\delta) & V_S^\Gamma(\delta) \\ D_{12}(\delta)W_S^\Gamma(\delta) & D_{12}(\delta)W_S^\Gamma(\delta) \\ 0 & 0 \\ G^\Gamma & 0 \\ 0 & G^\Gamma \end{array}\right] \left[\begin{array}{cccccc} I & 0 & 0 & 0 & -\epsilon I & 0 \\ 0 & I & 0 & 0 & 0 & -\epsilon I \end{array}\right] + \left(*\right)^T \ll 0 \qquad (67)$$

D.4 Proof of the Theorem

Proof *Since the controller matrix $B_c(\delta)$ is parameter-independent ($B_c(\delta) = B_c$), Lemma 2 can be applied to inequalities (49)–(52), which correspond to inequalities (62)–(65) respectively with $D = D^\Pi$. Then the following parameter-dependent matrix inequalities are obtained for any $(\delta, \omega) \in (\Theta_{val} \times \Omega_{val})$, where*

$$\begin{cases} Q_{11} := A(\delta)Y(\delta) + Y(\delta)A^T(\delta) - \omega\frac{\partial Y(\delta)}{\partial \delta}, \\ Q_{12} := A(\delta)S(\delta) + Y(\delta)C_2^T(\delta)B_c^T - \omega\frac{\partial S(\delta)}{\partial \delta} \\ Q_{22} := B_cC_2(\delta)S(\delta) + S(\delta)C_2^T(\delta)B_c^T - \omega\frac{\partial S(\delta)}{\partial \delta}. \end{cases}$$

Define $A_c(\delta) := V_S^\Gamma(\delta)G^{\Gamma-1}$ and $C_c(\delta) := W_S^\Gamma(\delta)G^{\Gamma-1}$, then the inequality (67) leads to (60) with $G = G^\Gamma$ of Lemma 2. This concludes the proof.

E Time Histories of the In-orbit Experiment

All time histories of the in-orbit experiment are summarized here. The housekeeping (HK) data, that were downlinked every 4 sec from the spacecraft, are used to draw time histories. Each command/disturbance response, except for random disturbance (B), began at the same paddle rotation angle for all control laws. For example, the 1st step command response started at the paddle rotation angle $\delta = 45$ (see Table 3).

As for the 2nd random disturbance response (B), the large disturbance was found in yaw axis during the experiment of the PD control law (see Fig. 77), which was caused by the Sun being visible from FSS. Thus, in order to avoid the disturbance, the starting time of the 2nd random disturbance response (B) for

other control laws was delayed for 40 minutes and consequently the starting angle of PD control law became different from those of other control laws.

E.1 PD control law

Step command and impulse/large disturbance responses were obtained on 21 and 22 June 2009, and rectangular/random disturbance responses were obtained on 28 February and 1 March 2010.

- Step command responses: Fig. 66 (1st) and Fig. 67 (2nd)

- Impulse disturbance responses: Fig. 68 (1st) and Fig. 69 (2nd)

- Large disturbance responses: Fig. 70 (1st) and Fig. 71 (2nd)

- Rectangular disturbance responses: Fig. 72 (1st) and Fig. 73 (2nd)

- Random disturbance responses (A): Fig. 74 (1st) and Fig. 75 (2nd)

- Random disturbance responses (B): Fig. 76 (1st) and Fig. 77 (2nd)

E.2 μ-synthesis based control law

Step command and impulse/large disturbance responses were obtained on 22 and 23 June 2009, and rectangular/random disturbance responses were obtained on 1 and 2 March 2010.

- Step command responses: Fig. 78 (1st) and Fig. 79 (2nd)

Table 3: Starting angle of paddle rotation for each response (unit: deg).

	1st	2nd
Step command	45	86
Impulse disturbance	75	135
Large disturbance	120	150
Rectangular disturbance	45	137.5
Random disturbance (A)	60	153.75
Random disturbance (B)	117.5	170(PD) 180(other)

- Impulse disturbance responses: Fig. 80 (1st) and Fig. 81 (2nd)

- Large disturbance responses: Fig. 82 (1st) and Fig. 83 (2nd)

- Rectangular disturbance responses: Fig. 84 (1st) and Fig. 85 (2nd)

- Random disturbance responses (A): Fig. 86 (1st) and Fig. 87 (2nd)

- Random disturbance responses (B): Fig. 88 (1st) and Fig. 89 (2nd)

E.3   DDFB control law

Step command and impulse/large disturbance responses were obtained on 23 and 24 June 2009, and rectangular/random disturbance responses were obtained on 6 and 7 March 2010.

- Step command responses: Fig. 90 (1st) and Fig. 91 (2nd)

- Impulse disturbance responses: Fig. 92 (1st) and Fig. 93 (2nd)

- Large disturbance responses: Fig. 94 (1st) and Fig. 95 (2nd)

- Rectangular disturbance responses: Fig. 96 (1st) and Fig. 97 (2nd)

- Random disturbance responses (A): Fig. 98 (1st) and Fig. 99 (2nd)

- Random disturbance responses (B): Fig. 100 (1st) and Fig. 101 (2nd)

E.4   Gain scheduling control law

Step command and impulse/large disturbance responses were obtained on 25 and 26 June 2009, and rectangular/random disturbance responses were obtained on 2 and 3 March 2010.

- Step command responses: Fig. 102 (1st) and Fig. 103 (2nd)

- Impulse disturbance responses: Fig. 104 (1st) and Fig. 105 (2nd)

- Large disturbance responses: Fig. 106 (1st) and Fig. 107 (2nd)

- Rectangular disturbance responses: Fig. 108 (1st) and Fig. 109 (2nd)

- Random disturbance responses (A): Fig. 110 (1st) and Fig. 111 (2nd)

- Random disturbance responses (B): Fig. 112 (1st) and Fig. 113 (2nd)

E.5   DVDFB control law

Step command and impulse/large disturbance responses were obtained on 26 and 29 June 2009, and rectangular/random disturbance responses were obtained on 7 and 8 March 2010.

- Step command responses: Fig. 114 (1st) and Fig. 115 (2nd)

- Impulse disturbance responses: Fig. 116 (1st) and Fig. 117 (2nd)

- Large disturbance responses: Fig. 118 (1st) and Fig. 119 (2nd)

- Rectangular disturbance responses: Fig. 120 (1st) and Fig. 121 (2nd)

- Random disturbance responses (A): Fig. 122 (1st) and Fig. 123 (2nd)

- Random disturbance responses (B): Fig. 124 (1st) and Fig. 125 (2nd)
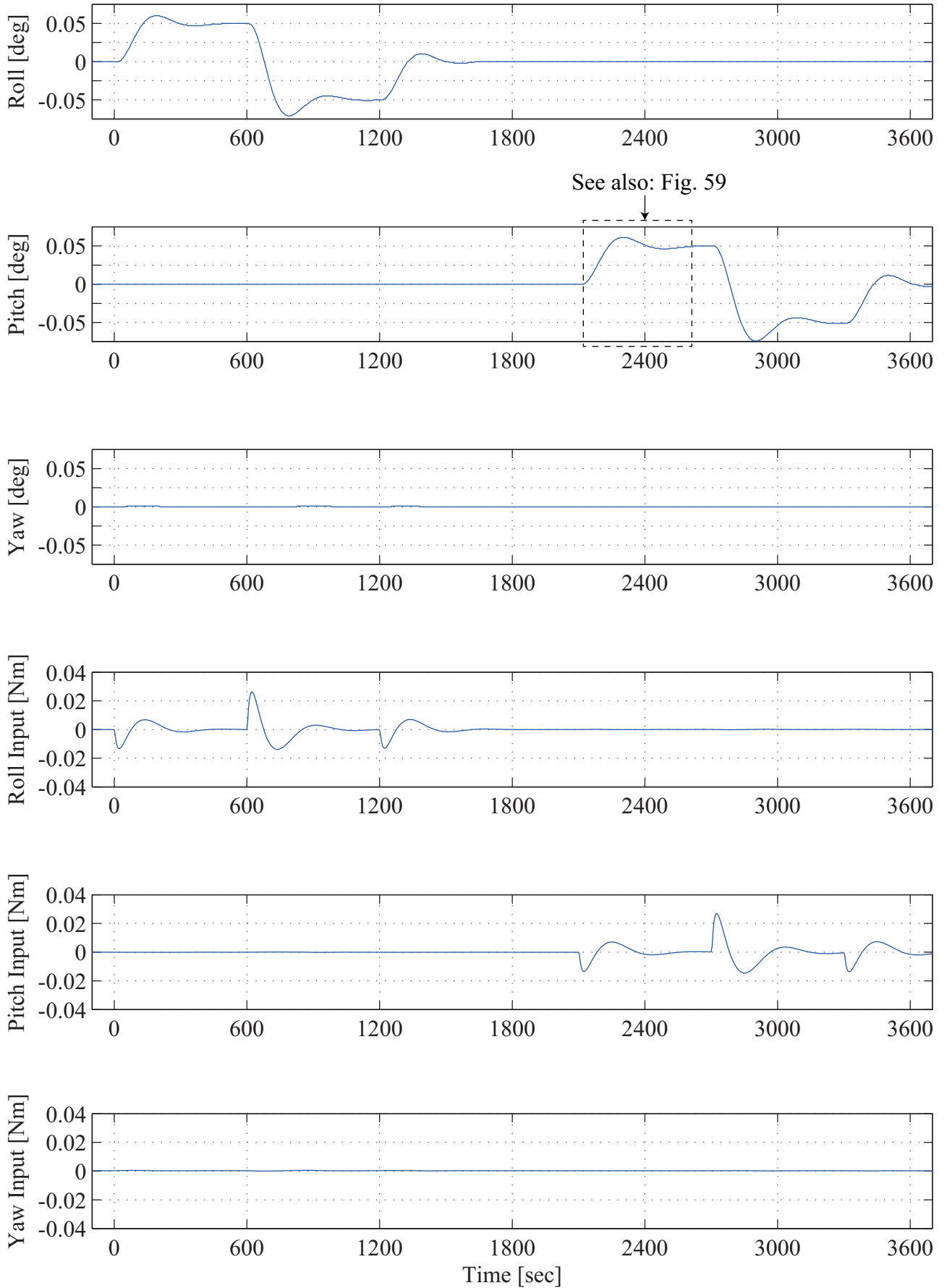
Figure 66: Step command response using the PD control law. The paddle rotation angle $\delta = 45$ at $t = 0$.

See also: Fig. 61
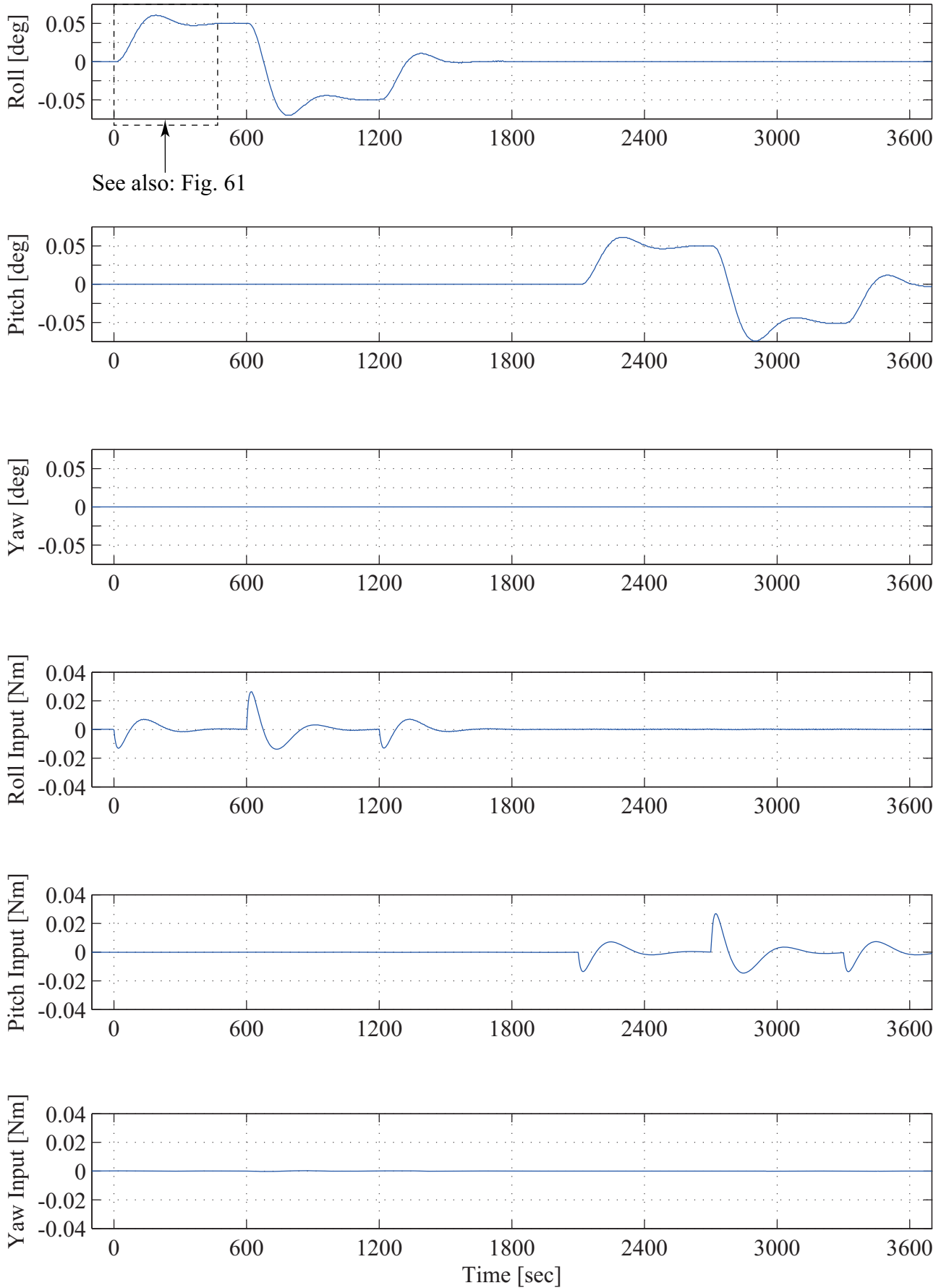
Figure 67: Step command response using the PD control law. The paddle rotation angle $\delta = 86$ at $t = 0$.
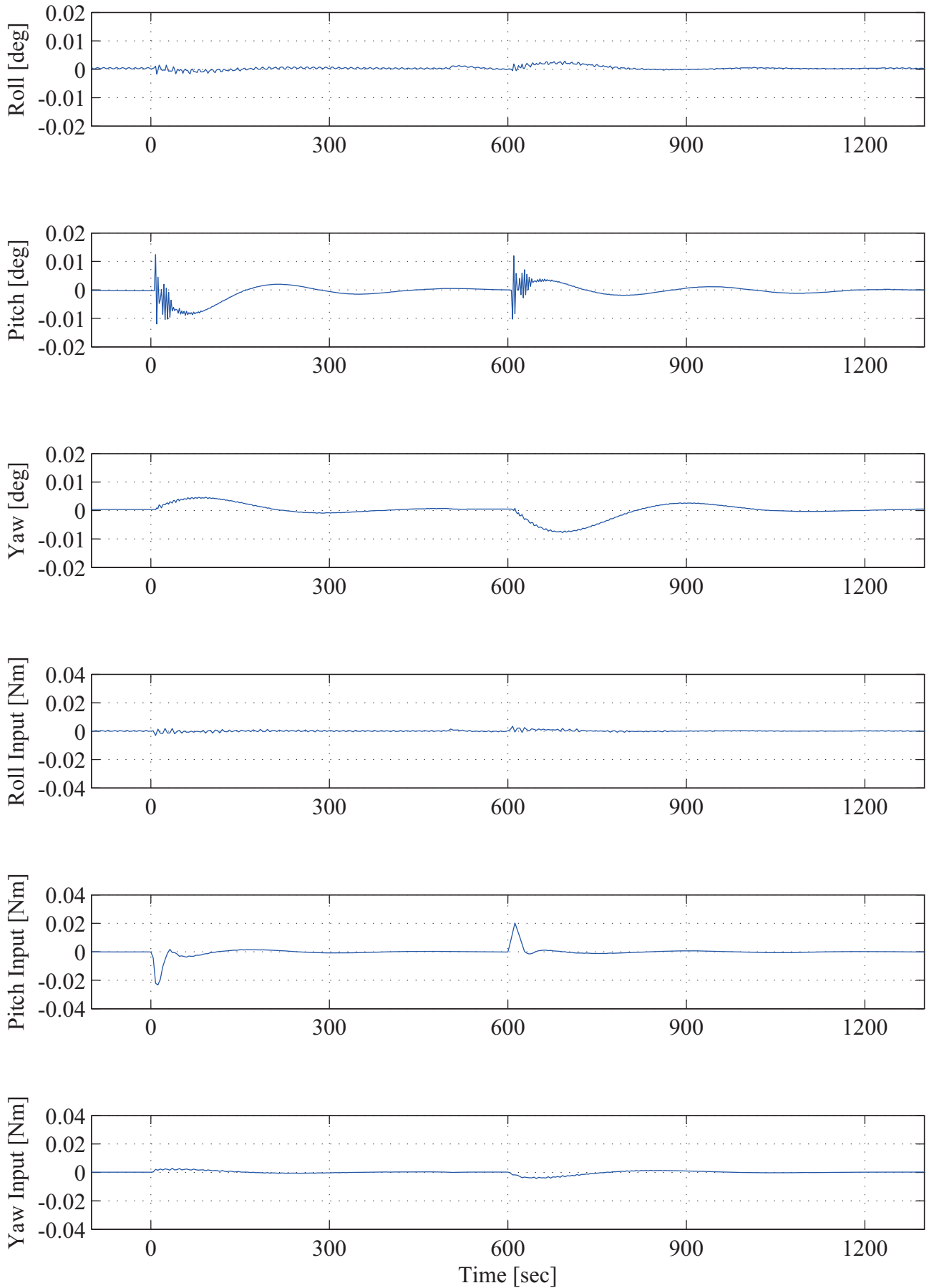
Figure 68: Impulse disturbance response using the PD control law. The paddle rotation angle $\delta = 75$ at $t = 0$.
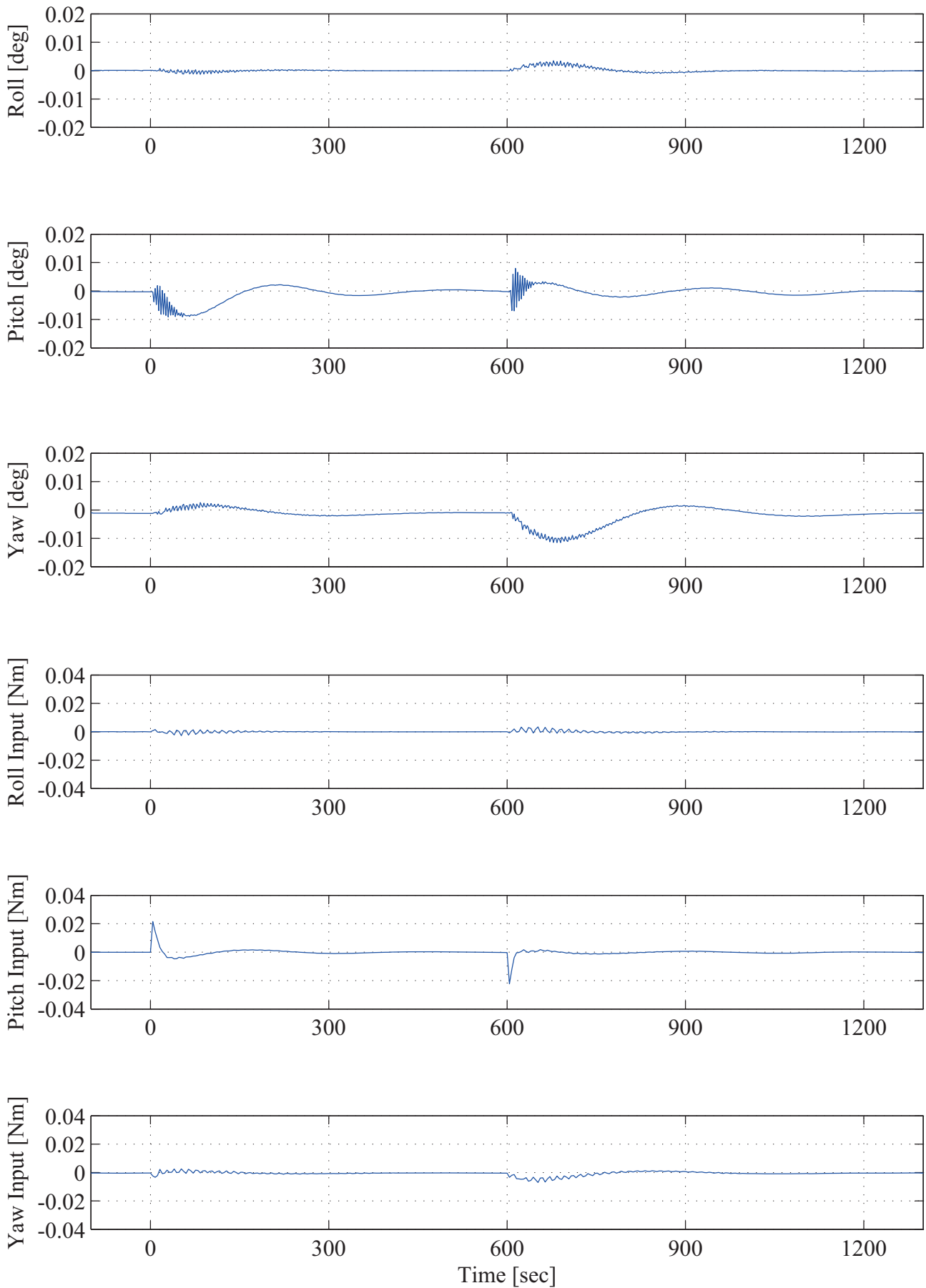
Figure 69: Impulse disturbance response using the PD control law. The paddle rotation angle $\delta = 135$ at $t = 0$.
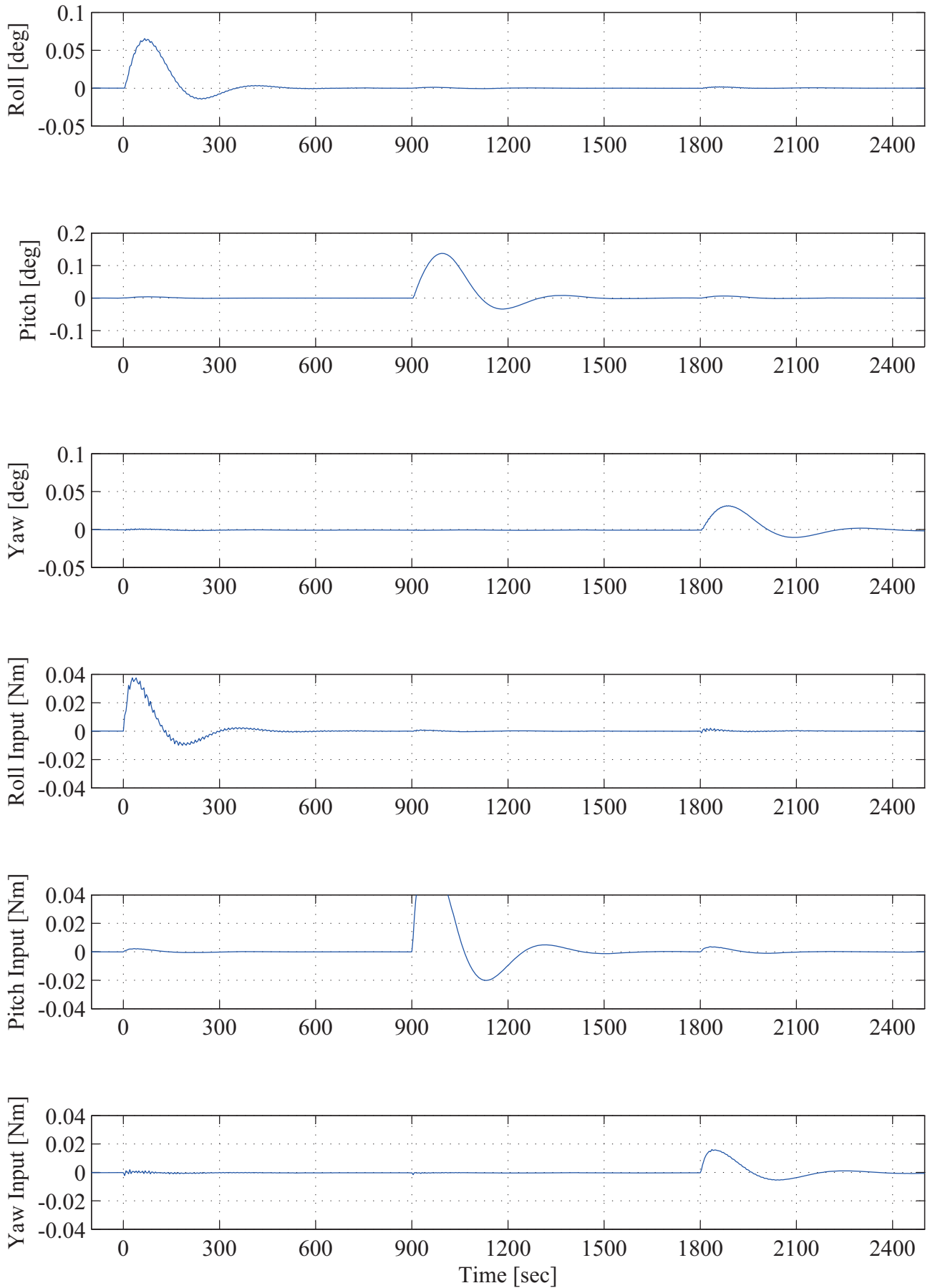
Figure 70: Large disturbance response using the PD control law. The paddle rotation angle $\delta = 120$ at $t = 0$.
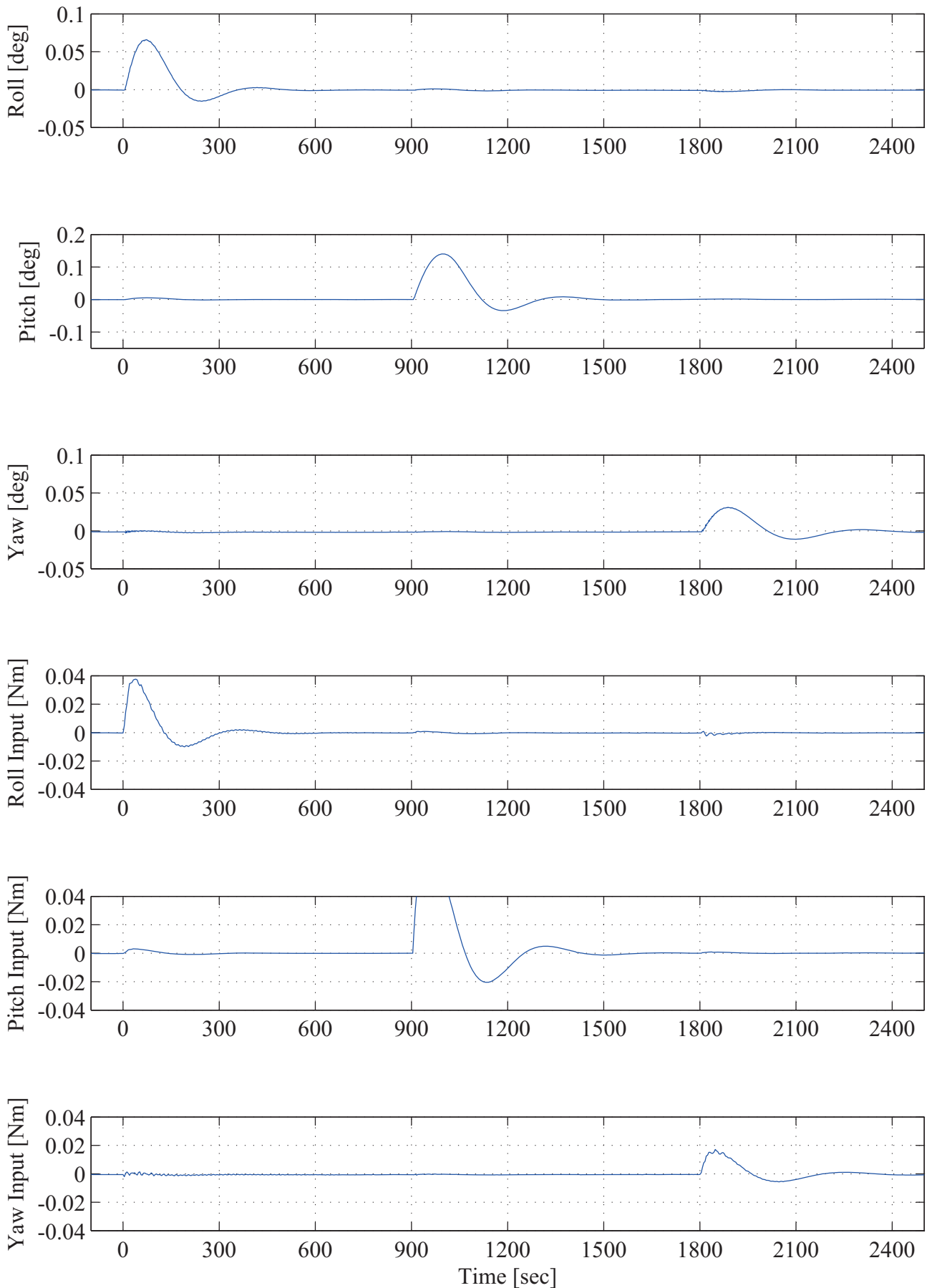
Figure 71: Large disturbance response using the PD control law. The paddle rotation angle $\delta = 150$ at $t = 0$.

See also: Fig. 63
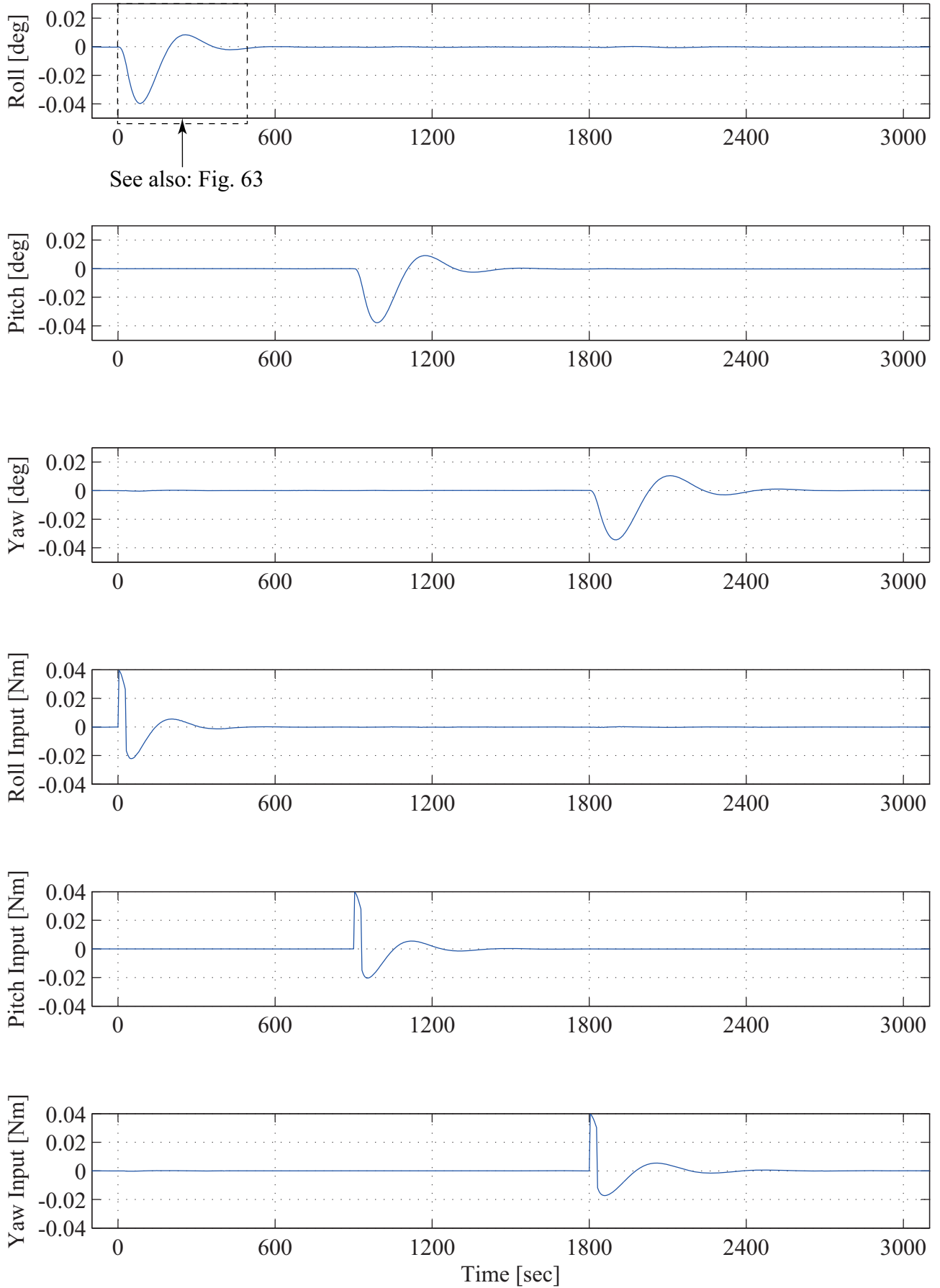
Figure 72: Rectangular disturbance response using the PD control law. The paddle rotation angle $\delta = 45$ at $t = 0$.
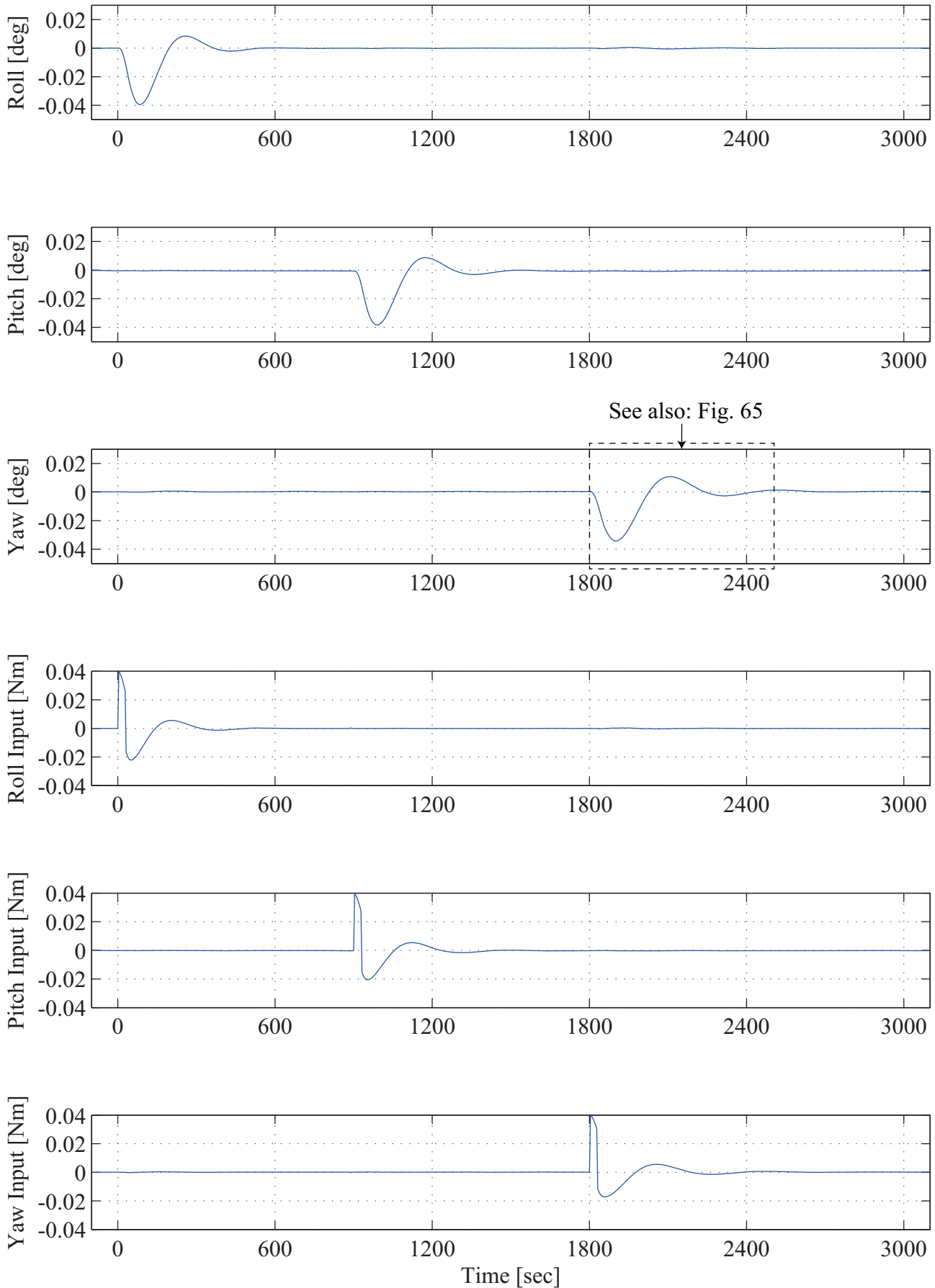
Figure 73: Rectangular disturbance response using the PD control law. The paddle rotation angle $\delta = 137.5$ at $t = 0$.
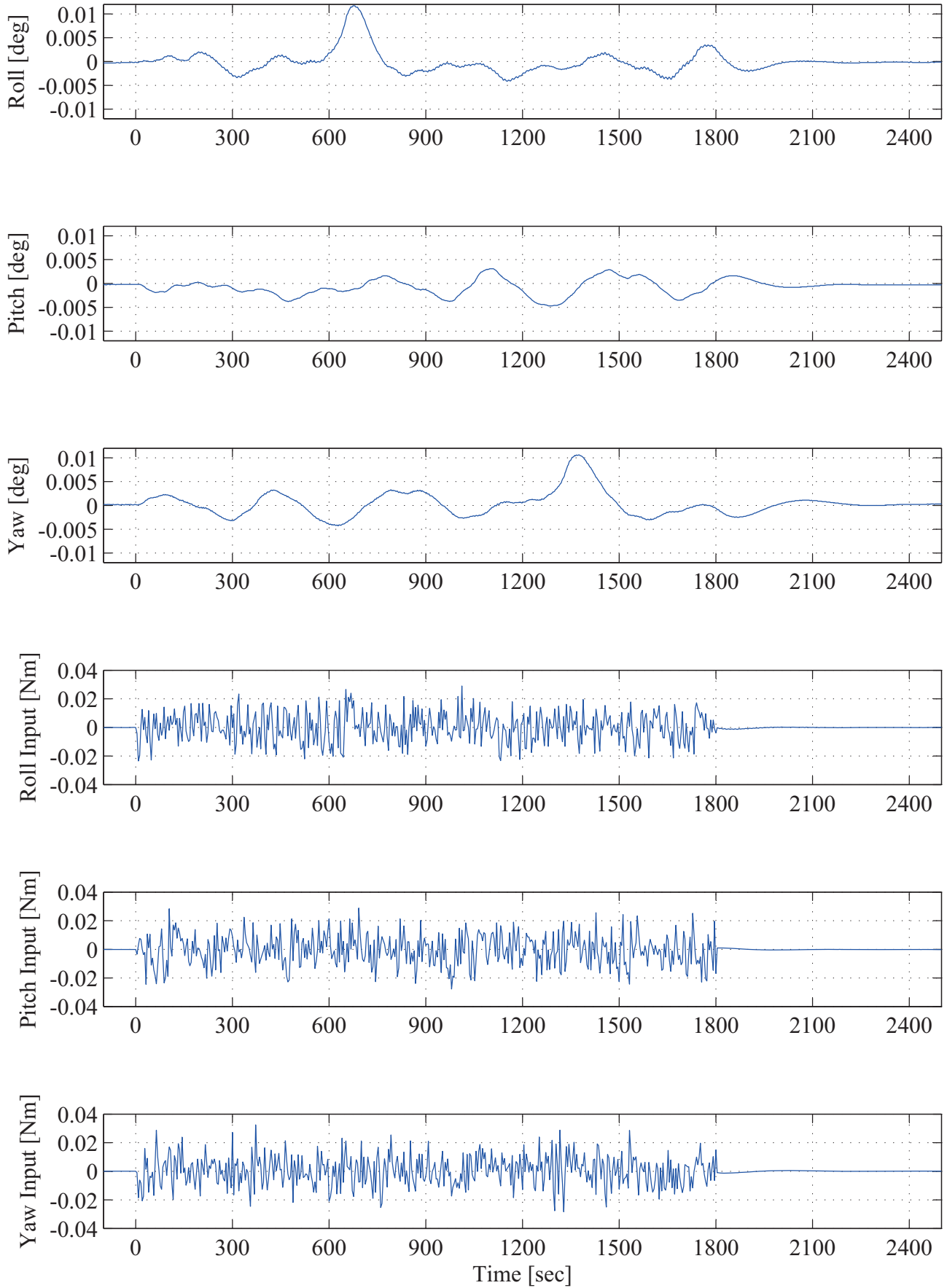
Figure 74: Random disturbance response (A) using the PD control law. The paddle rotation angle $\delta = 60$ at $t = 0$.
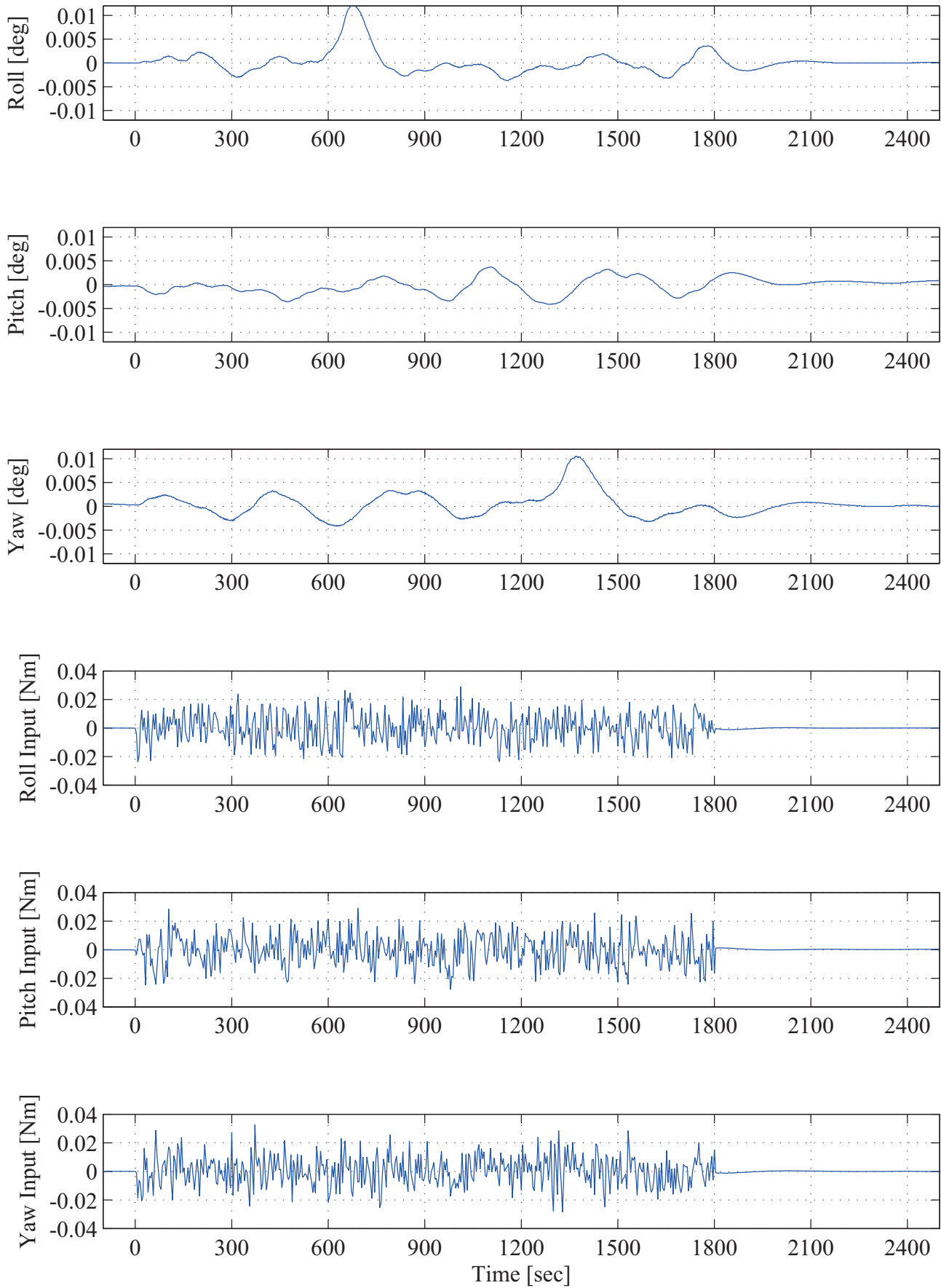
Figure 75: Random disturbance response (A) using the PD control law. The paddle rotation angle $\delta = 153.75$ at $t = 0$.
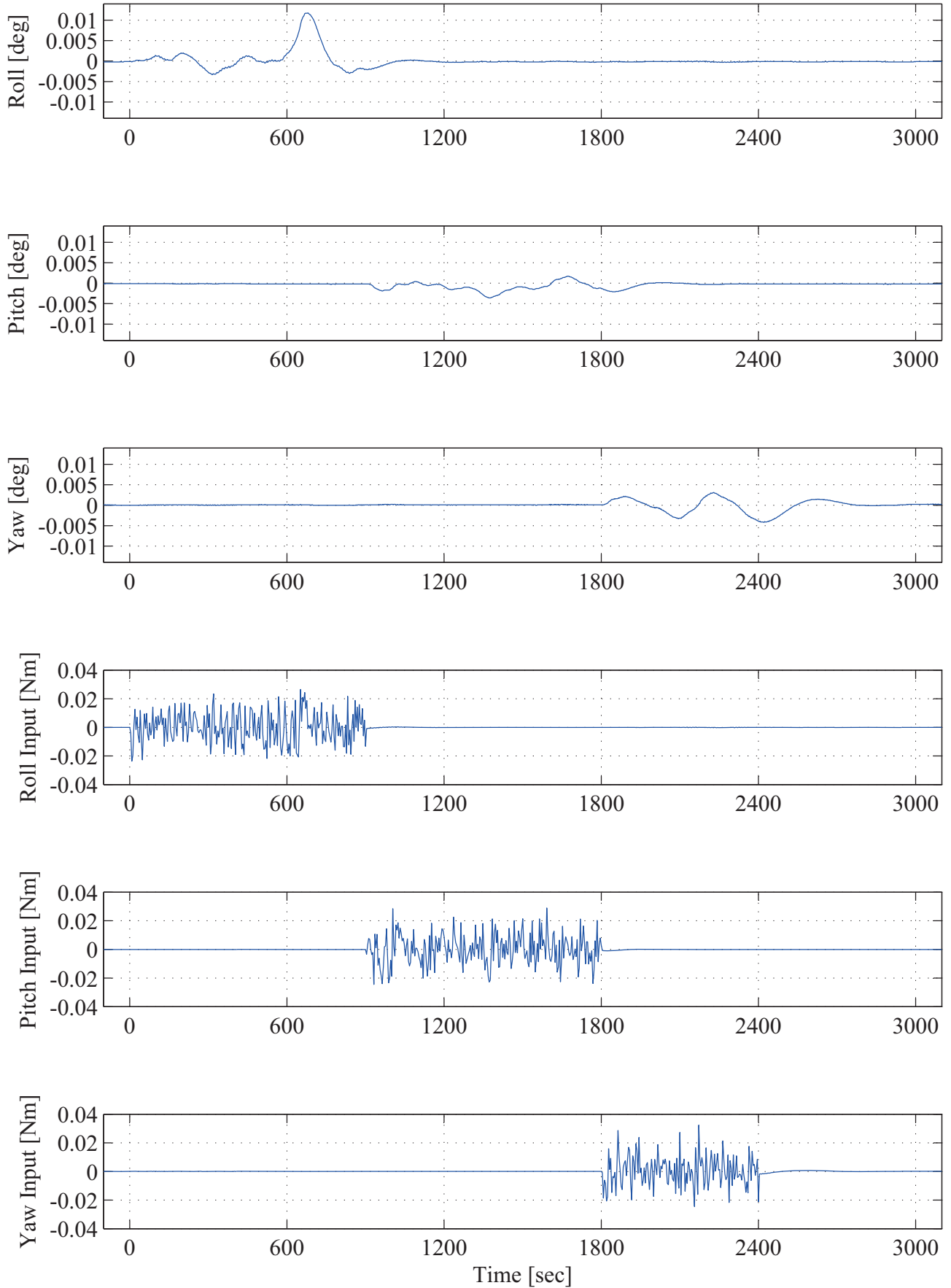
Figure 76: Random disturbance response (B) using the PD control law. The paddle rotation angle $\delta = 117.5$ at $t = 0$.
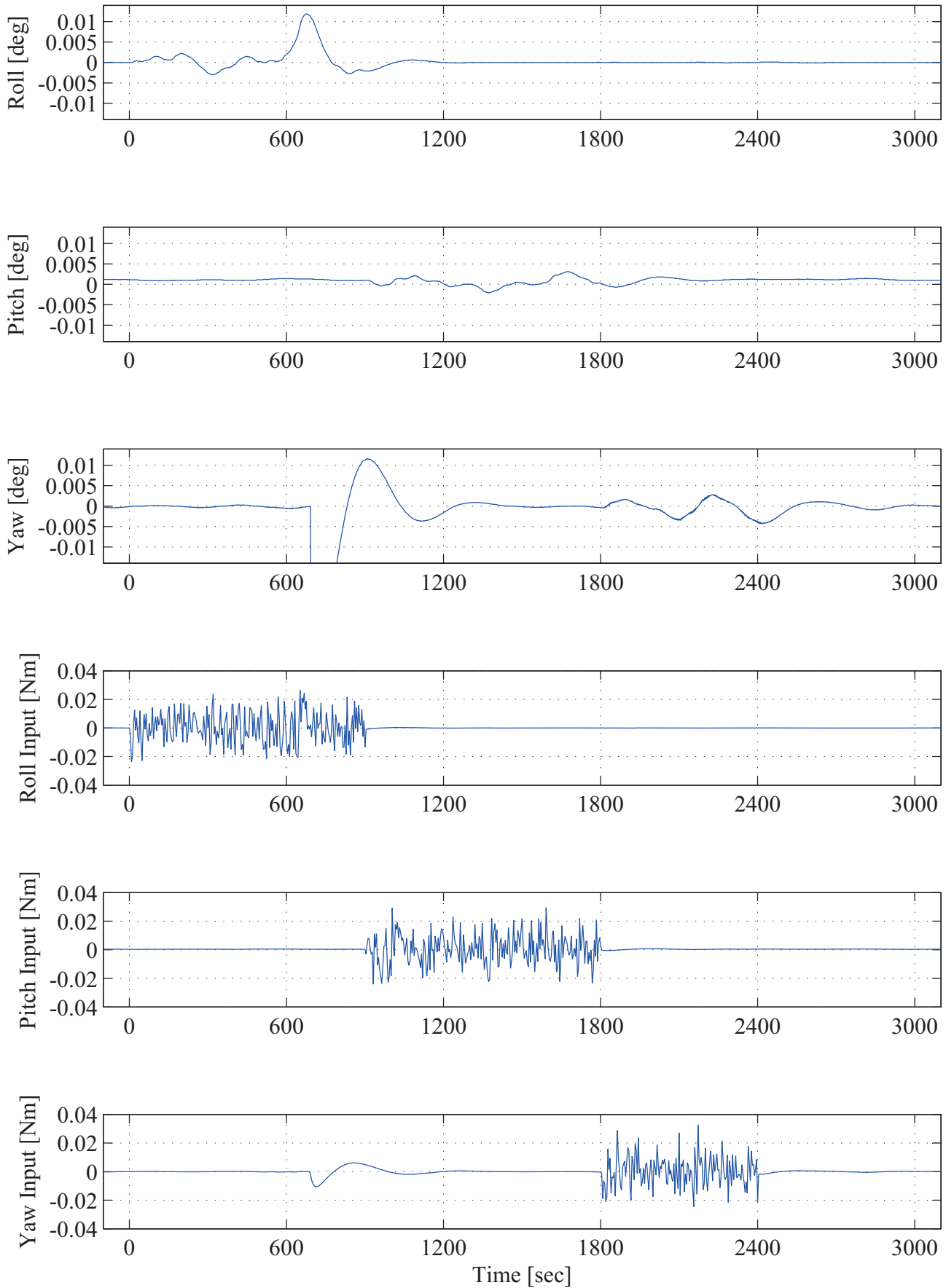
Figure 77: Random disturbance response (B) using the PD control law. The paddle rotation angle $\delta = 170$ at $t = 0$.
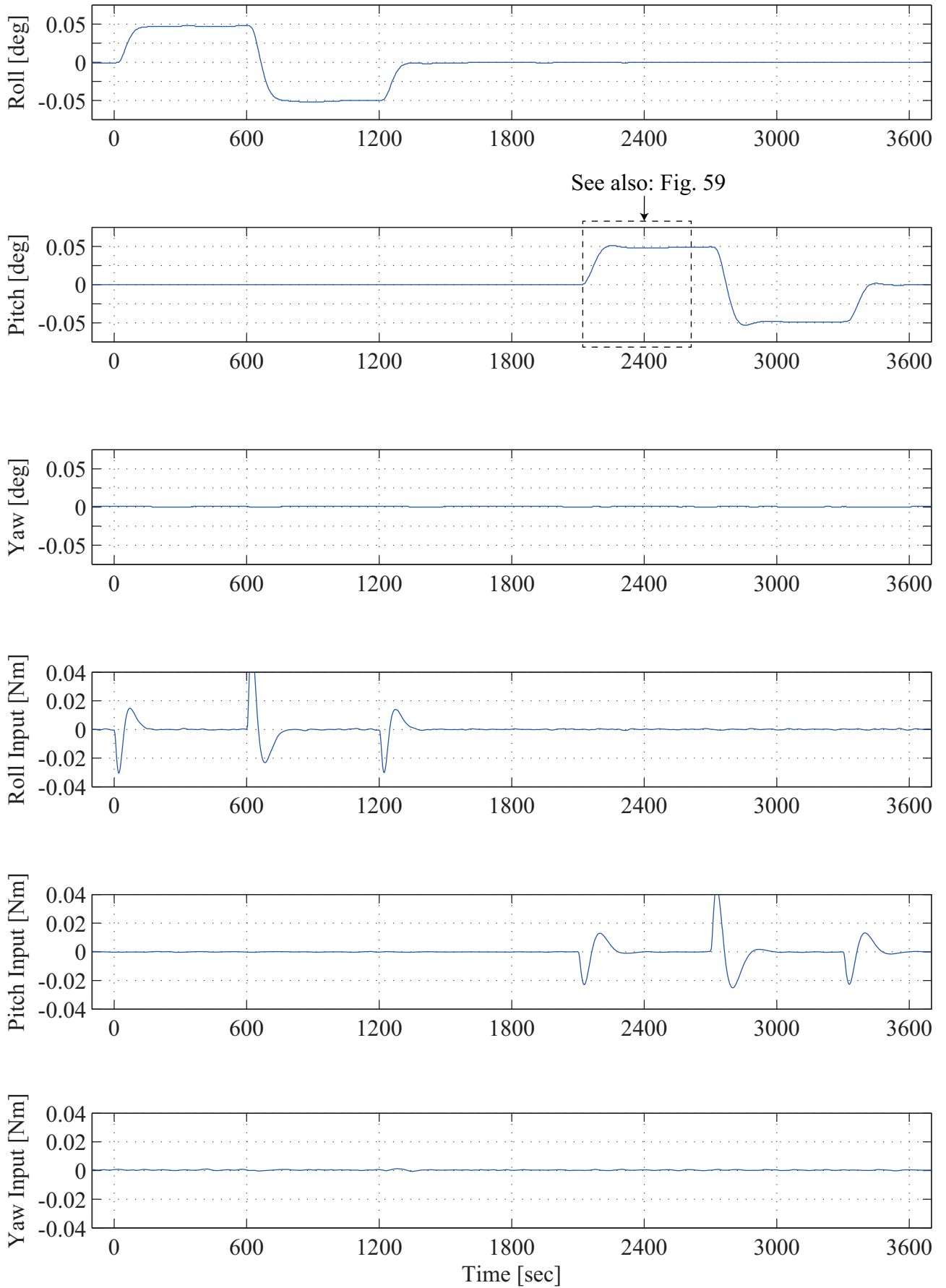
Figure 78: Step command response using the μ-synthesis based control law. The paddle rotation angle $\delta = 45$ at $t = 0$.

See also: Fig. 61
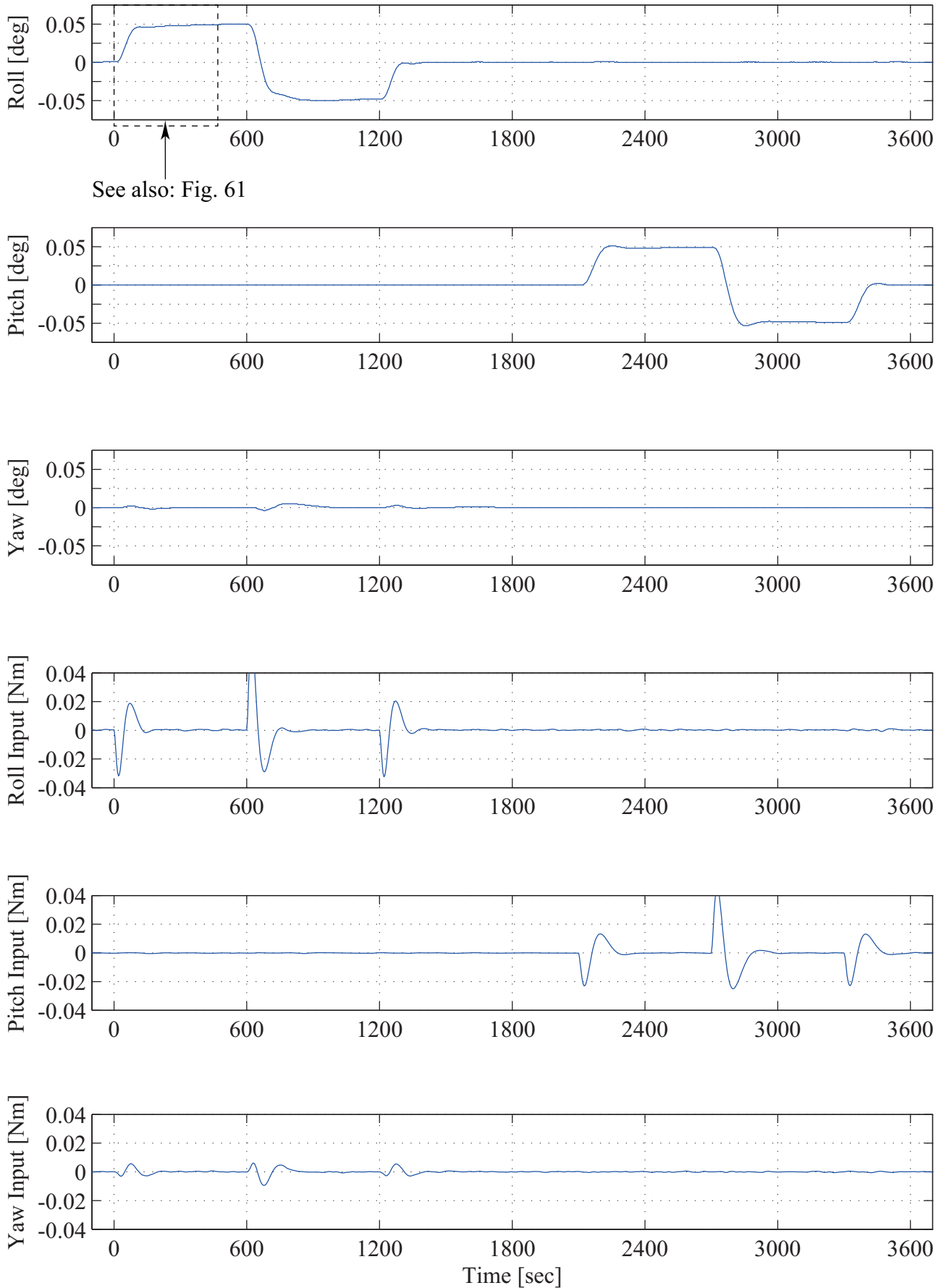
Figure 79: Step command response using the μ-synthesis based control law. The paddle rotation angle $\delta = 86$ at $t = 0$.
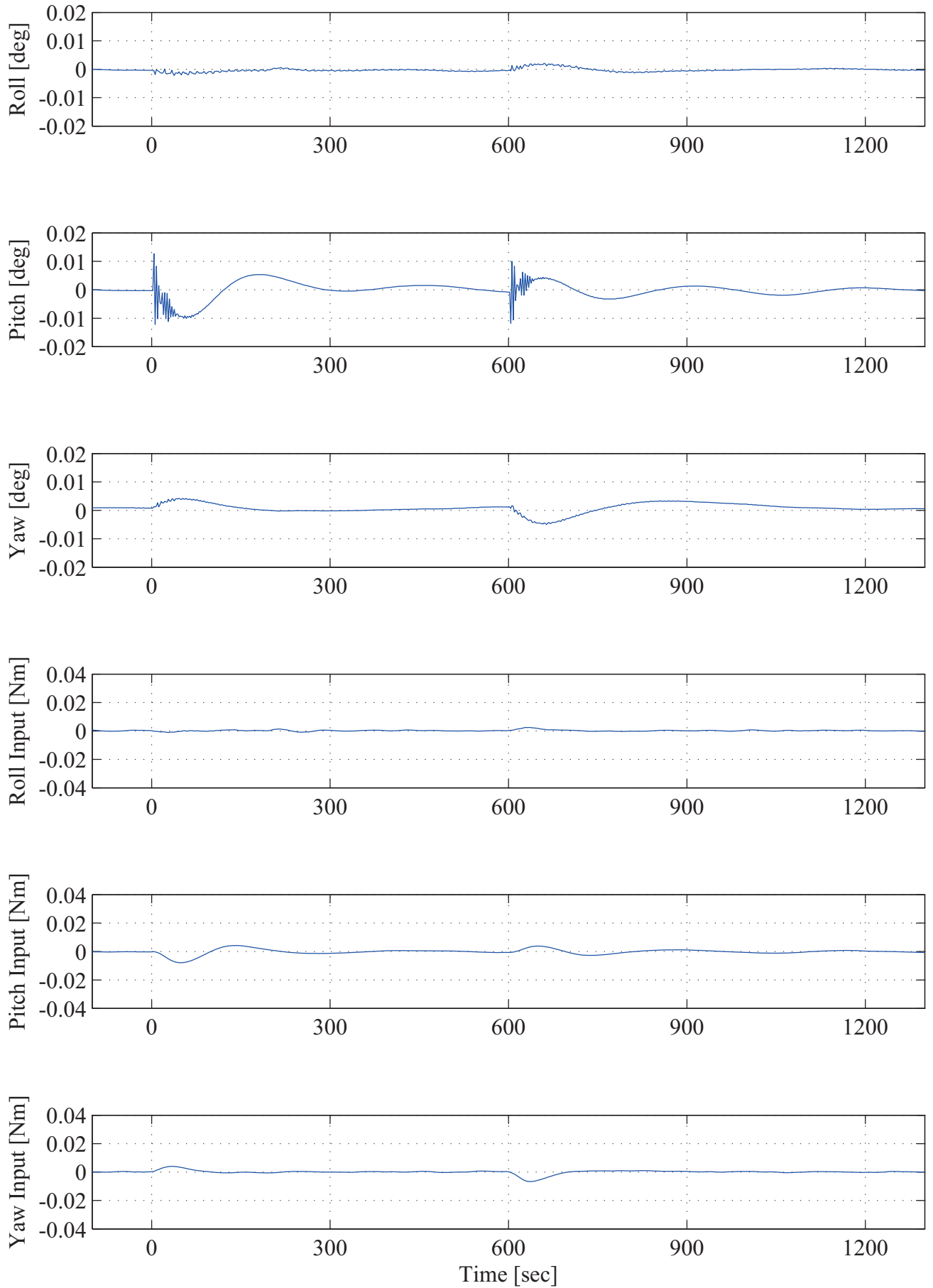
Figure 80: Impulse disturbance response using the μ-synthesis based control law. The paddle rotation angle $\delta = 75$ at $t = 0$.
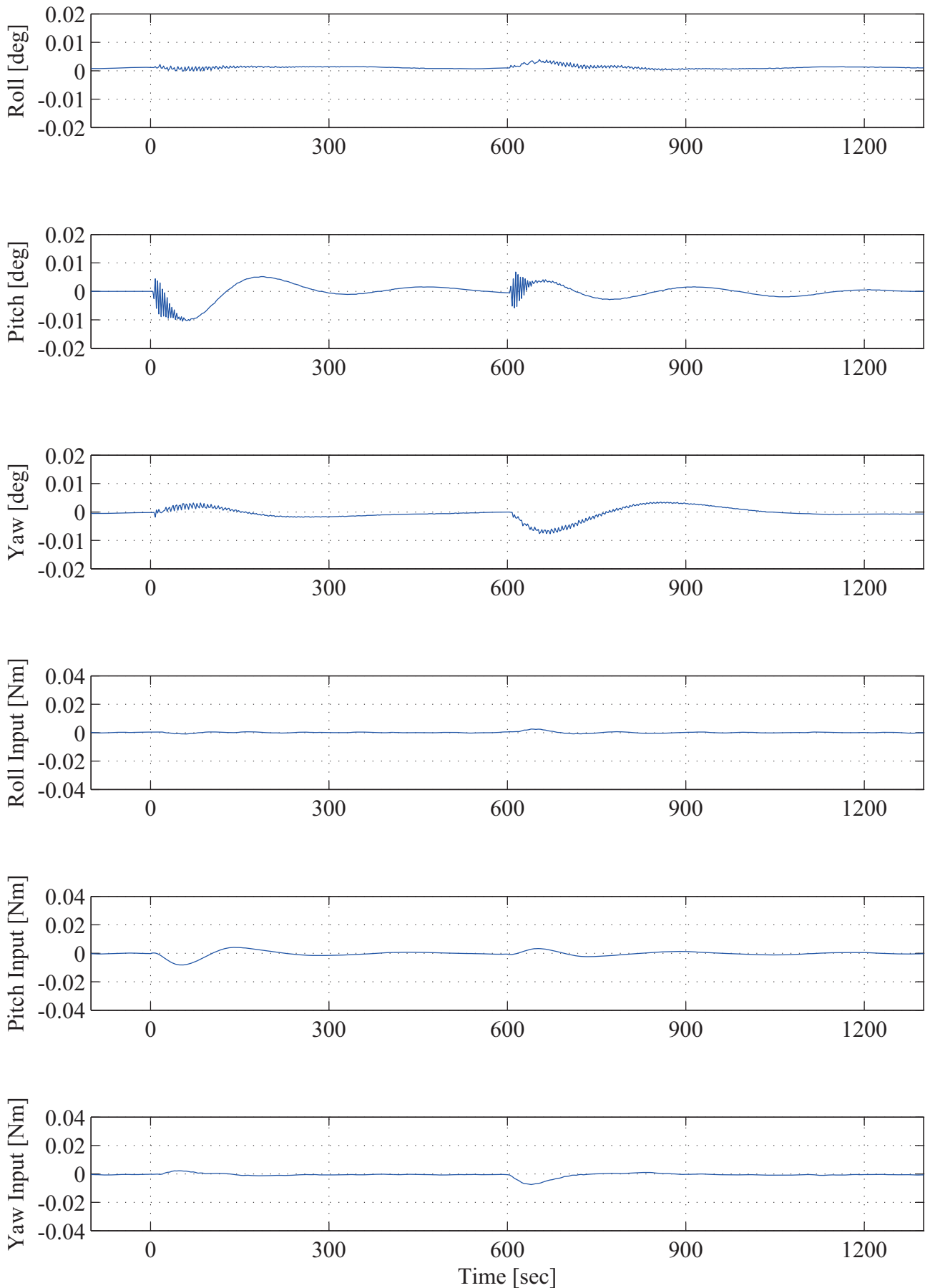
Figure 81: Impulse disturbance response using the μ-synthesis based control law. The paddle rotation angle $\delta = 135$ at $t = 0$.
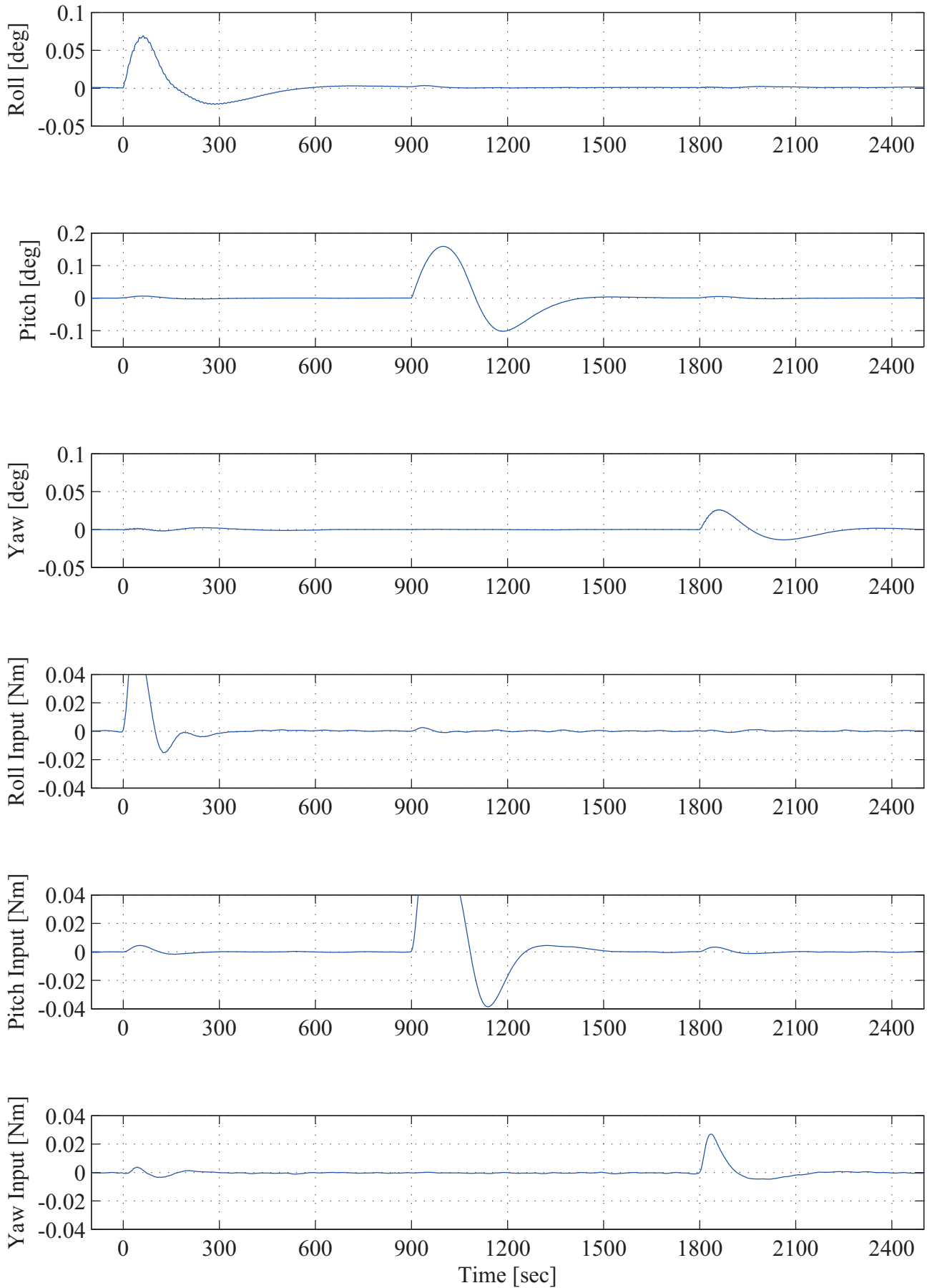
Figure 82: Large disturbance response using the μ-synthesis based control law. The paddle rotation angle $\delta = 120$ at $t = 0$.
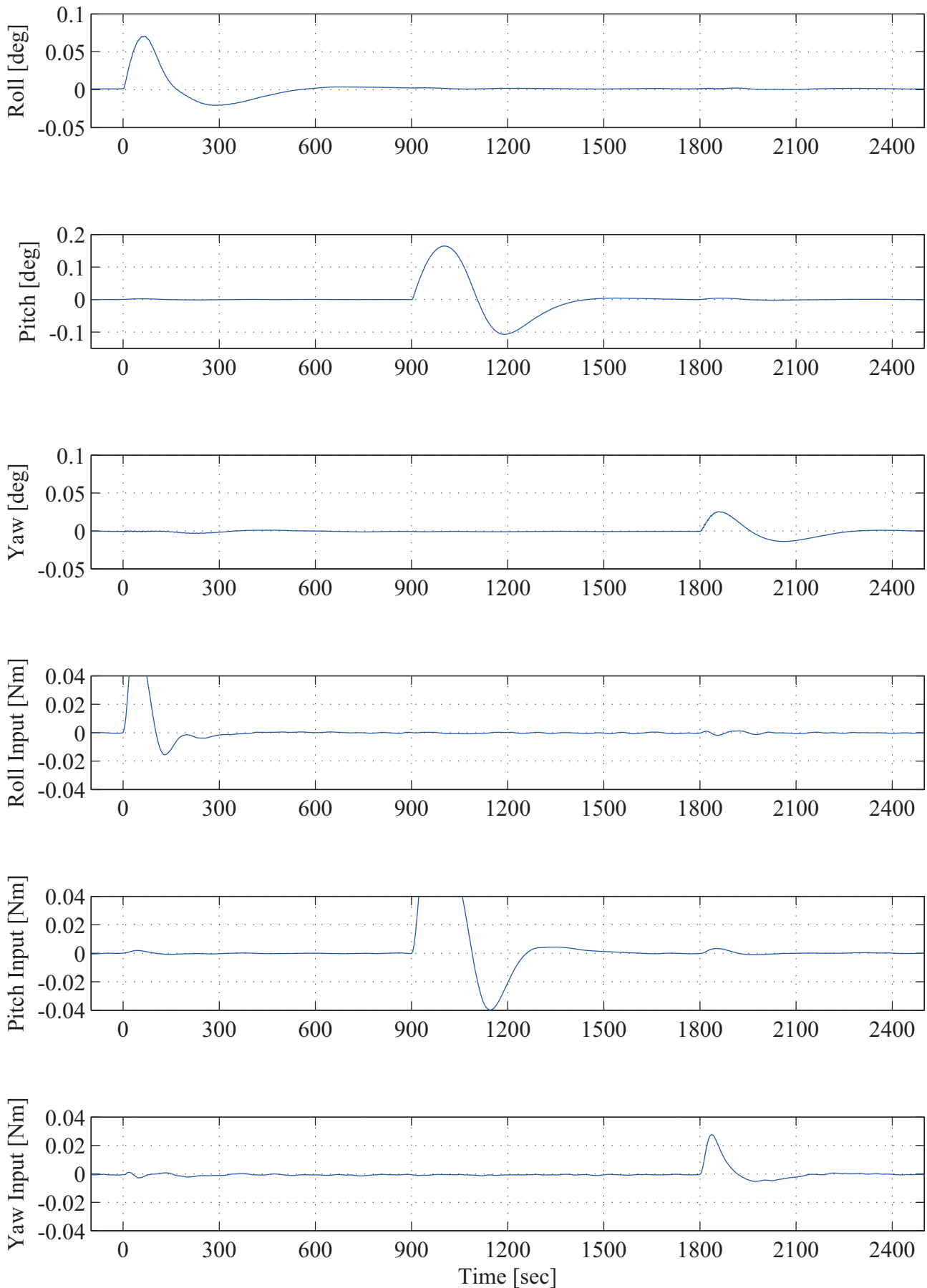
Figure 83: Large disturbance response using the μ-synthesis based control law. The paddle rotation angle $\delta = 150$ at $t = 0$.
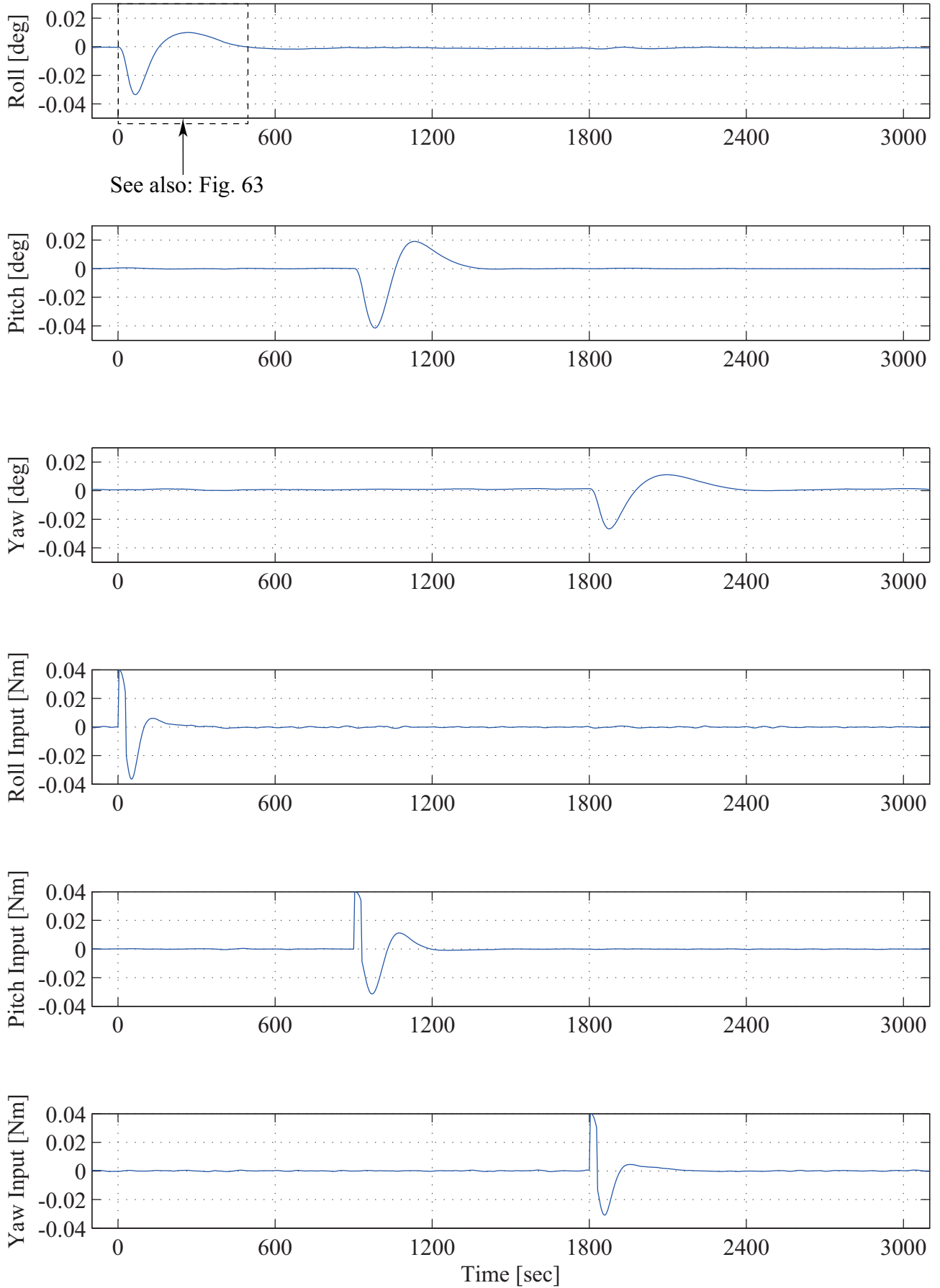
Figure 84: Rectangular disturbance response using the μ-synthesis based control law. The paddle rotation angle $\delta = 45$ at $t = 0$.
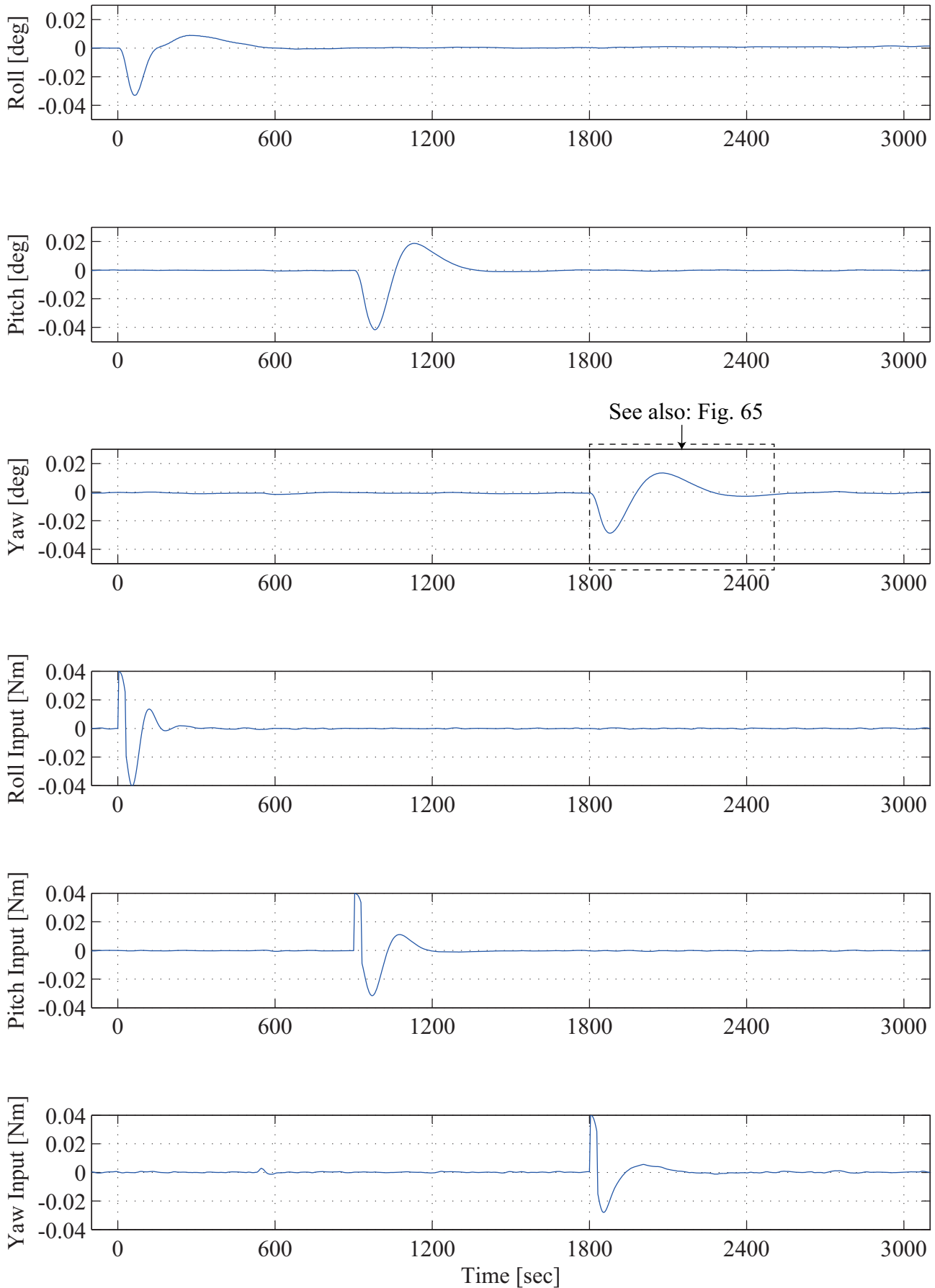
Figure 85: Rectangular disturbance response using the μ-synthesis based control law. The paddle rotation angle $\delta = 137.5$ at $t = 0$.
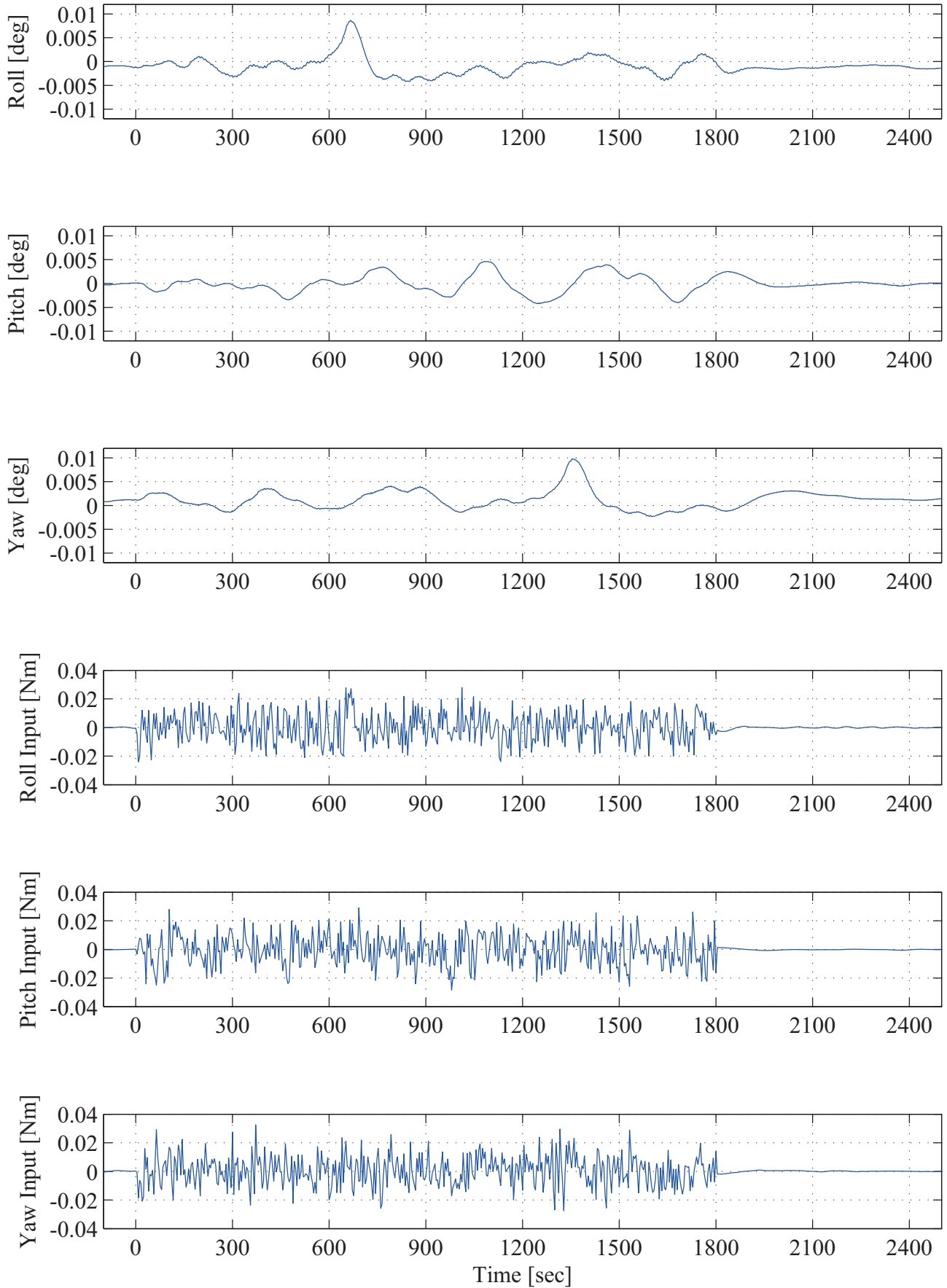
Figure 86: Random disturbance response (A) using the μ-synthesis based control law. The paddle rotation angle $\delta = 60$ at $t = 0$.
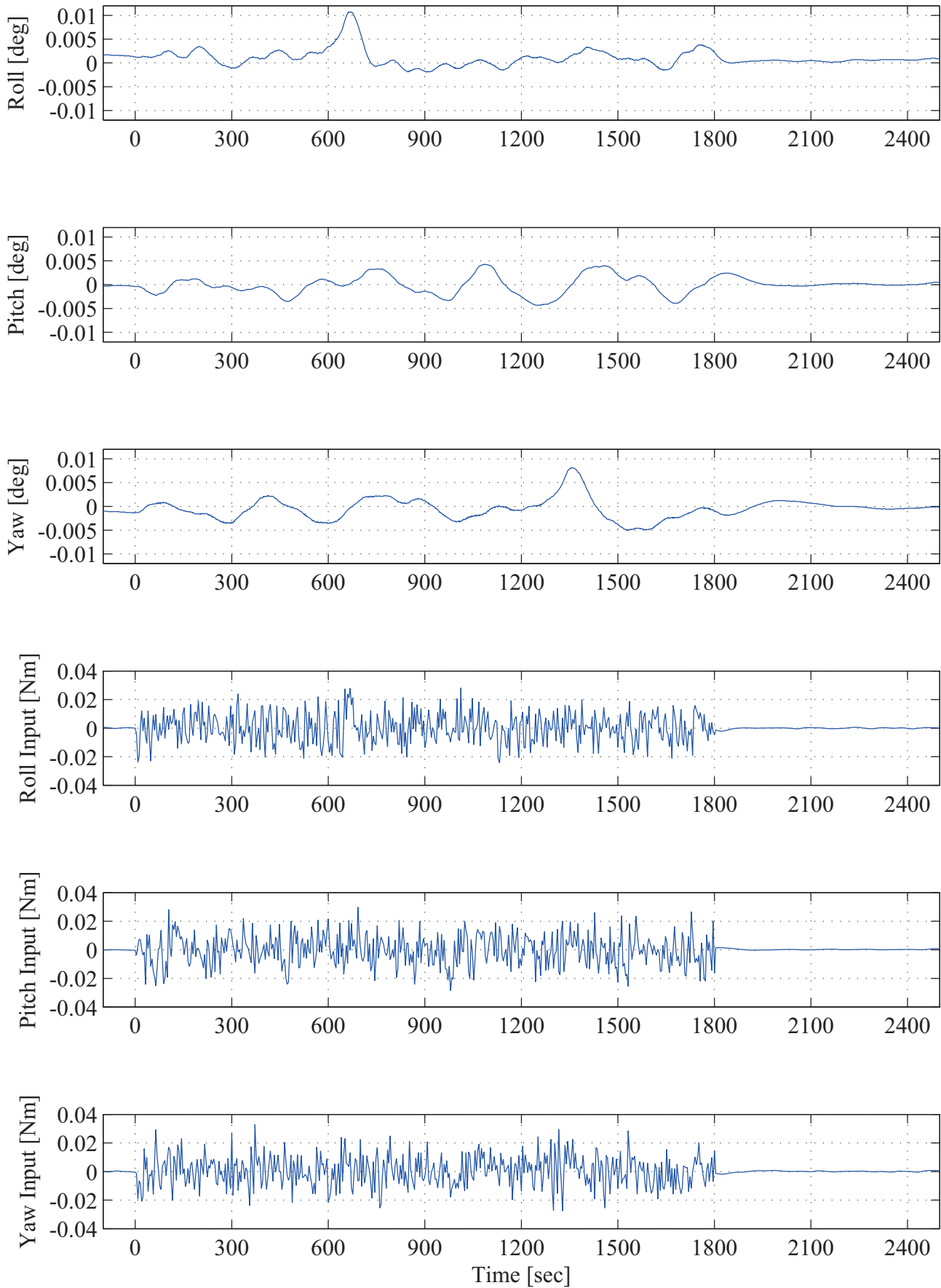
Figure 87: Random disturbance response (A) using the μ-synthesis based control law. The paddle rotation angle $\delta = 153.75$ at $t = 0$.
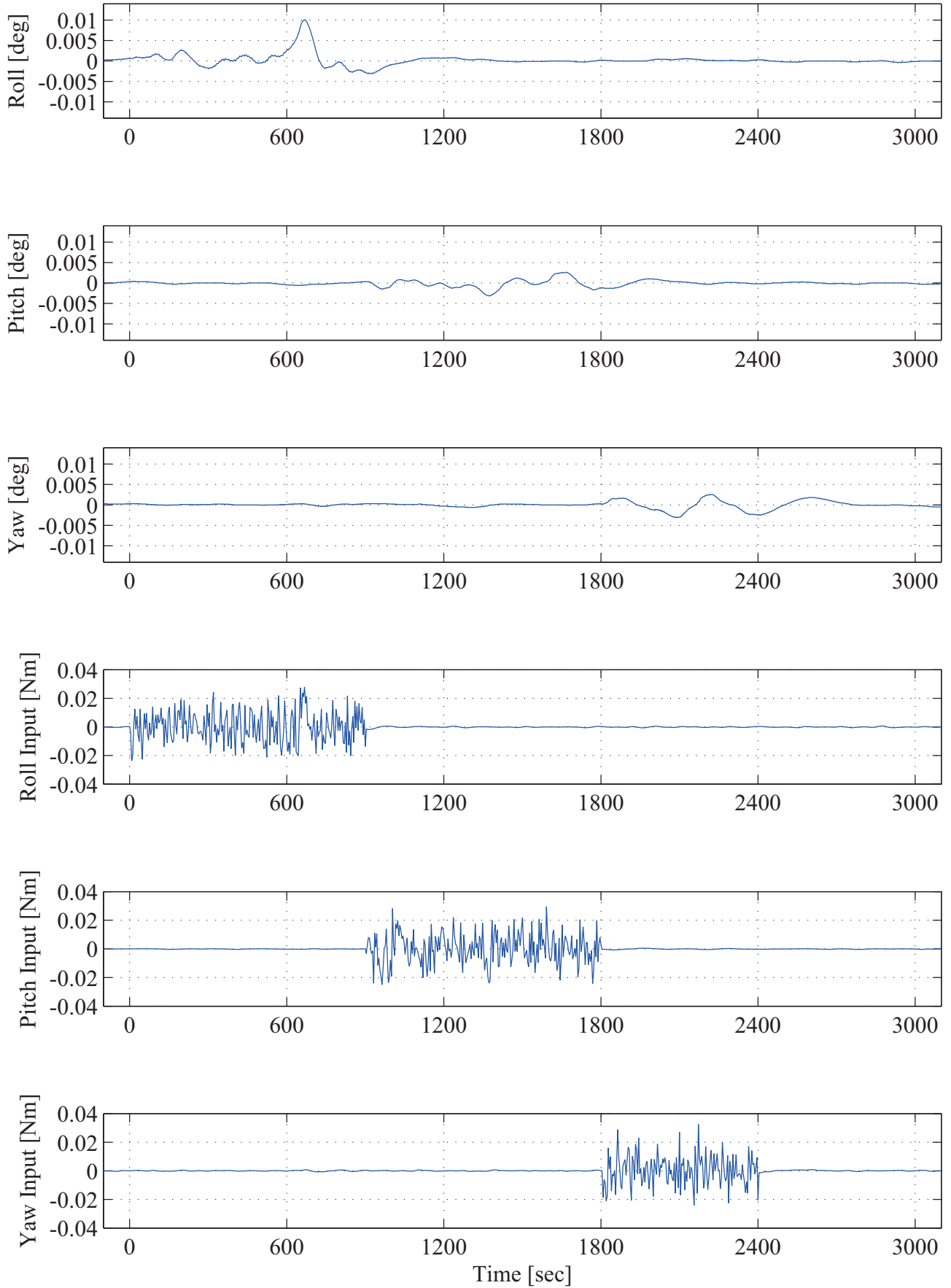
Figure 88: Random disturbance response (B) using the μ-synthesis based control law. The paddle rotation angle $\delta = 117.5$ at $t = 0$.
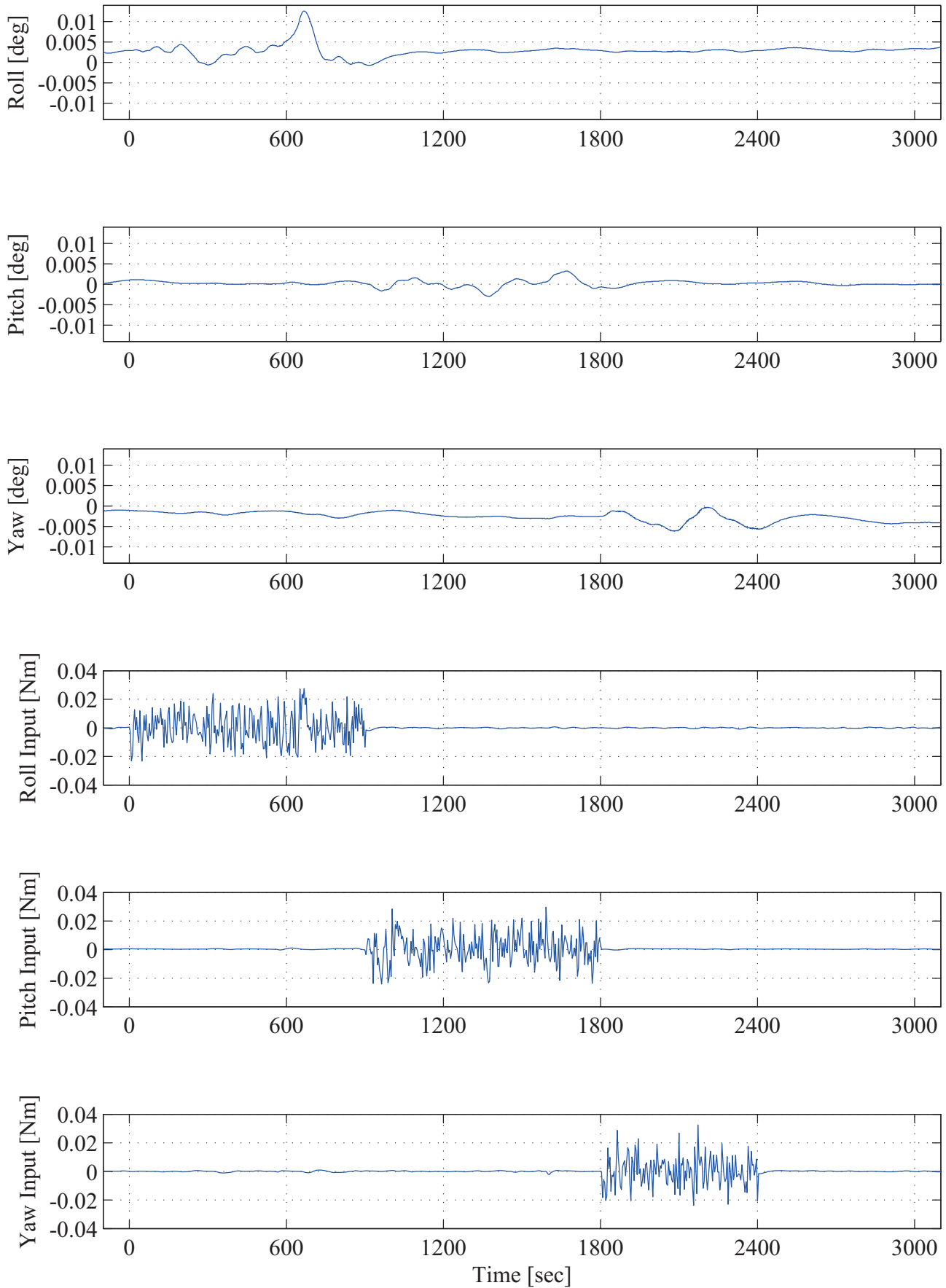
Figure 89: Random disturbance response (B) using the μ-synthesis based control law. The paddle rotation angle $\delta = 180$ at $t = 0$.
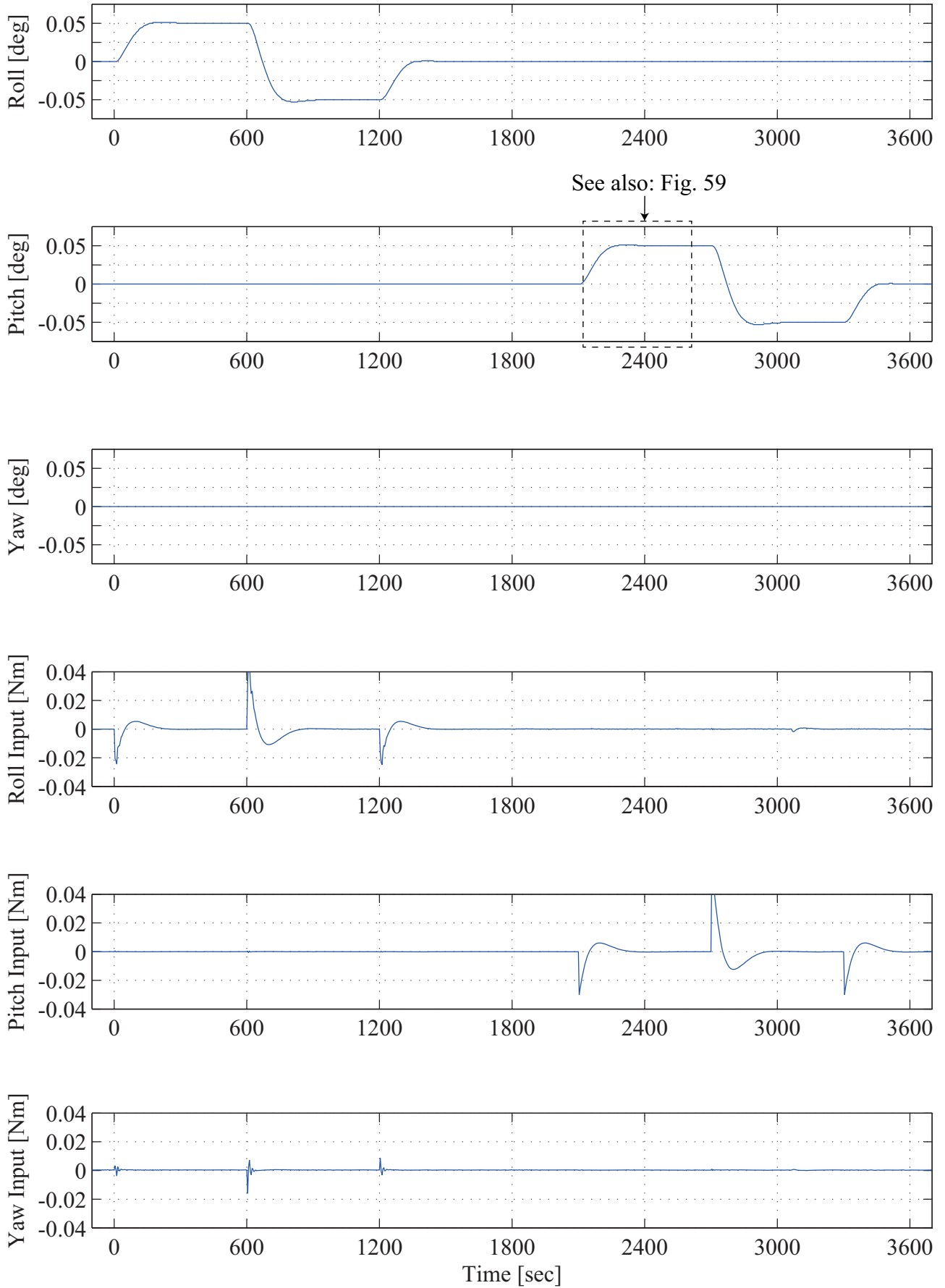
Figure 90: Step command response using the DDFB control law. The paddle rotation angle $\delta = 45$ at $t = 0$.

See also: Fig. 61
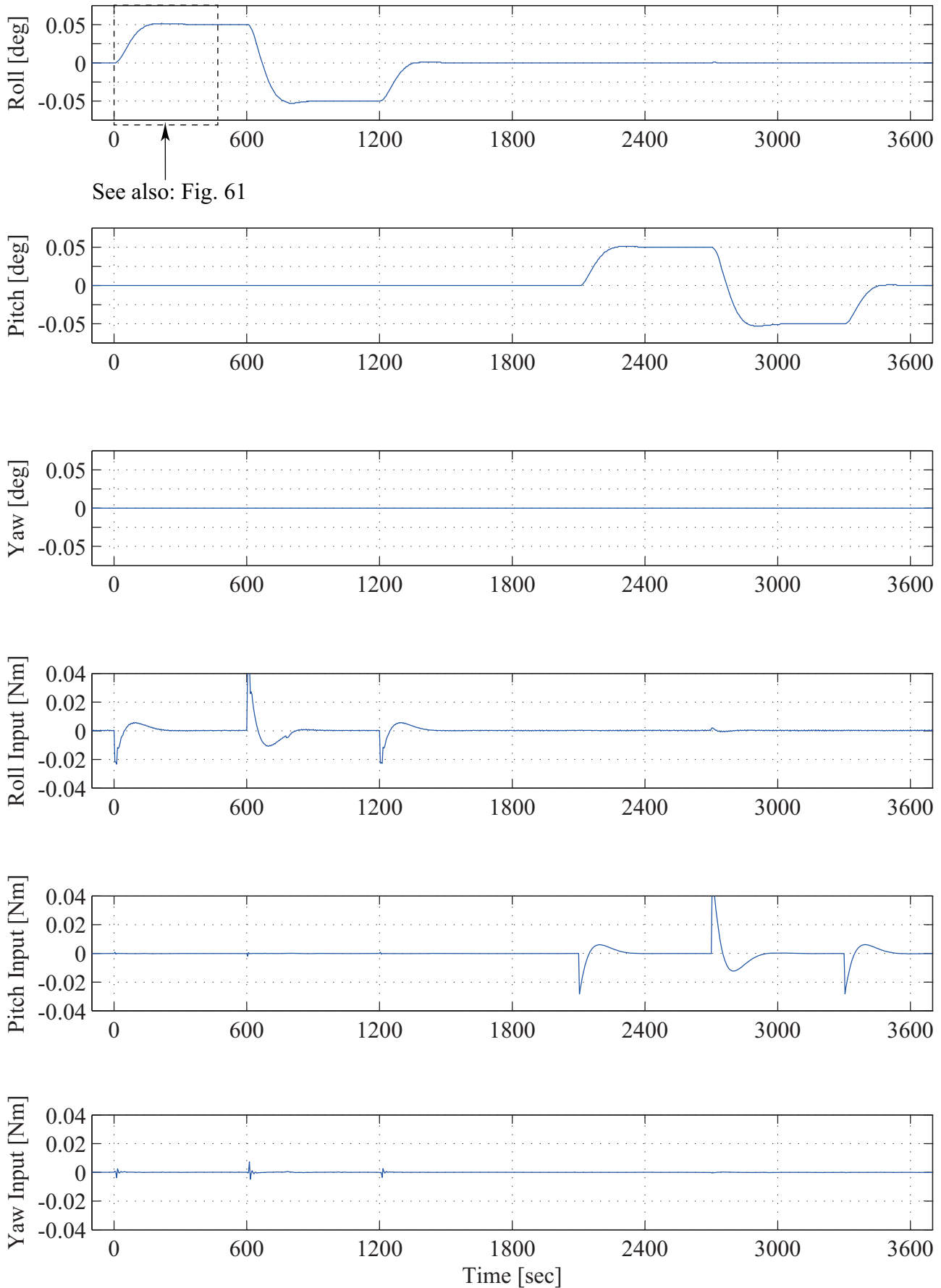
Figure 91: Step command response using the DDFB control law. The paddle rotation angle $\delta = 86$ at $t = 0$.
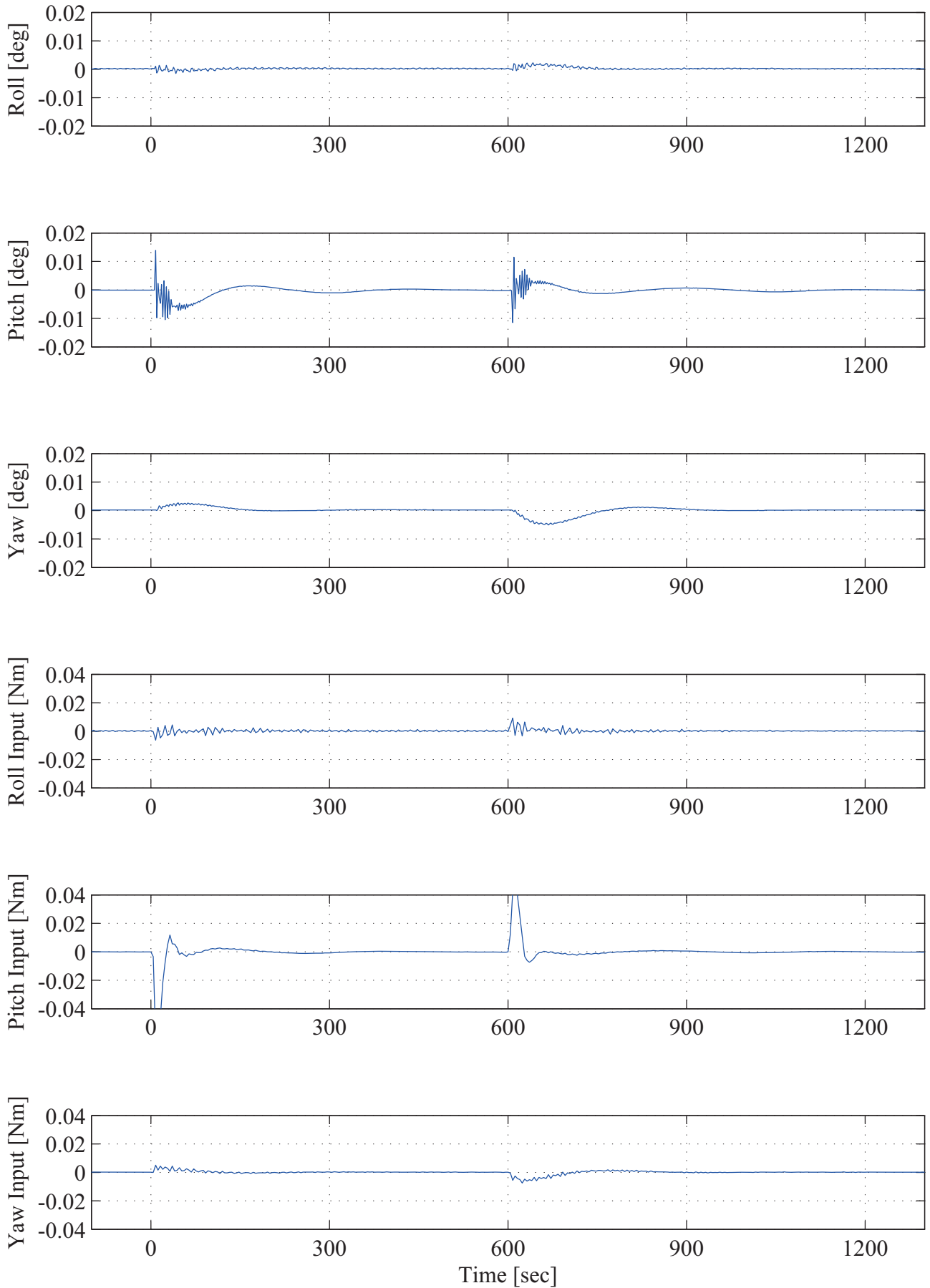
Figure 92: Impulse disturbance response using the DDFB control law. The paddle rotation angle $\delta = 75$ at $t = 0$.
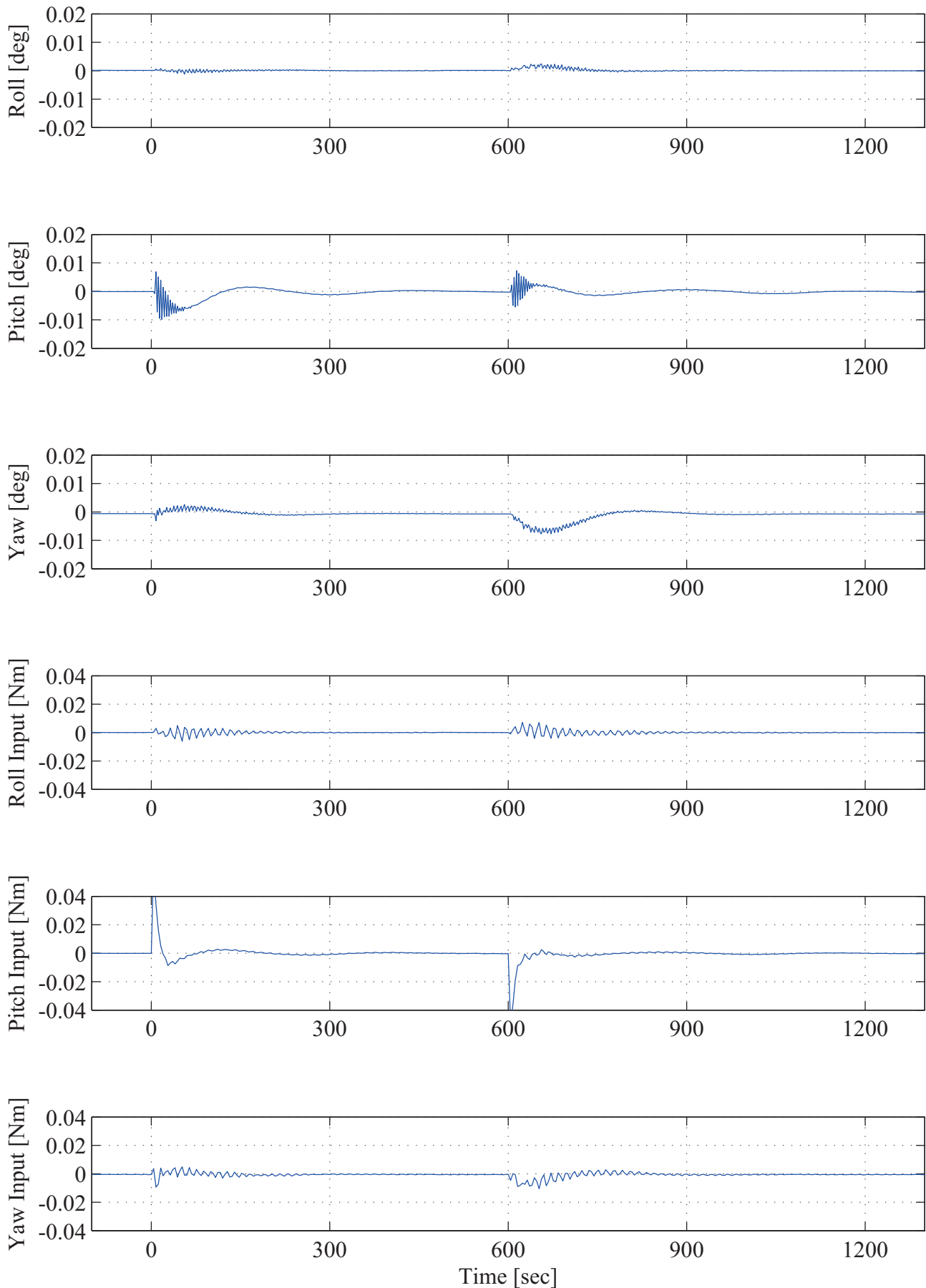
Figure 93: Impulse disturbance response using the DDFB control law. The paddle rotation angle $\delta = 135$ at $t = 0$.
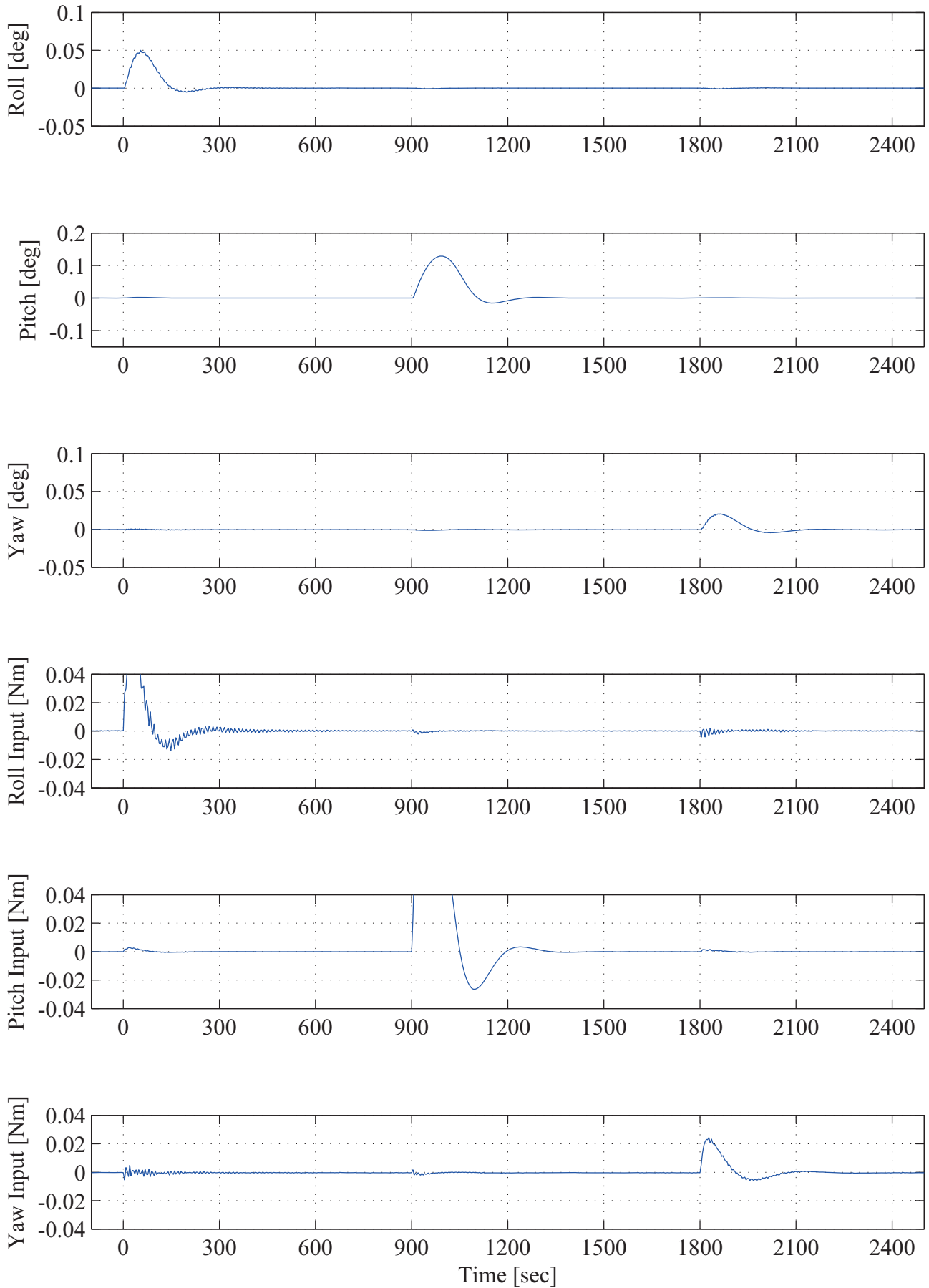
Figure 94: Large disturbance response using the DDFB control law. The paddle rotation angle $\delta = 120$ at $t = 0$.
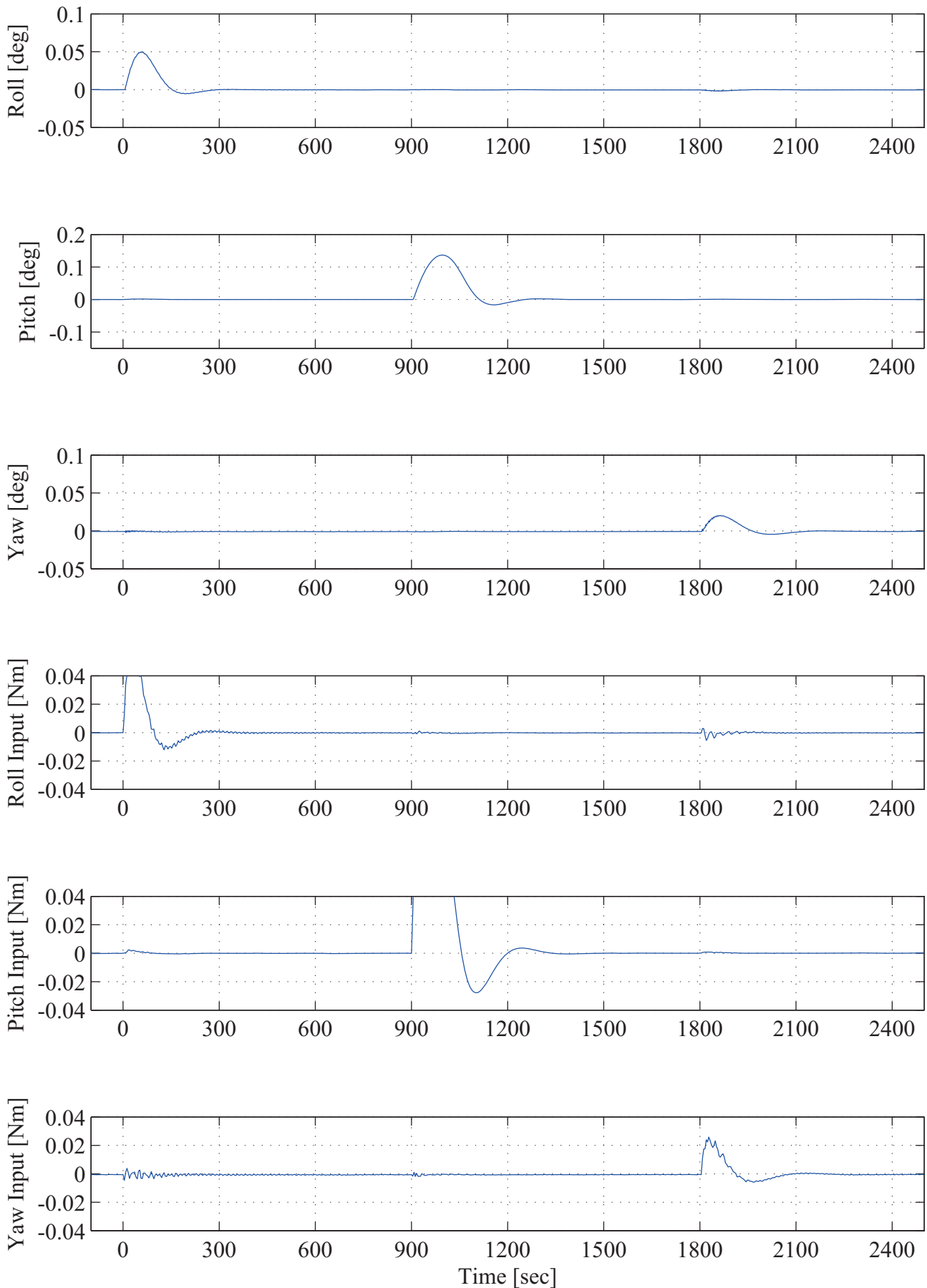
Figure 95: Large disturbance response using the DDFB control law. The paddle rotation angle $\delta = 150$ at $t = 0$.
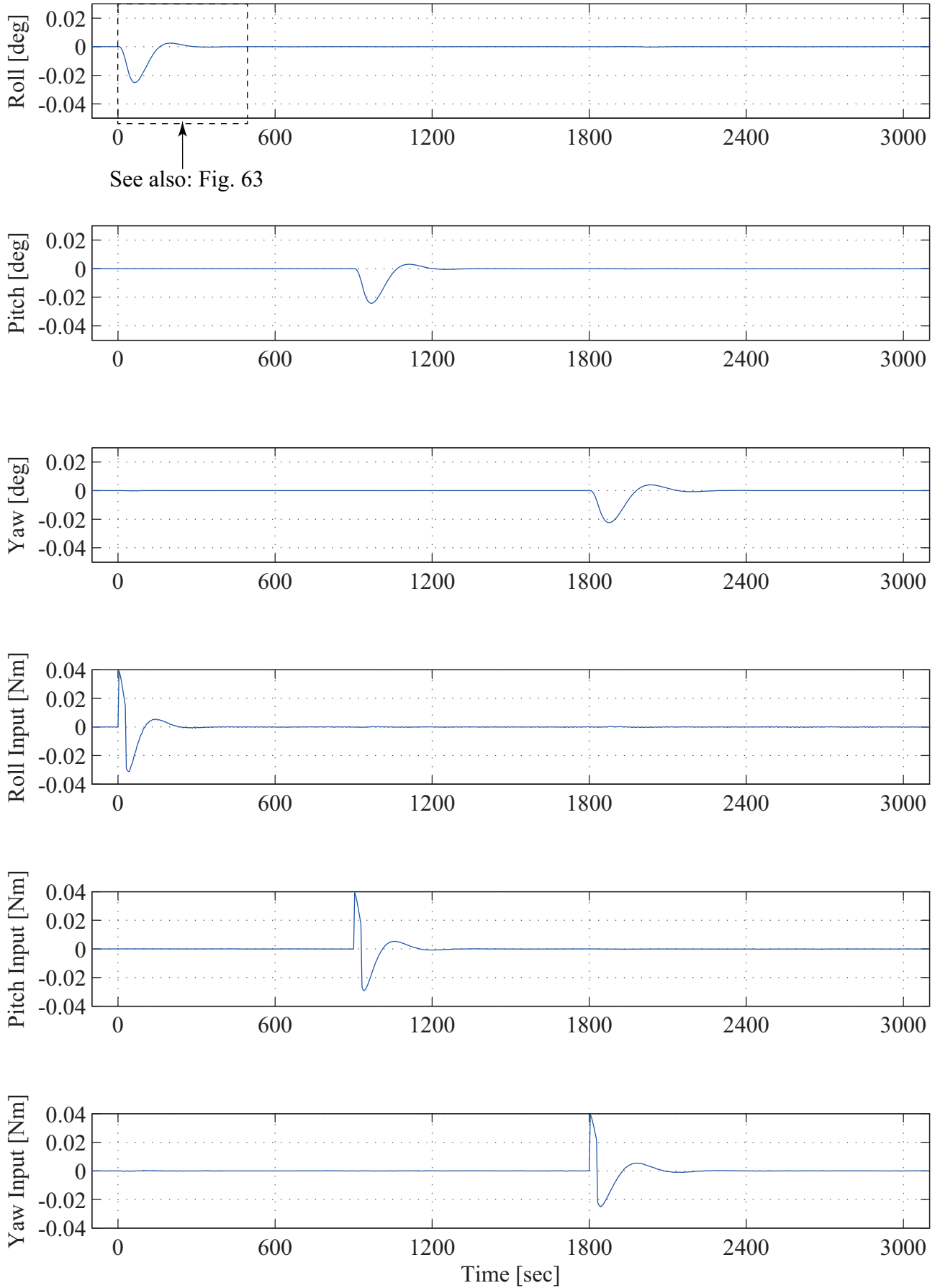
Figure 96: Rectangular disturbance response using the DDFB control law. The paddle rotation angle $\delta = 45$ at $t = 0$.
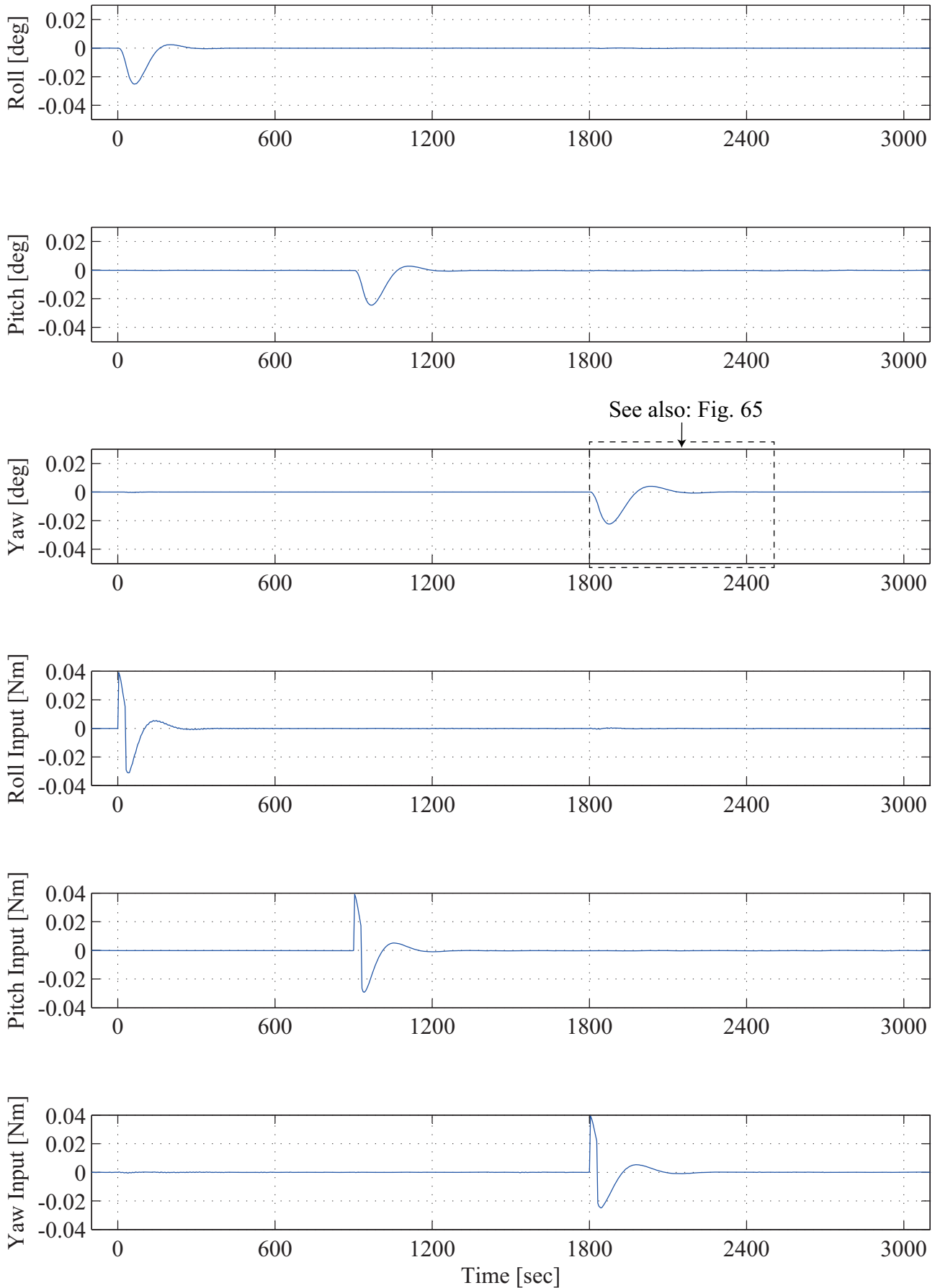
Figure 97: Rectangular disturbance response using the DDFB control law. The paddle rotation angle $\delta = 137.5$ at $t = 0$.
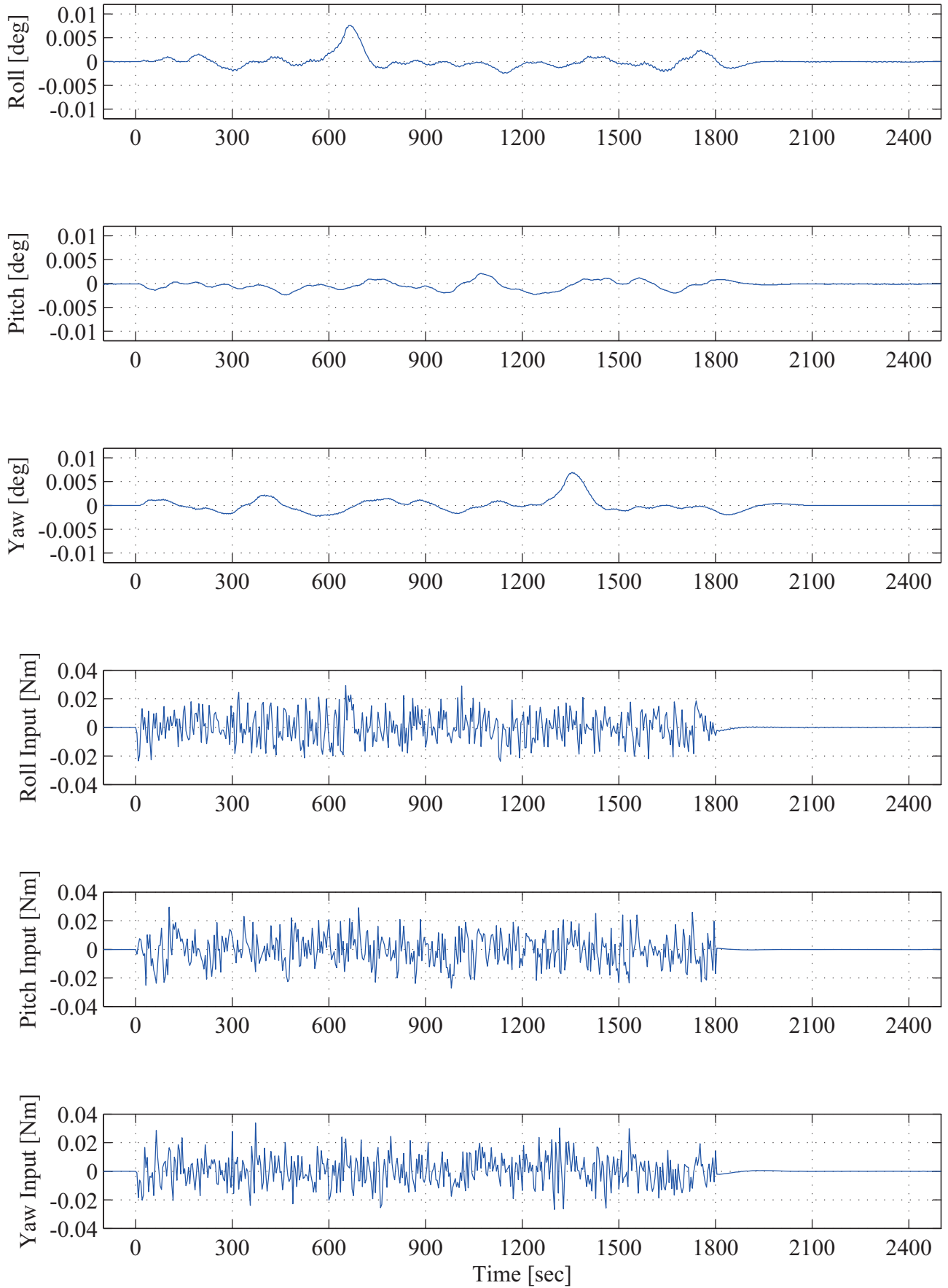
Figure 98: Random disturbance response (A) using the DDFB control law. The paddle rotation angle $\delta = 60$ at $t = 0$.
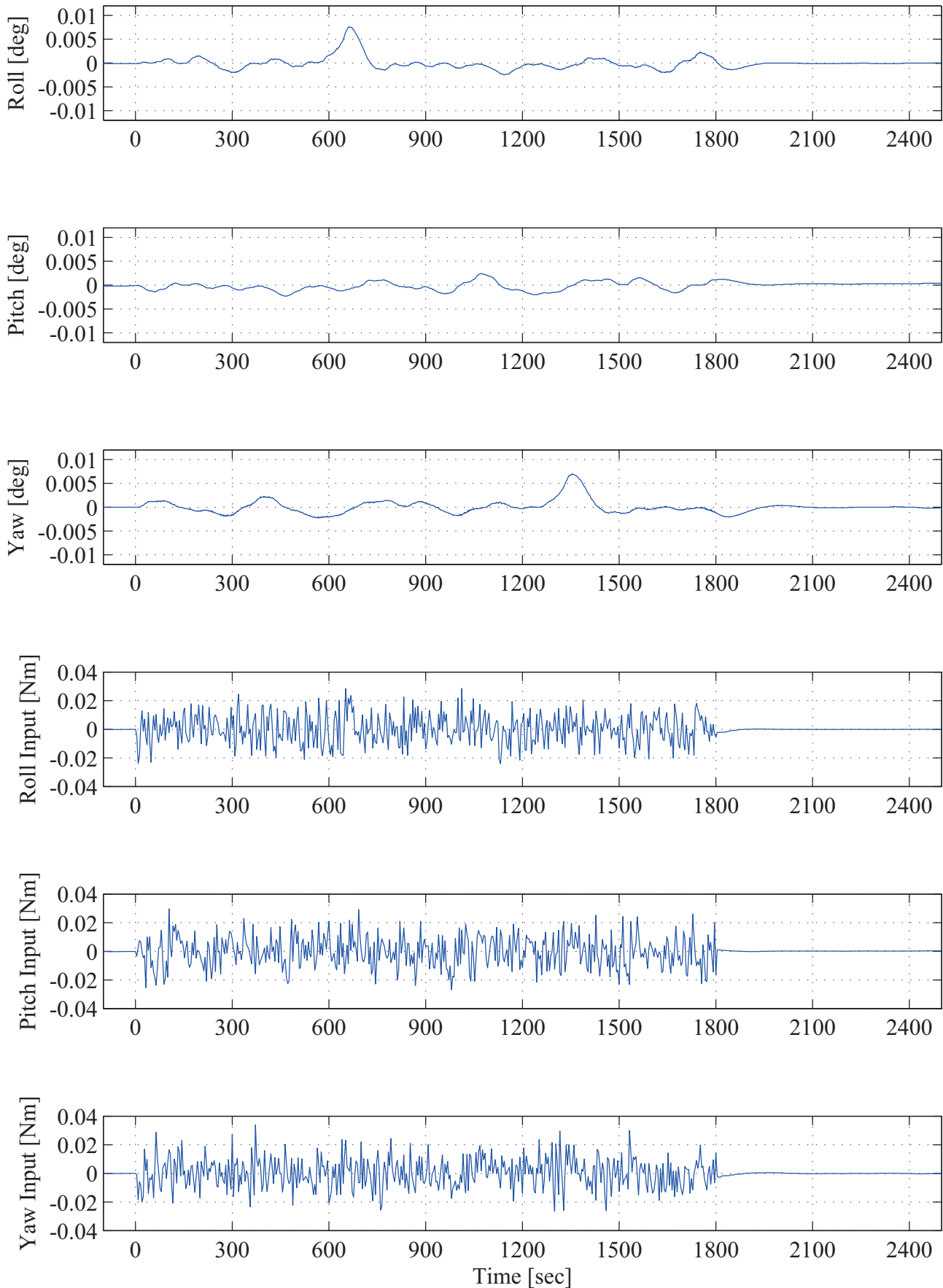
Figure 99: Random disturbance response (A) using the DDFB control law. The paddle rotation angle $\delta = 153.75$ at $t = 0$.
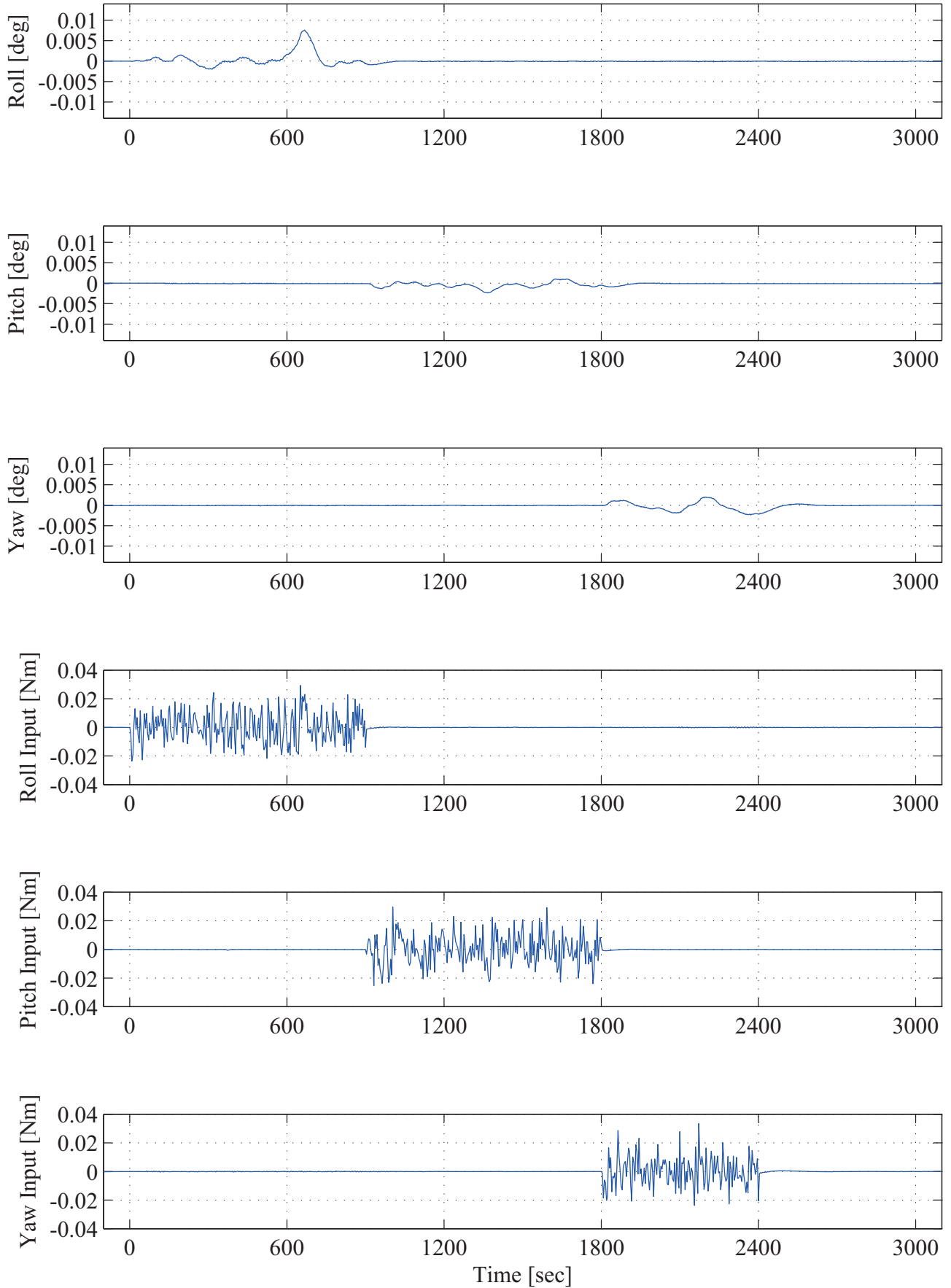
Figure 100: Random disturbance response (B) using the DDFB control law. The paddle rotation angle $\delta = 117.5$ at $t = 0$.
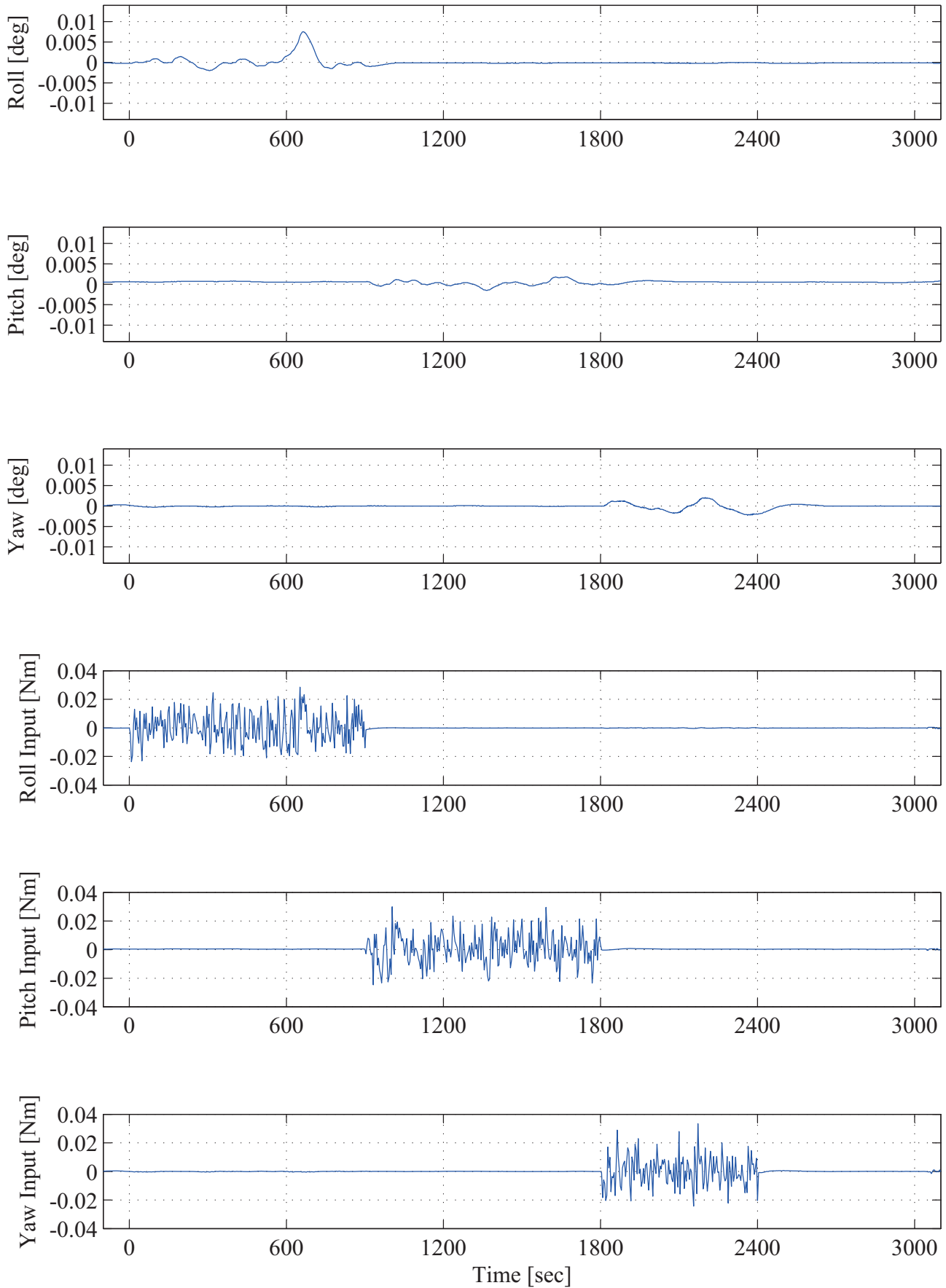
Figure 101: Random disturbance response (B) using the DDFB control law. The paddle rotation angle $\delta = 180$ at $t = 0$.
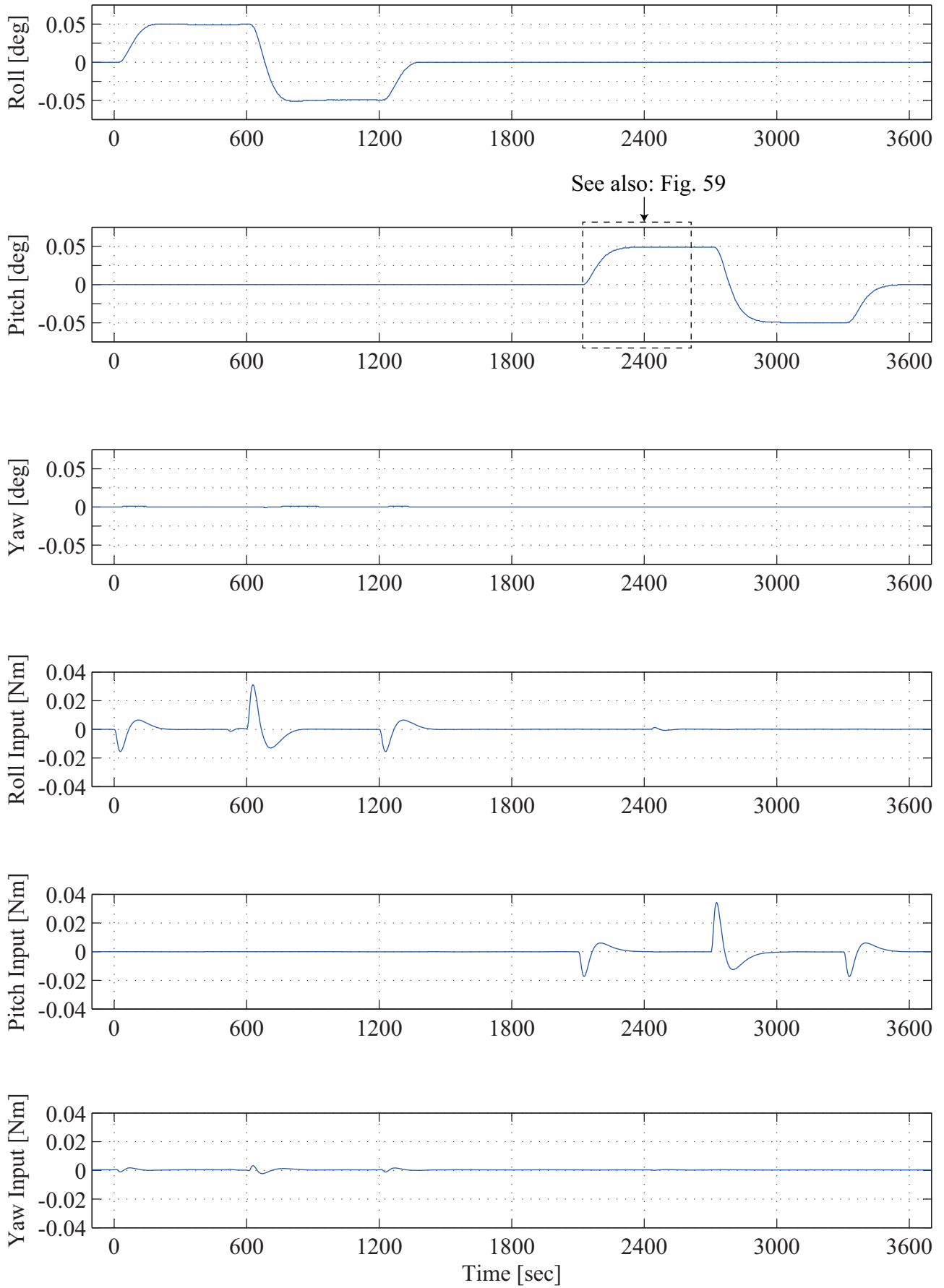
Figure 102: Step command response using the gain scheduling control law. The paddle rotation angle $\delta = 45$ at $t = 0$.

See also: Fig. 61
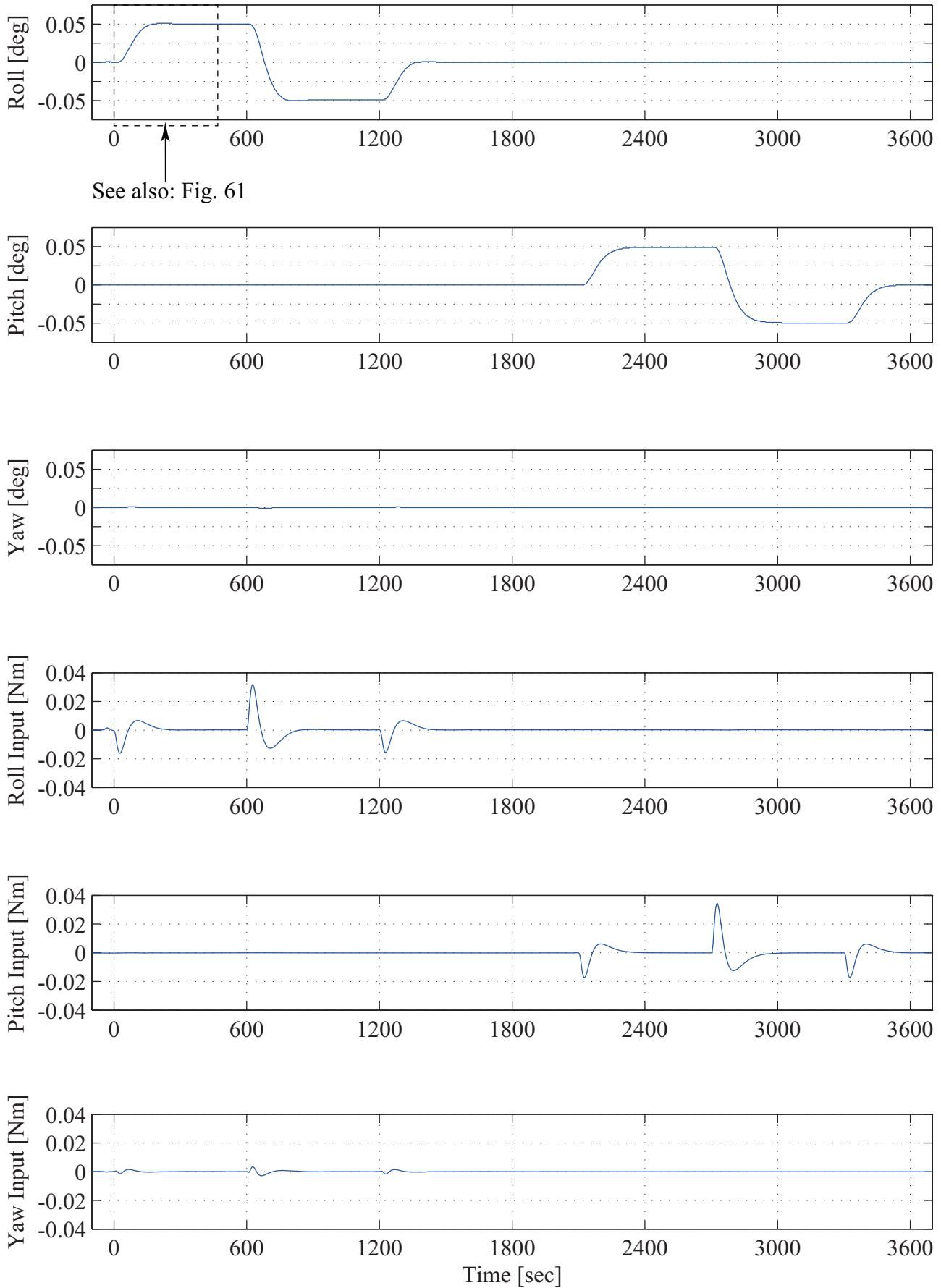
Figure 103: Step command response using the gain scheduling control law. The paddle rotation angle $\delta = 86$ at $t = 0$.
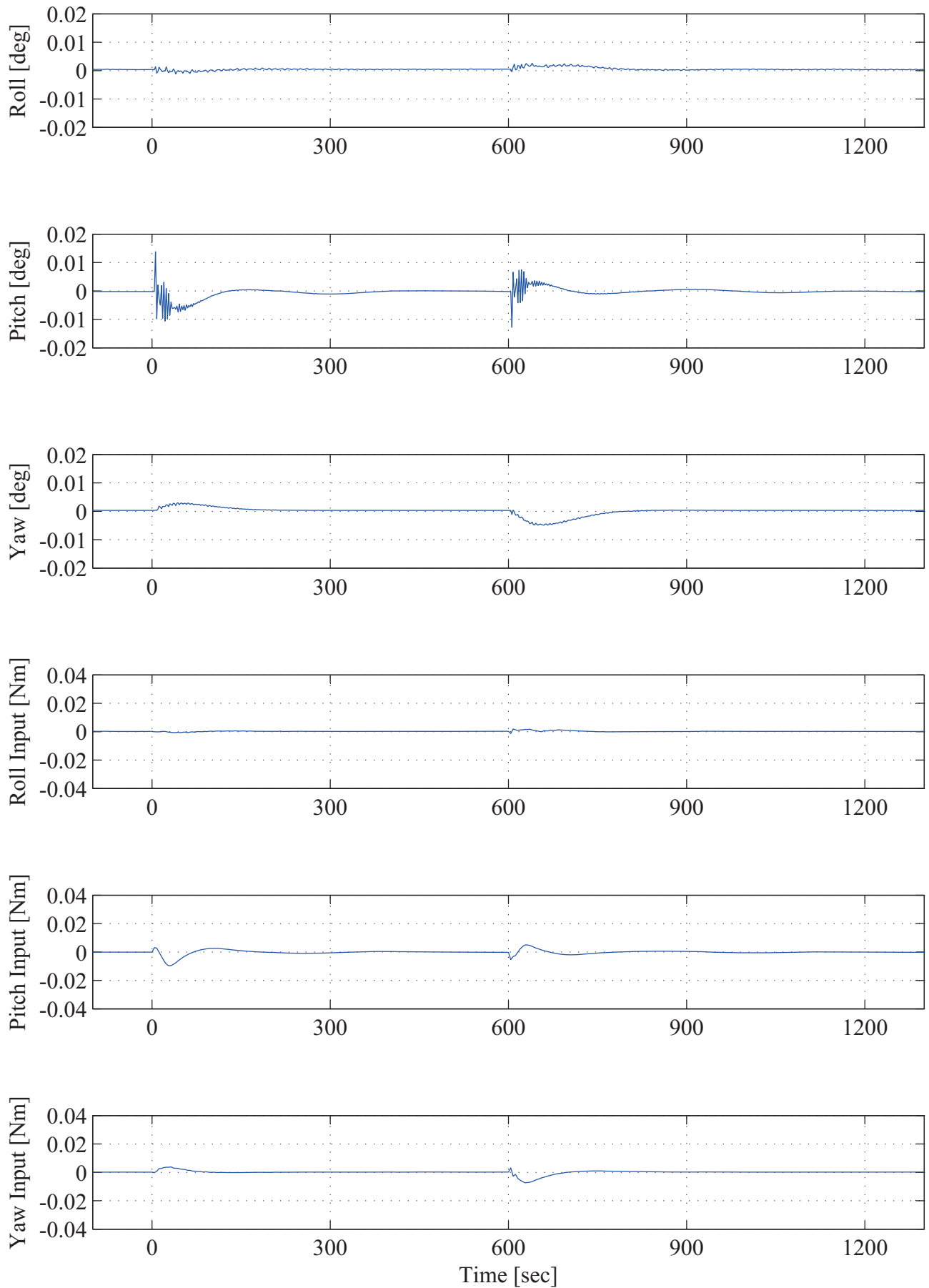
Figure 104: Impulse disturbance response using the gain scheduling control law. The paddle rotation angle $\delta = 75$ at $t = 0$.
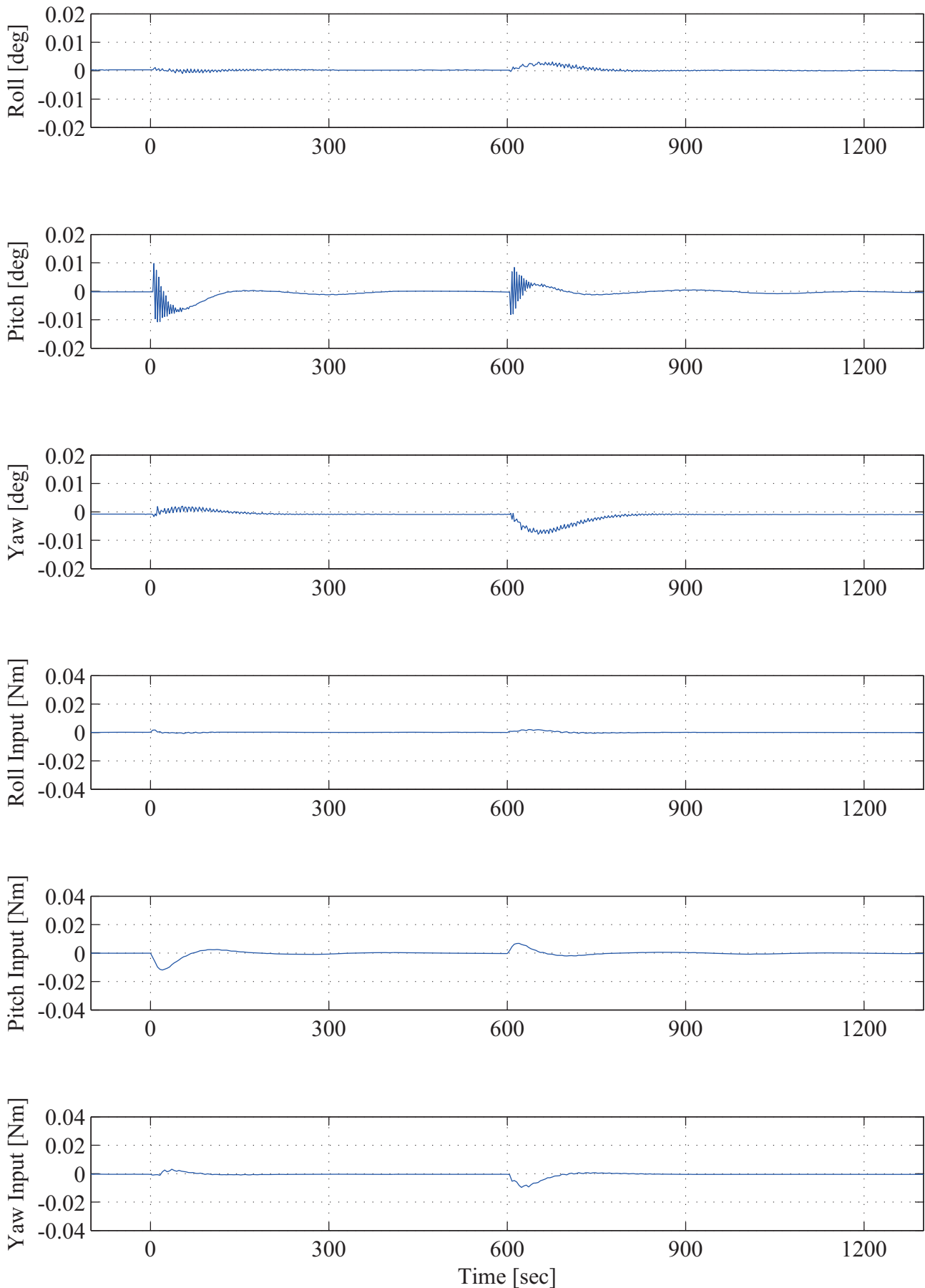
Figure 105: Impulse disturbance response using the gain scheduling control law. The paddle rotation angle $\delta = 135$ at $t = 0$.
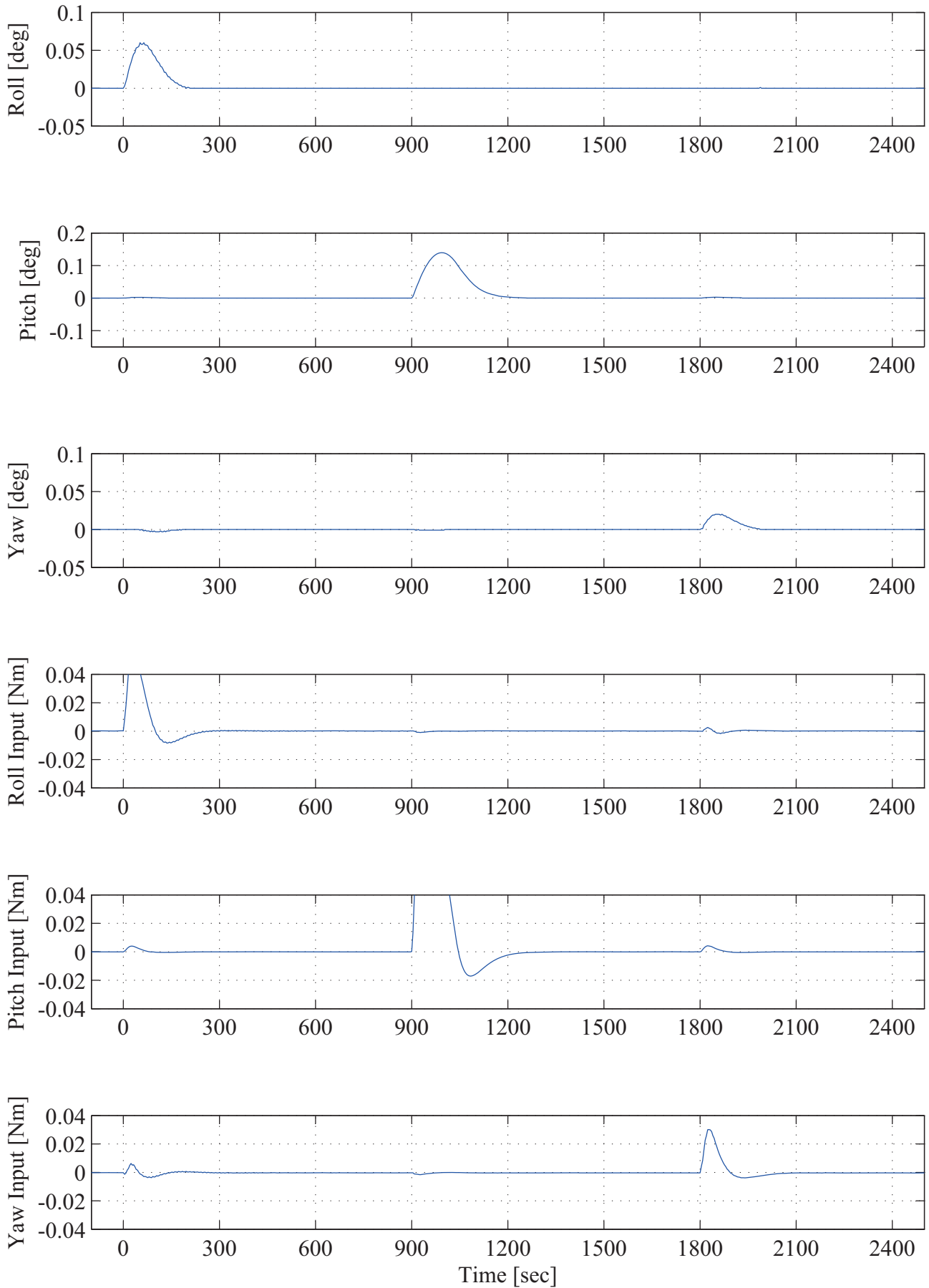
Figure 106: Large disturbance response using the gain scheduling control law. The paddle rotation angle $\delta = 120$ at $t = 0$.
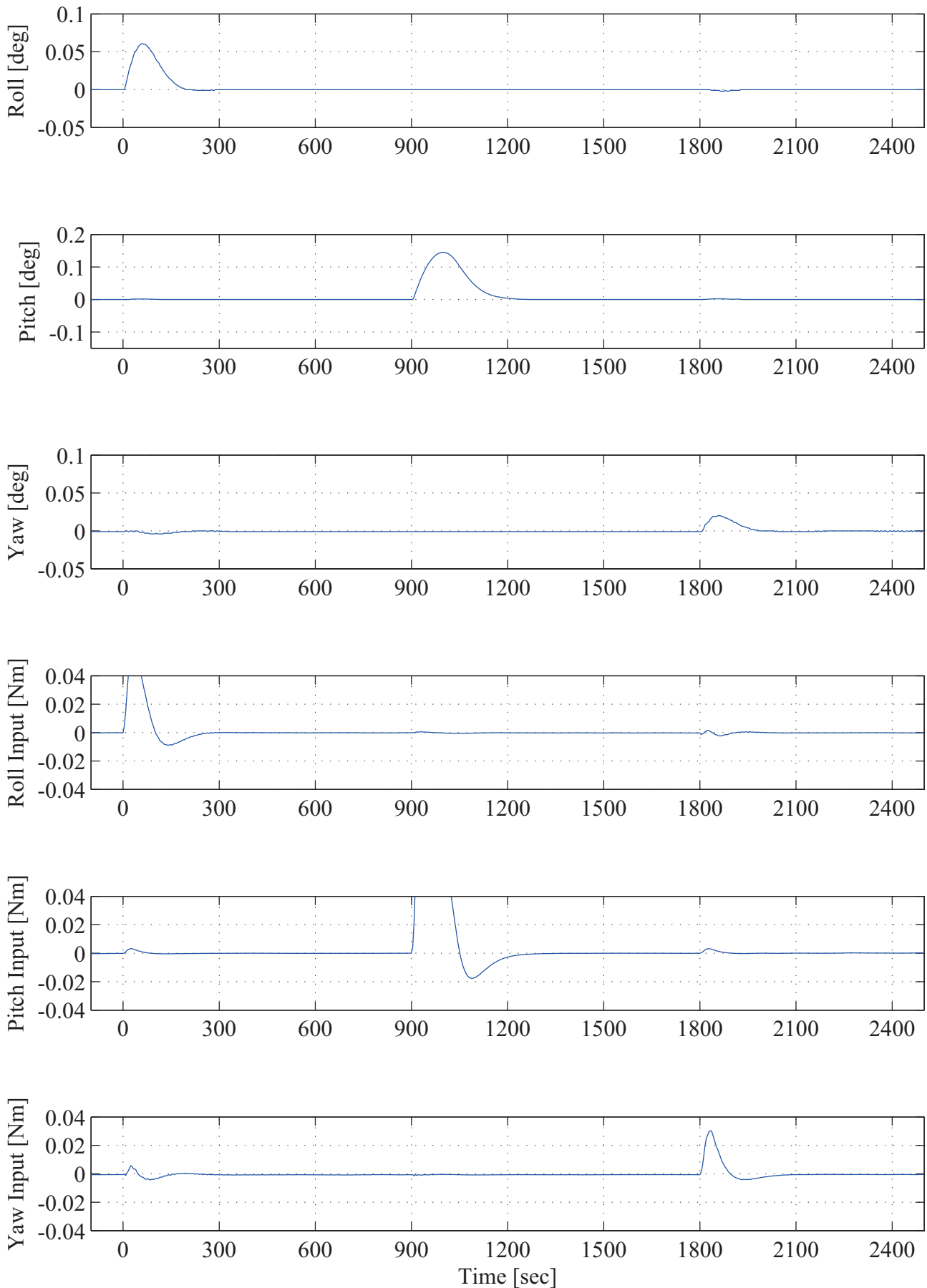
Figure 107: Large disturbance response using the gain scheduling control law. The paddle rotation angle $\delta = 150$ at $t = 0$.
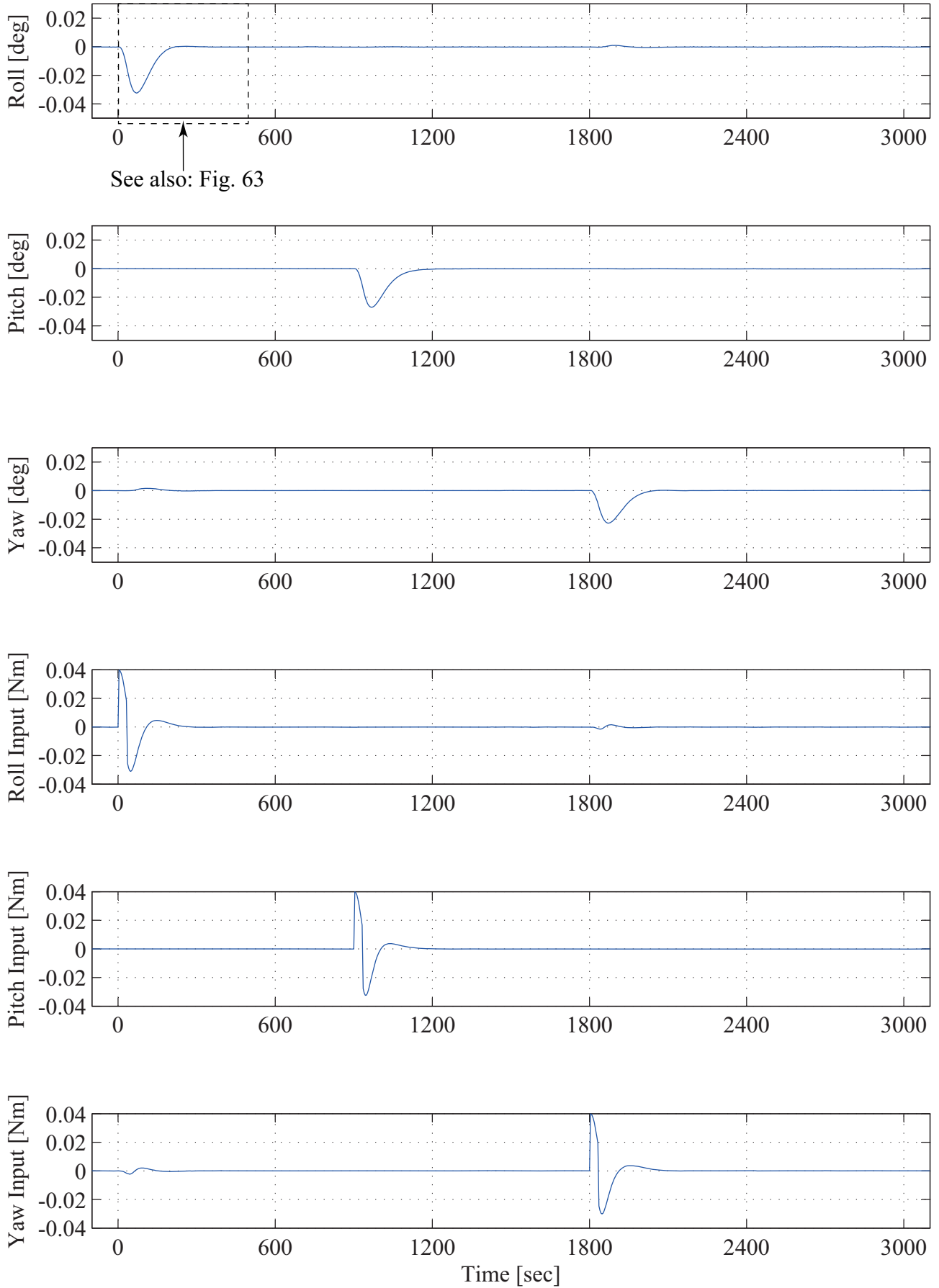
Figure 108: Rectangular disturbance response using the gain scheduling control law. The paddle rotation angle $\delta = 45$ at $t = 0$.
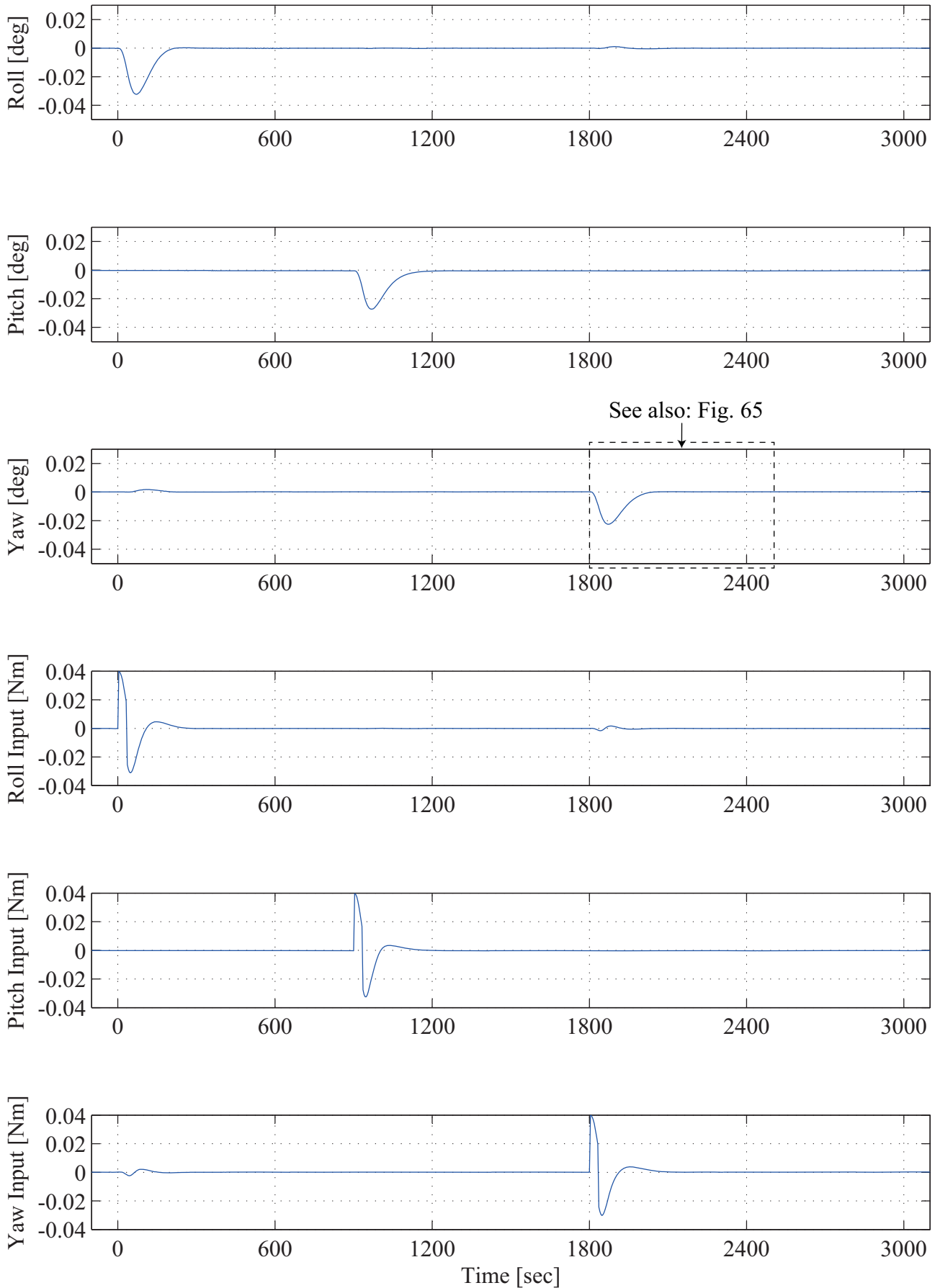
Figure 109: Rectangular disturbance response using the gain scheduling control law. The paddle rotation angle $\delta = 137.5$ at $t = 0$.
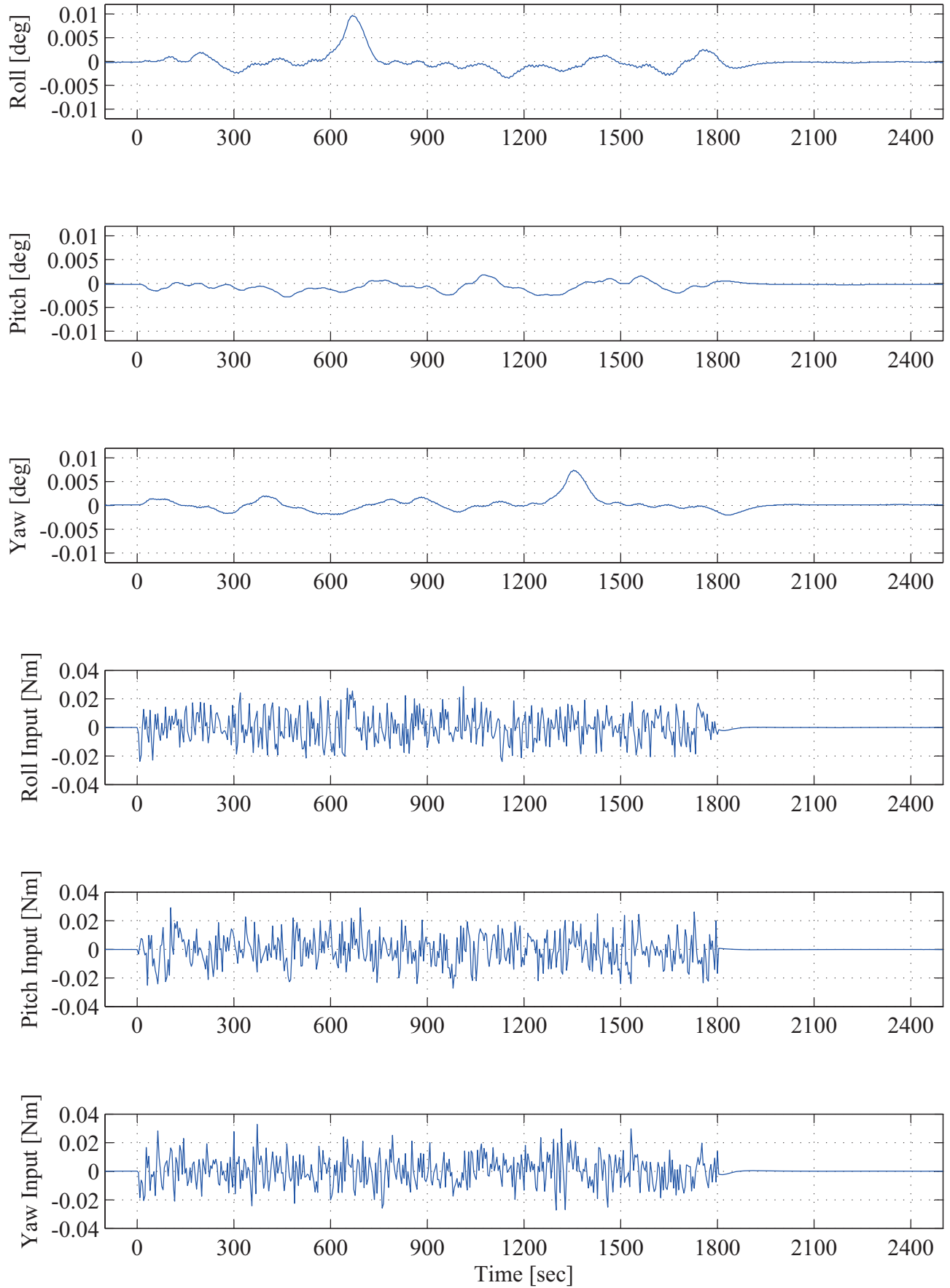
Figure 110: Random disturbance response (A) using the gain scheduling control law. The paddle rotation angle $\delta = 60$ at $t = 0$.
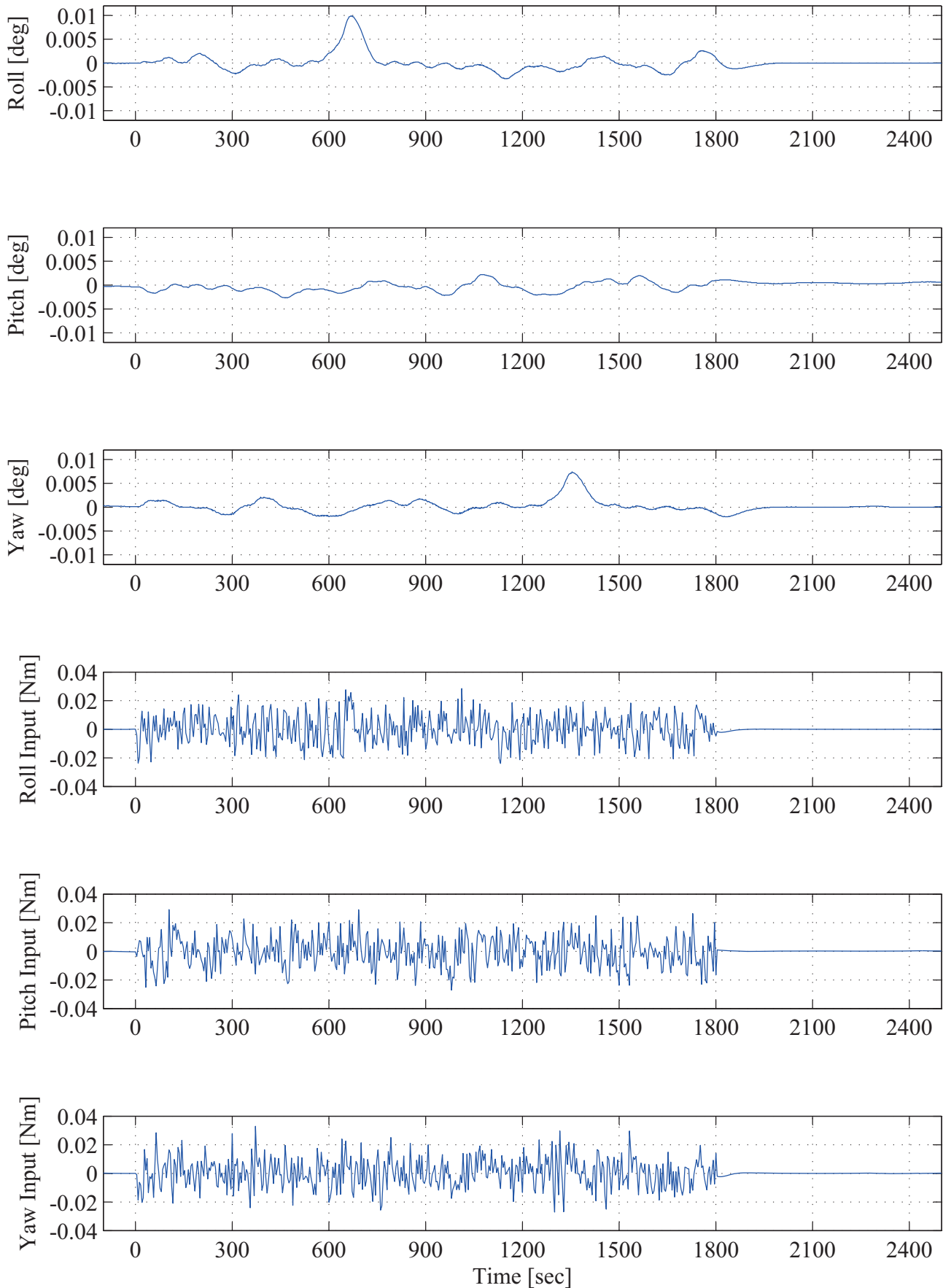
Figure 111: Random disturbance response (A) using the gain scheduling control law. The paddle rotation angle $\delta = 153.75$ at $t = 0$.
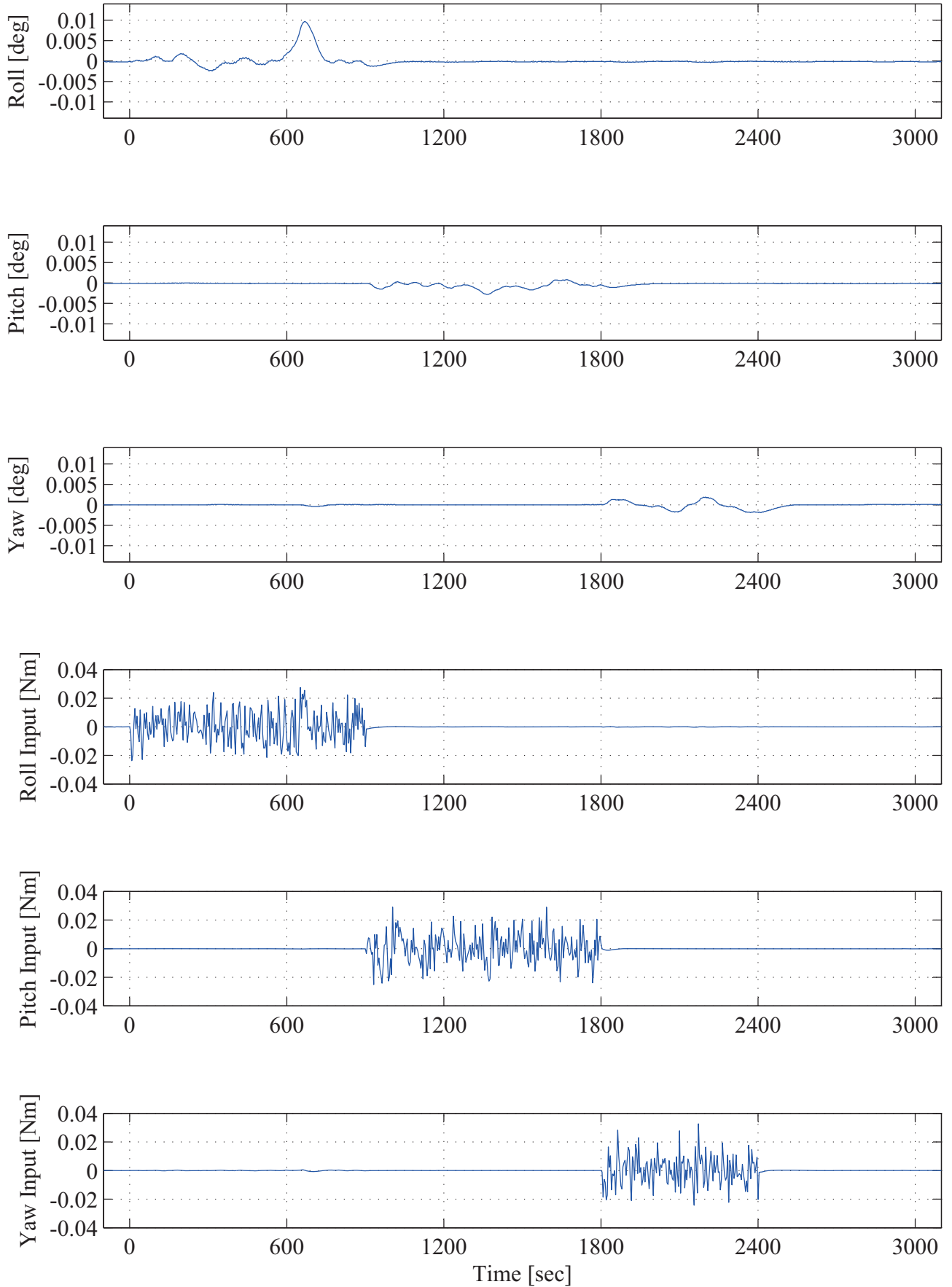
Figure 112: Random disturbance response (B) using the gain scheduling control law. The paddle rotation angle $\delta = 117.5$ at $t = 0$.
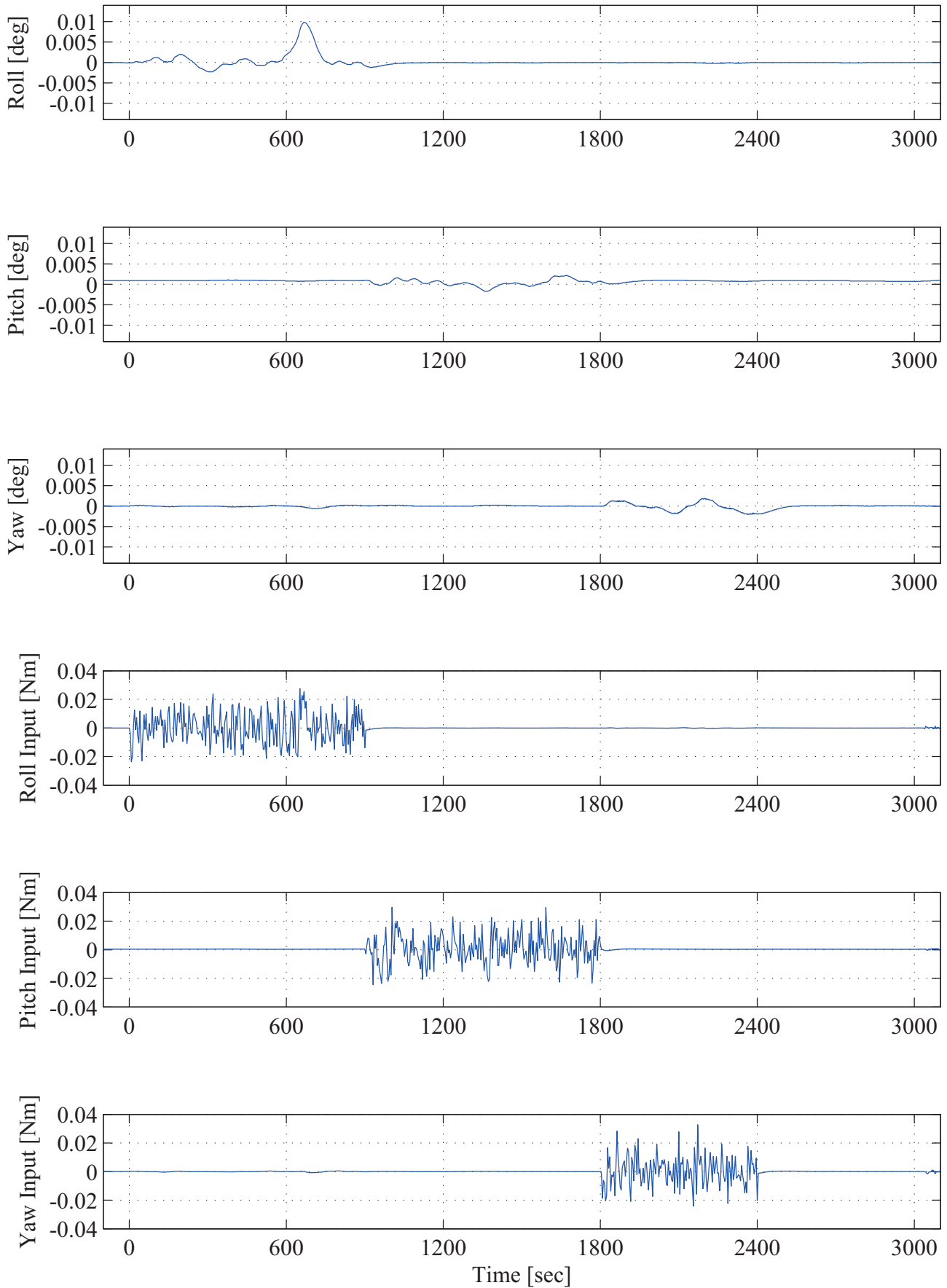
Figure 113: Random disturbance response (B) using the gain scheduling control law. The paddle rotation angle $\delta = 180$ at $t = 0$.
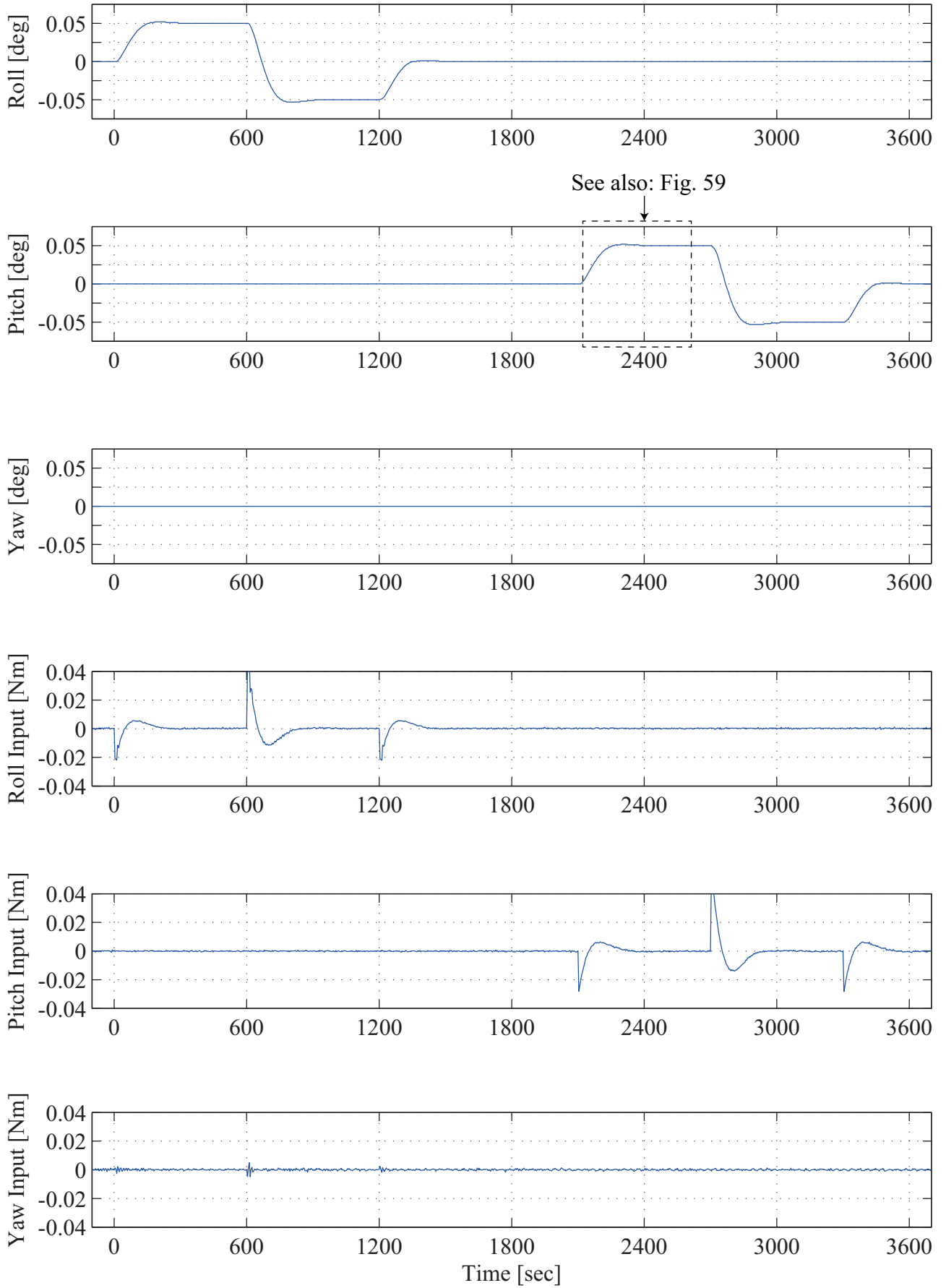
Figure 114: Step command response using the DVDFB control law. The paddle rotation angle $\delta = 45$ at $t = 0$.
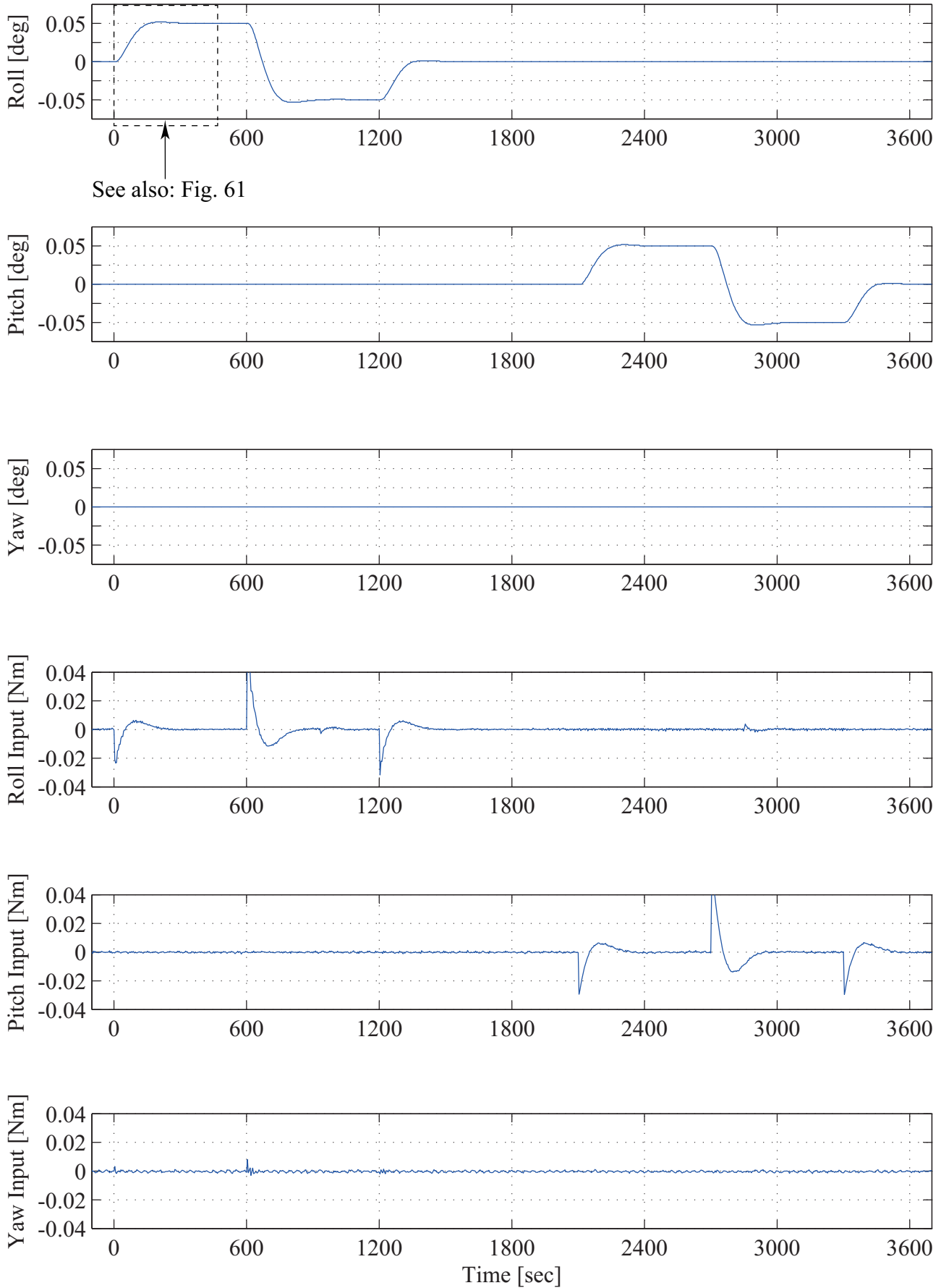
Figure 115: Step command response using the DVDFB control law. The paddle rotation angle $\delta = 86$ at $t = 0$.
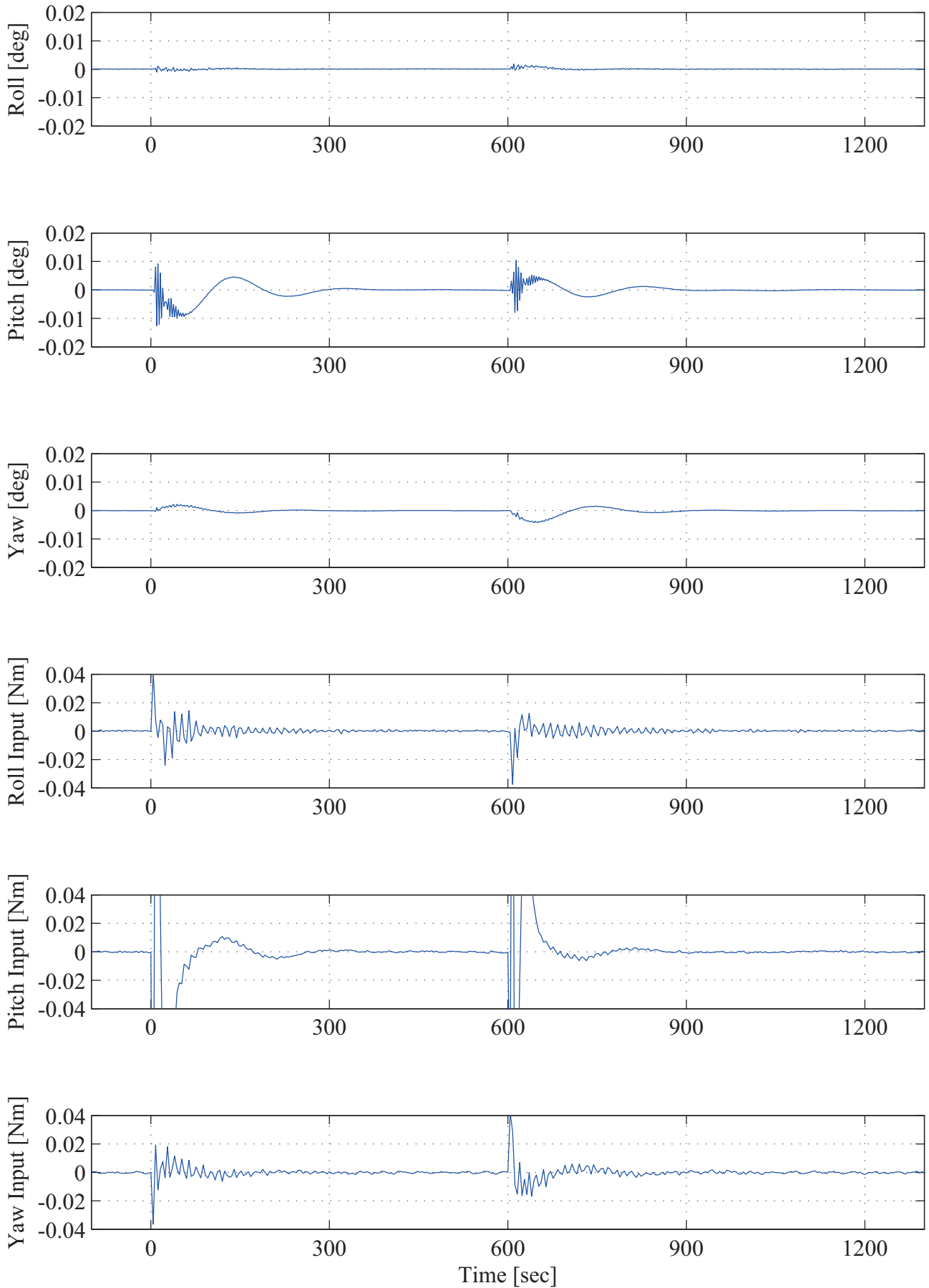
Figure 116: Impulse disturbance response using the DVDFB control law. The paddle rotation angle $\delta = 75$ at $t = 0$.
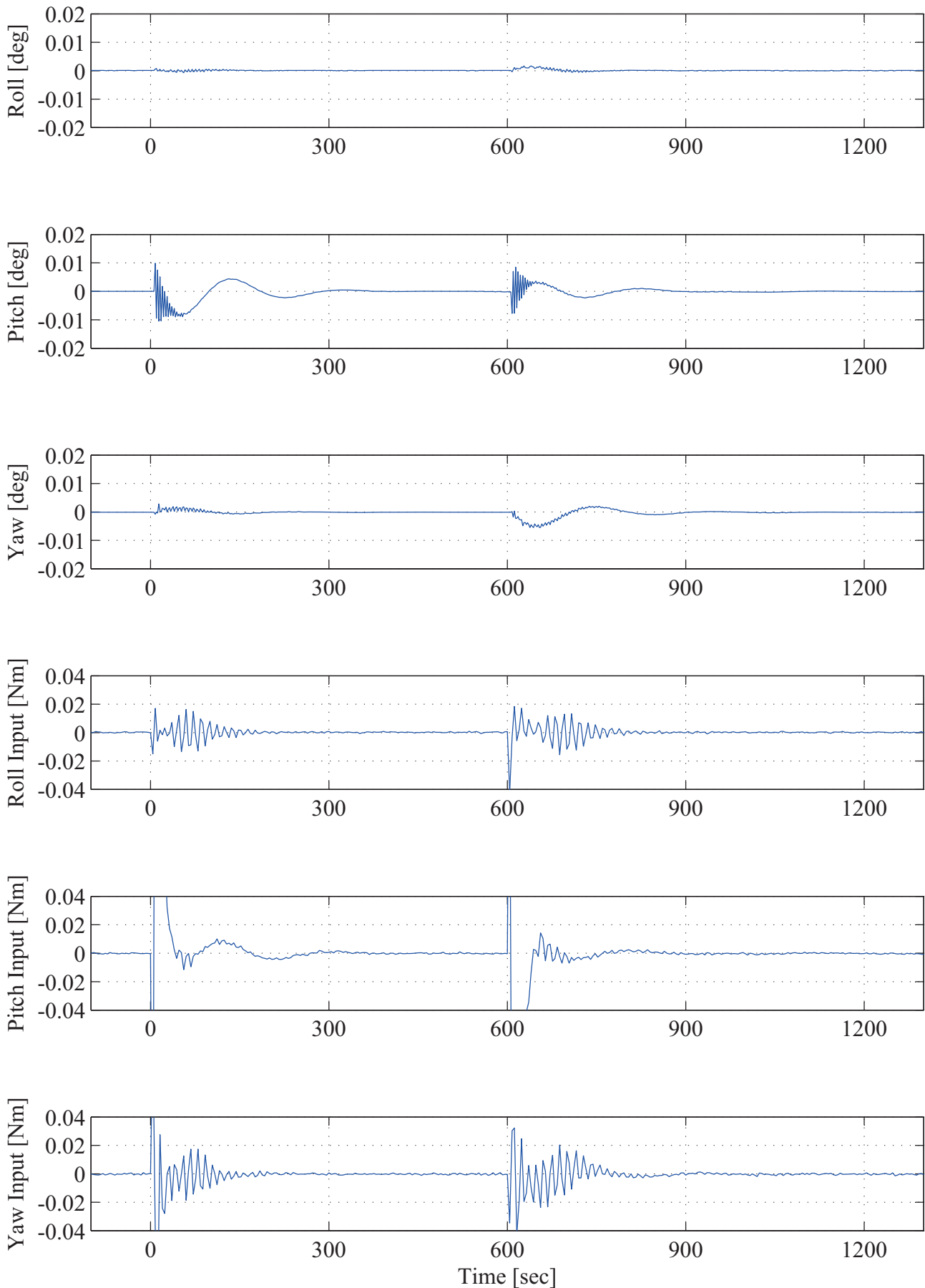
Figure 117: Impulse disturbance response using the DVDFB control law. The paddle rotation angle $\delta = 135$ at $t = 0$.
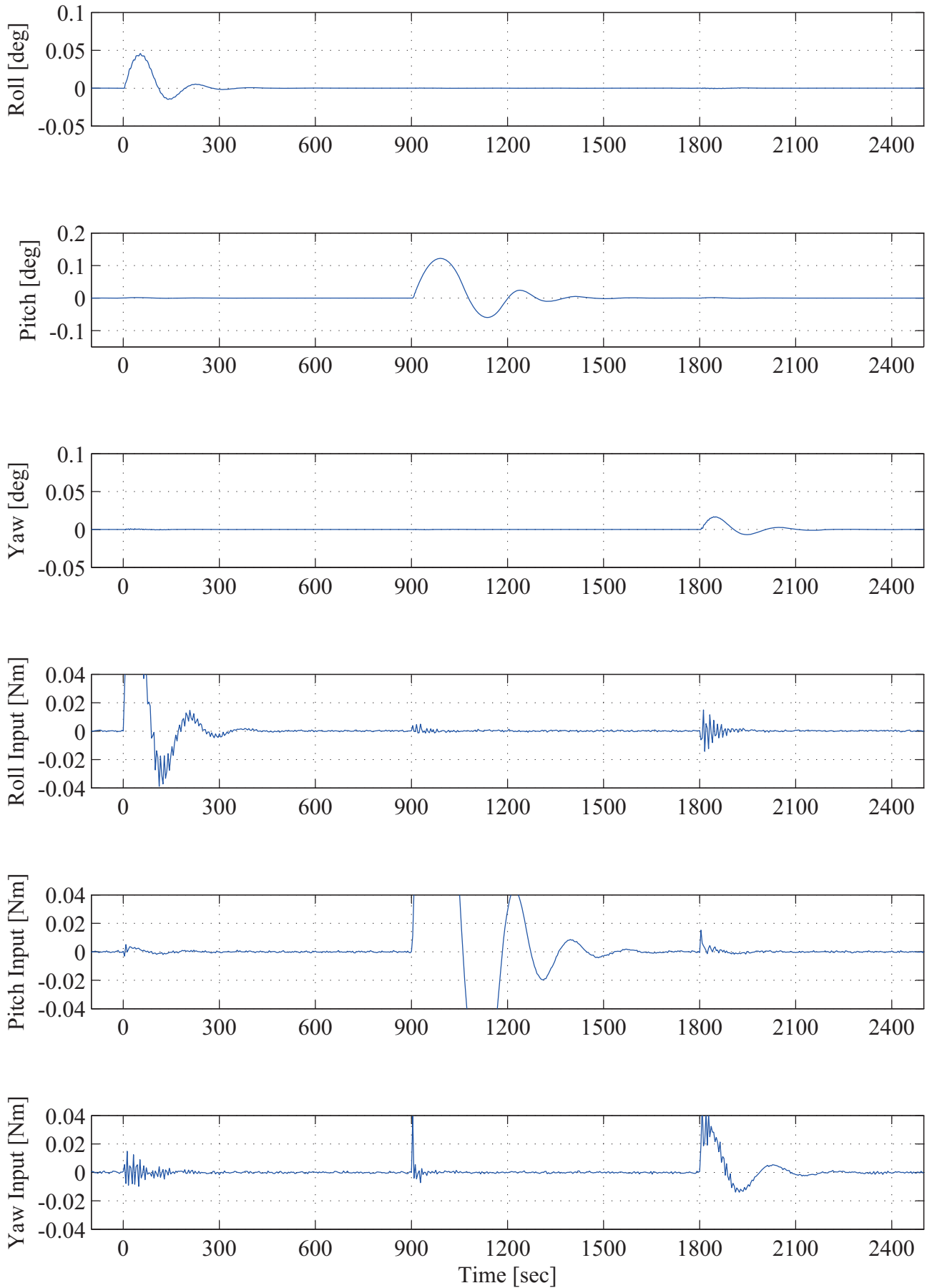
Figure 118: Large disturbance response using the DVDFB control law. The paddle rotation angle $\delta = 120$ at $t = 0$.
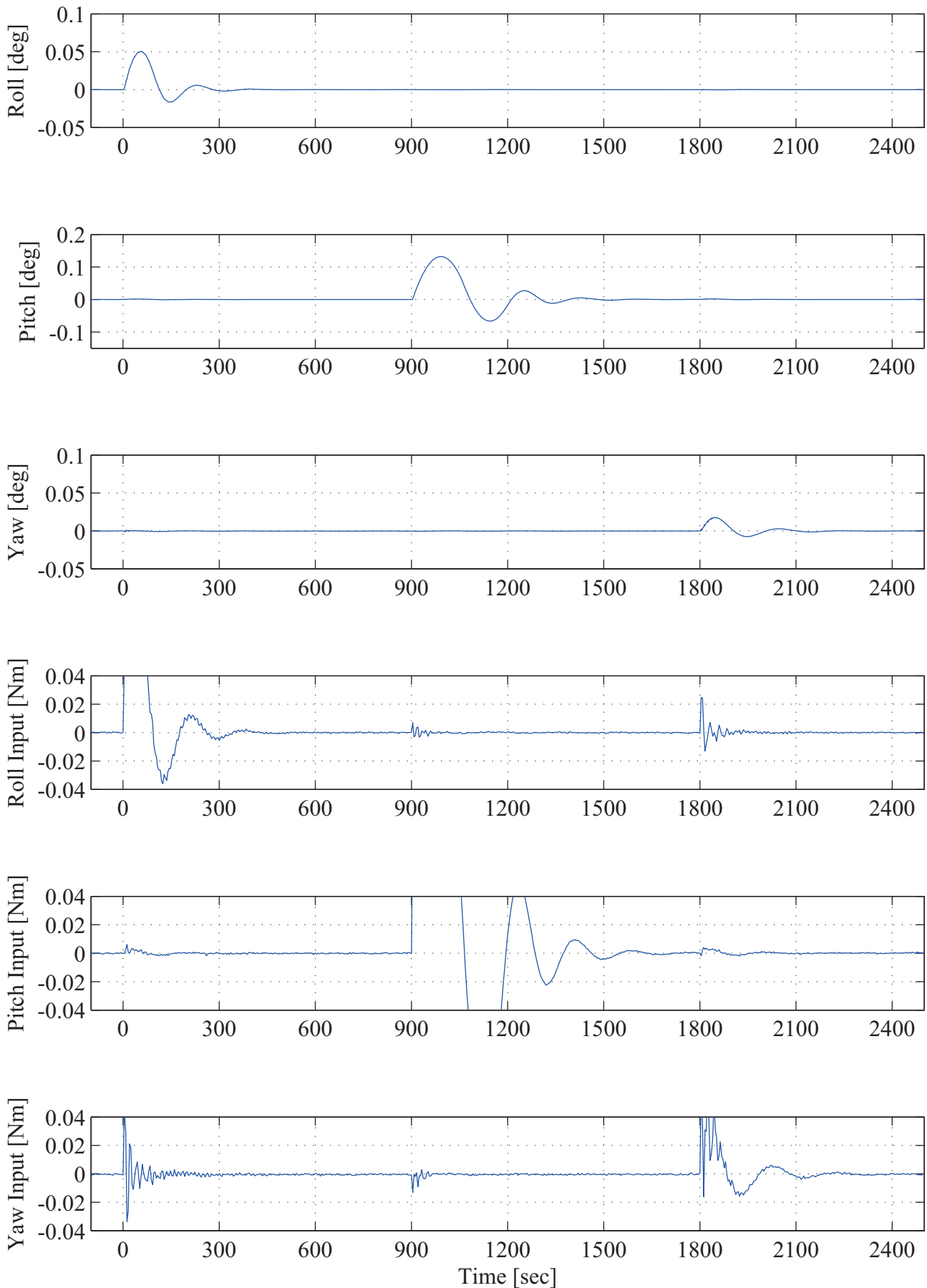
Figure 119: Large disturbance response using the DVDFB control law. The paddle rotation angle $\delta = 150$ at $t = 0$.
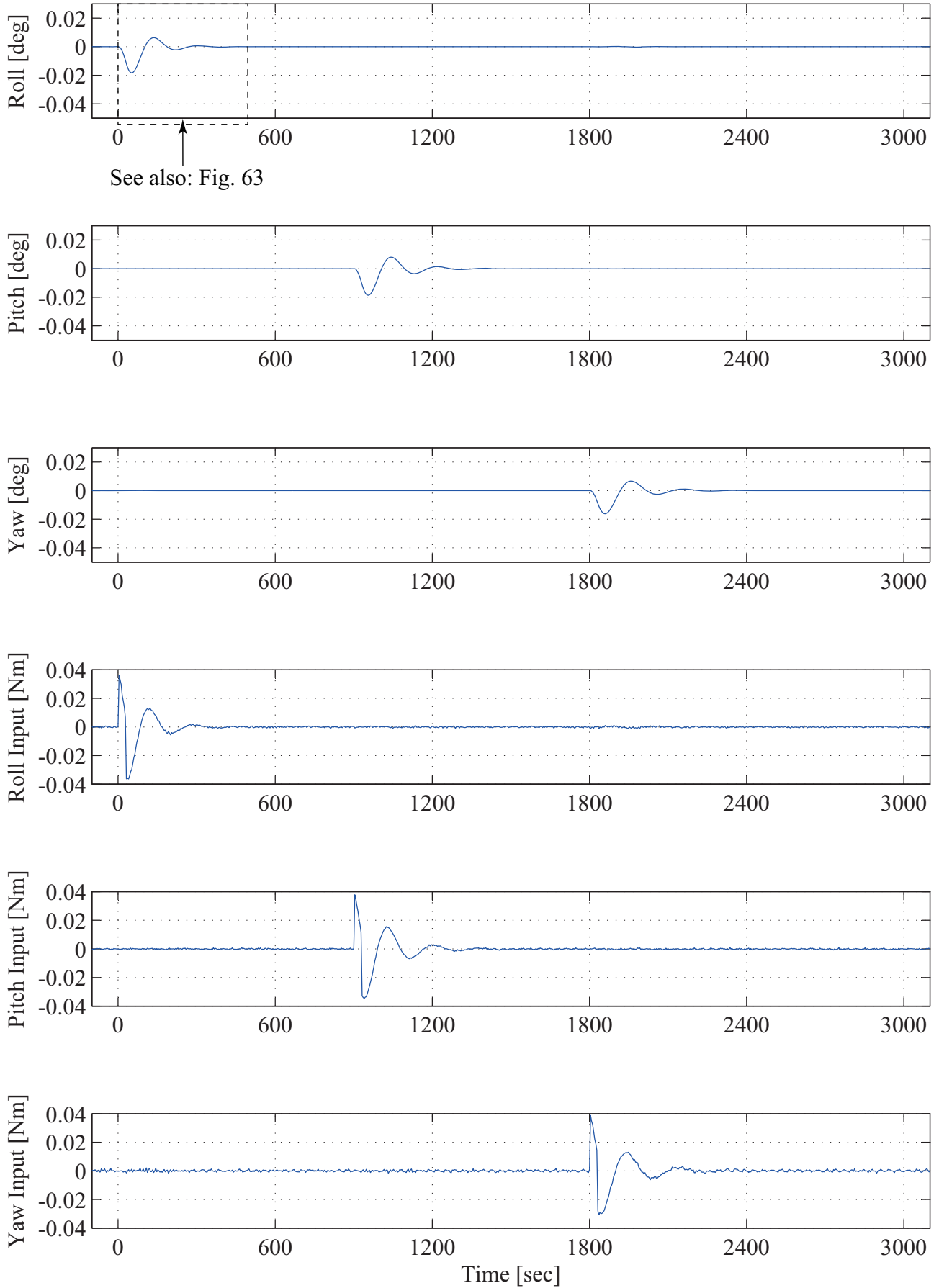
Figure 120: Rectangular disturbance response using the DVDFB control law. The paddle rotation angle $\delta = 45$ at $t = 0$.
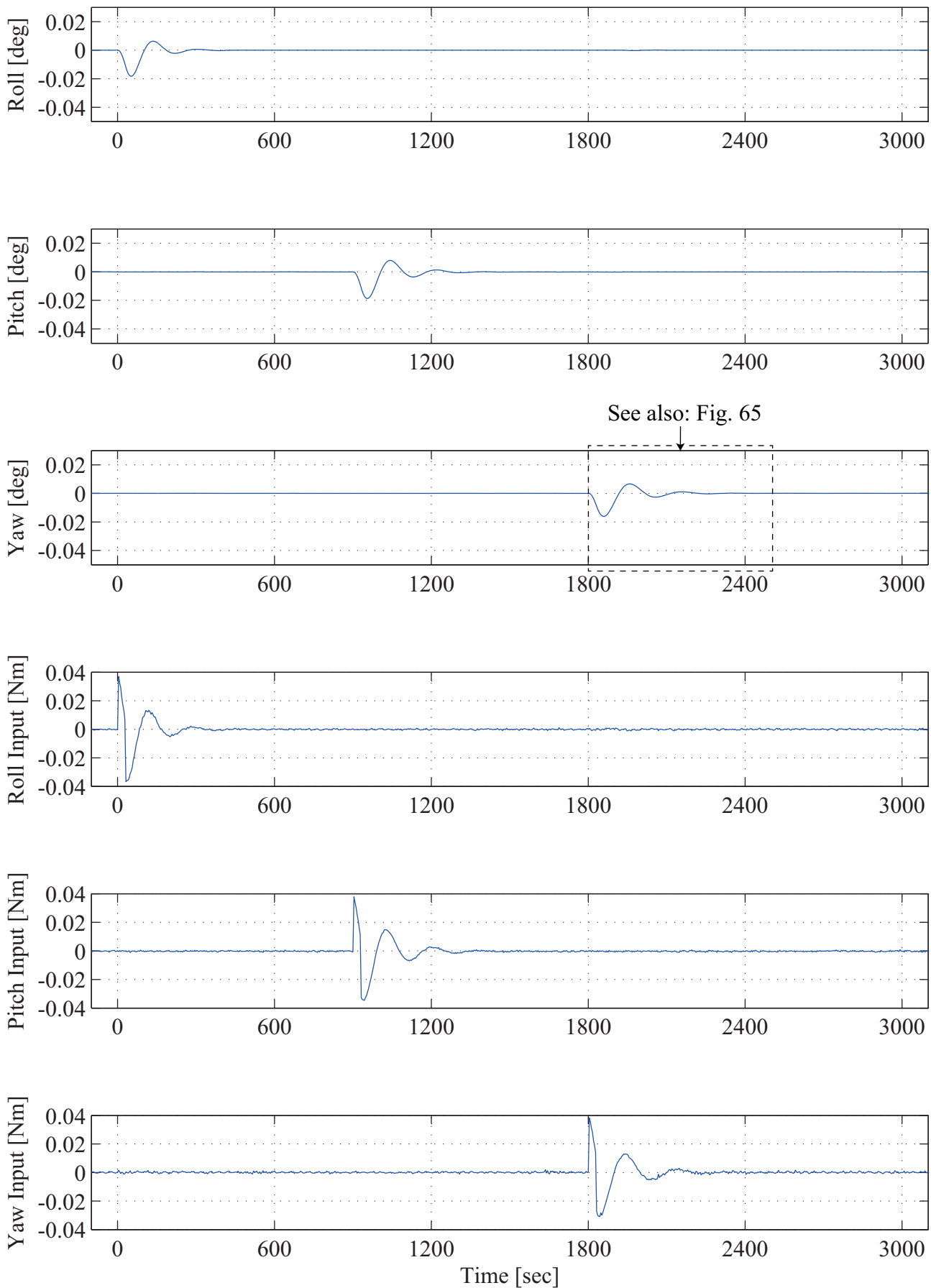
Figure 121: Rectangular disturbance response using the DVDFB control law. The paddle rotation angle $\delta = 137.5$ at $t = 0$.
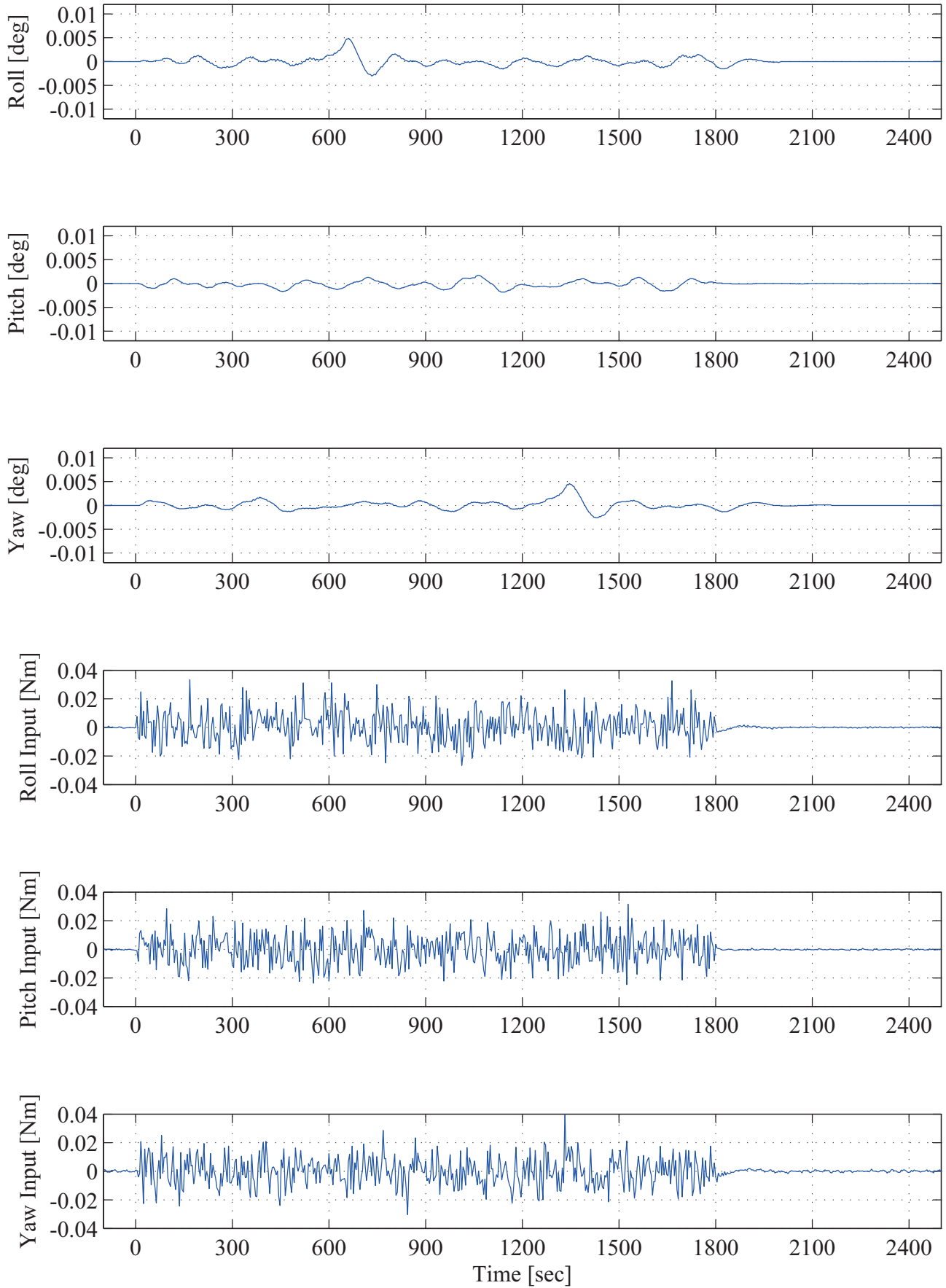
Figure 122: Random disturbance response (A) using the DVDFB control law. The paddle rotation angle $\delta = 60$ at $t = 0$.
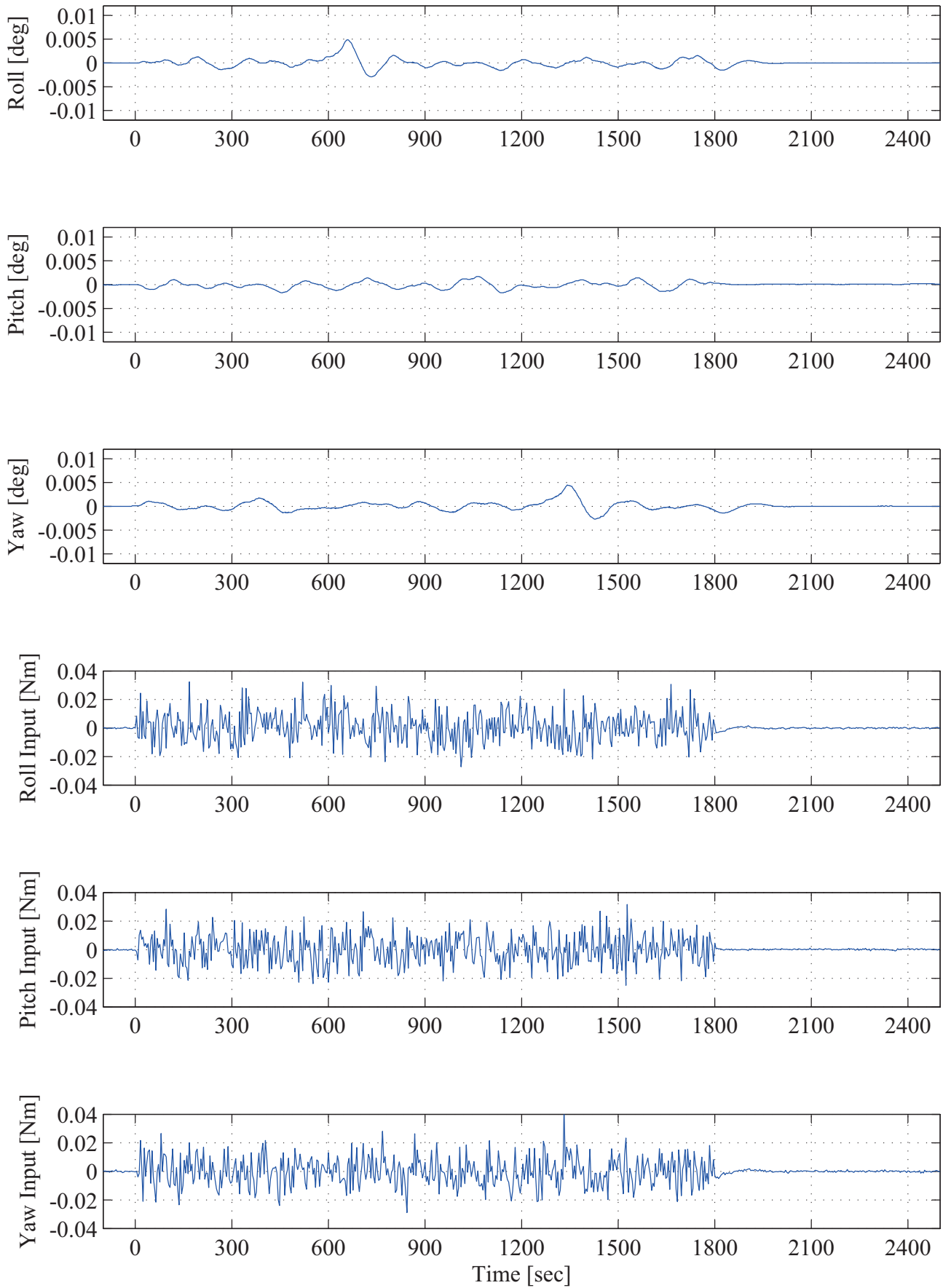
Figure 123: Random disturbance response (A) using the DVDFB control law. The paddle rotation angle $\delta = 153.75$ at $t = 0$.
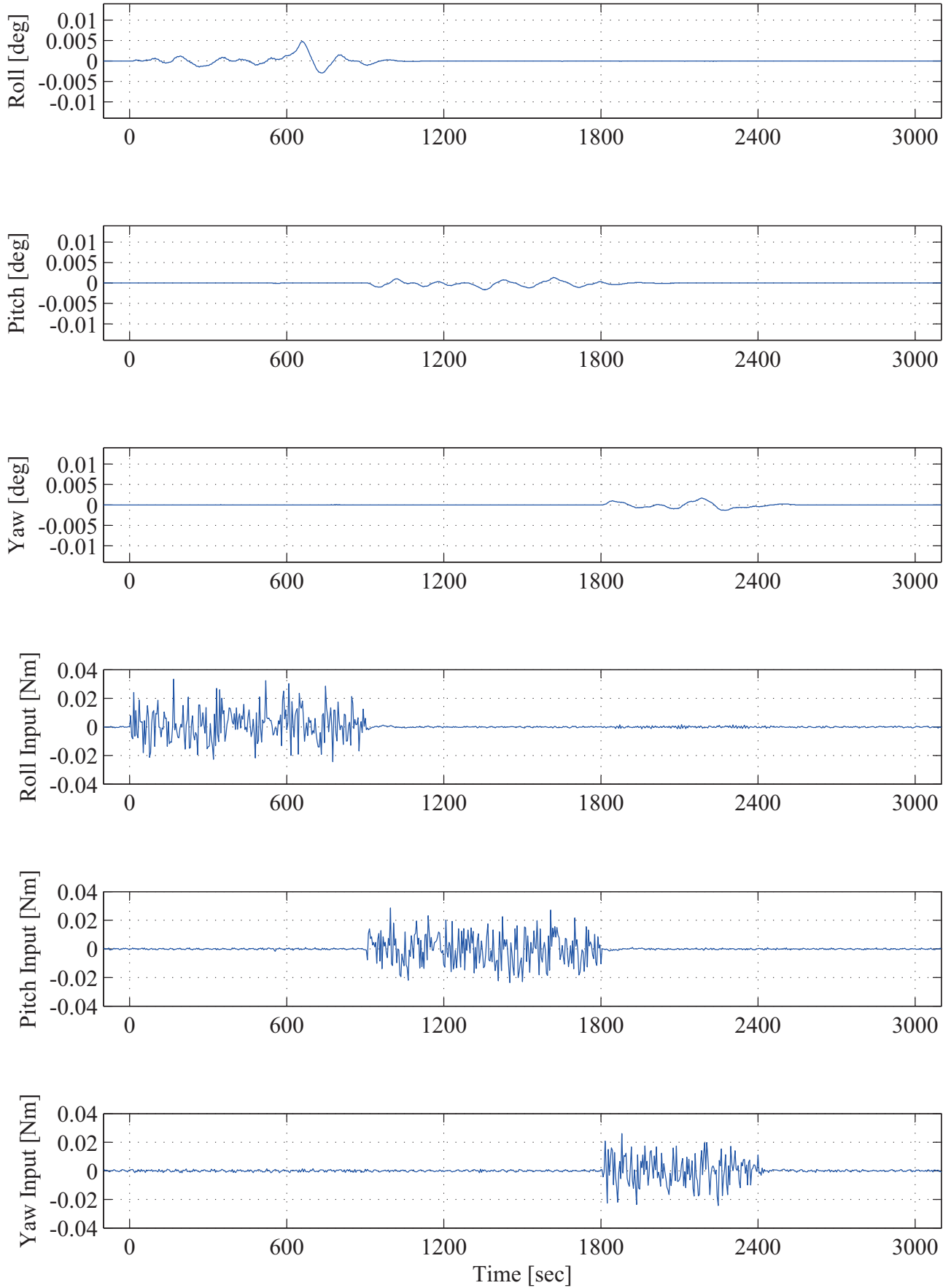
Figure 124: Random disturbance response (B) using the DVDFB control law. The paddle rotation angle $\delta = 117.5$ at $t = 0$.
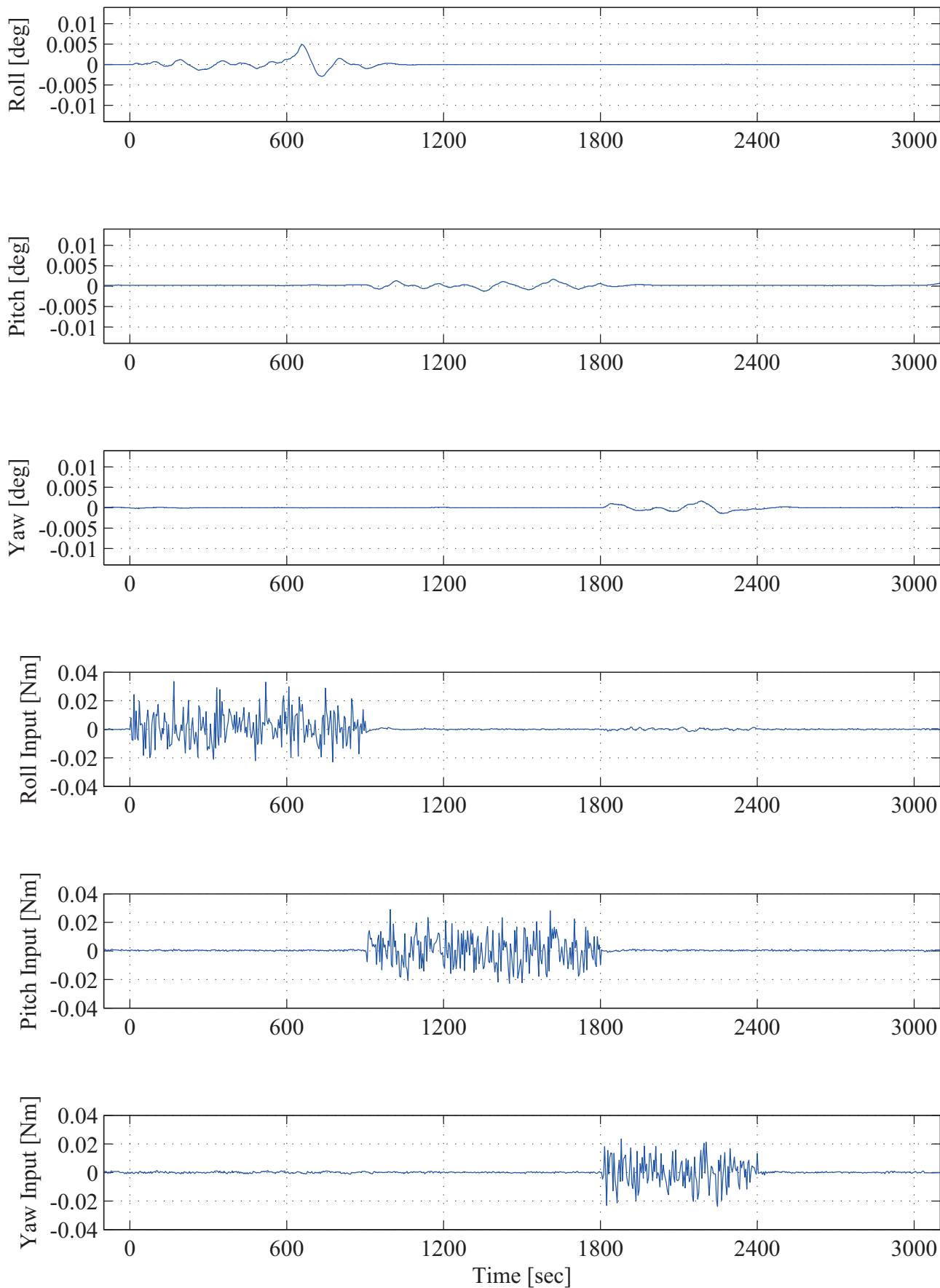
Figure 125: Random disturbance response (B) using the DVDFB control law. The paddle rotation angle $\delta = 180$ at $t = 0$.